UNIVERSITY OF SOUTHAMPTON

Faculty of Engineering and Physical Sciences
School of Electronics and Computer Science

Concentration Polarization Electroosmosis: Theory and Applications

DOI: 10.5258/SOTON/T0063

by

Raúl Fernández-Mateo

ORCiD: 0000-0003-1413-8046

A thesis for the degree of
Doctor of Philosophy

July 2023

University of Southampton

Abstract

Faculty of Engineering and Physical Sciences
School of Electronics and Computer Science

Doctor of Philosophy

Concentration Polarization Electroosmosis: Theory and Applications

by Raúl Fernández-Mateo

Electrokinetics plays a significant role in microfluidic and Lab on Chip systems. Over the last 25 years, the understanding of electrokinetic phenomena has matured considerably, leading to new ways of manipulating fluids and particles on the micro-scale efficiently.

This thesis describes experimental characterization and theoretical modelling of a new AC electrokinetic effect termed Concentration-Polarization Electroosmosis, or CPEO. This phenomenon describes steady-state electroosmotic flows that occur around charged insulating micro-structures in the presence of a low-frequency AC electric field. CPEO arises from concentration polarization (CP) and is driven by surface conductance, meaning that the characteristic time is governed by diffusion, $t \sim a^2/D$ (a is the length scale and D the diffusion constant of the electrolyte ions). As a result, CPEO is observed at low frequencies, e.g. around 300 Hz and below for a 1 μm-sized object immersed in a low-conductivity KCl electrolyte.

In this thesis CPEO flows are studied around features fabricated within microfluidic channels, such as pillars and constrictions. A theoretical framework is presented based on recent analytical approaches that provided macroscale boundary conditions for the electric and hydrodynamic problem; these are extended for the case of AC fields. A linear expansion for small Dukhin numbers gives an analytical description for the flows, which is found to be in excellent agreement with experimental observations. Further description for arbitrary Dukhin numbers (large surface conductance) and small electric field magnitudes predicts CPEO flows around charged microparticles. New image analysis methods allow experimental measurements of CPEO on a smaller scale, matching theoretical predictions.

It is known that during electrophoresis, particles are repelled from the channel walls. This behaviour is magnified at low frequencies and low conductivities, something that has been reported in the literature but remains unexplained. For these experimental conditions, CPEO flows around suspended particles in microchannels predict hydrodynamic wall-particle repulsive interactions. Experiments confirm that the observed repulsion is caused by quadrupolar fluid flows around the particles, and a detailed characterization has demonstrated that the phenomenon is due to CPEO. Given the known dependence of these flows upon the particle size and surface charge (zeta-potential), CPEO was exploited to fractionate different polystyrene particles.

The thesis also describes novel procedures and techniques developed to deliver the main results of the project. A simplified method was discovered for measuring the zeta potential of a microfluidic channel with improved precision. Also, a user-friendly software has been developed for rapid particle detection called Particle Finder. This tool performs automated image analysis of large numbers of images allowing rapid analysis of particles moving in a continuous flow. Finally, the thesis describes how the ideas of CPEO can be used to explain the low-frequency behaviour of an electrokinetic biased Deterministic Lateral Displacement (DLD) device, where the CPEO flows were initially observed. Numerical simulations of particle trajectories were made considering the wall repulsion from the pillars in the DLD array. These show agreement with previous experiments, providing a full quantitative understanding of the DLD separation system for all frequencies and conductivities.

Contents

Declaration of Authorship

I declare that this thesis and the work presented in it is my own and has been generated by me as the result of my own original research.

I confirm that:

1. This work was done wholly or mainly while in candidature for a research degree at this University;
2. Where any part of this thesis has previously been submitted for a degree or any other qualification at this University or any other institution, this has been clearly stated;
3. Where I have consulted the published work of others, this is always clearly attributed;
4. Where I have quoted from the work of others, the source is always given. With the exception of such quotations, this thesis is entirely my own work;
5. I have acknowledged all main sources of help;
6. Where the thesis is based on work done by myself jointly with others, I have made clear exactly what was done by others and what I have contributed myself;
7. Parts of this work have been published as:

   (a) V. Calero, R. Fernández-Mateo, H. Morgan, P. García-Sánchez, and A. Ramos, "Stationary electro-osmotic flow driven by ac fields around insulators," *Physical Review Applied*, vol. 15, no. 1, p. 014047, 2021

   (b) R. Fernández-Mateo, P. García-Sánchez, V. Calero, H. Morgan, and A. Ramos, "Stationary electro-osmotic flow driven by ac fields around charged dielectric spheres," *Journal of Fluid Mechanics*, vol. 924, 2021

   (c) R. Fernández-Mateo, V. Calero, H. Morgan, A. Ramos, and P. García-Sánchez, "Concentration–polarization electroosmosis near insulating constrictions within microfluidic channels," *Analytical Chemistry*, vol. 93, no. 44, pp. 14667–14674, 2021

   (d) R. Fernández-Mateo, P. García-Sánchez, V. Calero, A. Ramos, and H. Morgan, "A simple and accurate method of measuring the zeta-potential of microfluidic channels," *Electrophoresis*, vol. 43, p. 1259–1262, 2022

   (e) R. Fernandez-Mateo, V. Calero, H. Morgan, P. Garcia-Sanchez, and A. Ramos, "Wall repulsion of charged colloidal particles during electrophoresis in microfluidic channels," *Physical Review Letters*, vol. 128, p. 074501, 2022

   (f) R. Fernandez-Mateo, H. Morgan, A. Ramos, and P. Garcia-Sanchez, "Wall repulsion during electrophoresis: Testing the theory of concentration-polarization electroosmosis," *Physics of Fluids*, vol. 35, no. 012019, 2023

(g) R. Fernández-Mateo, V. Calero, P. García-Sánchez, A. Ramos, and H. Morgan, "Particle finder: a simple particle detection tool for continuous-flow systems," *Microfluidics and Nanofluidics*, vol. 27, no. 3, p. 19, 2023

(i) Víctor Calero, Raúl Fernández-Mateo, Pablo García-Sánchez, Antonio Ramos, and Hywel Morgan. Rectified ac electroosmosis induced by surface conductance around insulating posts. micro-TAS 2020

(ii) Raúl Fernández-Mateo, Víctor Calero, Pablo García-Sánchez, Antonio Ramos, and Hywel Morgan. Stationary Electro-osmotic flow vortices on insulating surfaces induced by ac electric fields. Dielectrophoresis 2021

(iii) Raúl Fernández-Mateo, Víctor Calero, Pablo García-Sánchez, Antonio Ramos, and Hywel Morgan. Concentration-Polarization Electroosmosis. micro-TAS 2021

(iv) Raúl Fernández-Mateo, Víctor Calero, Hywel Morgan, Pablo García-Sánchez, and Antonio Ramos. Hydrodynamic Particle-Wall Interaction in Electrophoresis. ELKIN 2022

(v) Raúl Fernández-Mateo, Pablo García-Sánchez, Antonio Ramos, and Hywel Morgan. Concentration-Polarization Electroosmosis for Particle Fractionation. NanoBio Tech 2022

(vi) Raúl Fernández-Mateo, Víctor Calero, Hywel Morgan, Pablo García-Sánchez, and Antonio Ramos. Insulating Travelling-Wave Electrophoresis. Gordon Research Conference 2023

Signed:..... Date:.....

Acknowledgements

I would like to thank Antonio Ramos and Pablo García-Sánchez for first offering me the opportunity to start this journey, and then for providing guidance and support in the kindest and most effective way throughout the project. I would also like to thank my supervisor, Hywel Morgan, for providing the life-changing opportunity to begin my scientific career, for his continued guidance and support, and for giving me the freedom to make this project my own. I would like to especially thank Víctor Calero, who introduced me to the lab work and to the PhD life in general. Through this project he has been an integral part of the journey, acting as a supervisor, as a colleague, and most importantly as a friend. Together with my supervisors, with this team I have taken my first steps in science, learning that kindness and generosity are key to success. Although this project has come to an end, I am sure our collaboration will be long-lasting.

I would like to thank Alberto T. Pérez from the University of Sevilla, who introduced me to the world of academic research and who initially gave his essential support to pursue a scientific career. I would also like to thank the people within the CHB group at the University of Southampton who where friends in addition to work colleagues, always willing to help and support me: Roel, Nikita, João, Wahida, Xiang, Tom, Zijin, Miguel, Junyu, Xueping, and many others. Especially to Ric Gillams, with whom I shared many hours in the lab during the pandemic and always provided good advice and kind support; Fernando García who was my Spanish safety net during my project and with whom I shared great laughs and discussions during lunches; and Jon Butement who always gave support in the lab and greatly contributed to make Southampton feel as home after the pandemic.

To Patricia whose love, support, understanding and generosity made this journey possible. With her I have shared the joys of reuniting and sorrows of farewells during these years living apart. Together we have also shared the experiences of pursuing our own PhD, which have allowed me to witness her own journey to the great scientist she will become. To my family that have always backed my decisions and provided constant and unconditional loving support and care, for which I will never be grateful enough. Finally, to the rest of my friends in Southampton, who welcomed me as I was born there, and to my friends back in Spain, who make me feel as I never left.

A mi madre, Aurora

A mi padre, Ramón

A mi hermano, Daniel

List of Abbreviations

AC	alternating current
ACEO	AC electroosmosis
CA	carrier ampholites
CM	Clausius-Mossotti factor
CP	concentration-polarization
CPEO	concentration-polarization electroosmosis
CTC	circulating tumor cell
DEP	dielectrophoresis
DI	deionised
DP	diffusiophoresis
EDL	electrical double layer
EK	electrokinetic
EO	electroosmosis
EP	electrophoresis
EV	extracellular vesicle
fps	frames per second
GUI	graphical user interface
ICEO	induced-charge electroosmosis
iDEP	insulator-based dielectrophoresis
IEF	isoelectric focusing
iHP	inner Helmholtz plane
KCl	potassium chloride
nDEP	negative dielectrophoresis
oHP	outer Helmholtz plane
pDEP	positive dielectrophoresis
PDMS	polydimethylsiloxane
PMMA	Poly(methyl methacrylate)
PNP	Poisson-Nernst-Planck
RBC	red blood cell
SY	Schnitzer-Yariv
UV	Ultraviolet
WBC	white blood cell

List of Symbols

as used in Parts I and III of the thesis

a	particle radius
Bi	Bikerman number
c	ionic concentration
D	diffusion constant
$\mathbf{D}$	electric displacement field
Du	Dukhin number
e	electron charge
$\mathbf{E}$	electric field
E_0	applied electric field magnitude
f_{CM}	Clausius-Mossotti factor
$\mathbf{f}_m$	body force per unit mass
$\mathbf{F}_D$	viscous drag force
$\mathbf{F}_{DEP}$	dielectrophoretic force
i	imaginary unit
$\mathbb{I}$	identity matrix
I_s	surface current
$\mathbf{j}$	electric current density
k_B	Boltzmann constant
K_L	bulk conductance
K_s	surface conductance
$\hat{n}$	unit vector perpendicular to surface
p	pressure field
$\mathbf{p}$	dipole moment
p_m	punctual dipole moment
Pe	Peclet number
q_p	point charge magnitude
q_s	surface charge density
Q_s	surface charge
Re	Reynolds number
t	time
T	absolute tempreature

$\mathbf{u}$	particle velocity
$\mathbf{u}_{DP}$	diffusiophoretic velocity
$\mathbf{u}_{EP}$	electrophoretic velocity
$\mathbf{v}$	fluid velocity field
$\mathcal{V}$	maximum slip velocity
Z	ionic valence
α	ionic drag coefficient
γ	asymmetry parameter of the electrolyte
γ_E	Euler–Mascheroni constant
δ	scaled Debye length
ε	electric permittivity
ε_p	particle permittivity
ε_0	vacuum permittivity
ζ	zeta potential
ζ_p	particle zeta potential
η	dynamic viscosity of the fluid
λ_D	Debye length
μ	mobility
ξ	± 1
ρ	volumetric charge of electrolyte
ρ_m	density of the fluid
σ	electrolyte conductivity
σ_p	particle conductivity
σ_s	surface conductivity
$\hat{\tau}$	unit vector tangential to surface
$\bar{\bar{\tau}}$	viscous stress tensor
ϕ	electric potential
ϕ_{th}	thermal electric potential
ψ	stream function
$\mathbf{\Psi}$	velocity vector potential
ω	angular frequency of the electric field
ω_c	dielectrophoresis crossover angular frequency

Part I

Introduction

Chapter 1

Context

1.1 Microfluidics for Particle Separation

Biological fluids are generally composed of a complex mixture of cells, Extracellular Vesicles (EVs), proteins and salt at different concentrations and with sizes ranging from a few tens of microns down to the nanoscale [8]. They can also contain particles that are indicative of a disease. One example is the presence of circulating tumor cells, or CTCs, in blood. These are cells released from a solid tumor that cross the endotheluim and enter the blood stream, initiating metastasis [9]. Another example is the presence of bacteria (or fungi) in blood, i.e. bacteremia, one of the main causes of sepsis [10]. Both these examples share that the particle concentration is very low compared with the majority of other particles of similar sizes, with numbers as low as 100 cells/mL.

For the case of cancer, early diagnosis has also focused on EVs, which are lipid bilayer coated vesicles secreted by virtually every cell type, and considered to be a main source of intercellular communication [11]. Their size ranges from ~ 30 nm to ~ 250 nm [12], and are present in body fluids including blood and urine at high concentration [13]. Isolation of EVs for diagnostic purposes is therefore minimally invasive. They carry a cargo of molecules that reflect the tissues they are released from – most importantly DNA, RNA, proteins and lipids produced at an abnormal concentration when a disease is present. Thus, profiling these molecules could provide a powerful diagnostic tool, for example determining biomarkers to indicate cancer [14].

A critical step towards improving diagnostics is the isolation and enrichment of the target particles from the other components of the fluid. This is a formidable challenge given the size of the particles that need to be isolated (for EVs), or the low concentration in which they are present (bacteria or CTCs). Current separation techniques are lengthy, costly, and require substantial pieces of equipment with large amounts of sample and reagents. For example, isolation of EVs relies on ultracentrifugation, or immuno-affinity capture, requiring costly equipment and specialized skills [15, 16], with a high risk of sample damage. In the case of bacteremia, the current practice is to isolate bacteria after growth in blood bottles, which

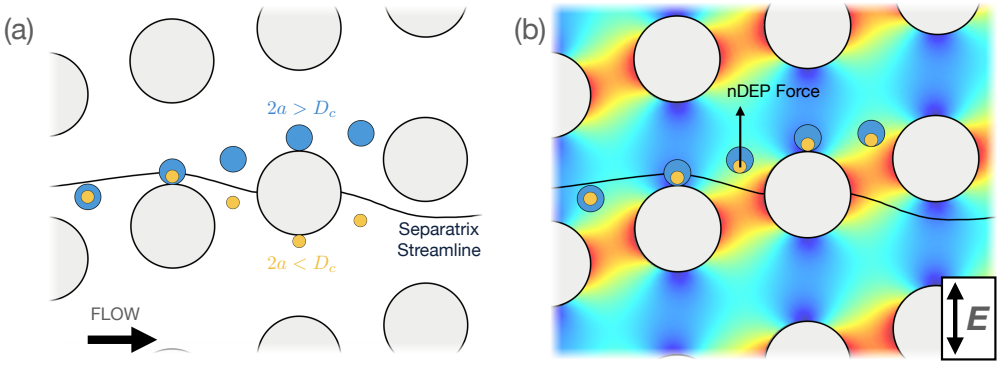

FIGURE 1.1: (a) Diagram showing the DLD separation mechanism. (b) Separation enhancement of the DLD array when coupled with an orthogonal electric field.

requires a long incubation of at least 8 hours, a technique that has not changed for decades. After incubation, a phenotypic analysis is obtained through an antibiotic susceptibility test (AST), which again involves up to 48 hours of antibiotic exposure [17].

Microfluidics could provide new approaches to particle isolation providing a high yield, high throughput solution for isolation and enrichment of particles at the micron and sub-micron scale. Microfluidics has been used for high-resolution particle fractionation at the micron-scale in continuous flow, achieved through hydrodynamic particle-wall interactions involving no externally applied forces (e.g. inertial lift, viscoelastic lift, flow-focusing) and/or collision with channel features as in the case of the Deterministic Lateral Displacement (DLD) [18, 19, 20]. The techniques requiring no external fields are often referred as passive techniques [21], and have been extensively used for blood debulking, that is, separation of larger white blood cells (WBCs) from the smaller components (red blood cells (RBCs), platelets, bacteria and EVs) [19, 22]. Inertial techniques have achieved unmatched throughputs for this task [22], and are a realistic alternative to the current techniques used in hospitals.

Microfluidic separation devices have also been developed that use external forces to act on the fluid flow or the particles. An example of a practical application of this technique is microfluidics for isolation of CTCs from clinical samples for the early detection of metastasis initiation [23]. Such platform would be simply not possible using only hydrodynamic interactions given the size similarities between CTCs and WBCs in blood. Specific antibody-mediated binding of the WBCs (using the CD45 surface antigen) to magnetic beads allowed using magnetophoresis (the manipulation of particles using external magnetic fields) to achieve high efficiency negative selection of the CTCs [24].

Another microfluidic technique that has undergone a major development through the use of external fields is DLD [25, 26]. A DLD device consists of a two-dimensional pillar array in which each row of pillars is displaced a small distance with respect to the preceding row in the downstream direction (Fig 1.1). This means the array is tilted with respect to the net direction of the fluid flow. As shown in Figure 1.1(a), the difference in directions implies that streamlines of the fluid flow will eventually intersect with the pillars in the array, called *separatrix streamlines*. The tilting of the array with respect to the fluid flow, together with the size of the pillars and the

separation between rows, marks the distance between separatrix streamlines and posts in the row previous to intersection. Particles bigger than this separation will eventually collide with the pillars in the array and be forced to follow the direction of the array. Therefore, the technique exploits the collisions of particles with the posts to achieve fractionation: smaller particles will follow the direction of the fluid flow (zigzagging mode) and larger particles will flow following the net direction marked by the pillar array (bumping mode). The minimum particle diameter that forces crossing the separatrix streamline is known as the critical diameter D_c. Thus, the term *separatrix* makes reference to the mode change implied in crossing this particular set of streamlines, in analogy to the mathematical definition [27].

Experimentally it has been shown that the critical diameter is of the order of the dimensions of the pillars and gaps between pillars in the array. Therefore in order to fractionate (nano-scale) EVs nanometric-scale silicon pillars have been developed [28, 29], however these devices are complicated to fabricate and have very low throughput with extremely high back-pressure. Micrometric pillar arrays coupled with external electric fields applied orthogonal to the fluid flow, as shown in Figure 1.1(b), have been used to reduce the critical diameter down to the nanoscale [30], enabling EV fractionation with no additional fabrication complexity. During a suspension in my thesis project, I joined an EU project[1] whose aim was to develop a microfluidic platform for achieving a standardised method for obtaining EVs, from which we demonstrated proof of principle that it is possible to fractionate EVs based on size using a micron-scale DLD platform biased with electrokinetics at high conductivity [31].

1.2 Electrokinetics and Microfluidics

Integration of electrical forces with microfluidics has proven tremendously beneficial not only in DLD, allowing tunability inside microchannels and new ways of actuation on fluid flows and sample for improved efficiency. In doing so, microfluidics has opened to the study of very rich and novel physical phenomena. In this context, electrokinetics plays a particularly important role, as it benefits from the scaling laws of surface effects at the microscale. Over the last two decades, with the development of microfluidic and Lab on Chip (LoC) systems, the understanding of electrokinetic phenomena has improved substantially leading to new ways of manipulating fluids and particles on the micro- and nano-scale.

As an example, more than two decades ago it was shown that fluid can be set into motion on microelectrode surfaces subjected to AC electric fields [36, 37] as shown in Figure 1.2(a). This phenomenon was termed AC electroosmosis or ACEO, and a complete theoretical and experimental characterization [38, 39, 32] inspired new ways of pumping electrolytes and moving particles in microfluidics. This was done either by asymmetric electrode configurations [40] or travelling-wave electric field signals [41, 42]. This pioneering work led to the generalization of ACEO to conducting surfaces of arbitrary shapes such as the ones shown in Figure 1.2(b)

[1] The European project "The Extracellular Vesicle Foundry" http://www.evfoundry.eu

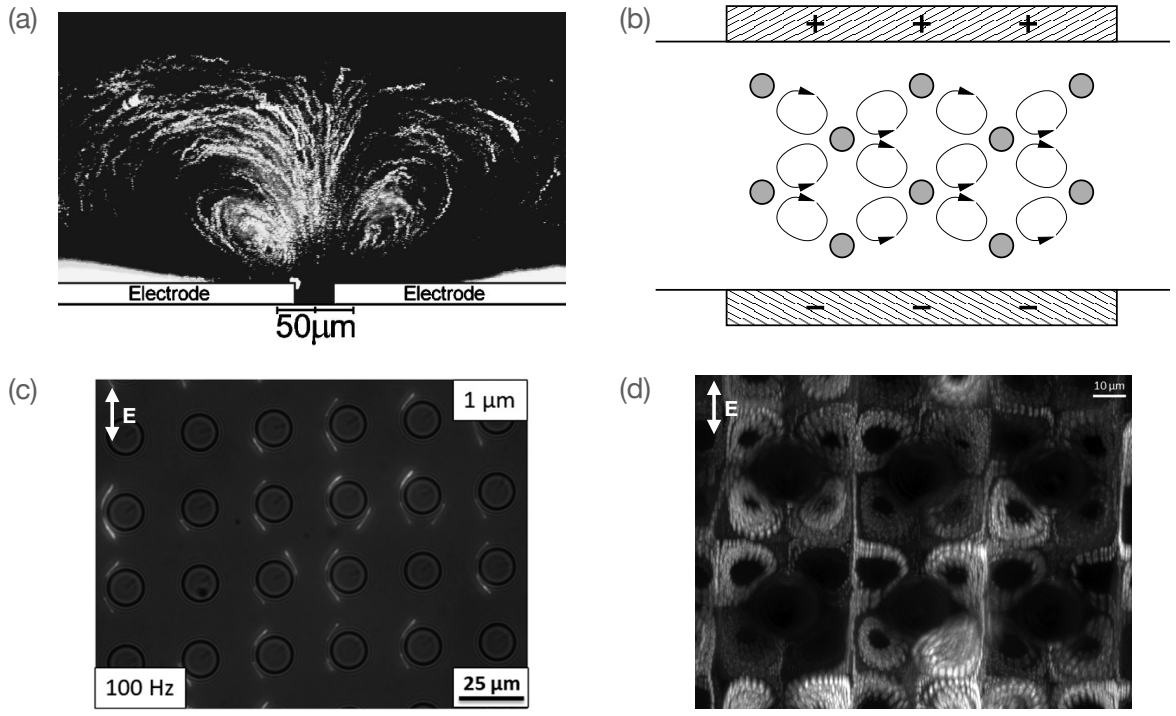

FIGURE 1.2: (a) Experimental observation of ACEO fluid flow on top of microelectrodes with an AC voltage (2 Volts and 100 Hz). Electrolyte conductivity is 2.1 mS/m. Image taken from Ref. [32]. (b) Diagram showing quadrupolar fluid flows around metallic pillars using ICEO; from Ref. [33]. (c) Experimental observation of particle oscillations around dielectric pillars in low frequency AC fields and DI water; image from Ref. [34] (d) Quadrupolar flows around dielectric pillars in low frequency (70 Hz) electric fields in 2.8 mS/m conductivity electrolyte; image from Ref. [35]

[33, 43]. The flow was termed induced-charge electroosmosis (ICEO), and had extremely impactful applications in fluid flow and particle manipulation in microfluidics.

More recently, the application of AC voltages to electrodes placed along a DLD microfluidic channel [34, 30] revealed steady-state electroosmotic fluid flows at low electric field frequencies and low electrolyte conductivities around the insulating pillars when the pressure-driven flow was stopped (see Figure 1.2(c,d)). In the regime where these flows dominated, fractionation by DLD could not be explained [35], and the phenomenon could not be described using classical electrokinetics.

1.3 Project Aim

This thesis describes a new AC electrokinetic phenomenon called **Concentration Polarization Electroosmosis** or CPEO. It provides a new framework that describes the steady-state electroosmotic flow vortices arising around dielectric objects in the presence of low-frequency AC electric fields and low-conductivity electrolytes. An example is the flow patterns observed around microfluidic pillars shown in Figure 1.2(d).

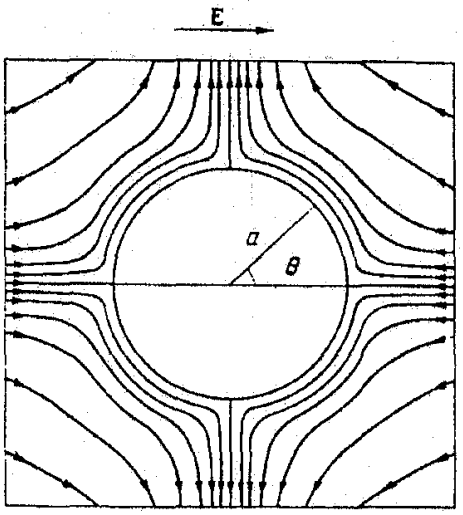

FIGURE 1.3: Streamlines showing quadrupolar fluid flow structures around a charged dielectric particle predicted by Gamayunov *et al.* in 1986 [48].

This fluid behaviour around microfluidic corners and constrictions [44, 45, 46], or insulating pillars [47] had been widely reported. These were attributed to ICEO given the similarities in the flow patterns around conducting surfaces and their apparent agreement with the scaling with the electric field magnitude and frequency. In this thesis it is demonstrated that ICEO theory cannot describe the observed electroosmotic phenomena around dielectrics, nor can any other electrokinetic model currently available.

It is shown that the observed electroosmotic flows arise from the polarization of the electrolyte concentration around the dielectric in the presence of the field. This phenomenon is known as Concentration Polarization (CP), and it arises from the surface conductance within the electrical double layer (EDL). Using CP as a mechanism to describe the electroosmotic flows demonstrates that the frequency behaviour scales with the inverse of the diffusion time, in agreement with experimental observations.

The influence of surface conductance and CP in predicting hydrodynamic flow around dielectrics was already predicted by Dukhin and co-workers in the context of electrophoresis of highly charged colloids [49, 48, 50, 51, 52]. They used physical arguments to argue that CP and/or induced charge within the electrical double layer (EDL) should be responsible for quadrupolar flows around charged dielectric spheres, and used this to explain the interaction between particles undergoing DC electrophoresis [48]. The predicted flow pattern is shown in Figure 1.3, and resembles the experimental observations of fluid flow around insulating pillars in Figure 1.2(d).

Recent mathematical approaches that describe surface conductance [53, 54] have allowed a systematic description of the phenomenon. This thesis builds on these publications and develops a generalised framework to describe the observed electroosmotic flows in AC electric fields around pillars. It predicts the appearance of similar flows around other dielectric microstructures such as constrictions and dielectric particles. CPEO provides a single framework for explaining observations of flows around microfluidic corners reported in the literature, around pillars in the

context of DLD, and the predictions of flows around colloids by Gamayunov. It is illustrated how these flows can be used to predict hydrodynamic particle-wall interactions, which unifies the apparently unrelated CPEO flows with the previously reported particle focusing in electrophoresis [55, 56] as well as the unexplained particle fractionation observed in DLD devices at low conductivities and low electric field frequencies.

This thesis also describes how the CPEO-induced wall-particle interaction can be exploited as a standalone technique for particle fractionation in continuous flow at the micron scale. It further discusses in brief how this novel technique could be coupled with current state-of-the-art separation technologies in microfluidics as an additional tuning parameter to enhance the efficiency of sample separation. Future research will build on the work presented in this thesis to develop new approaches aimed at the high-throughput sub-micron separation that could provide an alternative to the current gold-standard methods used in hospitals described at the beginning of the chapter.

Finally the thesis describes a novel method for experimentally determining the zeta potential in microfluidic channels as well as an analysis tool for detecting and positioning particles continuously flowing in microfluidic channels. These technical tools were developed to deliver the experimental CPEO data. Also described is a system for particle manipulation based on electrophoretic mobility using a rotating electric field with travelling wave components.

1.4 Thesis Outline

This thesis is divided into three parts. Part I is a general introduction to the work, and contains three chapters. The first two chapters provide context for the experimental observations of fluid flow and a motivation to the project. These chapters also describe the physical and mathematical tools developed to understand the results. Chapter 3 describes the design of the microfluidic channels used to perform the experiments, the device fabrication methods, the experimental set-up and the analysis methodology. It additionally contains two method papers describing new experimental measuring techniques (Paper A) and analysis tools (Paper B) developed specifically to deliver the main scientific results of this thesis.

Part II displays the published research work describing CPEO. Each paper is preceded by a contribution statement and followed by a discussion of the contributions made by the research article. The set of papers contain both the theory and experimental validation of CPEO. They are ordered such that they constitute a comprehensive and substantive contribution to the field. Papers C to I conform the main work on CPEO theory and its applications to continuous-flow particle separation. Finally Paper J describes a novel electrokinetic phenomenon also developed through this thesis but not related to CPEO.

Part III highlights the main results of the thesis and discusses future research building on the work presented in this thesis. The references list (and the indexed phrases) at the end of the document accounts for the literature cited throughout the thesis excepting the published

material, i.e. the research articles presented in Part II and Appendices, which contain their own references list at the end.

Chapter 2

Background

This chapter provides an introduction to fundamental Electrokinetics, and describes approaches to microfluidic particle manipulation. It also describes the mathematical tools used in the project along with a physical interpretation of the phenomena required to understand CPEO and related electrokinetic effects.

2.1 Fluid Dynamics at the Micrometric Scale

In fluid dynamics, the *Navier-Stokes* equation describes the motion of a Newtonian and incompressible fluid as

$$\rho_m \frac{\partial \mathbf{v}}{\partial t} + \rho_m(\mathbf{v} \cdot \nabla)\mathbf{v} = -\nabla p + \eta \nabla^2 \mathbf{v} + \mathbf{f}_m, \tag{2.1}$$

where ρ_m is the density of the fluid, η the dynamic viscosity, p pressure and $\mathbf{f}_m$ an applied body force density. The velocity field of the fluid is $\mathbf{v}(\mathbf{x}, t)$, and its *streamlines* are defined as the lines parallel to the direction of the field in its domain at a given instant.

The Navier-Stokes equation is usually expressed in non-dimensional form as

$$\mathrm{Re}\left[\frac{\partial \bar{\mathbf{v}}}{\partial \bar{t}} + (\bar{\mathbf{v}} \cdot \bar{\nabla})\bar{\mathbf{v}}\right] = -\bar{\nabla}\bar{p} + \bar{\nabla}^2 \bar{\mathbf{v}} + \bar{\mathbf{f}}_m, \tag{2.2}$$

where Re is the *Reynolds number*, which indicates the relative magnitude of the inertial term (left-hand side of equation (2.1)) and the viscous term ($\eta \nabla^2 \mathbf{v}$). This number is defined as

$$\mathrm{Re} = \frac{\rho_m v_0 x_0}{\eta}, \tag{2.3}$$

where the sub-script 0 indicates the magnitude scale. According to this definition, equation (2.2) defines the pressure scale $p_0 = \eta v_0 / x_0$ and force scale $\mathrm{f}_0 = \eta v_0 / x_0^2$. The scaled variables have been written with a bar "$-$" to discriminate these from the initial equation (2.1). For the

remainder of the chapter non-dimensional variables will be used and the bars will be ignored unless explicitly indicated.

In microfluidics, typical values of these variables are [57] $x_0 \sim 10^{-4}$ m, $v_0 \sim 10^{-3} - 10^{-2}$ m/s, $\rho_m \sim 10^3$ kg/m^3 and $\eta \sim 10^{-3}$ Pa s, meaning that $\mathrm{Re} \sim 10^{-2} - 10^{-1}$. Therefore, in most cases inertia is negligible and the fluid flow is said to be in the viscous limit, where $\mathrm{Re} \ll 1$. The *Stokes equation* describes the motion of viscous flows,

$$\nabla p = \eta \nabla^2 \mathbf{v} + \mathbf{f}_m, \tag{2.4}$$

often referred to as Stokes flows or creeping flows. This equation, together with the incompressibility condition given by the continuity equation,

$$\nabla \cdot \mathbf{v} = 0, \tag{2.5}$$

describes the fluid motion in this thesis.

2.1.1 Stream function. Bi-harmonic Equation

The incompressibility condition (2.5) mathematically implies that there exists some vector field $\mathbf{\Psi}$ which satisfies $\mathbf{v} = \nabla \wedge \mathbf{\Psi}$ since the divergence of the rotational of any given field is always identically zero, $\nabla \cdot (\nabla \wedge \mathbf{\Psi}) \equiv 0$. This vector field is known as the *velocity vector potential*. The symbol "$\wedge$" stands for the cross product.

The velocity vector potential is useful to describe the fluid flow in cases where it can be expressed using only one of its components (such as in bi-dimensional or axisymmetric flows) since it reduces the complexity of the equations to solve. If the flow is two-dimensional, $\mathbf{v} = v_x \hat{x} + v_y \hat{y}$, the velocity field can be fully described by a vector potential with only one component in the direction orthogonal to the velocity plane $\mathbf{\Psi} = \psi\, \hat{z}$, where

$$v_x = \frac{\partial \psi}{\partial y}, \quad v_y = -\frac{\partial \psi}{\partial x}.$$

In this situation, the contours $\psi =$ constant are the streamlines of the velocity field[1]. For this reason, under these circumstances the velocity vector potential is referred to as the *stream function*.

Taking the curl of the Stokes equation (2.4) and for the particular case where there are no external forces (or they can be described as the gradient of some pressure field), we write

$$\nabla \wedge (\nabla p) = \eta \nabla \wedge \nabla^2 \mathbf{v}.$$

However, the curl of the gradient of any given function f is identically zero, $\nabla \wedge (\nabla f) \equiv 0$. Moreover, the Laplacian of a vector field $\mathbf{v}$ is defined as $\nabla^2 \mathbf{v} \equiv \nabla(\nabla \cdot \mathbf{v}) - \nabla \wedge (\nabla \wedge \mathbf{v})$. Given

[1] $\psi = constant \Rightarrow d\psi = \frac{\partial \psi}{\partial x} dx + \frac{\partial \psi}{\partial y} dy = v_y dx - v_x dy = 0$; the equations for the streamlines of the field.

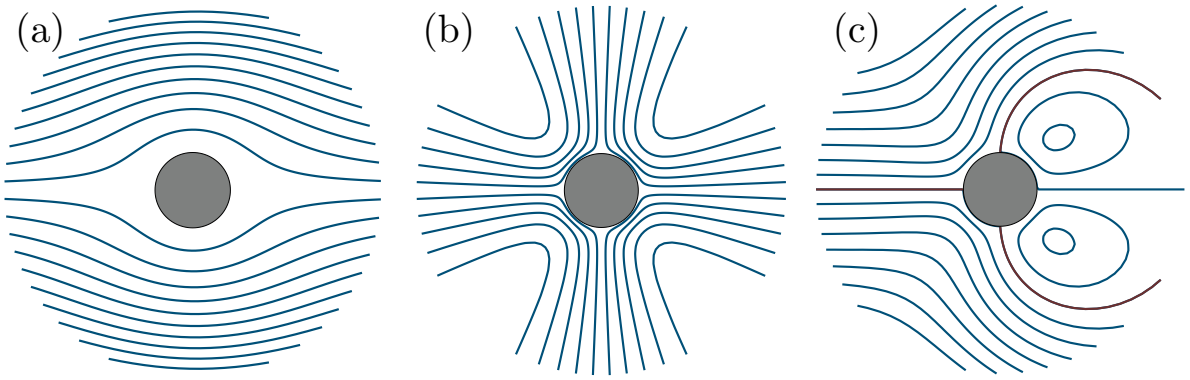

FIGURE 2.1: Streamlines of viscous flows around cylinders. (a) Flow past a cylinder: contours of equation (2.15). (b) Quadrupolar flow around a cylinder: contour lines given by equation (2.16). (c) The linear equations mean that stream functions can be added to give the final fluid movement, in this case given by the flow (a)+(b).

that the flow satisfies equation (2.5), we conclude that

$$\nabla \wedge \nabla^2 \mathbf{v} = -\nabla \wedge (\nabla \wedge (\nabla \wedge \mathbf{v})) = 0,$$

which can be expressed in terms of the velocity vector potential $\mathbf{\Psi}$ as:

$$\nabla^2(\nabla^2 \mathbf{\Psi}) \equiv \triangle^2 \mathbf{\Psi} = 0. \tag{2.6}$$

This equation is known as the *bi-harmonic equation*. This reflects the fact that the angular dependence of its solutions has two different frequencies, while the Laplace (harmonic) equation has only one.

In summary, flows in the viscous limit can be described by a velocity vector potential $\mathbf{\Psi}$ satisfying the bi-harmonic equation (2.6). Below it is described how this potential greatly simplifies the procedure for finding the fluid velocity fields that will be needed in this thesis.

2.1.2 Examples of Viscous Flows of Relevance to this Thesis

The vector potential description allows to exploit the symmetry of some geometries to reduce the Stokes vector equation (2.4) to a scalar one. This section briefly describes some examples of viscous flows that are helpful in understanding the electrokinetic behaviour of fluids. In all cases the objective is to find the stream function using the bi-harmonic equation, from which the fluid velocity field can be derived.

Flow Past a Sphere: Stokes Law First, the fluid velocity field of an otherwise homogeneous flow past a sphere of radius $a = 1$ is derived. Positioning the sphere at the origin of coordinates and the flow at infinity in the $\hat{z}$ direction, the boundary condition far from the sphere is written as

$$\mathbf{v}(r \to \infty) = V_\infty \, \hat{z} = V_\infty (\cos\theta \, \hat{r} - \sin\theta \, \hat{\theta}).$$

The problem has symmetry in the azimuth variable φ, so it is possible to write a stream function of the velocity field in the $\hat{\varphi}$ direction, $\mathbf{\Psi} = \psi/(r\sin\theta)\hat{\varphi}$. We divide the stream function by the quantity $r\sin\theta$ because this facilitates the treatment of the curl and Laplacian operators when using spherical coordinates. In this way, the velocity field may be obtained from the stream function as:

$$\mathbf{v} = \frac{1}{r^2\sin\theta}\frac{\partial\psi}{\partial\theta}\,\hat{r} - \frac{1}{r\sin\theta}\frac{\partial\psi}{\partial r}\,\hat{\theta}. \tag{2.7}$$

To solve the stream function the boundary conditions are required. At infinity, integrating the velocity field gives

$$\psi(r\to\infty) = \frac{1}{2}V_\infty r^2\sin^2\theta. \tag{2.8}$$

At the surface of the sphere, no-slip condition $\mathbf{v}(r=1)=0$ is required, which translates to the stream function as

$$\frac{\partial\psi(r=1)}{\partial r} = \frac{\partial\psi(r=1)}{\partial\theta} = 0. \tag{2.9}$$

From equation (2.8) the angular dependence of the resulting stream function is $\sim\sin^2\theta$. Imposing the bi-harmonic equation (2.6) on the general function $\psi(r,\theta) = F(r)\sin^2\theta$ yields

$$\left(\frac{d^2}{dr^2} - \frac{2}{r^2}\right)\left(\frac{d^2}{dr^2} - \frac{2}{r^2}\right)F(r) = 0,$$

with boundary conditions

$$F(r=1) = \frac{dF(r=1)}{dr} = 0, \quad F(r\to\infty) = \frac{1}{2}V_\infty r^2.$$

An efficient approach to solve this boundary value problem is to define an auxiliary function

$$f(r) = \left(\frac{d^2}{dr^2} - \frac{2}{r^2}\right)F(r).$$

The problem is then divided into two second-order ordinary differential equations that can be readily solved. Applying the boundary conditions leads to the stream function

$$\psi(r,\theta) = \frac{1}{2}V_\infty\left(r^2 - \frac{3}{2}r + \frac{1}{2r}\right)\sin^2\theta \tag{2.10}$$

from which the velocity field is obtained,

$$\mathbf{v} = V_\infty\left[\left(1 - \frac{3}{2r} + \frac{1}{2r^3}\right)\cos\theta\,\hat{r} - \left(1 - \frac{3}{4r} - \frac{1}{4r^3}\right)\sin\theta\,\hat{\theta}\right]. \tag{2.11}$$

Using this velocity field it is possible to compute the hydrodynamic force on a sphere due to a viscous drag. For this purpose, the *viscous stress tensor* $\bar{\bar{\tau}}$ needs to be integrated on the particle surface ∂S, $\mathbf{F}_D = \oint\bar{\bar{\tau}}\cdot d\mathbf{S}$. The viscous stress tensor is defined as [58]

$$\bar{\bar{\tau}} = -p\mathbb{I} + \left[\nabla\mathbf{v} + (\nabla\mathbf{v})^T\right], \tag{2.12}$$

where $\mathbb{I}$ is the identity matrix, and the super-index T is the transpose operation. From the Stokes equation (2.4) the pressure field is

$$p = -\frac{3}{2} V_\infty \frac{\cos\theta}{r^2},$$

which when introduced in the viscous stress tensor and integrated results in

$$\mathbf{F}_D = 6\pi V_\infty. \tag{2.13}$$

In microfluidics, the Stokes law gives a very accurate description of the viscous drag acting on micron and sub-micron particles, when $\mathrm{Re} \ll 1$. Given the negligible inertia of particles on the micron scale, the forces are always considered to be balanced. Thus, the velocity of a particle $\mathbf{u}$ of radius a suspended in a fluid with a velocity field $\mathbf{v}_\infty$ and on which an arbitrary external force $\mathbf{F}_{ext}$ is applied can be expressed (with dimensions) as

$$\mathbf{u} = \mathbf{v}_\infty + \frac{\mathbf{F}_{ext}}{6\pi a \eta}. \tag{2.14}$$

Flow Past a Cylinder: Stokes Paradox To obtain the apparently simpler stream function for the case of a bi-dimensional flow past a circle, the boundary conditions at both the surface of the cylinder and infinity cannot be simultaneously met. This is known as the *Stokes paradox*.

A detailed discussion of the problem, along with a consistent solution, can be found in the literature [59]. The reason is that far from the object, no matter how low the Reynolds number is, the inertial (convective) term is always of the same order of magnitude as the viscous term, so the Stokes approximation $\mathrm{Re} = 0$ cannot be used. In fact, this problem is also present for the case of a sphere: the description of the flow far enough from the object is as poor as for the cylinder, only satisfying the boundary conditions at its surface. However, because of the number of spatial dimensions of the problem, the two-dimensional problem is more dramatic since the boundary conditions do not match. The corrected stream function, computed introducing inertial effects [58], can be written as

$$\begin{aligned}\psi(r,\theta) \simeq \frac{V_\infty}{2C}\sin\theta\left[r(2\ln r - 1) + \frac{1}{r}\right] \\ + \mathrm{Re}\frac{V_\infty}{2}\sin 2\theta\left[\frac{1}{8C}r^2\ln r - \frac{r^2}{8} - \frac{1}{16C} + \frac{1}{4} + \left(\frac{1}{16C} - \frac{1}{8}\right)\frac{1}{r^2}\right],\end{aligned} \tag{2.15}$$

where $C = 1/2 - \gamma_E + \ln(8/\mathrm{Re})$ and γ_E is, in this context, the Euler–Mascheroni constant.

Figure 2.1(a) shows the contour lines of the stream function, that is, the streamlines of the flow past a circle in two dimensions.

Quadrupolar Flow around a Cylinder Of importance to this thesis is the velocity field created by a slip velocity of the form $\sim \sin(2\theta)$ around a sphere and cylinder situated at the coordinates origin. The stream function will now be derived, given by the velocity field boundary condition $\mathbf{v}(r=1) = \mathcal{V}\sin 2\theta\ \hat{\theta}$ at the circle interface and vanishing far away from the object.

From the stream function of the flow past a circle in two dimensions, it can be argued that the same angular dependence of the velocity field should translate into the stream function. That is, if $\mathbf{\Psi} = \psi\hat{z}$, $\psi = F(r)\sin(2\theta)$. Substituting into the bi-harmonic equation (2.6), gives the equation for $F(r)$,

$$\left[\frac{1}{r}\frac{d}{dr}\left(r\frac{d}{dr}\right) - \frac{4}{r^2}\right]\left[\frac{1}{r}\frac{d}{dr}\left(r\frac{d}{dr}\right) - \frac{4}{r^2}\right]F(r) = 0.$$

Following the same procedure as for the flow past a sphere, and using an auxiliary function $f(r)$ that absorbs the first two orders of the differential equation leads to a general solution to which these boundary conditions can be applied:

$$F(r=1) = 0, \quad \frac{dF(r=1)}{dr} = -\mathcal{V}, \quad \frac{dF(r\to\infty)}{dr} = 0.$$

This finally leads to the stream function

$$\psi(r,\theta) = \frac{1}{2}\mathcal{V}\frac{1-r^2}{r^2}\sin 2\theta, \tag{2.16}$$

from which the velocity field is obtained,

$$\mathbf{v}(r,\theta) = \mathcal{V}\left(\frac{1-r^2}{r^3}\cos 2\theta\ \hat{r} + \frac{1}{r^3}\sin 2\theta\ \hat{\theta}\right). \tag{2.17}$$

Figure 2.1(b) shows the contours of the stream function and therefore the streamlines of the quadrupolar flow around a cylinder.

Quadrupolar Flow around a Sphere The analogous fluid flow found for a two-dimensional circle is the case of a three-dimensional sphere which gives a quadrupolar flow around a sphere[2].

To maintain the $\sin 2\theta$ slip velocity function whilst preserving the particularities of the spherical coordinates, it can be argued [60] that the angular dependence of the stream function $\mathbf{\Psi} = \psi/(r\sin\theta)\hat{\varphi}$ should be $\psi(r,\theta) = F(r)\sin^2\theta\cos\theta$. Substituting into the bi-harmonic equation,

$$\left(\frac{d^2}{dr^2} - \frac{6}{r^2}\right)\left(\frac{d^2}{dr^2} - \frac{6}{r^2}\right)F(r) = 0.$$

The boundary conditions of the velocity field at the sphere surface $r = 1$ $\mathbf{v}(r=1) = \mathcal{V}\sin 2\theta\ \hat{\theta}$, and vanishing flow at infinity, translates into

$$F(r=1) = 0, \quad \frac{dF(r=1)}{dr} = -2\mathcal{V}r, \quad \frac{dF(r\to\infty)}{dr} = 0.$$

[2]The term "quadrupolar" is used due to the analogy with the two-dimensional problem around a circle. Note that in three dimensions the fluid flow is no longer quadrupolar.

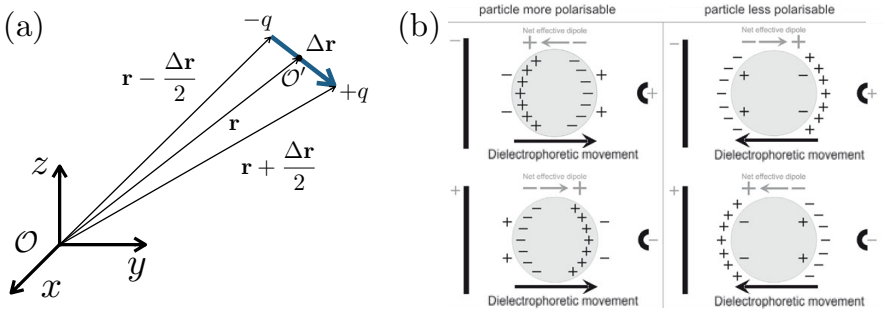

FIGURE 2.2: (a) Diagram showing a point dipole with an arbitrary position and orientation. (b) Examples representing pDEP (left column) and nDEP (right column) force direction. This behaviour is included in f_{CM}. Fig. (b) modified from Ref. [64].

Substituting the general solution into the boundary conditions yields the stream function

$$\psi(r,\theta) = \mathcal{V}\frac{1-r^2}{r^2}\sin^2\theta\cos\theta, \tag{2.18}$$

and the velocity field of the fluid

$$\mathbf{v}(r,\theta) = \mathcal{V}\left[\frac{1-r^2}{2r^4}(1+3\cos 2\theta)\,\hat{r} + \frac{1}{r^4}\sin 2\theta\,\hat{\theta}\right]. \tag{2.19}$$

From now on, this fluid velocity field is referred to as Gamayunov flows because Gamayunov *et al.* [48] were the first to argue that stationary quadrupolar flows, as described in this thesis, should appear around charged dielectric spheres as a consequence of concentration polarization (CP), and/or induced-charge within the electrical double layer (EDL). Fluid flows similar to Gamayunov flows have been observed for fluid droplets in the presence of electric fields [61, 62] and in induced-charge electroosmosis (ICEO) [43]; examined in detail in section 2.6.2.

Further Examples There are many geometries that can be solved using this procedure that are interesting for electrokinetic flows. These range from simple examples such as a uniform flow to the more interesting cases of flows around corners of arbitrary angles (of particular interest to this thesis). An excellent description of viscous flows around corners and wedges using the stream function formulation can be found in Ref. [63].

2.2 Electrostatics. Dielectrophoresis

Dielectrophoresis (DEP) is caused by the action of a non-uniform electric field on induced dipoles of particles with both non-zero *and* zero net charge [65, 66]. To understand this phenomenon, consider a sphere of radius a and electric permittivity ε_p immersed in a medium of permittivity ε and in the presence of an electric field that far from the particle is $\mathbf{E} = E_0\,\hat{z}$. Imposing this boundary condition far from the sphere, together with the continuity of the normal component of electric displacement field at the interface (no surface charge), solving the equation $\nabla\cdot\mathbf{D} = 0$

gives the potential

$$\phi(r,\theta) = \frac{\varepsilon_p - \varepsilon}{\varepsilon_p + 2\varepsilon} E_0 a^3 \frac{\cos\theta}{r^2} - E_0 r \cos\theta \tag{2.20}$$

outside the sphere. Also, the electrical potential given by a point dipole of moment $\mathbf{p} = q_p \Delta\mathbf{r}$ situated at the origin of a coordinate system and oriented in the $\hat{z}$ direction is

$$\phi(r,\theta) = \frac{p_m}{4\pi\varepsilon} \frac{\cos\theta}{r^2}, \tag{2.21}$$

where p_m is the magnitude of the dipole moment. Comparing this equation with (2.20), the behaviour of a polarizable sphere can be modelled as a point dipole with magnitude

$$p_m = 4\pi\varepsilon \frac{\varepsilon_p - \varepsilon}{\varepsilon_p + 2\varepsilon} a^3 E_0.$$

The *Clausius-Mossotti* factor f_{CM} is defined as

$$f_{\mathrm{CM}} = \frac{\varepsilon_p - \varepsilon}{\varepsilon_p + 2\varepsilon}. \tag{2.22}$$

This equation is used to compute the electric force on a polarizable particle as follows. The force on a point dipole due to a field $\mathbf{E}(\mathbf{r})$ is obtained from the Coulomb force (see Figure 2.2(a)) as $\mathbf{F} = q_p \mathbf{E}(\mathbf{r} + \Delta\mathbf{r}/2) - q_p \mathbf{E}(\mathbf{r} - \Delta\mathbf{r}/2)$. If $\Delta\mathbf{r}$ is much smaller than any typical electric field spatial variation, we can apply a *Taylor vector expansion* around $\mathbf{r}$,
$\mathbf{E}(\mathbf{r} \pm \Delta\mathbf{r}/2) = \mathbf{E}(\mathbf{r}) \pm [(\Delta\mathbf{r}/2) \cdot \nabla]\mathbf{E}(\mathbf{r}) + ...$, so that the force can be written as
$\mathbf{F} = (\mathbf{p} \cdot \nabla)\mathbf{E}(\mathbf{r})$.

Thus, the force of an external electric field on a particle polarized by the field itself may be modelled as $\mathbf{F}_{DEP} = 4\pi\varepsilon f_{\mathrm{CM}} a^3 (\mathbf{E} \cdot \nabla)\mathbf{E}$. Using the vector identity $2(\mathbf{A} \cdot \nabla)\mathbf{A} = \nabla\mathbf{A}^2$, gives the commonly used expression for the DEP force,

$$\mathbf{F}_{DEP} = 2\pi\varepsilon a^3 f_{\mathrm{CM}} \nabla\mathbf{E}^2. \tag{2.23}$$

This equation is valid as long as the non-uniformity of the field is small across the particle dimensions, i.e. $a\nabla\mathbf{E}^2/\mathbf{E}^2 \ll 1$. The following notation is used for the square of a vector field: $\mathbf{A}^2 = \mathbf{A} \cdot \mathbf{A} = |\mathbf{A}|^2$.

One important consequence of this equation is that the direction of the force will depend on whether the particle is more or less polarizable than the medium, which is reflected by the Clausius-Mossotti factor. When the particle is more polarizable than the medium, the force is called *positive* dielectrophoresis or pDEP, and the force is directed up the electric field gradient. When the particle is less polarizable than the medium, the force is referred to as *negative* dielectrophoresis or nDEP, with the force expelling the particles from the higher-intensity electric field regions. These situations are illustrated in Figure 2.2(b). A detailed derivation and discussion on the f_{CM} factor, as well as a recent biological applications for cell trapping and focusing can be found in Ref. [66].

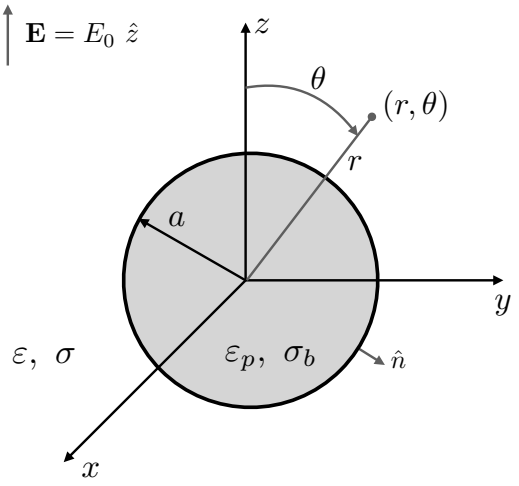

FIGURE 2.3: Diagram showing the electrical problem of a sphere with dielectric (permittivity ε_p) and conducting (conductivity σ_p) properties immersed in a conducting solution of permittivity ε and conductivity σ.

Equation (2.23) also shows that the DEP force scales with the magnitude of the electric field squared. This means that if an AC field is applied with angular frequency of ω, $\mathbf{E}(\mathbf{r}, t) = \mathbf{E}(\mathbf{r}) \cos \omega t$, while the magnitude of the electric field averages to zero, $\langle \mathbf{E}(\mathbf{r}, t) \rangle = 0$, the squared electric field averages to $\langle \mathbf{E}^2(\mathbf{r}, t) \rangle = \mathbf{E}^2(\mathbf{r})/2$. In other words, the DEP force is time-averaged for AC electric fields, and thus it will still dominate in AC fields if particles are charged.

Conductivity effects can be considered in the DEP model which allow describing conducting particles immersed in conducting solutions, as shown in Figure 2.3. Conservation of current must be satisfied which implies time-dependent accumulation of free electrical surface charge q_s [67],

$$\frac{\partial q_s}{\partial t} = \hat{n} \cdot [\sigma \mathbf{E}_{\text{out}}(\mathbf{r}, t) - \sigma_b \mathbf{E}_{\text{in}}(\mathbf{r}, t)]_{r=a}. \tag{2.24}$$

where σ is the conductivity of the electrolyte and σ_b the conductivity of the particle. This surface charge modifies the continuity of the normal component of displacement vector at the particle surface, $\hat{n} \cdot [\varepsilon \mathbf{E}_{\text{out}}(\mathbf{r}, t) - \varepsilon_p \mathbf{E}_{\text{in}}(\mathbf{r}, t)]_{r=a} = q_s$. Here, $\hat{n}$ is the unit vector perpendicular to the surface (see Fig. 2.3), $\mathbf{E}_{\text{out}}$ is the field outside the particle, and $\mathbf{E}_{\text{in}}$ the field inside the particle.

Both conditions can be integrated in a single equation, which represents the complete current conservation equation, including the Ohmic and displacement currents,

$$\left(\varepsilon - i\frac{\sigma}{\omega}\right) \mathbf{E}_{\text{out}}(r = a, \theta) \cdot \hat{n} = \left(\varepsilon_p - i\frac{\sigma_b}{\omega}\right) \mathbf{E}_{\text{in}}(r = a, \theta) \cdot \hat{n}, \tag{2.25}$$

this being valid for an AC field where the phasor $\mathbf{E}(\mathbf{r}, t) = \mathbf{E}(\mathbf{r}) e^{i\omega t}$ is used to describe the oscillating electric field. Defining a *complex permittivity* as

$$\tilde{\varepsilon} = \varepsilon - i\frac{\sigma}{\omega}\ , \tag{2.26}$$

the boundary condition for the continuity of the displacement vector is completely analogous to the non-charged case. Thus, we can define a *complex* Clausius-Mossotti factor

$$\tilde{f}_{\mathrm{CM}} = \frac{\tilde{\varepsilon}_p - \tilde{\varepsilon}}{\tilde{\varepsilon}_p + 2\tilde{\varepsilon}} \tag{2.27}$$

that gives the DEP force of a sphere with a conductivity σ_b as

$$\langle \mathbf{F}_{DEP} \rangle = \pi \varepsilon a^3 \Re \left\{ \tilde{f}_{\mathrm{CM}} \right\} \nabla \mathbf{E}^2(\mathbf{r}). \tag{2.28}$$

Therefore, in AC fields, the f_{CM} factor can be tuned by the frequency of the field. This is an important consideration since permittivity is a characteristic parameter of the particle and cannot be modified with ease, while complex permittivity can be modified simply by changing the frequency of the field. Under certain conditions (see section 2.5.2) there is a change in sign above a certain frequency, known as *crossover frequency* ω_c. Using $\Re \left\{ \tilde{f}_{\mathrm{CM}} \right\} = 0$ and equation (2.27), the crossover frequency for a solid homogeneous particle is [68]

$$\omega_c = \sqrt{\frac{(\sigma - \sigma_b)(\sigma_b + 2\sigma)}{(\varepsilon_p - \varepsilon)(\varepsilon_p + 2\varepsilon)}}. \tag{2.29}$$

Dielectrophoresis has been widely used as a tool for focusing, trapping and separating particles at the micrometric and nanometric scale. Models have been developed that describe solid spheres along with biological particles containing internal structures. The shell model [69, 70, 71] consists of different concentric spheres each having different complex permittivities and models differences between the cytoplasm and cellular membranes.

Two common ways of creating non-homogeneous fields needed for DEP are using arrays of metal electrodes in direct contact with the electrolytes (see for example Ref. [72]), and also shaping the electric field by using dielectric microstructures inside the microfluidic channels, a technique known as insulator-based DEP or *iDEP* (e.g. Ref. [73]).

2.3 Electrokinetic Equations

In this thesis the fluids are *electrolytes*, i.e. aqueous solutions of ions. Thus, to obtain a complete picture of the fluid dynamics requires a description of the motion of those ions. For simplicity, monovalent electrolytes are considered, whose concentration distribution are given by $c_+(\mathbf{r})$ for the positive ions and $c_-(\mathbf{r})$ for the negative ions.

Such ions can move because of three different reasons:

1. **Electric field** The ions respond to an external electric field $-\nabla\phi(\mathbf{r})$ characterized by their *electric mobility* μ.

2. **Non-homogeneous ion distribution** Because of diffusion, ions will tend to be distributed uniformly across the system.

3. **Convection** A net fluid flow in the system, $\mathbf{v}$, will drag the ions.

Thus, the ion flux may be described as $\mathbf{j}_\xi = -\xi\mu_\xi c_\xi \nabla\phi - D_\xi \nabla c_\xi + c_\xi \mathbf{v}$, subjected to the conservation equation $\partial_t c_\xi + \nabla \cdot \mathbf{j}_\xi = 0$. Here, ξ is $+1$ when referring to positive ions, and -1 for negative ions; D_ξ is the diffusion constant of the positive ($\xi = +1$) and negative ($\xi = -1$) ions. Taking into account that the fluid is incompressible [equation (2.5)] and then combining with the above equation gives

$$\frac{\partial c_\xi}{\partial t} + \nabla \cdot (-\xi\mu_\xi c_\xi \nabla\phi - D_\xi \nabla c_\xi) + \mathbf{v} \cdot \nabla c_\xi = 0. \tag{2.30}$$

This equation together with Stokes equation (2.4) provides the scaling for the variables. First, $\phi_{th} \equiv kT/e$ scales the electric potential[3], and c_0 the concentration scale for both positive and negative ions. To find the fluid velocity field scale, we return to the Stokes equation (2.4) with a body force density on the ions in the electrolyte expressed as $\varepsilon\nabla^2\phi\nabla\phi$, i.e. the Lorentz force on a charge density ($\mathbf{f}_m = \rho\mathbf{E}$). The scaling for this force is $\mathrm{f}_0 = \varepsilon\phi_{th}^2/x_0^3$, that when equaled to the force scaling imposed by the Stokes equation ($\mathrm{f}_0 = \eta v_0/x_0^2$) yields the velocity scale $v_0 = \varepsilon\phi_0^2/(x_0\eta)$. This is usually written in terms of the *thermal electric field* $E_{th} = \phi_{th}/x_0$ as [53]

$$v_0 = \frac{\varepsilon x_0 E_{th}^2}{\eta}. \tag{2.31}$$

Finally the scaled equations are the *Nernst-Planck equations*,

$$\alpha_\xi \frac{\partial c_\xi}{\partial t} + \alpha_\xi \mathbf{v} \cdot \nabla c_\xi - \xi\nabla \cdot (c_\xi \nabla\phi) - \nabla^2 c_\xi = 0. \tag{2.32}$$

where the *ionic drag coefficients* is defined as

$$\alpha_\xi = \frac{\varepsilon k^2 T^2}{\eta D_\xi e^2}, \tag{2.33}$$

through the *Einstein relations* for the kinetic theory, $D_\xi = \mu_\xi \phi_{th}$. Introducing the average concentration and volumetric charge

$$c = \frac{1}{2}(c_+ + c_-), \qquad \rho = e(c_+ - c_-), \tag{2.34a,b}$$

allow equations (2.32) to be written in a more convenient way. After some manipulation, they can be rewritten as [75]

$$\nabla \cdot (\nabla c + \rho\nabla\phi) = \frac{\alpha_+ + \alpha_-}{2}\frac{\partial c}{\partial t} + \frac{\alpha_+ - \alpha_-}{2}\frac{\partial \rho}{\partial t} + \frac{\alpha_+ + \alpha_-}{2}\mathbf{v} \cdot \nabla c + \frac{\alpha_+ - \alpha_-}{2}\mathbf{v} \cdot \nabla\rho, \tag{2.35}$$

[3] This is the *thermal potential*, where k is the *Boltzmann constant*, T the absolute temperature and e the charge of the electron. At 25^oC $\phi_{th} = 25.7$ mV. Note that monovalent ions are considered, meaning that the valence is set to ($z = +1$) [74]. This scaling arises as a result of the Einstein-Smoluchowski equation $D_\xi = \mu_\xi kT/e$.

$$\nabla \cdot (\nabla \rho + c \nabla \phi) = \frac{\alpha_+ - \alpha_-}{2} \frac{\partial c}{\partial t} + \frac{\alpha_+ + \alpha_-}{2} \frac{\partial \rho}{\partial t} + \frac{\alpha_+ - \alpha_-}{2} \mathbf{v} \cdot \nabla c + \frac{\alpha_+ + \alpha_-}{2} \mathbf{v} \cdot \nabla \rho. \quad (2.36)$$

where the scale of the charge is $q_0 = 2ec_0$.

Equations (2.35) and (2.36) describe the movement of ions in an electrolyte in the presence of an electric field $-\nabla\phi$.

The electric field follows *Poisson's equation*

$$\nabla^2 \phi = -\frac{\rho}{\varepsilon} = -\frac{c_+ - c_-}{\varepsilon} e, \quad (2.37)$$

which expressed non-dimensionally is:

$$\delta^2 \nabla^2 \phi = -(c_+ - c_-). \quad (2.38)$$

The Nernst-Planck equations together with Poisson equation are often referred to as the Poisson-Nernst-Planck (PNP) equations. The parameter δ is the *Debye length* λ_D scaled with the typical length of the system,

$$\delta = \sqrt{\frac{\varepsilon \phi_{th}}{2 x_0^2 e c_0}}. \quad (2.39)$$

Equations (2.35-2.36) and (2.38), together with Stokes equation (2.4) in the presence of an electric field (and correspondingly scaled) gives

$$\nabla p = \nabla^2 \mathbf{v} + \nabla^2 \phi \nabla \phi, \qquad \nabla \cdot \mathbf{v} = 0, \quad (2.40)$$

which is a complete electrohydrodynamic description of the behaviour of an electrolyte .

2.3.1 Electrical Double Layer

The description of a charged surface in contact with the electrolyte is fundamental in describing the behaviour of particles and interfaces. This section describes the case of an infinite plane positioned at $x = 0$ with the fluid extending into the semi-space $x > 0$, as represented in Figure 2.4.

2.3.1.1 Diffuse Layer

The electroneutrality of an electrolyte cannot be preserved in the vicinity of a charged surface. A region of imbalanced ion concentration arises near the surface and equations (2.44) and (2.45) do not hold since $c_+ \neq c_-$. This region is known as the *electrical double layer* (EDL), and is characterised by the Debye length λ_D.

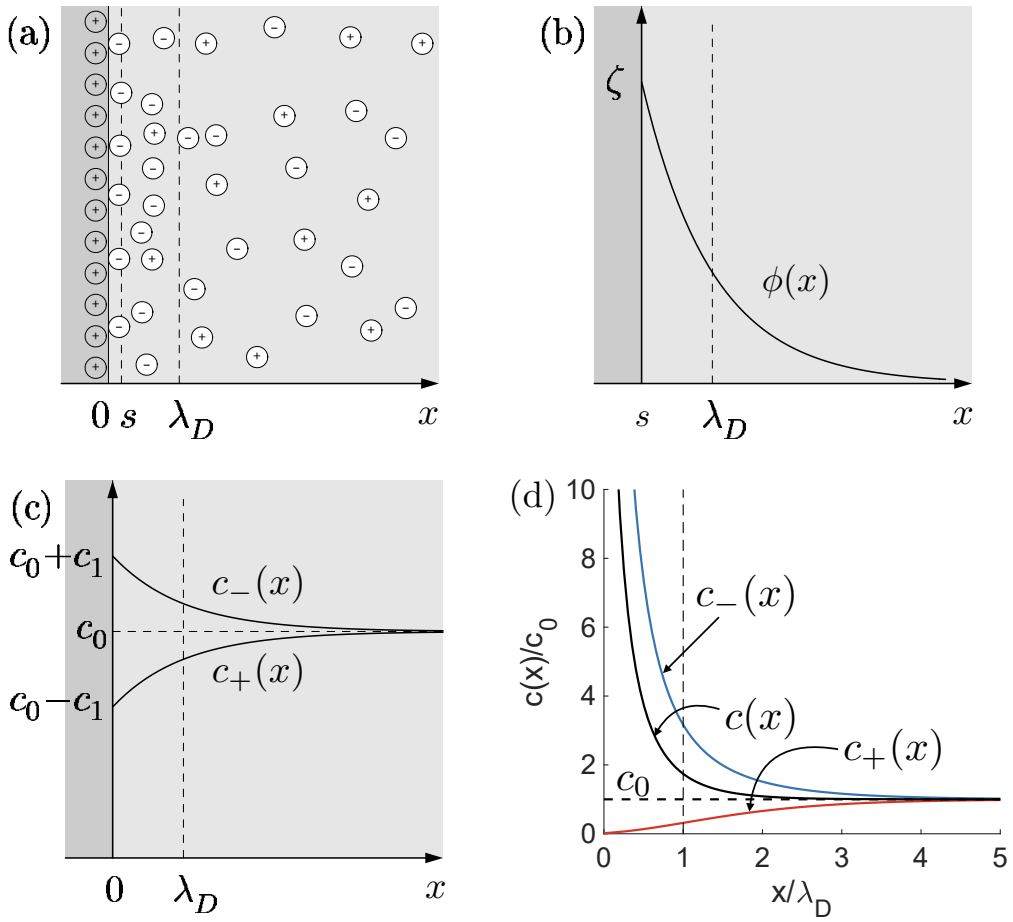

FIGURE 2.4: The basic concepts of the electrical double layer. (a) Counter-ions approach the charged surface create the diffuse layer $s < x < \lambda_D$ and the Stern layer $0 < x < s$. (b) Plot of the zeta potential and the electric potential in the diffuse layer. (c) Plot of the concentration of positive and negative ions in the diffuse layer in the limiting case $\zeta \ll 1$, known as *Debye-Hückel approximation*. (c) Plot of the ion concentration in the general case described by the Gouy-Chapman potential in equation (2.43). Figures (a-c) modified from Ref. [68].

Consider equation (2.30) in the stationary state, $\partial_t c_\xi \approx 0$, with the bulk of the fluid at rest ($\mathbf{v} \cdot \nabla c_\xi = 0$). Then, except for an integration constant which can be taken to be zero,

$$c_\xi = e^{-\xi\phi}, \tag{2.41}$$

where the boundary condition $c_\xi(x \to \infty) = 1$ is used. This concentration profile is known as the *Boltzmann distribution*.

The electric potential must follow Poisson equation (2.38), with a charge source given by the difference in positive and negative ion concentration, $\rho = e(c_+ - c_-)$. Using (2.41),

$$\delta^2 \nabla^2 \phi = \sinh \phi. \tag{2.42}$$

Note that the constant earlier referred to as the Debye length characterises the spatial extension of the double layer. This equation is the *Poisson-Boltzmann equation*, which can be solved

analytically for simple cases, such as the one depicted in Figure 2.4 where the charged surface is completely flat and variables only depend on one axis.

In this situation, it can be shown that the solution to equation (2.42), is given by the *Gouy-Chapman potential*, expressed as [68]

$$\phi(x) = 4\text{arctanh}\left[\tanh\left(\frac{\zeta}{4}\right)e^{-x/\delta}\right], \tag{2.43}$$

with the boundary condition $\zeta \equiv \phi(x=0)$ known as the *zeta potential* of the surface [see Fig. 2.4(b)]. The Boltzmann distribution given by the Gouy-Chapman potential predicts an increased ion concentration inside the EDL, as plotted in Figure 2.4(d).

2.3.1.2 Stern Layer

The above discussion only holds for the case of ions that can freely move through the media. However, the exponentially large ion concentration close to the wall predicted by (2.41) is unrealistic when the finite size of the ions is taken into account, and limits the maximum concentration near the surface. For this reason, between the slip plane and the surface there exist other inner layers which cannot be described by the Poisson-Nernst-Planck equations; these make a contribution to the conduction in the double layer.

To address this an inner layer is introduced between the EDL we have considered until now, from now on referred as the *diffuse layer*, and the wall surface known as *Stern layer*, *stagnant layer* or compact layer [74, 76]. This region is of a thickness of one or two solvated ions [57]; tightly packed and immobile. The closest ions are modelled to be in direct contact with the wall, and therefore not hydrated. In this situation, the ions are *specifically adsorbed* to the surface. The plane that encloses these adsorbed ions is known as the *inner Helmholtz plane* (iHP), and the population consists only of co-ions.

The remainder of the Stern layer comprises immobile hydrated counter-ions, and defines the *outer Helmholtz plane* (oHP), or the *slip plane* – the plane in which the fluid moves with respect to the surface. A representation of the different contributions to the EDL is illustrated in Refs. [74, 57]. In this picture the zeta potential is defined as the potential at the slip plane [57]. Later in this chapter it is shown how this has important implications in the description of the fluid motion.

2.3.2 Thin Double Layer Limit

The magnitude of the Debye length for the case of KCl is [57]
$\lambda_D = 1.764 \times 10^{-11}(\text{m K})^{-1/2}\sqrt{T/c_0}$, which is typically of the order of units of nanometres. Since the typical length scales x_0 used in this thesis are of the order of units of microns and above, we may consider $\delta \ll 1$ and $\delta^2 \approx 0$. This approximation is known as *thin double layer limit*. This approximation ensures *bulk electroneutrallity*, that is $c_+ = c_-$, $\rho = 0$ in the system

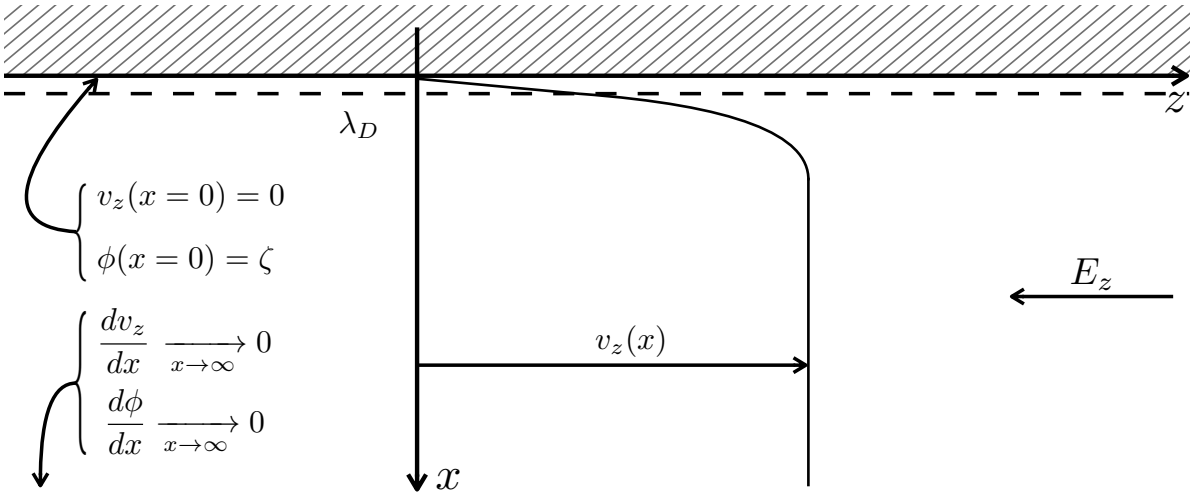

FIGURE 2.5: Representation of the electroosmotic flow near a charged wall in contact with an electrolyte. The effective boundary condition for the electric potential is the zeta potential following the definition given in section 2.3.1.2: the value of the potential at the slip plane (zeta potential) is responsible for the mobility of the electrolyte.

bulk. For this reason, the Poisson equation (2.38) is embedded in the Nernst-Planck equations for this approximation,

$$D\nabla^2 c = \frac{\partial c}{\partial t} + \mathbf{v}\cdot\nabla c, \tag{2.44}$$

$$\nabla\cdot(c\nabla\phi) = \gamma\left(\frac{\partial c}{\partial t} + \mathbf{v}\cdot\nabla c\right). \tag{2.45}$$

Here the *scaled diffusion constant* and the *asymmetry parameter* of the electrolyte are defined as, respectively,

$$D = \frac{2}{\alpha_+ + \alpha_-}, \qquad \gamma = \frac{\alpha_+ - \alpha_-}{2}. \tag{2.46a,b}$$

As a reference, the equations of motion for the electrohydrodynamic problem in the thin double layer approximation are highlighted since they will be extensively used throughout this thesis.

2.3.3 Electroosmosis

The EDL is important in understanding why do electrolytes in contact with charged surfaces acquire a net flow in an external electric field, a phenomenon known as *electroosmosis* (EO).

Consider a pressure-free, stationary electrolyte flow described by equation (2.40). The simplest configuration is shown in Figure 2.5, with an electric field is applied in the $\hat{z}$ direction, $\mathbf{E} = E_z\hat{z}$ ($E_z < 0$ in Figure 2.5) so that equation (2.40) can be written as $\nabla^2\mathbf{v} = \nabla^2\phi\mathbf{E}$.

In this configuration, both variables only depend on the transverse coordinate x, $\mathbf{v} = v_z(x)\hat{z}$, $\phi = \phi(x)$, so the equation can be expressed as

$$\frac{d^2 v_z}{dx^2} = \frac{d^2\phi}{dx^2} E_z,$$

Applying the boundary conditions shown in Figure 2.5, the solution to this equation is [74]

$$v_z(x) = -\zeta \left[1 - \frac{\phi(x)}{\zeta}\right] E_z.$$

However, as $\phi(x)$ decays rapidly (2.43), for moderate values of x/δ we assume that $\phi(x)/\zeta \ll 1$. In other words the electroosmotic velocity it is widely accepted to be

$$v_{EO} = -\zeta E_z. \tag{2.47}$$

This equation is known as the *Helmholtz-Smoluchowski* formula, which outside the double layer represents a flat profile, known as *plug flow*. The profile of the flow is independent of the particular description of the potential in the double layer $\phi(x)$ as long as it decays rapidly away from the wall, $\phi(x)/\zeta \ll 1$.

2.4 Boundary Conditions for Dielectrics in Electrokinetics

In this section the electrokinetic concepts introduced for electrolytes in contact with charged dielectric surfaces are used to obtain a consistent set of boundary conditions for the bulk equations presented in the previous section to establish a formulation of the CPEO model.

2.4.1 Classical (microscale) Conditions

For every viscous flow, no-slip conditions are assigned to the Stokes equation on the surface (2.40),

$$\mathbf{v} = 0. \tag{2.48}$$

For the case of the equations of concentration and charge (2.35-2.36), it is required that in the boundaries of the domain no flux condition can appear, $\mathbf{j} \cdot \hat{n} = 0$ in order to characterise chemically inert walls [53]. Considering the scaled equations (2.32) and the boundary condition for the viscous flow (2.48),

$$-\xi c_\xi \frac{\partial \phi}{\partial n} - \frac{\partial c_\xi}{\partial n} = 0.$$

Following the same procedure used to obtain the bulk equations for concentration and charge, adding and subtracting these equations yields

$$\rho \frac{\partial \phi}{\partial n} + \frac{\partial c}{\partial n} = 0, \quad c \frac{\partial \phi}{\partial n} + \frac{\partial \rho}{\partial n} = 0. \tag{2.49a,b}$$

Finally, the boundary conditions for the Poisson equation (2.38) are the usual for any electrostatic problem

$$\frac{\partial \phi}{\partial n} - \frac{\varepsilon_s}{\varepsilon}\frac{\partial \phi_s}{\partial n} = \frac{q_s}{\delta}, \tag{2.50}$$

where ε_s is the permittivity of the wall, ϕ_s the electric potential and q_s the surface charge, scaled by $q_{s,0} = \varepsilon \phi_{th}/\delta$.

2.4.2 Surface Conduction and the Dukhin Number

The concentration enhancement predicted in the diffuse part of the double layer (2.41) implies that when an electric field $\mathbf{E}$ is applied parallel to the surface, an excess current density occurs in that region [77]. This conductivity in the double layer is referred to as *surface conductivity* σ_s, and is different from the bulk conductivity. It is common in electrokinetics to work with the total conductance over the region of interest, i.e. the *surface conductance* K_s.

The surface conductance in the diffuse part of the double layer can be determined by evaluating the excess current density I_s in the EDL in the presence of an electric field of magnitude E parallel to the wall $x = 0$,

$$I_s = \int_{x=0}^{+\infty} dx\ [\mathbf{j}(x) - \mathbf{j}(x \to \infty)].$$

Using the current density given in previous section, and considering an homogeneous concentration in the direction parallel to the wall, and the Boltzmann distribution in the direction perpendicular to the wall given by equation (2.41), we obtain

$$ec_0 \frac{\varepsilon \phi_{th}^2}{\eta} \int_{x=0}^{+\infty} dx \sum_{\xi=-,+} \left\{ \frac{\xi}{\alpha_\xi}(e^{-\xi\phi} - 1)E + \zeta \left[-e^{-\xi\phi}\left(1 - \frac{\phi}{\zeta}\right) + 1 \right] E \right\}.$$

This means that the conduction in the double layer is due to the movement of ions due to the application of an electric field (first addend) together with the electroosmotic movement (second addend) [78, 79]. The variables in this equation are now non-dimensional with the usual scaling.

To solve the integrals, the above expression is rewritten as

$$ec_0 \frac{\varepsilon \phi_{th}^2}{\eta} \sum_{\xi=-,+} \left\{ \frac{\xi}{\alpha_\xi} \int_{x=0}^{+\infty} dx\ (e^{-\xi\phi} - 1) + \zeta \int_{x=0}^{+\infty} dx\ \left[-e^{-\xi\phi}\left(1 - \frac{\phi}{\zeta}\right) + 1 \right] \right\} E.$$

Using the Gouy-Chapman potential (2.43) it is possible change the integration variable

$$dx = -\frac{1}{4}\frac{d\phi}{\sinh\frac{\phi}{4}\cosh\frac{\phi}{4}},$$

with the integration limits changed accordingly: $\phi(x = 0) = \zeta$ and $\phi(x \to \infty) = 0$. The integrals now become

$$\int_{x=0}^{+\infty} dx\ (e^{-\xi\phi} - 1) = \frac{1}{4}\int_0^{\zeta} d\phi\ \frac{e^{-\xi\phi} - 1}{\sinh(\phi/4)\cosh(\phi/4)} = 2(e^{-\xi\zeta/2} - 1),$$

$$\int_0^\infty dx\ \phi e^{-\xi\phi} = \frac{1}{4}\int_0^\zeta d\phi\ \frac{\phi e^{-\xi\phi}}{\sinh(\phi/4)\cosh(\phi/4)} \approx 4\xi(e^{-\xi\zeta/2}-1) + 2\zeta(e^{-\xi\zeta/2}-1)$$

when the limit $\phi(x)/\zeta \ll 1$ is considered, as for the electroosmotic velocity (2.47). Substituting,

$$q_0\frac{\varepsilon\phi_{th}^2}{\eta}\sum_{\xi=-,+}\left\{\frac{\xi}{\alpha_\xi}\left(1+2\alpha_\xi\right)\left(e^{-\xi\zeta/2}-1\right)\right\}E.$$

Finally, for a **symmetrical electrolyte** ($D_+ = D_-$) it is possible to sum the above quantity. Taking into account that both charges will contribute to the current in the same direction, the surface conductance due to the EDL is determined from the excess intensity using Ohm's law,

$$K_s = \frac{2q_0 D\delta}{\phi_{th}}\left(\cosh\frac{\zeta}{2}-1\right)(1+2\alpha), \tag{2.51}$$

To quantify the relative importance of the surface conductance with respect to the bulk conductance, the *Dukhin number* is defined as the ratio of both magnitudes,

$$\mathrm{Du} = \frac{K_s}{K_L}. \tag{2.52}$$

The bulk conductance is determined from the bulk conductivity σ as $\sigma = ec_0(D_+ + D_-)/\phi_{th}$. This quantity does not depend on any spatial coordinate and therefore the bulk conductance may be computed as $K_L = \sigma a$, where a is a characteristic length of the problem. Thus, for symmetrical electrolytes the Dukhin number is [77]

$$\mathrm{Du} = 2\delta\left(\cosh\frac{\zeta}{2}-1\right)(1+2\alpha). \tag{2.53}$$

This equation gives the Dukhin number when the double layer is described solely by the diffuse layer. However, this equation usually predicts unrealistic values for the Dukhin number, and it must be decoupled from the zeta potential (measured from the electroosmotic mobility) to take into account the Stern layer. This is the case in most synthetic particles or bioparticles such as bacterial cells, where the surface conductance is determined by equation (2.52) using an experimental value for the surface conductance [80, 81].

2.4.3 Macroscale Boundary Conditions. Large Zeta Potentials

The boundary conditions described above lead to a very complex, highly non-linear boundary problem which is only solvable for the simplest scenarios. For this reason, many authors have tried to obtain analytically tractable simplifications for specific cases. A review of the different approaches is given by Schnitzer & Yariv for the case of dielectrics [53] and metallic boundaries [82]. They provide a comprehensive and systematic procedure for obtaining boundary conditions which will be followed throughout this thesis, and which is referred to as the Schnitzer-Yariv (SY) model.

The SY model is based on the method of asymptotic matching between the bulk variables and a set of redefined *boundary-layer variables* that scale with the Debye length δ and which serve as boundary conditions for the bulk variables. In other words, this approach divides the domain into a charged boundary layer and an electroneutral bulk which satisfies equations (2.40-2.45). The resulting boundary conditions in the case of small zeta potential and small applied electric field are

$$\frac{\partial \phi}{\partial n} = 0, \qquad \frac{\partial c}{\partial n} = 0 \tag{2.54a,b}$$

for the potential and concentration, and

$$\mathbf{v} = \zeta \nabla_s \phi + 2 \ln \left(1 - \tanh^2 \frac{\zeta}{4} \right) \nabla_s \ln c \tag{2.55}$$

for the velocity field. In this expression, the *surface gradient* is defined as $\nabla_s = (\mathbb{I} - \hat{n}\hat{n}) \cdot \nabla$, the component of the gradient which is tangential to the surface.

At large zeta potentials it is necessary consider a sublayer within the Debye (diffuse) layer in order to account for the high surface charge predicted by the logarithmically large zeta potentials associated with the Boltzmann distribution (2.41). In the SY model, this is referred to as the Dukhin layer, and an additional set of scaled variables is needed to describe it. This time the limiting process, in addition to $\delta \to 0$, also considers $e^{|\zeta|/2} \to \infty$, with the product $\delta e^{|\zeta|/2}$ bounded. The quantity $\mathrm{Bi} = \delta e^{|\zeta|/2}$ is known as the *Bikerman number*, and it is proportional to the Dukhin number in the limit $|\zeta| \gg 1$ (see the diffuse contribution in equation (2.53)), $\mathrm{Du} = \mathrm{Bi}(1 + 2\alpha)$. Therefore, the full domain in the system is divided into three different regions where the "solid surface" of the boundary is below the Dukhin layer.

The SY model accounts for this sublayer by performing an asymptotic expansion with respect to the boundary-layer, with the inner variables scaled by the Debye length δ, i.e. δ^2 with respect to the bulk scales. The result is the appearance of a surface conduction governed by the Dukhin (Bikerman) number. For the case of positive counter-ions, the ones used in this thesis, the boundary conditions are

$$c \frac{\partial \phi}{\partial n} - \frac{\partial c}{\partial n} = 0, \tag{2.56}$$

$$\frac{\partial c}{\partial n} = -\mathrm{Du} \nabla_s^2 (\phi + \ln c), \tag{2.57}$$

$$\mathbf{v} = \zeta \nabla_s \phi - 4 \ln \left(\cosh \frac{\zeta}{4} \right) \nabla_s \ln c. \tag{2.58}$$

This means that the conduction appears in the Dukhin sublayer with a magnitude controlled by the Dukhin number itself, expressed mathematically through a surface Laplacian in equation (2.57). These boundary conditions are highlighted for future reference, as together with equations (2.40, 2.44-2.45) define the boundary value problem needed for this thesis.

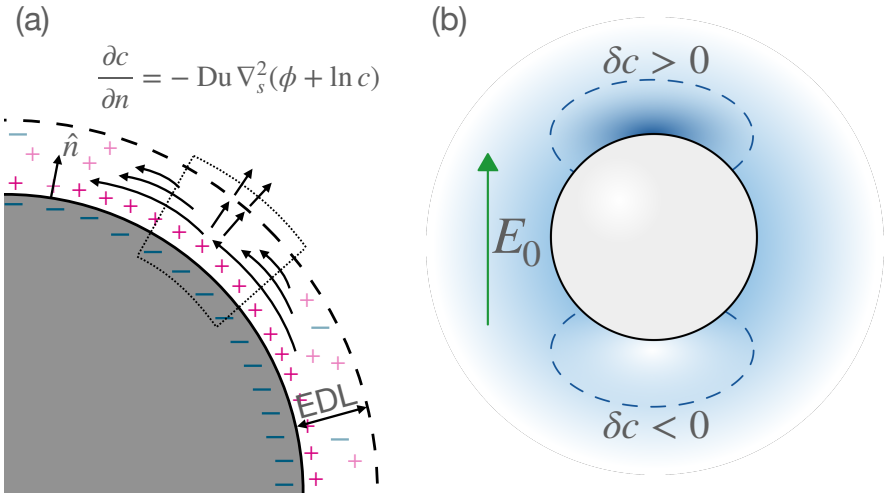

FIGURE 2.6: (a) Diagram showing ion flux conservation in the EDL given by equation(2.57): The change in surface current in a closed surface (represented by the divergence of the surface current $-\mathrm{Du}\nabla_s^2(\phi + \ln c)$) is balanced by an exchange in counter-ions with the electrolyte bulk. (b) In the case of a charged particle in an electric field, this leads to a perturbation in the bulk salt concentration, known as Concentration Polarization (CP).

These boundary conditions are physically interpreted as follows. First, from the microscale boundary conditions presented earlier we find that the boundary condition (2.56) represents a flux of co-ions, while (2.57) is the flux of counter-ions. This means that while the normal flux of co-ions remains zero for the case of a highly-charged surface, there exists a normal flux of counter-ions into (or out of) the double layer due to the surface conductance (represented by its divergence $\mathrm{Du}\nabla_s^2(\phi + \ln c)$). This exchange of counter-ions between the bulk and the double layer is explained in Figure 2.6, and provides a means of modifying the electrolyte overall concentration beyond the double layer given that electroneutrality should be preserved outside the EDL. This phenomenon is known as *Concentration Polarization* (CP). Finally, equation (2.58) represents the electroosmotic slip velocity considering an additional term which accounts for the chemical gradients [83].

An analogous SY model using this asymptotic matching procedure was developed for the case of conducting surfaces [82]; discussed in section 2.6 for the phenomenon of induced-charge electro-osmosis (ICEO).

As a summary of the approximations we have used to obtain the equations and boundary conditions that conform our boundary value problem, we have:

- Negligible Reynolds number. The Stokes equation is used to describe the fluid velocity field.
- Thin EDL, so the original domain is divided into an electroneutral bulk and a charged double layer in which the boundary conditions are imposed.

2.5 Electrokinetics and Dielectric Particles

Using the methodology presented in last sections it is now possible to describe some classical electrokinetic results with ease.

2.5.1 Electrophoresis

When a particle is immersed in an electrolyte, an EDL develops such that its surface charge is completely screened. However, as described above the diffuse part of the double layer is composed of mobile ions, which means that in an electric field they are influenced by electroosmosis.

Therefore, there is an overall relative motion between the electrolyte and the particle. But as the particles are small enough to be in the viscous limit, the fluid far from the particle remains at rest while the particle experiences a net displacement in the opposite direction to the electroosmosis of the counter ions. Therefore in an external DC field, particles acquire a net motion described by

$$\mathbf{u}_{EP} = \frac{\varepsilon \zeta_p}{\eta} \mathbf{E}, \tag{2.59}$$

(in dimensional variables) which is known as *Electrophoresis* (EP). This linear expression was first obtained by Smoluchowski [84], and it is independent of the particle shape and size as long as the thin EDL approximation is valid. The ratio between the electrophoretic velocity and the applied electric field is known as the electrophoretic mobility $\mu_{EP} = \varepsilon \zeta_p / \eta$.

Applications of EP for continuous particle separation include *isotachophoresis*[4] [85, 86] or gel electrophoresis. These methods exploit the principle that different particles may have different electrophoretic mobilities, so that different particles can have different velocities, leading to fractionation.

Smoluchowski's expression for electrophoresis (2.59) builds upon the assumptions of thin double layer and small zeta potential, and represents the simplest scenario in which surface conductance is not considered. The influence of surface conductance in electrophoresis was already discussed by Dukhin & Derjaguin [49], and a weak-field model presenting effective boundary conditions was proposed by O'Brien [87]. The development of a model beyond the weak-field approximation was later described using physical arguments by Dukhin and co-workers [50, 51, 52]. This thesis follows the systematical approach provided by the SY model. However, as the full equations and boundary conditions described in the model are analytically intractable, it has only been solved for the limiting cases of weak field magnitudes [54] and small surface conductance ($\mathrm{Du} \ll 1$) [75]. The former weak-field approximation predicts a deviation to the electrophoretic velocity for Dukhin numbers as small as $\mathrm{Du} \sim 10^{-2}$, with a corrected EP velocity that can be expressed in leading order as

$$\mathbf{u}_{EP} = \frac{\zeta_p + \mathrm{Du}[\zeta_p - 4\ln(\cosh[\zeta_p/4])]}{1 + 2\mathrm{Du}} \mathbf{E}. \tag{2.60}$$

[4] The name is self-explanatory for the phenomenon: *iso* means equal, *tachos* velocity and *phoresis* migration.

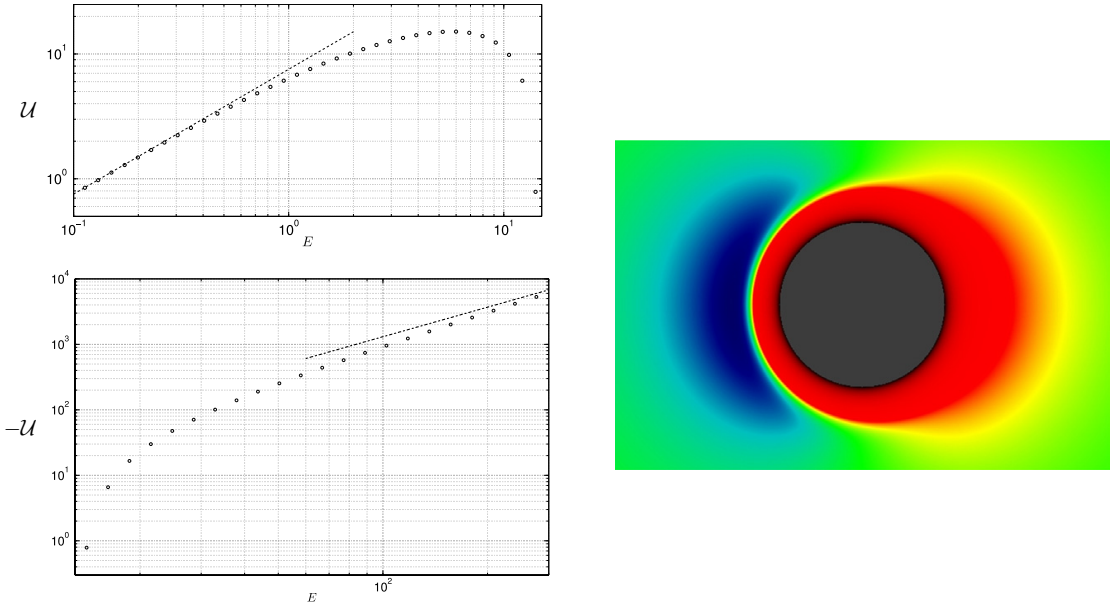

FIGURE 2.7: (a) Non-dimensional EP velocity correction predicted by the SY model as a function of the applied electric field in the Small-Dukhin number analysis. Plot represented in two logarithmic graphs due to the sign change. Dots represent the results of numerical simulations, and dashed lines represent the limiting cases of weak and strong fields. $\zeta_p = 5$, $D = 4$. Figure modified from Ref. [75]. (b) Representation of the counter-ion concentration around a sphere resulting from surface conductance, leading to the effects of nonlinear EP. Arbitrary scale where red is the most enhanced concentration and blue the most depleted concentration. Figure taken from Ref. [88].

It also predicts velocity corrections proportional to the third power of the electric field magnitude, $\sim E^3$. For this reason, these contributions are often referred to as *non-linear electrophoresis* [75]. A further analysis for arbitrary field magnitudes (and small Dukhin numbers) using numerical solutions to the problem predicts a reversal in the correction to the particle velocity, as seen in Figure 2.7(a). The physical interpretation of the modified velocity is related to the CP around the particle due to the surface conductance (see Figure 2.7(b)). As a consequence, the Debye length is modified leading to a modified slip velocity, affecting the overall EP velocity.

Experimental verification of the non-linear terms in EP has encountered great difficulties, with apparently contradictory results between different works [89, 90]. This is partly attributed to the uncontrolled Faradaic reactions that occur at electrodes, releasing new species into the electrolyte when high-intensity DC fields are applied. Experiments with moderate fields in more reproducible situations [91, 92] verify the predicted behaviour.

2.5.2 Dielectrophoresis Revisited

Having described the surface conductance phenomena, it becomes possible to improve the physical analysis of the conductivity on the surface of the particles in DEP, as introduced in section 2.2.

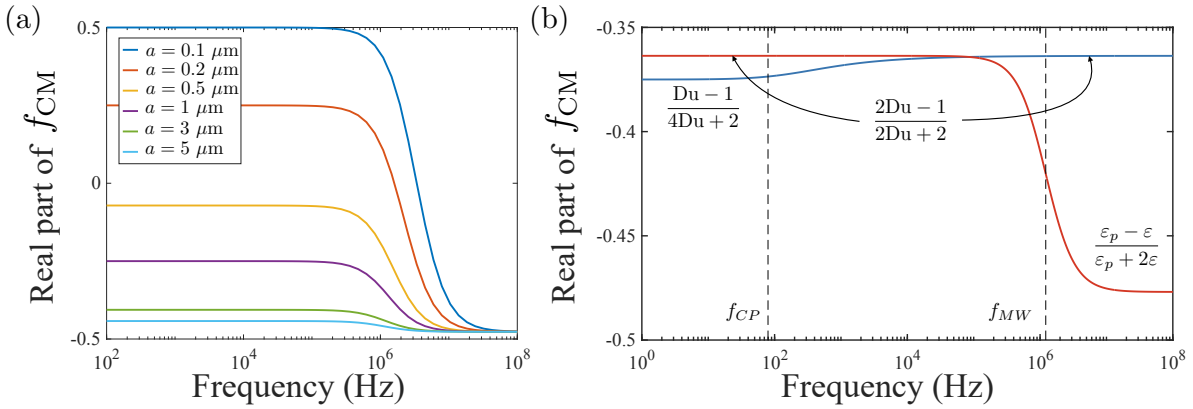

FIGURE 2.8: (a) Real part of f_{CM} for particles of different radii in a 5 mS/m conducting medium. For some sizes, the sign depends on the frequency of the applied AC field. (b) Generalised CM factor introducing concentration polarization effects at low frequency. Red line represents equation (2.27) with the particle conductivity given by $2K_s/a$. Blue line represents equation (2.67). Limiting cases are shown in the plot. Particle size is $a = 1\ \mu$m. In both plots, $\varepsilon = 80\varepsilon_0$, $\varepsilon_p = 2.5\varepsilon_0$, $K_s = 1$ nS.

Sections 2.3.1 and 2.4 described how the surface charge leads to an electrical double layer in which conduction effects appear. From the boundary condition (2.57), the surface conduction of the particle is represented by $-\mathrm{Du}\nabla_s^2\phi$, i.e. its divergence, evaluated at the particle surface. Including this in Ohm's law (equation (2.24)), and taking the scaling into account gives

$$\frac{\partial q_s}{\partial t} = \hat{n}\cdot\left[\sigma\mathbf{E}_{\mathrm{out}}(\mathbf{r},t) - \sigma_b\mathbf{E}_{\mathrm{in}}(\mathbf{r},t)\right]_{r=a} - K_s\nabla_s^2\phi_{\mathrm{in}}\big|_{r=a}\,. \tag{2.61}$$

It can be shown that the potential inside the sphere gives a constant field, $\phi_{\mathrm{in}}(r,\theta) = CE_0 r\cos\theta$, where C is determined by the boundary conditions. Operating the surface Laplacian, equation (2.61) can be rewritten as [93]

$$\frac{\partial q_s}{\partial t} = \hat{n}\cdot\left[\sigma\mathbf{E}_{\mathrm{out}}(\mathbf{r},t) - \left(\sigma_b + \frac{2K_s}{a}\right)\mathbf{E}_{\mathrm{in}}(\mathbf{r},t)\right]_{r=a}. \tag{2.62}$$

The conductivity of the particle σ_p can be divided into a bulk conductivity σ_b and a surface conductivity $\sigma_s = 2K_s/a$, so that $\sigma_p = \sigma_b + \sigma_s$. Note that the relation between surface conductivity and surface conductance is particular to a sphere, and other geometries may have different coefficients. Finally, this redefinition of the particle conductivity maintains the definition for the CM factor. In fact, for most particles used in electrokinetics on the micrometric scale and below, bulk conductivity inside the particles can be safely neglected when compared to the conductivity due to the EDL, so that $\sigma_p \approx 2K_s/a$.

From the boundary condition at the particle interface, a time constant can be determined which scales with $\sim \varepsilon/\sigma$. This divides the polarization of the particles into two distinct responses depending on the frequency of the applied field: an interfacial polarization governed by the electrical permittivity, and a surface polarization governed by the conductivity in the EDL. Further polarization mechanisms (orientational, atomic and electronic [57]) can be considered

constant for the purposes of this thesis given the differences between frequency regimes. The interfacial polarization dominates up to a frequency of approximately 10^{10} Hz.

The relaxation time of interfacial polarization is described by the CM factor (in particular, by the maximum of its imaginary part), leading to a typical relaxation frequency of

$$\tau_{MW} = \frac{\varepsilon_p + 2\varepsilon}{\sigma_p + 2\sigma} \Rightarrow f_{MW} = 10^6 \text{ Hz} \tag{2.63}$$

for the conditions presented in Figure 2.8(a) with a particle radius of $a = 1$ μm. This is known as the *Maxwell-Wagner* relaxation, sometimes also referred to as β-relaxation. Above this frequency, the EDL polarization cannot follow the oscillations of the field and the contributions decays. This implies that the interfacial polarization dominates, as observed by taking the limit $\omega \to \infty$,

$$f_{\mathrm{CM}}(\omega \to \infty) = \frac{\varepsilon_p - \varepsilon}{\varepsilon_p + 2\varepsilon}. \tag{2.64}$$

At frequencies below the Maxwell-Wagner relaxation time, conduction of the EDL dominates and the CM factor can be written in terms of the Dukhin number:

$$f_{\mathrm{CM}}(\omega \to 0) = \frac{\sigma_p - \sigma}{\sigma + 2\sigma} = \frac{2\mathrm{Du} - 1}{2\mathrm{Du} + 2}. \tag{2.65}$$

The boundary conditions (2.56-2.58) describe surface conduction effects without interfacial polarization, i.e. the electrokinetic phenomena below the Maxwell-Wagner relaxation frequency. Paper D describes solutions of the equations and boundary conditions presented in last two sections for the case of a sphere in an AC field. The limiting case at high frequencies is found to coincide with the DEP description of the CM factor at low frequencies, given by equation (2.65). However, at low frequencies it is known that for moderate to high surface charges, a further polarization arises beyond the double layer: concentration polarization (CP), already described in the context of DEP by Dukhin & Shilov [94] and by Lyklema [79], who introduced a generalised CM containing the effects of CP.

Paper D describes how the relaxation time for the CP, referred as the α-relaxation, is governed by the diffusion equation, and therefore the characteristic time is given by

$$\tau_{CP} = \frac{a^2}{2D} \Rightarrow f_{CP} \approx 300 \text{ Hz} \tag{2.66}$$

for a KCl electrolyte ($D = 2 \times 10^{-9}$ m^2/s) and a particle radius of $a = 1$ μm. A generalised CM factor is given in equation (2.15b) of that paper,

$$\tilde{f}_{CM} = \frac{2\mathrm{Du}(1 + k + k^2) - (2 + 2k + k^2)}{2 + 2k + k^2 + \mathrm{Du}(k + 2)^2}, \tag{2.67}$$

where $k = \sqrt{i\omega a^2/D}$. The different descriptions of the CM factor describing the CP, EDL polarization and interfacial polarization are shown in Figure 2.8(b).

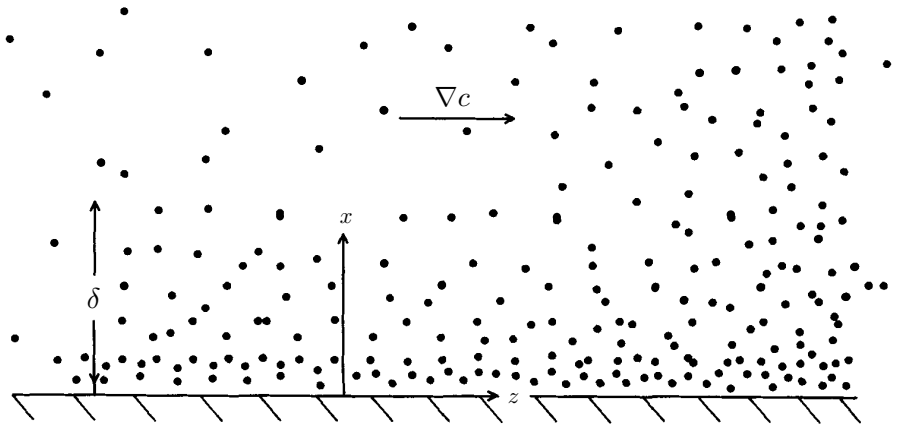

FIGURE 2.9: Representation of counterions in the problem of diffusiophoresis, where an external concentration gradient ∇c is imposed. Modified from [83].

2.5.3 Diffusiophoresis

Diffusiophoresis (DP) describes the motion of particles driven by ion concentration gradients in electrolytes. This is can be described by using the equations and boundary conditions highlighted in sections 2.3 and 2.4 imposing a concentration gradient ∇c. Figure 2.9 shows a surface in a concentration gradient of ions, where the double layer can also be observed.

Examining the bulk equations (2.44) and (2.45), equating the right-hand side of both equations shows that if a concentration gradient is imposed, then an electric field arises.

$$\nabla \cdot (c\nabla\phi) = \gamma D\nabla^2 c, \quad \nabla \cdot (c\nabla\phi) = \nabla \cdot (\gamma D\nabla c),$$

and except for an integration function which is taken to be zero, the electric field created by a concentration gradient in a non-symmetrical ($\gamma \neq 0$) electrolyte is

$$\nabla\phi = \gamma D\nabla \ln c. \tag{2.68}$$

With this equation, the velocity field at the slip plane can be derived by substituting the boundary condition (2.58),

$$\mathbf{v} = \left[\gamma D\zeta - 4\ln\left(\cosh\frac{\zeta}{4}\right)\right]\nabla \ln c. \tag{2.69}$$

This equation gives a physical interpretation of the two main contributions to diffusioosmosis:

- **Electrophoretic** Ion separation in the electrolyte creates an electric field if the diffusion constants of positive and negative ions are different [see equation (2.68)]. This field creates an electroosmotic motion as described in section 2.3.3.
- **Chemiphoretic** The Debye length is inversely proportional to the square root of the ion concentration in the electrolyte. Therefore, regions with higher concentration have less overall zeta potential, i.e. regions of lower energy to which the fluid will tend to move.

Finally, considering a particle instead of a surface, and assuming that the radius a is much greater than the Debye length, $\delta \ll 1$, the above reasoning can be applied, except for the fact that the final particle velocity is in the opposite direction as for the EP mobility:

$$\mathbf{u}_{DP} = -\left[\gamma D\zeta_p - 4\ln\left(\cosh\frac{\zeta}{4}\right)\right]\nabla \ln c. \tag{2.70}$$

This expression was first derived by Prieve *et al.* [83], but the systematic approach based in the SY model [53] leads to this without further complexity from the equations and boundary conditions. Note that if the electrolyte is completely *symmetrical* (e.g. KCl), $\gamma = 0$ so that the particles will always move towards higher concentrations regardless of the sign of the zeta potential.

This phenomenon was first recognised by Derjaguin *et al.* [95], but due to the experimental difficulties in producing stable concentration gradients at the micrometric scale, the applications of this phenomenon to continuous particle separation has not occured until recently. Concentration gradients have been reported using gas filtration in microchannels [96, 97], semi-permeable membranes [98, 99], and *Nafion membranes* [100, 101], which are ion-exchange membranes that adsorbs the cations of the solution releasing H^+ ions. The advantage of the latter is that the diffusivity of protons is much higher than other salt cations such as Na^+ and K^+. Therefore according to equation (2.68), this creates a significant electric field for the electrophoretic part of diffusiophoresis.

Continuous flow methods for generating concentration gradients have been published. One is known as a universal microfluidic gradient generator (MGG) [102, 103]. The idea is that two different concentration electrolytes enter through two different inlets and merge at will, overcoming diffusion by means of arrays of inner walls. By controlling the number, length and distribution of the walls, defined concentration gradients can be created.

Another method for generating these gradients is the widely-used technique of Isoelectric Focusing (IEF) (the theory of IEF and its development is given in [104]) in a continuous flow, known as Free-Flow Isoelectric Focusing (FF-IEF) [105]. These techniques make use of *Carrier Ampholites* (CA), substances that reach a steady-state position in an electrolyte of a certain conductivity when an electric field is applied, and that are also both good conductors and good buffers. The final position of these carriers generates a pH gradient that is used to discriminate proteins according to their *isoelectric point* pI. A work that combines the ideas of CA with continuous-flow separation was that of Song *et al.* [106]. Its aim is also to sort proteins based on pI, but with a concentration gradient was created due to the diffusion of two buffer solutions introduced from lateral channels instead of CA. Very narrow bands of proteins were obtained when an electric field was applied perpendicular to the direction of the fluid flow. For this reason, this work is similar to the observations of Calero *et al.* [30], but from a completely different perspective.

2.6 Electrokinetics on Metallic Surfaces

When an electric field is applied to a conductor in contact with an electrolyte, the slip velocities on the surfaces may lead to electrohydrodynamic flows that share common features with CPEO in some circumstances. The simplest case of induced charge on a metallic surface can explain this ICEO phenomenon.

2.6.1 Boundary Conditions in DC Fields

For the case of metallic boundaries, consider the limiting scenario of small surface charge and weak electric fields, described by Squires & Bazant [43] and Yariv [107]. A more detailed model based on the asymptotic matching of variables inside the double layer was developed by Schnitzer & Yariv [108], analogous to the SY model for dielectrics described in previous sections.

Upon the application of an electric field E in an electrolyte in contact with a metallic surface, a redistribution of the surface charge happens so that the field remains outside the metal. Note that a surface charge Q_s may exist prior to the application of the electric field, which is conserved,

$$Q_s = \oint_{\partial S} q_s dS.$$

The *induced* surface charge distribution creates an EDL on the metallic surface that screens the charge and therefore, under the conditions of weak fields and small surface charge in which no CP effects are considered ($c = 1$ everywhere in the bulk), the boundary condition for the electric potential is

$$\frac{\partial \phi}{\partial n} = 0. \tag{2.71}$$

The boundary condition of the velocity field is the electroosmotic condition when no surface conduction is present, i.e.

$$\mathbf{v} = \zeta \nabla_s \phi. \tag{2.72}$$

The difference for conducting surfaces is that the zeta potential is determined or *induced* by the applied electric field, since the surface charge is not fixed. Specifically, the zeta potential is the difference between the potential at the solid wall and the potential in the boundary of the EDL. The former is given by the net surface charge of the surface (as explained above), and can be related in this limit through the Debye-Hückel approximation (see Figure 2.4) as $\rho_s = \varepsilon \zeta / \delta$.

2.6.2 Electrokinetics and Metallic Particles: ICEO

This section derives the electric field and fluid velocity field around an uncharged metallic particle of radius $r = a$ when an external field $\mathbf{E} = E_0 \, \hat{z}$ is applied. After the application of the field, the electrolyte in the vicinity of the surface undergoes a charging process as described above to form an induced double layer. This layer has a characteristic transient time of polarization known as

the charging time of the EDL. Given the governing diffuse behaviour of the EDL in the weak-field limit, it can be shown that this charging time is given by

$$\tau_c = \frac{\delta a}{D} \Rightarrow f_c \approx 2 \text{ kHz} \tag{2.73}$$

for KCl at a conductivity of 5 mS/m and a particle radius of 1 μm.

After this time, the boundary condition (2.71) can be applied taking the potential at the metal to be zero, leading to

$$\phi = -E_0 r \left(1 + \frac{1}{2r^3}\right) \cos\theta. \tag{2.74}$$

As the particle is considered to be initially uncharged, the zeta potential is given by

$$\zeta_p(\theta) = -\phi(r = 1, \theta) = \frac{3}{2} E_0 \cos\theta, \tag{2.75}$$

which allows the slip velocity to be derived on the particle surface using (2.72)

$$\mathbf{v}_s = \frac{9}{8} E_0^2 \sin 2\theta. \tag{2.76}$$

Note that the velocity field created by this boundary condition is the Gamayunov field given by equation (2.18) with $\mathcal{V} = \frac{9}{8} E_0^2$, so that the streamlines will be the ones represented in Figure 2.1(b). Also, as the velocity scales with the square of the electric field magnitude, it is independent of the orientation of the electric field. Thus, if the external field is oscillating with frequency ω, $\mathbf{E} = E_0 e^{i\omega t}\, \hat{z}$, the fluid velocity field will remain the same as long as its period is much smaller that the charging time of the electrolyte, $\omega \tau_c \ll 1$.

Following similar arguments to the ones described in section 2.5.2 for the polarization times in DEP, it can be shown [43] that when the period of the electric field is of the order of τ_c, the time-averaged component of the slip velocity can be described as

$$\langle \mathbf{v}_s \rangle = \frac{4}{8} E_0^2 \sin 2\theta \frac{1}{1 + \omega^2 \tau_c^2}. \tag{2.77}$$

This thesis describes how time-averaged electroosmotic fluid flows arise around dielectric particles subjected to AC electric fields. It is shown (see Paper D) how these flows exhibit the Gamayunov field as in the case of ICEO, meaning that an analogous qualitative behaviour is to be expected between metallic and dielectric particles, but differing in the origin of the maximum slip velocity. For this reason, many of the theoretical analysis of particle manipulation can be readily adapted from those of ICEO (as done in Paper F).

2.7 Summary

This section has introduced the minimal electrohydrodynamic and electrokinetic theory required to understand the analysis developed in this thesis that leads to the theoretical framework

describing Concentration Polarization Electroosmosis. It is intended to be as self-contained as possible, describing the mathematical tools from first principles. It is also be descriptive, so that the main concepts are described with the help of diagrams. Each paper in Part II in the thesis has its own background section which provides a link between the concepts introduced here and any new analyses.

Chapter 3

Experimental Methods and Technologies

This chapter describes the experimental techniques used in this thesis, from the design of the microfluidic devices to the tools used for the analysis of the results. Although a brief description of the specific devices, fabrication steps and materials used for delivering each part of the work are detailed in each Paper of Part II, this chapter describes common procedures.

3.1 Device Design

The first step for producing the microfluidic channels is the design. This is an iterative process in which the physical phenomena to be analysed serve as a guide to find the optimal shape and dimensions for the channel and its features. Microfluidic devices are first designed in 2D using the CAD software CleWin 4 (MESA+ Research Institute, University of Twente; Deltamask, The Netherlands). The height of the channels is later determined by the photolithography fabrication process in the cleanroom, and the final thickness of the devices is regulated in the mold replication process described in section 3.2, which is repeated every time a device is produced.

This section gives a detailed description of the different channel designs used, and references the papers in which each design was used.

3.1.1 Design 1. Pillar Arrays

The first features used for the characterisation of the CPEO flows was a square array of pillars consisting of 20 μm diameter posts separated by 40 μm between centres in both directions, as shown in Figure 3.1(a). These features were embedded in a channel which was 200 μm wide, 1 cm long and 50 μm tall. This device also contained isolated pillars of different diameters (20, 40, 60, 80, and 100 μm) to test different situations. CPEO flows around an isolated 20 μm post are

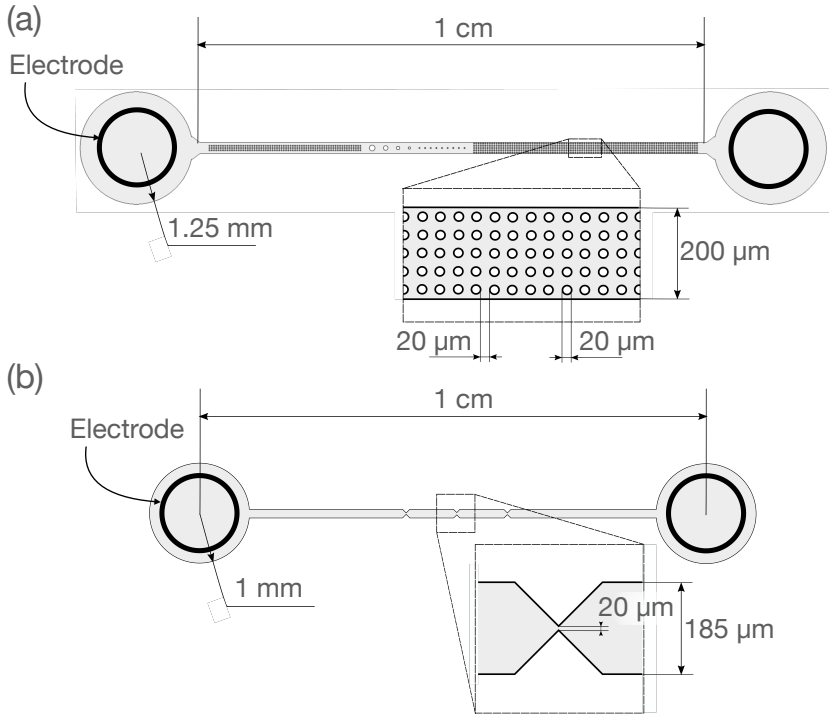

FIGURE 3.1: Diagram of device designs 1 and 2 presented in sections 3.1.1 and 3.1.2. These designs have optimal dimensions to study the fluid flow induced by CPEO around the features.

shown in the Supplementary Material for Paper C; Figure S1 of Appendix A. The channels have reservoirs at both ends which serve as inlets to the device. The experiments using this design were published in Paper C.

3.1.2 Design 2. Constrictions

The second design is presented in Figure 3.1(b). It consists of a device with similar external dimensions as the design 1, but fabricated in two different thicknesses: a shallow channel 10 μm tall, and a higher device of 50 μm. The features inside the channel were three triangular constrictions of 90-degree angle at their tip, producing a gap of 20 μm. CPEO flows were characterized around the tips of these constrictions in Paper E.

3.1.3 Design 3. Straight Rectangular

Design 3 is the simplest device design. It consists of a rectangular channel 50 μm wide, 50 μm tall, and 1 cm long, with reservoirs at both ends serving as fluidic inlets as well as electrodes, as shown in Figure 3.2(a). This design was used to observe CPEO flows around microparticles in Paper D, and to examine the particle-wall repulsion in Papers F and G. It was also used in paper 3.4.1 to develop the simplified method for zeta potential measurements.

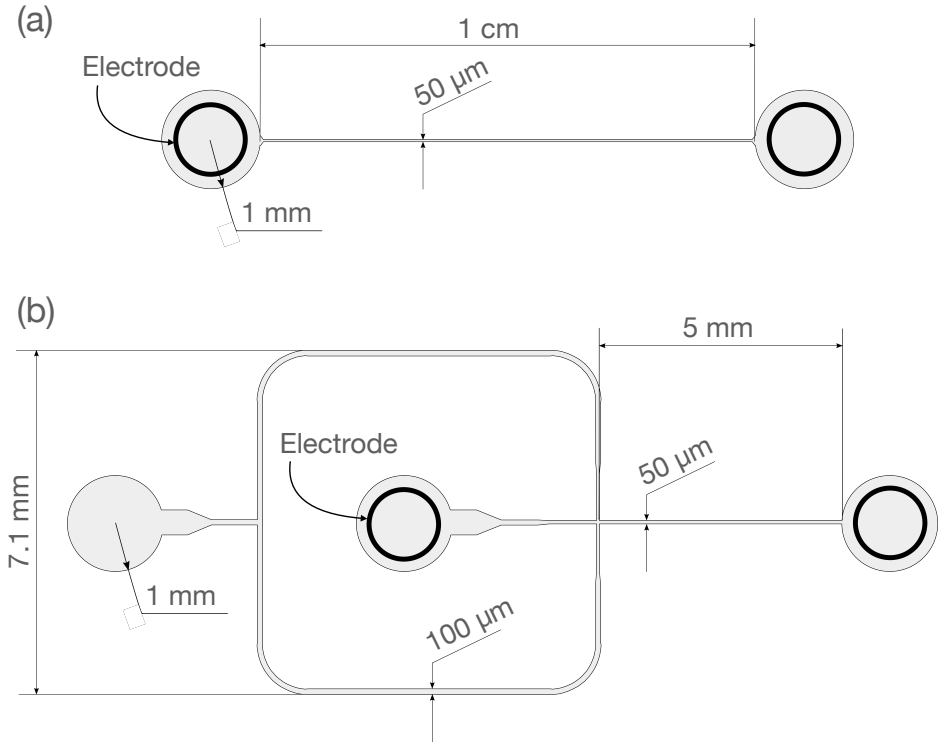

FIGURE 3.2: Diagram of designs 3 and 4 presented in sections 3.1.3 and 3.1.4. The dimensions of these channels are optimal for exploiting the particle-wall repulsion resulting from CPEO flows.

3.1.4 Design 4. Co-Flow

The co-flow design shown in Figure 3.2(b) is often used in microfluidics for particle fractionation using hydrodynamic-mediated particle-wall interactions, such as inertial or viscoelastic lifting. This design was used as a proof-of-concept device for particle fractionation using CPEO. This was used in Paper H to fractionate populations mixtures of micron-sized particles based on size and surface charge. However, the design has only one outlet as it was used to test the separation capabilities and not for real sample separation. The design was also used to test the software performance of the GUI presented Paper 3.4.2.

In this design, the sample is introduced through the left-most inlet, as in Figure 3.2(b). Then a sheath flow, introduced through the central inlet meets the sample flow at the junction, and pushes the sample towards the lateral walls of the central channel, which is 50 μm wide.

3.1.5 Design 5. Travelling-Wave around a Pillar

The last microchannel design is shown in Figure 3.3(a). This design consists of a microfluidic channel with inlets at both ends to control the flow and eventually stop it to perform experiments. The channel divides in two curved arms that intersect at right angles, with a 20 μm pillar in the centre of the intersection. The design is made so that when aligned with a set of quadrupolar electrodes, as shown in part (b) of the Figure, a $\times$-shape is achieved which preserves

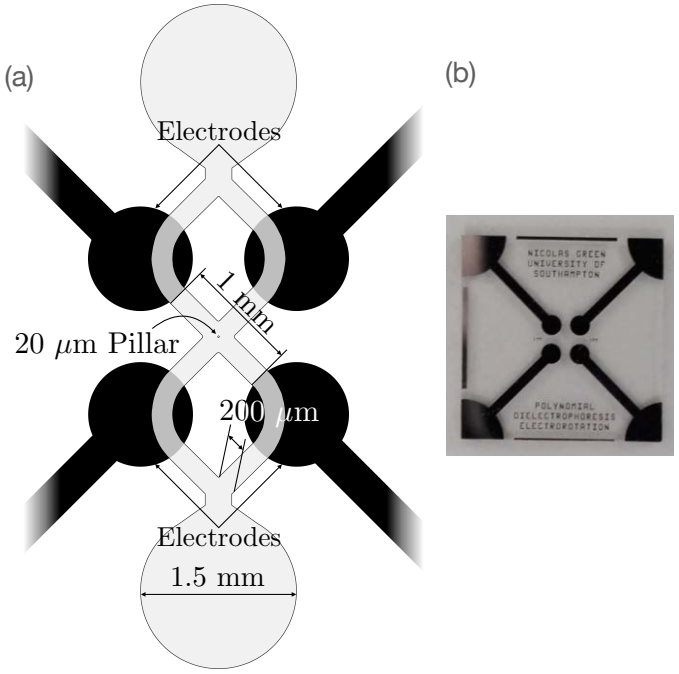

FIGURE 3.3: Diagram of design 5 presented in section 3.1.5. The channel dimensions described in (a) were designed to fit electrodes already fabricated for electrorotation, shown in (b).

the symmetry of the electrodes. The channel shape and electrodes create a rotating field around the pillar. The channels are 50 μm tall.

3.2 Device Fabrication

Devices were made by replica molding of polydimethylsiloxane (PDMS) on masters, fabricated following standard photolithography procedures. This is visually presented in Figure 3.4. The process is as follows. First a silicon wafer is spin-coated with a negative photoresist (SU-8) of the desired thickness, which defines the height of the channel. Then, a chrome mask with the channel designs (section 3.1) is placed onto the coated wafer and the resist exposed to UV light through the mask. As the resist is negative, the portion that is exposed to light hardens in the photoresist developer while the rest of the resin gets washed away.

Wafers were made with several different designs. Poly(methyl methacrylate) (PMMA) was laser-cut to fabricate molds of the desired thickness for the final device. These simple molds covered the unused designs on the wafer and exposed the required design in which the PDMS is cast. Wafers were treated with perfluore-silane to avoid adhesion of the PDMS during the curing process.

For device fabrication, PDMS monomer is mixed with 10 %(w/w) curing agent. Then, the mixture is degassed and poured on top of the mold. The PDMS is cured for at least two hours in an oven at 60° C. Devices are peeled from the wafer and holes are punched at both ends of the channel to create inlets. The resulting PDMS block is oxygen-plasma bonded to a glass slide. For

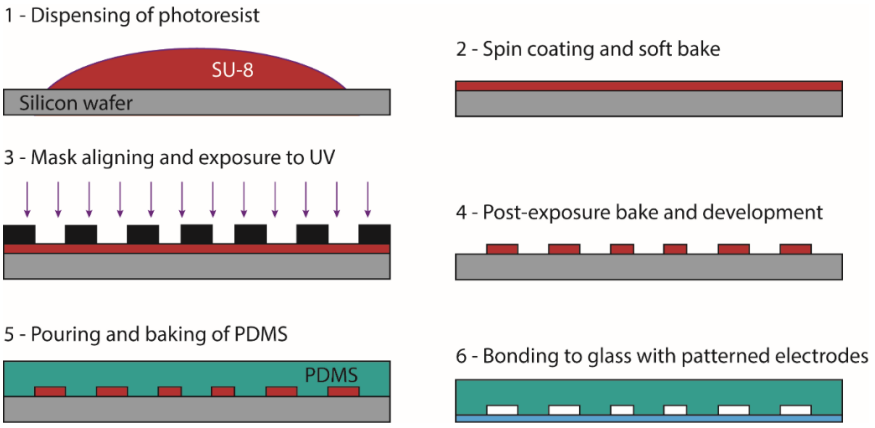

FIGURE 3.4: Fabrication process for microfluidic devices, from the master wafer to final PDMS-glass device. Figure copied from Ref. [26].

this step, the glass and PDMS surfaces to be bonded are exposed for 30 seconds to an oxygen plasma. After exposure, surfaces are mated and the device is baked again for two hours at 60° C. This final step creates the covalent bonding between both surfaces.

Design 5 required an additional alignment step between the PDMS and the glass which has the patterned electrodes. These were reused and de-bonding was achieved by soaking the entire device in pure Ethanol overnight.

3.3 Methods

3.3.1 Device Preparation

In practice particles adhere to the walls of the channel, as explained by the DLVO theory [109]. To avoid this effect, the surfaces were treated with a non-ionic surfactant. These are molecules consisting in long carbon chains with a hydrophilic head. After surface treatment, the heads attach to the wall surface with the tails extending into the fluid bulk, preventing particles reaching the surface. In this work, Pluronic F-127 was used.

The treatment with Pluronic was achieved by flowing a solution of 0.1 %(w/v) surfactant in deionised (DI) water through the device for at least 30 minutes. As discussed in Paper 3.4.1, surfactant-treated walls have a reduced electroosmotic mobility compared to untreated surfaces. This paper describes the differences in the zeta potential of microfluidic channels after treatment with Pluronic.

Particle Diameter	Functionalization	Zeta Potential (mV) [conductivity]	Used in Paper
500 nm	Carboxylate	-63±6 [6.6 mS/m]	C-H, 3.4.2, J
1 μm	Carboxylate	-62 [1.7 mS/m]	E-H
2 μm	Carboxylate	-72 [1.7 mS/m]	F-H, 3.4.2
3 μm	Carboxylate	-81 [1.7 mS/m]	D,F-H
	None (Plain)	-27 [1.7 mS/m]	F-H

TABLE 3.1: Polystyrene particles used for the experiments in the thesis. Measurements of zeta potential were done with the Malvern Zetasizer Nano ZS with particles suspended in a KCl electrolyte of the conductivity given between square brackets.

3.3.2 Samples

The electrolytes were solutions of potassium chloride (KCl) in DI water at different concentrations/conductivities, usually ranging from 1.5 $\mathrm{mS/m}$ to 15 $\mathrm{mS/m}$. For experiments the electrolyte was seeded with a range of different polystyrene particles; a summary is provided in Table 3.1. The concentration of particles varied depending on the study, roughly varying between $\sim 10^6$ mL^{-1} for particles that were analysed independently, to $\sim 10^8$ mL^{-1} when used as tracers of the fluid.

Paper H describes the use of a gram-positive bacteria culture, *S. Aureus* 9144, in the stationary phase of growth at $\sim 10^8$ $\mathrm{cfu/mL}$. Details of the bacteria culture and harvesting are summarised in the paper.

3.3.3 Setup and Measuring Equipment

In most experimental circumstances, no net fluid flow or a very low-velocity was required in order to observe the electroosmotic flows. For this reason, a precise pressure controller was used (Fluigent MFCS-4C) which had a ± 0.01 mbar pressure control. The pressure controller was used to pressurize reservoirs connected to the inlets of the device. For the case of the flow-focusing described in Paper F, flow was controlled using two independent syringe pumps (Chemyx Fusion 200) to maintain the required ratio of flow velocities.

Connection to the inlets of the devices was made using metallic cylinders or needles which also served as electrodes, made of grade 316 stainless steel. This avoided the need for patterned electrodes on the glass substrate (excepting Design 5). The needles were connected to a high-voltage amplifier (Trek Model PZD700A), which provided a 200$\times$ amplification of the voltage from a signal generator (TTi, Inc TGA12104). The signal was continuously monitored using an oscilloscope (Agilent Technologies DSO3202A). The amplifier could deliver up to 2000 Vpp with frequencies up to 50 kHz.

Particle motion was recorded using a fluorescence camera (Hamamatsu ORCA-ER C4742-95) installed on an inverted microscope (Zeiss Axiovert 200) which allowed visualization of the channels through the glass wall of the device. The optics of the microscope allowed a range of

magnifications from $5\times$ up to $63\times$. Particles smaller than 2 μm were visualized with fluorescence using a mercury lamp and filter cubes.

3.3.4 Analysis Tools

The output of a typical experiment was a video of approximately two minutes taken at a constant frame rate of 16 frames per second (fps). Offline analysis of the videos provided the experimental information shown in the papers. The image analysis depended greatly on the specific objectives of the research, but a common set of tools were used.

MATLAB was used for frame analysis and particle identification, either for tracking or just positioning in image frames. Particle tracking was done using the software PIVlab [110, 111] as specified in the Supplementary Material found in Appendix A. This software was written in MATLAB, and can be installed as a toolbox in the main MATLAB GUI. Particle positioning was performed using a custom-written MATLAB code, which is published in Paper 3.4.2. MATLAB was also used for statistical analysis and data representation.

COMSOL Multiphysics was used as the finite element method tool for simulating the electric and fluid flow fields when no analytical approach could be used, for example in the complex 3D geometries of the microfluidic channels.

3.4 Method Articles

3.4.1 Paper A: A simple and accurate method of measuring the Zeta-Potential of microfluidic channels

Summary of Results

An important experimental parameter for the validation of the CPEO theory is the zeta potential. A simplified technique was developed to determine the zeta potential of the walls of a microfluidic PDMS channel from the electroosmotic mobility. A simplified experimental setup and technique is presented.

Contribution Statement

I had the idea of using a simplified method which relied on experimental measurements rather than calculations from models using the Current-Monitoring method for determining the zeta-potential in a microfluidic channel. I did the experimental work and the experimental data analysis. Morgan and I developed the simplified method for the experimental procedure, and I wrote the first version of the manuscript. Morgan, Garcia-Sanchez, Calero and Ramos provided supervisory support. All authors contributed to the final version of the manuscript.

Raúl Fernández-Mateo[1]
Pablo García-Sánchez[2]
Víctor Calero[2]
Antonio Ramos[2]
Hywel Morgan[1]

[1]School of Electronics and Computer Science, University of Southampton, Southampton, United Kingdom
[2]Depto. Electrónica y Electromagnetismo, Facultad de Física, Universidad de Sevilla, Sevilla, Spain

Received August 25, 2021
Revised October 11, 2021
Accepted October 23, 2020

Short Communication

Short communication: A simple and accurate method of measuring the zeta-potential of microfluidic channels

We describe an improved method for determining the electroosmotic mobility and zeta potential of surfaces based on a current-monitoring method. This technique eliminates the requirement for measurements of channel dimensions and sample conductivities, leading to a simple high precision measurement. The zeta potential of PDMS is measured for native surfaces and surfaces treated with a nonionic surfactant in low-conductivity electrolytes.

Keywords:
Current-monitoring method / Electroosmosis / PDMS / Zeta-potential
DOI 10.1002/elps.202100267

The zeta potential (ζ) is widely used to characterize the properties of a surface in contact with an electrolyte, particularly the surface charge density [1]. Determination of the zeta potential after surface chemical modification provides a means of characterising the effects of these modifications on polymer substrates which are widely used in microfluidic devices [2–5]. It is also important for applications such as capillary zone electrophoresis, where charged substances such as biopolymers are separated based on their electrophoretic mobilities [6].

Many different microfluidic techniques have been developed to determine the zeta potential of materials, and a summary and detailed comparison of these methods can be found in [7]. The most widely used method for fast and simple measurement of zeta potential is the so-called current-monitoring method, first reported by Huang et al. [8], which measures the electroosmotic velocity u_{EO} inside a channel. The principle involves measuring the DC current flowing through a microchannel when an interface between two electrolytes of slightly different conductivity move through the channel due to electroosmosis. A common experimental setup is shown in Fig. 1 and the experimental procedure is as follows.

Electroosmosis arises from the action of the electric field on the counterions that screen the surface charges. Assuming negative surface charges, electroosmosis drives the fluid from left to right in Fig. 1 if the applied voltage is positive. One electrolyte with a known conductivity is loaded in reservoir 1 while another electrolyte with a slightly different conductivity fills the channel and reservoir 2. When the DC voltage is applied, the electrical resistance of the device is dominated by the conductivity of the electrolyte in the channel because of its small cross-section compared to the reservoirs. That is, the resistance of the device R_{ch} is given by

$$R_{ch} = \frac{1}{A}\left(\frac{L_1}{\sigma_1} + \frac{L_2}{\sigma_2}\right), \tag{1}$$

where A is the cross section of the channel and L_i is the length of the channel occupied by the electrolyte with conductivity σ_i ($i = 1, 2$). Thus, $L_1 + L_2 = L$ is the total length of the channel.

As the electrolyte in reservoir 1 slowly replaces the electrolyte that initially filled the channel, the resistance of the channel changes. This variation in resistance is monitored by measuring the voltage drop (V) across a series resistor with resistance R; see Fig. 1. The voltage drop V changes until the original electrolyte is completely replaced. The electroosmotic velocity $\mathbf{u}_{EO}$ is obtained from a measurement of the time it takes for one of the solutions to replace the other, which in turn is determined from the duration of the voltage (or current) transient described above. The zeta potential is then obtained from the velocity of the fluid displacement through the Helmholtz–Smoluchowski equation:

$$\mathbf{u}_{EO} = -\frac{\varepsilon\zeta}{\eta}\mathbf{E}, \tag{2}$$

where ε and η are, respectively, the electrical permittivity and dynamic viscosity of the electrolyte, and $\mathbf{E}$ is the applied electric field.

This simple method has been widely used and improved, particularly with respect to the S/N of the current [9] and throughput and repeatability [10]. Most techniques now use the so-called "slope method" for determining $\mathbf{u}_{EO}$ [11], which addresses the problem of the lack of precision in timing the liquid displacement owing to the gradual transitions at the end of the process. With this method only the rate of change in the current is measured when the displacing electrolyte interface is at the central position of the microchannel.

Correspondence: Dr. Hywel Morgan, School of Electronics and Computer Science, University of Southampton, Southampton SO17 1BJ, United Kingdom E-mail: hm@ecs.soton.ac.uk

Color online: See article online to view Figs. 2 and 3 in color.

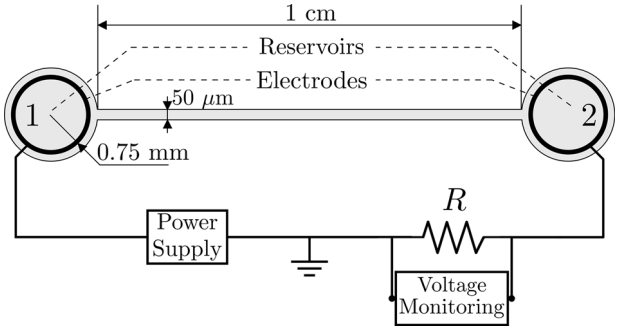

Figure 1. Diagram of an experimental setup of the current-monitoring method along with device dimensions used for measurements.

In this work, we describe an improved current monitoring method that significantly reduces the number of experimental parameters while increasing the precision of the measurements; all performed on-chip. The complexity and size of the device is reduced meaning that experiments can be performed with short channels. The zeta potential was measured for a PDMS microchannel of 50 μm × 50 μm cross-section and 1 cm long (see Fig. 1). This is a significant reduction in size compared to the most recent reported work [9], where the channels were 6 cm long, 1 mm wide, and 35 μm tall. In the original work by Huang et al. [8], a capillary of 75 μm of inner diameter and a length of 63 cm is used.

Two metallic cylinders were inserted in the inlet and outlet of the PDMS channel—these acted as reservoirs as well as electrodes (see Fig. 1). Three different KCl electrolytes were used with conductivities of 1.5, 5.2, and 11.4 mS/m. For each conductivity, a second solution was prepared with a concentration at 95% of the original solution [8]. The electrical current was measured from the voltage drop across a resistor R connected in series with the channel (Fig. 1). The applied voltage (V_0) was selected so that the transient time of the conductivity displacement is approximately one minute. The resistance R was much smaller than the channel resistance ($R \ll R_{\text{ch}}$) and, therefore, the field in the channel can be calculated from $E = V_0/L$. However, R was large enough for the voltage drop across the resistor to be accurately measured. This meant that R was in the range between 1 and 10 MΩ, for an applied voltage of $V_0 = 20$ V.

The channel was initially filled with the electrolyte with a higher conductivity. The voltage across the resistor therefore decreases during the current transient. If the change in current is only due to differences in bulk electrolyte conductivity, the rate of change of current with time $m_I = \Delta I/\Delta t$ is [11]:

$$m_I = \frac{EA(\sigma_1 - \sigma_2)}{\Delta t} = \mathbf{u}_{\text{EO}} \frac{EA(\sigma_1 - \sigma_2)}{L}, \tag{3}$$

where E is the applied field , which can be considered constant because of the small change in conductivity. The two conductivities of the electrolytes are σ_1 and σ_2, which are measured independently. Finally, using (2) to relate the velocity with the zeta potential:

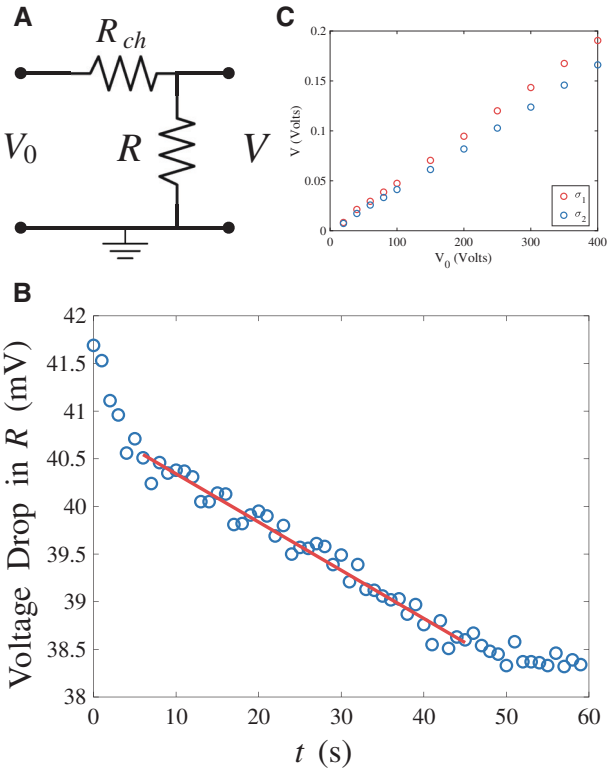

Figure 2. Technique for measuring the prefactors in Eq. (4). (A) Voltage divider with channel and test resistor. (B) Voltage drop across the resistor as a function of time for a conductivity of 5.2 mS/m. The electric field is applied at $t = 0$ s. The red line represents a linear fit to the data points between 5 and 45 s, which correspond to the transient due to the displacement of the higher conductivity electrolyte. (C) Example of voltage sweep experiment for two electrolyte conductivities: $\sigma_1 = 1.7$ mS/m and $\sigma_2 = 0.95\sigma_1$.

$$\zeta = \frac{\eta m_I L}{\varepsilon E^2 A(\sigma_1 - \sigma_2)}, \tag{4}$$

which is the common expression used to determine the zeta potential for the state-of-the-art slope method. However, this approach requires at least five independent experimental measurements, namely, channel cross section and length, two electrolyte conductivities and the slope of the current–time plot, each of which can contribute to a final relatively large experimental error.

As stated above, in this method the current is evaluated by measuring the voltage drop across a series resistor R, according to

$$m_I = \frac{\Delta I}{\Delta t} = \frac{1}{R}\frac{\Delta V}{\Delta t} = \frac{m_V}{R},$$

where V is the voltage drop across the resistor, and we have defined the rate of change of voltage with time as $m_V = \Delta V/\Delta t$. In doing so, the circuit becomes a voltage divider from which the total resistance of the channel R_{ch} can be estimated, as shown in Fig. 2A.

Figure 2B is an example of the voltage drop across the resistor as a function of time for an electrolyte of 5.2 mS/m

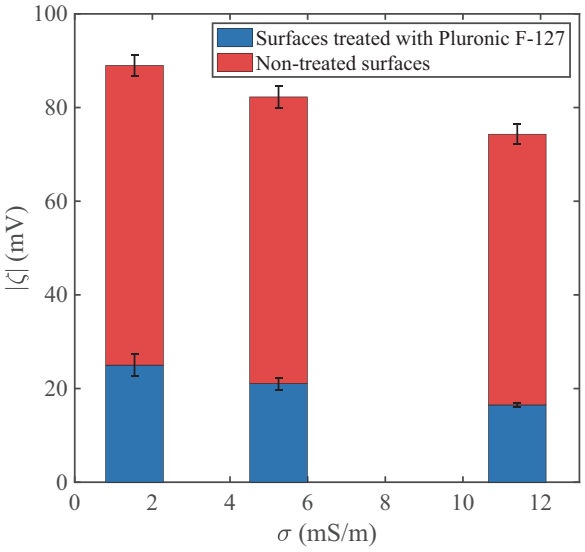

Figure 3. Estimation of zeta potential of PDMS for KCl electrolytes of 1.5, 5.2, and 11.4 mS/m. The ratio of zeta potential for treated and nontreated surfaces is 3.5, 3.9, and 4.5, respectively.

conductivity. Upon application of the electric field, a sudden decrease in voltage is observed, which does not seem related to the movement of the fluid. After a few seconds, the voltage decreases linearly with time, which corresponds to the change in channel electrical resistance due to the displacement of the more conductive solution. Finally, a plateau is reached corresponding to when the channel is filled with the lower conductivity electrolyte. The rate of change of the voltage m_V is obtained by fitting the data of the linear transient part of the graph as shown in the figure (solid line).

The channel resistance is $R_{\mathrm{ch}}(\sigma) = L/(\sigma A)$ when filled with a homogeneous electrolyte of conductivity σ. By defining the ratio of channel resistance to R as $r_{\sigma_i} = R_{\mathrm{ch}}(\sigma_i)/R$, Eq. (4) can be rewritten as

$$\zeta = \frac{\eta}{\varepsilon E^2} \frac{r_{\sigma_1} r_{\sigma_2}}{r_{\sigma_2} - r_{\sigma_1}} m_V . \tag{5}$$

It is clear that the important parameters are r_{σ_i}, the ratios of the channel resistances to R, which can be accurately measured through the slope of a voltage sweep when the system is filled entirely with one of the two conductivities, as shown in Fig. 2C. Significantly, this method circumvents the need for quantification of the resistances of both channel and resistor, cross section and conductivities of the solutions.

The above method was used to experimentally determine the zeta potential of PDMS. The results are summarized in Fig. 3, and are in agreement with the results in [12]. Experiments using PDMS pretreated with 0.1% w/v Pluronic F-127 for at least 30 min were also performed and strong reduction of electroosmotic mobility was found, consistent with data in the literature [13]. The zeta potential was reduced by the following ratios: 3.5, 3.9, and 4.5 for the 1.5, 5.2, and 11.4 mS/m conductivity solutions, respectively, in accordance with our estimation for the electroosmotic mobility reduction on PDMS surfaces due to the Pluronic treatment [14].

PGS and AR acknowledge Grant PGC2018-099217-B-I00 funded by MCIN/AEI/ 10.13039/501100011033 and by "ERDF A way of making Europe".

The authors have declared no conflict of interest.

Data availability statement

The data that support the findings of this study are openly available in the University of Southampton repository at doi: 10.5258/SOTON/D1.

References

[1] Hunter, R. J., *Introduction to Modern Colloid Science*, Oxford University Press, Oxford 1993.

[2] Shadpour, H., Musyimi, H., Chen, J., Soper, S. A., *J. Chrom.* 2006, *A1111*, 238–251.

[3] Goddard, J., Hotchkiss, J., *Prog. Polym. Sci.* 2007, *32*, 698–725.

[4] García, C. D., Dressen, B. M., *Electrophoresis* 2005, *26*, 703–709.

[5] Wheeler, A. R., Trapp, G., Trapp, O., Zare, R. N., *Electrophoresis* 2004, *25*, 1120–1124.

[6] Jorgenson, J. W., Lukacs, K. D., *Science* 1983, *222*, 266–274.

[7] Kirby, B. J., Hasselbrink, E. F., *Electrophoresis* 2004, *25*, 187–202.

[8] Huang, X., Gordon, M. J., Zare, R. N., *Anal. Chem.* 1988, *60*, 1837–1838.

[9] Saucedo-Espinosa, M. A., Lapizco-Encinas, B. H., *Biomicrofluidics* 2016, *10*, 033104.

[10] Zeyad, A. A., Glawdel, T., Ren, C. L., Johnson, D. A., *Microfluid. Nanofluid.* 2009, *6*, 241–251.

[11] Sze, A., Erickson, D., Ren, L., Li, D., *J. Colloid Interface Sci.* 2003, *261*, 402–410.

[12] Kirby, B. J., Hasselbrink, E. F., *Electrophoresis* 2004, *25*, 203–213.

[13] Viefhues, M., Manchanda, S., Chao, T-C, Anselmetti, D., Regtmeier, J., Ros, A., *Anal. Bioanal. Chem.* 2011, *401*, 2113.

[14] Calero, V., Fernández-Mateo, R., Morgan, H., García-Sánchez, P., Ramos, A., *Phys. Rev. Appl.* 2021, *15*, 014047.

3.4.2 Paper B: Particle Finder: A Simple Particle Detection Tool for Continuous Flow Systems

Summary of Results

Measurement of particle-wall separation described in papers F and G were done by positioning the particles at the end of a microlfuidic channel. Each measurement consisted of identifying the position of particles in around 2000 frames. I developed a user-friendly software tool that automatically performs this measurement with no previous knowledge of image analysis methods needed.

Contribution Statement

I and Calero wrote the original source code for the analysis of the data of paper F. I had the idea to transition it to a user-friendly application when I was working on a paper for an European project (the evFoundry Project) I joined during a four-month suspension in my PhD [31], and envisioned how useful it could be for the microfluidics community. I prepared the first draft of the manuscript, the Figures in the paper and the Video Tutorial in the Supplementary material. I, Calero and Garcia-Sanchez contributed to the transition from the source code to the GUI application. Garcia-Sanchez, Ramos and Morgan provided supervisory support and funding. All authors provided review, validation, testing of the software. All authors reviewed the manuscript.

Microfluidics and Nanofluidics (2023) 27:19
https://doi.org/10.1007/s10404-023-02626-7

RESEARCH PAPER

Particle finder: a simple particle detection tool for continuous-flow systems

Raúl Fernández-Mateo[1] · Víctor Calero[2] · Pablo García-Sánchez[3] · Antonio Ramos[3] · Hywel Morgan[1]

Received: 6 October 2022 / Accepted: 11 January 2023

Abstract
We describe a user-friendly, open source software for single-particle detection/counting in a continuous-flow. The tool automatically processes video images of particles, including pre-conditioning, followed by size-based discrimination for independent detection of fluorescent and non-fluorescent particles of different sizes. This is done by interactive tuning of a reduced set of parameters that can be checked with a robust, real-time quality control of the original video files. The software provides a concentration distribution of the particles in the transverse direction of the fluid flow. The software is a versatile tool for many microfluidic applications and does not require expertise in image analysis.

Keywords Continuous-flow microfluidics · Particle detection · GUI · Particle counting software

1 Introduction

In continuous-flow microfluidics there is a common need for simple, rapid estimation of particle positions in the transverse direction of the fluid flow. The increasing amount of processed sample and volumetric throughput achieved in microfluidics demands for tools of particle detection which can process large amounts of information systematically. This is specially critical in processes intended for Point-of-Care applications (Lakhera et al. 2022).

Areas of interest include particle focusing (Motosuke et al. 2013; Jia et al. 2015; Fernandez-Mateo et al. 2022) and particle fractionation caused by phenomena such as Deterministic Lateral Displacement (DLD) (Calero et al. 2019, 2020), pinched-flow fractionation (PFF) (Yamada et al. 2004; Pødenphant et al. 2015), viscoelastic flow (Liu et al. 2017; Tian et al. 2017) or electrokinetics (Tayebi et al. 2021; Emmerich et al. 2022), among others. For different populations of particles flowing simultaneously, differentiation is critical in order to estimate parameters such as fractionation efficiency or relative concentration (Thomas et al. 2017).

Often the methodology for performing this kind of analysis (summarised in Fig. 1) is not reported (Liang et al. 2010; Liu et al. 2017, 2018) or standardised, and in many occasions relies on manual counting of particles (Ho et al. 2021) or indirect measurements such as fluorescence intensity (Ho et al. 2020) and/or image stacking (Liang et al. 2010). Apart from a time-consuming task, these methods do not provide an estimate of the accuracy of the resulting measurements.

We describe a simple, open-source software tool based on MATLAB programming language (MathWorks, Natick, Massachusetts) for particle detection and classification. It estimates particles centre positions with sub-pixel precision and allows for real-time visualization of the results. It stores particle positions data from all analyzed frames and plots a histogram of particle counts in the transverse direction to

✉ Raúl Fernández-Mateo
r.fernandez-mateo@soton.ac.uk

Víctor Calero
victor.calero@inl.int

Pablo García-Sánchez
pablogarcia@us.es

Antonio Ramos
ramos@us.es

Hywel Morgan
hm@ecs.soton.ac.uk

[1] School of Electronics and Computer Science, University of Southampton, University Street, Southampton SO17 1BJ, UK

[2] International Iberian Nanotechnology Laboratory (INL), Avenida Mestre José Veiga s/n, Braga 4710, Portugal

[3] Depto. Electrónica y Electromagnetismo. Facultad de Física, Universidad de Sevilla, Avda. Reina Mercedes s/n, Seville 41012, Spain

Published online: 03 February 2023

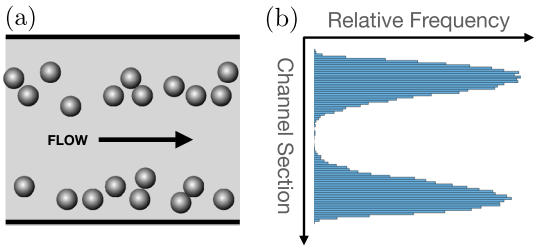

Fig. 1 Example of **a** the initial images of particles flowing in a microfluidic channel and **b** the final histogram that bins the positions of the particles in the direction transverse to the flow

the fluid flow. The width of the resulting histograms can be determined in the software, and exporting options allow further processing of the data.

2 Running the GUI

The software general workflow is summarised in Fig. 2 and it is openly available at Fernandez-Mateo (2022) . The Graphic User Interface (GUI) contains four tabs (shown in Fig. 3) which are designed to be simple and straightforward to use. Navigating through them in order will result in the

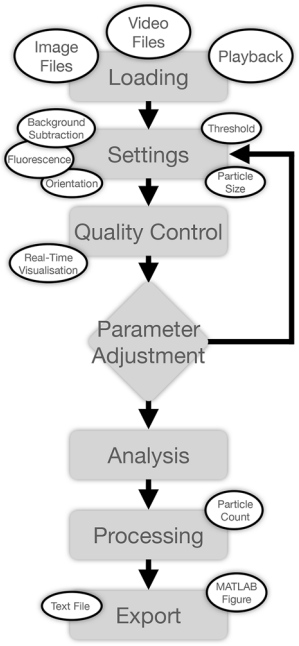

Fig. 2 Workflow of the program while navigating through the tabs. After loading the Video or Image files selecting the first set of parameters, the results are displayed in real-time to allow the user to fine-tune the selection to optimise the image processing. The image or video file is then analysed without visualization to maximise the processing speed. The results can be exported to a MATLAB figure or a text file

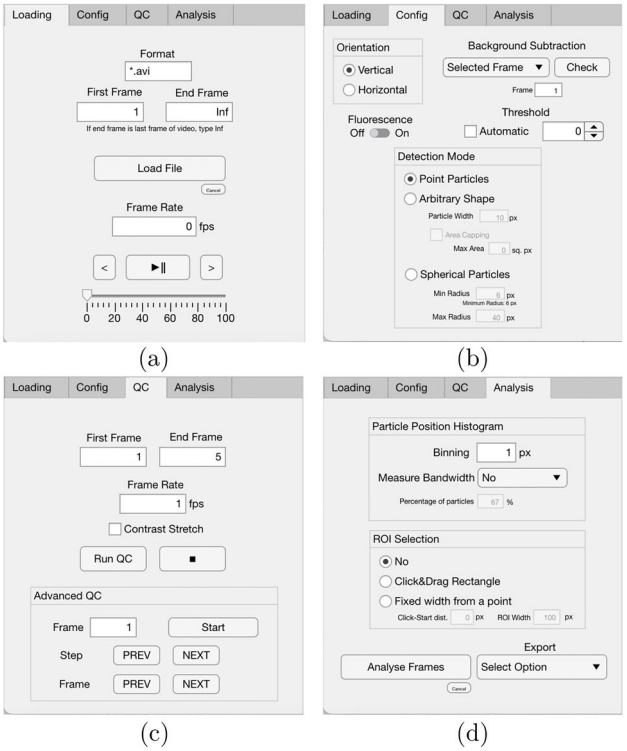

Fig. 3 The four tabs of the *Particle Finder* App, with the functions described in Sects. 2.1–2.4

detection, visualization and whole file analysis. Finally, the results may be exported to either a MATLAB figure or a text file with the raw data of transverse positions found for further post-processing of the results. Preliminary versions of the software have been tested to work flawlessly on different MATLAB versions (2019b to 2021b) under the main operating systems macOS X, Windows 10 and Ubuntu/LINUX. The final application has been packaged in the 2021b Runtime for Windows 10 operating system, and 2020b for macOS X. These are automatically added during the installation of the software and can be run without the necessity of having MATLAB installed.

2.1 Loading and playback

The software interactively imports data from local folders. This may be video or a sequence of image files from the *Load* (see Fig. 3a). Supported common image file formats are *.bmp*, *.jpeg*, *.png*, and *.tiff*. Supported video formats are *.avi*, *.mp4*, *.m4v* and *.mj2*, but these may depend on the operating system and MATLAB Runtime version installed with the software. When loading video files, the user can select the initial and final frames to be imported.

Once loaded, the frames appear in the graphical screen located at the right-hand side of the GUI window. The software provides play/pause of frames at original or selected

rates, displays the images frame by frame, or move to a selected frame, as shown in Fig. 3a.

2.2 Configuration of parameters

The specification of the general properties of the frames, as well as the particles to be detected is done in the *Config* tab of the GUI (Fig. 3b). The user selects the direction of flow on the frame sequence, and also whether the particles are fluorescent or non-fluorescent (i.e. shades in bright-field images).

The next step is background correction. Five different background subtraction options are available depending on the relationship between the target particles and the environment.

Selected frame—A frame without target particles is used as a reference to identify unimportant and static features in the images. The frame number is input below the drop-down menu.

Last frame—If the concentration of particles is low enough so that frames without particles are found, these can be used to set a dynamic background subtraction. This regenerates each time a frame with no particles is detected. This feature is convenient if images have slight variations in background illumination during an experiment. In order to start this process, a seed frame is selected to generate an initial background. The user inputs the seed frame number in the same location as the "selected frame" option below the drop down menu.

AVG—The software averages the intensity of each pixel position over all frames. This is the most versatile type of subtraction since it may be used for fluorescent or non-fluorescent particles.

MIN and MAX—When MIN is selected, the software returns the minimum intensity found in each pixel position for all the evaluated frames. This is normally the most robust background when evaluating fluorescent particles. In the same way, the MAX option selects the maximum intensity of all frames for each pixel position, which is most convenient for non-fluorescent objects.

For a simple robust platform, no correlation of particles is performed between frames. The optimal procedure for identifying objects is binarization of the images to completely isolate the objects and an important parameter in this process is the threshold. The threshold is the intensity value above which the software allocates an intensity value of 1 to a certain pixel position. Else, the value 0 is assigned.

The Particle Finder automatically designates a threshold estimation for the images based on the Otsu method (Otsu 1979). To improve the estimation, the fluorescent nature of the particles and the background subtraction method should be previously selected. The automatically chosen value may be further optimised by the user. To tune the value of the threshold, it is important to consider that the threshold is the intensity value which marks the difference between the targeted particles and the background noise, once the selected background is subtracted from the original frame. The magnitude of this intensity value is measured in the scale of the bit depth of the frames (for example, from 0 to 255 in 8-bit depth images).

The last stage is the detection mode, which is the criterion the software uses to discern a target particle between all pixels that have passed the threshold and noise reduction cuts. Particle Finder provides three different detection modes depending on the particle sizes and shape.

First the *Point Particles* mode detects particles that occupy single pixels in the frames. To achieve this the software makes use of the MATLAB custom function *find*, which locates the non-zero elements of a given matrix (here images are represented as matrices). This function is outstandingly fast in detecting particles when compared to the other two detection modes. Also, when this detection mode encounters particles that extend more than one pixel, it automatically removes them from the count. This featured may also be used for a size-based discrimination.

The second detection mode, *Arbitrary Shape* isolates particles of arbitrary size whose characteristic length is given by input parameter *Particle Width*, expressed in pixels. The function is *regionprops*, in the image processing toolbox of MATLAB. This function is flexible in terms of the size of the detected particles and may select sizes much larger than specified. Therefore an option to select a maximum detected area of the objects is included (in square pixels). The versatility of this detection mode lies in its ability to detect arbitrary shapes of any size. The particle position is finally given by the centroid of the detected distribution.

The last available detection mode, *Spherical Particles*, detects circles with radii ranging between two given input values; with a minimum value of 6 pixels in order to consistently discern circular patterns. If the apparent size of the spherical particles is below 6 pixels, the second detection option may be used. The software uses the function *imfindcircles*. The power of this algorithm lies in the ability to discern different particles even when they are aggregated due to the condition of spherical shape, while ignoring non-spherical shapes.

Finally, we note that the apparent size in pixels may vary depending on threshold conditions—higher thresholds could cause a reduction of the apparent size of the objects, and this should be considered when selecting the size parameters. However, as the histograms are built on the particle number count and not their intensity integration, the final histogram count is independent of the value set for the threshold as long as it allows the identification of the targeted particles. That is, if two similar but not equal thresholds that properly identify the targeted particles are found (which is often

possible when particles are clearly distinguishable from the background), then the resulting histograms are identical.

2.3 Quality control and visualization

Once all parameters have been set, the next tab *QC* shown in Fig. 3c previews in real time the accuracy of the particle detection for the chosen parameters. This provides a means of fine-tuning the parameters without processing all the frames.

For this purpose, the user inputs a range of frames to preview and the frame rate. Pressing *Run QC* button, the software displays the original frames with the centres of the detected objects marked with red dots. The visualization can be stopped at anytime by pressing the stop "■" button. For the case where the background is similar in intensity to the detected objects making them difficult to distinguish, the *Contrast Stretch* option labels the maximum and minimum value of intensity for each frame.

Finally, for the case where the detection parameters are particularly complex to optimise, the tool *Advanced QC* provides a feature for the user to explore each step in the particle detection for the selected settings and detection mode. Pressing *Start* takes the user to the first unmodified frame selected. From this point, it is possible to navigate through the different steps of the detection process i.e. background subtraction, binarization, noise reduction and particle identification. At any stage it is possible to move to the adjacent frames at the same detection step.

2.4 Complete analysis, data exploration and exporting

The detection process is summarised as follows: First, the background is subtracted from each frame; next, the resulting image is binarized where the selected threshold and noise reduction filters are automatically applied. Finally the selected detection mode is applied. This process is visually described in Fig. 4.

Particle Finder is designed to analyse a large number of frames in a single session. The tool was tested with videos up to 3000 frames. To reduce the time taken to analyse a large set of images, pressing the *Analyse Video* button in the *Analysis* tab (Fig. 3d), hides the displayed images.

To target the required objects and optimise the computational effort, this software can also select a Region of Interest (ROI). There are two different ways of selecting the ROI: The first is to click-and-drag with the cursor a rectangle of arbitrary shape. An alternative option allows the user to make a more accurate selection of the ROI by adjusting the width of the ROI rectangle in the direction of the fluid flow.

An important step is to configure how the data is processed. Particle Finder stores the transverse positions of the objects independent of their longitudinal position within the ROI. This is the most direct way for particle counting. Although this counting method does not reflect the number of particles detected, since one particle may appear in two or more consecutive frames as they flow, for a large enough number of frames the relative frequency of appearance across the transverse direction to the fluid motion represents the relative concentration of particles in this direction. Therefore, the information that can be extracted from the software meets the requirements for the type of analysis described in the literature.

Following the notation described in Fig. 5, in which the transverse direction to the fluid flow is denoted as $\hat{y}$ and the longitudinal direction as $\hat{x}$, we see that for an initial random concentration of particles in $\hat{x}$, and on average a spacing with distance $\bar{x}$, the average time $\bar{t}$ it takes for the next particle to cross the same y position is $\bar{t} = \bar{x}/u(y)$. Here, $u(y)$ is the fluid velocity profile across the section of the channel. Therefore, the number of particles crossing into the ROI on average per unit time N_t at position y is

$$N_t(y) = \frac{u(y)}{\bar{x}}. \tag{1}$$

This means that the number of particles crossing into the ROI does not properly represent the relative concentration of

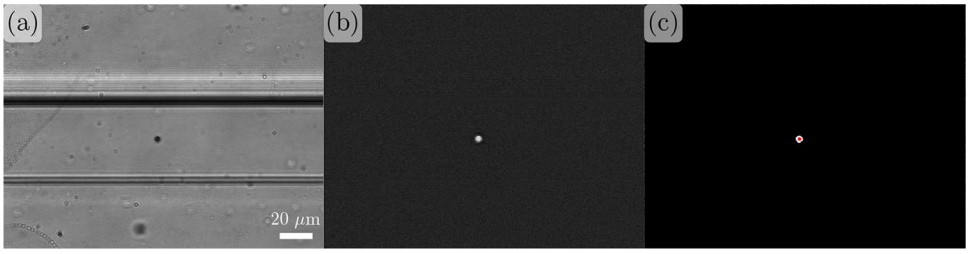

Fig. 4 The three primary steps taken by Particle Finder when detecting particles. **a** Original unmodified frame, where a non-fluorescent particle is seen in the center of the channel together with a background with uneven illumination. **b** Frame inverted and background subtracted. **c** Binarisation and noise reduction filters applied. The red dot marks the position of the particle in the frame assigned by the software. The example is for a 3 µm bead in a 50 µm wide channel

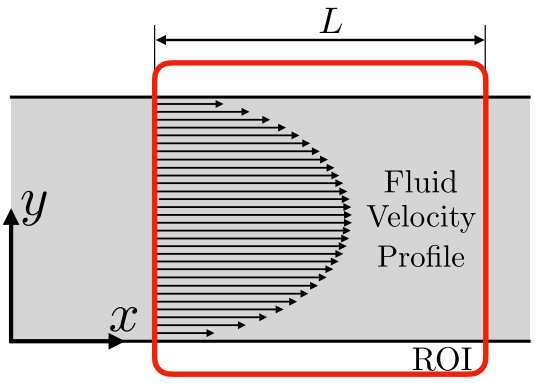

Fig. 5 Illustration of the parabolic profile for a straight channel with a region of interest (ROI) selected. If the concentration of particles is homogeneous along the x direction, for a fixed frame rate the number of counts is proportional to the particle concentration within the channel cross section

particles in the flow, but is biased by the particular velocity profile of the fluid. However, the software counts the number of times each particle appears in the ROI.

If the ROI has a length L in the $\hat{x}$ direction and frames are taken at a certain rate f_r, the number of times a particle appears in the ROI on average N_f is

$$N_f(y) = \frac{f_r L}{u(y)}, \tag{2}$$

so for image sets recorded for long enough time, the total number of counts C as a function of the $\hat{y}$ direction is the number of particles flowing through the ROI in that period, times the number of frames the particle spends in the ROI,

$$C(y) = N_t N_f \Delta t = f_r L \frac{\Delta t}{\bar{x}}. \tag{3}$$

This demonstrates that the number of counts is not influenced by the velocity profile of the fluid flow but responds to the real relative concentration of particles in the transverse direction, as none of the parameters in (3) depends on y. The reason behind this result is that in the y positions where the fluid flow is faster, the particles cross the ROI more frequently, but as they go faster they appear in fewer frames. These two facts compensate each other to obtain counts proportional to the actual particle concentration in the perpendicular direction to the fluid flow $\hat{y}$.

Finally, after analysing all frames, the software displays a histogram binning particle positions in the $\hat{y}$ direction. The user can select the width of the bins in pixels. The software exports the histogram into a MATLAB figure for further processing or as raw data in a text file.

Particle Finder also offers one post-processing option: measurement of the width of particle bands, i.e. the total width of the beam of particles detected or a selected percentage of the concentration. This measurement can be done in the *Analysis* tab of the software by choosing in the *Measure Bandwidth* selector either *From Median* if we want to count the percentage of particles from the median of the distribution, or *From Ends* if the count is to be made from the ends of the distribution.

3 Example

This section illustrates the operation of Particle Finder with an example video where two distinct particle populations flow in a straight channel. This video is openly available in the Supplementary Information.

In this case, particles flow in a 50×50 µm square cross-section straight microfluidic channel. The particle sample contains two distinct populations: the small particles are 500 nm diameter fluorescent beads, while the larger particles are 2 µm in diameter and non-fluorescent. They are suspended in an aqueous solution flowing at 7.5 µl/h.

After loading all the available frames of the .avi file, we start the independent detection of both populations. For the case of the 500 nm beads, we select the "Horizontal" direction of the flow, as in the video the particles are flowing from left to right. This population is fluorescent, so the particles are brighter than the background. This is indicated by selecting the "On" position in the fluorescence switch. Finally we choose the minimum projection of the stack of frames as the background, done by selecting the "MIN" option in the drop-down menu.

All these preconditioning options allow detection of the smaller particles when selecting a binarization threshold of 8 with the second detection mode "Arbitrary Shape". As seen in the example video, these particles have a typical length of 8 pixels. To avoid counting the 2 µm particles, we select the "Area Capping" checkbox to avoid particles above a certain area (200 square pixels) being counted.

Moving to the next tab into the QC section, we observe detection of the 500 nm beads, while the bigger particles are not counted. An example frame showing the two populations but with only smaller particles counted is presented in Fig. 6a. Finally, analysing the complete set of frames results in the blue bars of the histogram in Fig. 6c.

Detection of the larger 2 µm particles requires the third detection mode. Choosing 10 pixels as the minimum particle radius and 40 pixels as the maximum, the smaller beads will be ignored while the targeted particles are correctly identified. To compensate for the brighter objects, the binarization threshold is set as 35. This is seen in the example frame shown in Fig. 6b.

The final relative frequency for the larger particles is shown by the red bars in the histogram of Fig. 6c. For creating this figure, the results from both analysis have

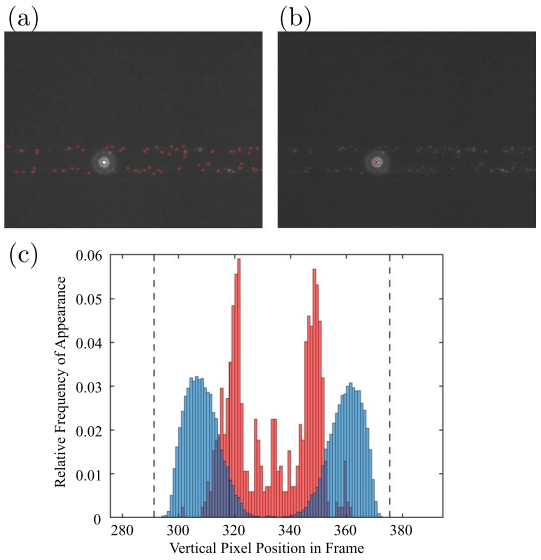

Fig. 6 Example of different populations of particles flowing simultaneously in a 50 µm-wide channel. **a** 500 nm particles detect by the QC in the software. **b** Larger 2 µm particles detected whilst ignoring the smaller particles. **c** Superimposed histogram of particle distribution in the ROI for 500 nm particles (blue bars) and 2 µm particles (red bars). The position of the channel walls are marked by the dashed vertical lines

been separately exported and combined in a single plot using MATLAB.

4 Conclusions

We have described a computational tool that provides users with no experience in image analysis with a user-friendly software for detection and analysis of particles in a flow. This is particularly useful in the case of microfluidic applications.

Preliminary versions of this software have already been used for previous publications (Fernandez-Mateo et al. 2022; Gillams et al. 2022) with different flow profiles, microchannel geometries and particle fluorescent intensities and size. The code is robust and versatile, and together with a simple GUI, it is very practical and easy to use for applications in particle analysis for microfluidics.

Supplementary Information The online version contains supplementary material available at https://doi.org/10.1007/s10404-023-02626-7.

Data availability statement The data supporting this publication is openly available from the University of Southampton repository at https://doi.org/10.5258/SOTON/D2503.

Declarations

Conflict of interest The authors declare no conflict of interest

References

Calero V, Garcia-Sanchez P, Honrado C, Ramos A, Morgan H (2019) Ac electrokinetic biased deterministic lateral displacement for tunable particle separation. Lab Chip 19(8):1386–1396. https://doi.org/10.1039/C8LC01416G

Calero V, Garcia-Sanchez P, Ramos A, Morgan H (2020) Electrokinetic biased deterministic lateral displacement: scaling analysis and simulations. J Chromatogr A 461151. https://doi.org/10.1016/j.chroma.2020.461151

Emmerich ME, Sinnigen A-S, Neubauer P, Birkholz M (2022) Dielectrophoretic separation of blood cells. Biomed Microdevices 24(3):1–19. https://doi.org/10.1007/s10544-022-00623-1

Fernandez-Mateo R (2022) Particle finder: detection tool for continuous-flow systems. MATLAB Central File Exchange. https://uk.mathworks.com/matlabcentral/fileexchange/117865-particle-finder-detection-tool-for-continuous-flow-systems (Matlab Central File Exchange). Accessed 22 Sept 2022

Fernandez-Mateo R, Calero V, Morgan H, Garcia-Sanchez P, Ramos A (2022) Wall repulsion of charged colloidal particles during electrophoresis in microfluidic channels. Phys Rev Lett 128:074501. https://doi.org/10.1103/PhysRevLett.128.074501

Gillams RJ, Calero V, Fernandez-Mateo R, Morgan H (2022) Electrokinetic deterministic lateral displacement for fractionation of vesicles and nano-particles. Lab Chip. https://doi.org/10.1039/D2LC00583B

Ho BD, Beech JP, Tegenfeldt JO (2020) Charge-based separation of micro-and nanoparticles. Micromachines 11(11):1014. https://doi.org/10.3390/mi11111014

Ho BD, Beech JP, Tegenfeldt JO (2021) Cell sorting using electrokinetic deterministic lateral displacement. Micromachines 12(30). https://doi.org/10.3390/mi12010030

Jia Y, Ren Y, Jiang H (2015) Continuous-flow focusing of microparticles using induced-charge electroosmosis in a microfluidic device with 3d agpdms electrodes. RSC Adv 5(82):66602–66610. https://doi.org/10.1039/C5RA14854E

Lakhera P, Chaudhary V, Bhardwaj B, Kumar P, Kumar S (2022) Development and recent advancement in microfluidics for point of care biosensor applications: a review. Biosens Bioelectron X 11:100218. https://doi.org/10.1016/j.biosx.2022.100218

Liang L, Ai Y, Zhu J, Qian S, Xuan X (2010) Wall-induced lateral migration in particle electrophoresis through a rectangular microchannel. J Colloid Interface Sci 347(1):142–146. https://doi.org/10.1016/j.jcis.2010.03.039

Liang L, Qian S, Xuan X (2010) Three-dimensional electrokinetic particle focusing in a rectangular microchannel. J Colloid Interface Sci 350(1):377–379. https://doi.org/10.1016/j.jcis.2010.06.067

Liu C, Guo J, Tian F, Yang N, Yan F, Ding Y, Sun J (2017) Field-free isolation of exosomes from extracellular vesicles by

microfluidic viscoelastic flows. ACS Nano 11(7):6968–6976. https://doi.org/10.1021/acsnano.7b02277

Liu Z, Li D, Saffarian M, Tzeng T-R, Song Y, Pan X, Xuan X (2018) Revisit of wall-induced lateral migration in particle electrophoresis through a straight rectangular microchannel: Effects of particle zeta potential. Electrophoresis 1–6. https://doi.org/10.1002/elps.201800198

Liu Z, Li D, Song Y, Pan X, Li D, Xuan X (2017) Surface-conduction enhanced dielectrophoretic-like particle migration in electric-field driven fluid flow through a straight rectangular microchannel. Phys Fluids 29(10):102001. https://doi.org/10.1063/1.4996191

Motosuke M, Yamasaki K, Ishida A, Toki H, Honami S (2013) Improved particle concentration by cascade ac electroosmotic flow. Microfluidics Nanofluidics 14(6):1021–1030. https://doi.org/10.1007/s10404-012-1109-1

Otsu N (1979) A threshold selection method from gray-level histograms. IEEE Trans Syst Man Cybern 9(1):62–66. https://doi.org/10.1109/TSMC.1979.4310076

Pødenphant M, Ashley N, Koprowska K, Mir KU, Zalkovskij M, Bilenberg B, Marie R (2015) Separation of cancer cells from white blood cells by pinched flow fractionation. Lab Chip 15(24):4598–4606. https://doi.org/10.1039/C5LC01014D

Tayebi M, Yang D, Collins DJ, Ai Y (2021) Deterministic sorting of submicrometer particles and extracellular vesicles using a combined electric and acoustic field. Nano Lett 21(16):6835–6842. https://doi.org/10.1021/acs.nanolett.1c01827

Thomas C, Lu X, Todd A, Raval Y, Tzeng T-R, Song Y, Xuan X (2017) Charge-based separation of particles and cells with similar sizes via the wall-induced electrical lift. Electrophoresis 18:320–326. https://doi.org/10.1002/elps.201600284

Tian F, Zhang W, Cai L, Li S, Hu G, Cong Y, Sun J (2017) Microfluidic co-flow of Newtonian and viscoelastic fluids for high-resolution separation of microparticles. Lab Chip 17(18):3078–3085. https://doi.org/10.1039/C7LC00671C

Yamada M, Nakashima M, Seki M (2004) Pinched flow fractionation: Continuous size separation of particles utilizing a laminar flow profile in a pinched microchannel. Anal Chem 76:5465–5471. https://doi.org/10.1021/ac049863r

Part II

Research Articles

Paper C

Stationary Electro-osmotic Flow Driven by ac Fields around Insulators

Summary of Results

This work was motivated by observations of unexpected electroosmotic fluid flows in the electrokinetic-biased DLD device during the PhD work of Calero [34, 30]. In the first paper I experimentally characterised the quadrupolar fluid flows that appeared in low-conductivity electrolytes in a low-frequency AC electric field. Following the theory by O. Schnitzer and E. Yariv [53] for electrokinetic flows at large zeta-potentials, the quadrupolar flows were modelled and the velocity field was compaed with the experiments. This phenomenon was termed Concentration-Polarization Electroosmosis (CPEO).

Contribution Statement

The idea of attributing the flow vortices to concentration polarization, and ultimately to surface charge, was conceived by my supervisors Morgan, Ramos and Garcia-Sanchez before the start of my project. In this paper, Calero designed and fabricated the devices. Calero and I contributed equally to the experiments, the theory was developed by my co-supervisor in Spain (Ramos) and simulations were performed by P. Garcia-Sanchez and myself. I found the appropriate tool for the analysis of the experimental data including comparison with the numerical simulations. Garcia-Sanchez and Ramos wrote the first version of the manuscript. Morgan, Ramos and Garcia-Sanchez provided supervisory support. All authors contributed to the final version of the manuscript.

Stationary Electro-osmotic Flow Driven by ac Fields around Insulators

Víctor Calero,[1] Raúl Fernández-Mateo,[1] Hywel Morgan,[1] Pablo García-Sánchez,[2] and Antonio Ramos[2,*]

[1] *School of Electronics and Computer Science, University of Southampton, Southampton SO17 1BJ, United Kingdom*

[2] *Departamento de Electrónica y Electromagnetismo, Facultad de Física, Universidad de Sevilla, Avda. Reina Mercedes s/n, Sevilla 41012, Spain*

(Received 25 August 2020; revised 22 October 2020; accepted 14 December 2020; published 26 January 2021)

Electric fields are commonly used for manipulating particles and liquids in microfluidic systems. In this work, we report stationary electro-osmotic flow vortices around dielectric micropillars induced by ac electric fields in electrolytes. The flow characteristics are theoretically predicted based on the well-known phenomena of surface conductance and concentration polarization around a charged object. The stationary flows arise from two distinct contributions working together: an oscillating nonuniform zeta potential induced around the pillar and a rectified electric field induced by the ion concentration gradients. We refer to this fluid flow as concentration-polarization electro-osmosis (CPEO). We present experimental data in support of the theoretical predictions. The magnitude and frequency dependence of the electro-osmotic velocity are in agreement with the theoretical estimates and are significantly different from predictions based on the standard theory for induced-charge electro-osmosis, which has previously been postulated as the origin of the stationary flow around dielectric objects. In addition to furthering our understanding of the influence of ac fields on fluid flows, we anticipate that this work will also expand the use of ac fields for flow control in microfluidic systems.

DOI: 10.1103/PhysRevApplied.15.014047

I. INTRODUCTION

Solid surfaces in contact with aqueous electrolytes usually carry a net surface charge arising from the different affinities of cations and anions [1]. This surface charge is screened by a diffuse ionic layer on the electrolyte side of the interface and liquid streaming can occur when an external electric field acts on these charges. This fluid flow is known as electro-osmosis (EO) [2] and is a common way of driving liquids within capillaries and microfluidic structures [3]. The thickness of the diffuse layer (the Debye length) for typical aqueous electrolytes is around tens of nanometers or smaller [1]. Thus, at length scales of micrometers or larger, the fluid motion that occurs within the diffuse layer can be modeled via an effective slip velocity tangential to the solid wall, $\mathbf{u}_{\text{slip}}$. The Helmholtz-Smoluchowski formula relates the slip velocity with the applied electric field ($\mathbf{E}$) and the zeta potential (ζ) of the interface [1]:

$$\mathbf{u}_{\text{slip}} = -\frac{\varepsilon\zeta}{\eta}\mathbf{E}, \tag{1}$$

where ε and η are, respectively, the electrolyte permittivity and its viscosity. The zeta potential is commonly defined as the electrical potential at the slip plane with the bulk solution [4].

In the case of ac electric fields, Eq. (1) predicts an oscillating slip velocity with a zero time-average value. However, recent experimental reports have shown a nonzero time-average slip velocity of electrolytes around dielectric pillars in an ac field [5]. Similar stationary (or rectified) flows have been observed around dielectric corners [6–8] and have been attributed to induced-charge electro-osmosis (ICEO) [9], i.e., electro-osmosis generated by the action of an electric field on the charges in the diffuse layer induced by the same field [10] [see Fig. 1(a)]. In this work, we show that ICEO is not the origin of these flows and demonstrate that a rectified fluid flow arises from the polarization of the modified electrolyte concentration (i.e., the concentration polarization, CP), which results from the surface conductance around a dielectric pillar [2].

Figure 1(b) shows a diagram of how the CP leads to a nonhomogeneous zeta potential. We assume that the pillar carries a negative intrinsic surface charge density (q_s) that is linked to ζ via the Gouy-Chapman equation $q_s = 2\sqrt{2c\varepsilon e\phi_{\text{ther}}}\sinh(\zeta/2\phi_{\text{ther}})$, where c is the electrolyte concentration and $\phi_{\text{ther}} = k_B T/e$ is the thermal voltage (in which k_B is Boltzmann's constant, T is the absolute temperature, and e is the proton charge; $\phi_{\text{ther}} \approx 25$ mV at 20 °C) [1]. A consequence of the surface charge is a local

*ramos@us.es

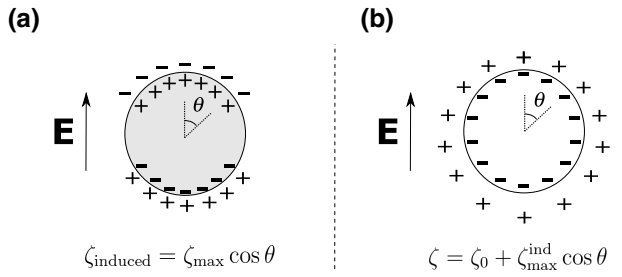

FIG. 1. (a) An applied electric field induces charges on an uncharged metal (conducting) cylinder. These are screened by ions in the liquid phase leading to an induced diffuse layer around the metal object. ICEO occurs due to the action of the applied field on these diffuse-layer charges. (b) A dielectric insulating cylinder has an intrinsic surface charge. Upon application of an electric field, surface conductance creates both a nonhomogeneous electrolyte concentration and a zeta potential around the cylinder. In (b), the distance of the positive ions (counter-ions) to the particle surface changes with the position—this indicates that the Debye length varies due to the concentration polarization (CP). For both (a) and (b) and using Eq. (1), the induced zeta potentials generate stationary quadrupolar flows around the cylinder.

increase in the counter-ion concentration within the diffuse layer and an accompanying enhancement in electrical conductivity, which manifests itself as a surface conductance that is in addition to the bulk electrolyte conductivity [2] [see Fig. 2(a)]. When an external electric field acts on the interface, the additional current near the wall leads to depletion of electrolyte on one side of the pillar and to a corresponding enhancement on the opposite side. Figure 2(b) depicts the variation in the electrolyte concentration that appears near a charged cylinder subjected to an external electric field. Thus, the electrolyte concentration near the wall is not homogeneous and since q_s is fixed, the Gouy-Chapman relation implies that ζ also varies over the solid wall. The effects of CP on colloids have been extensively studied [11–13]; it is responsible for the well-known low-frequency dispersion of a colloidal suspension—the so-called α relaxation.

In the following sections, we focus on developing a theoretical model for the effect of CP on the electro-osmotic slip velocity induced by an ac electric field around an insulating pillar. We show that two distinct mechanisms acting together give rise to stationary flows: an oscillating nonuniform zeta potential and a rectified electric field induced by the concentration gradients. We also present experimental data for these stationary flows. Both the magnitude and frequency dependence of the electro-osmotic velocity are in agreement with the theoretical estimates and differ significantly from predictions based on the theory for induced-charge electro-osmosis.

II. THEORY

Our analysis for an insulating cylinder follows the work of Schnitzer and Yariv [14,15] for the electrophoresis of charged particles immersed in a symmetrical electrolyte. We extend their analysis to the case of ac signals (see Appendix A for details). We perform a linear expansion of the governing equations for a small Dukhin number (Du); the ratio of the surface to the bulk conductance [2]. The linearization of the electrokinetic equations for ac voltages gives rise to a steady velocity field that scales linearly with Du but is quadratic with the amplitude of the electric field. In the approximation, the electrical potential is written as $\phi = \phi_0 + \delta\phi$, where ϕ_0 is the potential

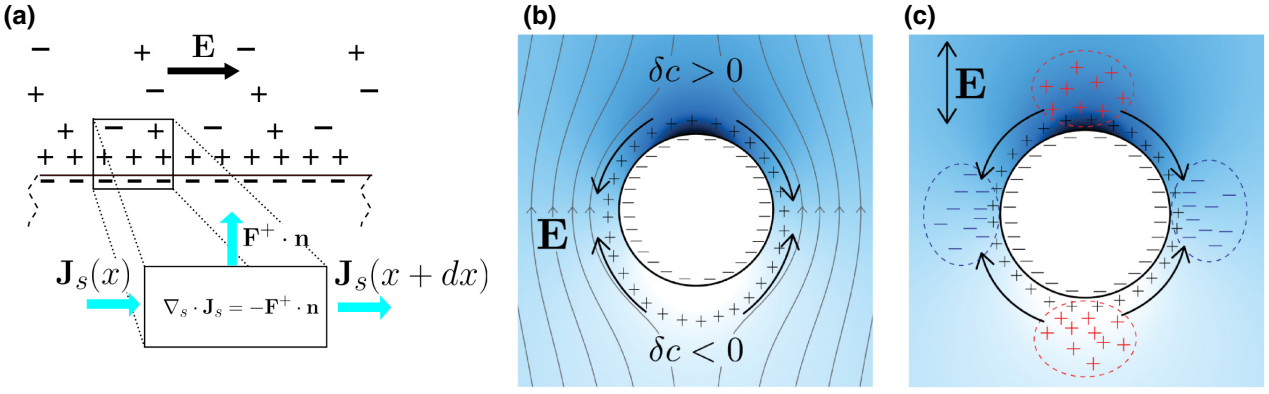

FIG. 2. (a) Negative charges on the dielectric surface attract (positive) counter-ions. The mean ion concentration increases near the surface, leading to a surface current density $\mathbf{J}_s$. Charge conservation implies that variations in the surface current must be balanced by a counter-ion flux ($\mathbf{F}^+$). (b) A color map showing the perturbation in the electrolyte concentration (δc) around a charged cylinder. The darker blue indicates a higher value of c. As a consequence of the CP, the screening thickness (the Debye length) depends on the position around the cylinder. The black arrows indicate the direction of the stationary electro-osmotic flow. (c) A consequence of the CP is induced free charge that is in addition to the concentration gradients. The rectified electric field due to these charges acts on the diffuse-layer charges and generates an electro-osmotic flow.

around a dielectric cylinder for $\mathrm{Du} = 0$ and $\delta\phi$ is the perturbation as a consequence of surface conductance. ϕ_0 satisfies the Laplace equation with zero normal derivative as the boundary condition on the cylinder surface. For an applied ac field of magnitude E_0 and angular frequency ω, ϕ_0 can be written as $\phi_0(t) = \mathrm{Re}[\tilde{\phi}_0 \exp(i\omega t)]$, where $\mathrm{Re}[\cdots]$ denotes the real part of the function between the brackets and $\tilde{\phi}_0$ is the potential phasor, which in cylindrical coordinates is written as

$$\tilde{\phi}_0 = -E_0 \left(r + \frac{a^2}{r} \right) \cos\theta. \tag{2}$$

Likewise, the salt concentration can be written as $c = c_0 + \delta c$, where c_0 is the bulk concentration and δc is the perturbation due to the applied field. For a relatively small surface conductance and neglecting advection, δc is given by the solution of the diffusion equation:

$$D\nabla^2 \delta c = \partial_t \delta c, \tag{3}$$

where D is the diffusion coefficient of the ions in the electrolyte.

For thin diffuse layers, the ion-flux balance shown in Figure 2(a) can be written as an effective boundary condition that incorporates the surface conductance as a parameter. Assuming that negative ions (co-ions) are expelled from the diffuse layer, the divergence of the surface current must be balanced by the normal flux of positive ions. The boundary condition for δc on the insulating surface is written as [15]

$$-\mathbf{n} \cdot \nabla \delta c / c_0 = \mathrm{Du}\, a \nabla_s^2 (\phi_0 / \phi_{\mathrm{ther}}), \tag{4}$$

where $\mathbf{n}$ is a unit vector normal to the wall, a is the cylinder radius, and ϕ_0 is the electrical potential. ∇_s^2 is the Laplacian operator tangential to the wall surface. As mentioned above, Du is the ratio of the surface to the bulk conductance ($\mathrm{Du} = K_s/a\sigma$, in which K_s is the surface conductance and σ is the electrolyte conductivity).

δc is also an oscillating function with angular frequency ω and with a frequency-dependent phasor given by

$$\delta\tilde{c}/c_0 = -2\mathrm{Du} \frac{E_0 a}{\phi_{\mathrm{ther}}} \frac{K_1(kr)}{kaK_1'(ka)} \cos\theta, \tag{5}$$

where $k = \sqrt{i\omega/D}$, $K_n(x)$ is the modified Bessel function of the second kind of order n, and $K_n'(x) = dK_n/dx$. The relaxation angular frequency for δc is the reciprocal of the typical time in the diffusion equation, $\tau = a^2/D$. Figure 2(b) shows the solution for δc around a cylinder for $\omega = 0$, i.e., a dc field.

According to the Gouy-Chapman relation, a change in the local concentration δc implies a perturbation in the zeta potential given by $\delta\zeta/\phi_{\mathrm{ther}} = -\delta c|_{r=a} \tanh(\zeta_0/2\phi_{\mathrm{ther}})/c_0$ and, thus, ζ can be written as shown in Fig. 1(b). For the case of an ac excitation, the inhomogeneous part of ζ is an oscillating function with angular frequency ω. Using the Helmholtz-Smoluchowski equation, it can be readily shown that a nonzero time-averaged electro-osmotic velocity appears, given by

$$\langle \mathbf{u}_{\mathrm{slip}} \rangle_{\mathrm{A}} = (\varepsilon/2\eta)\mathrm{Re}[\delta\tilde{\zeta} \nabla_s \tilde{\phi}_0^*], \tag{6}$$

where the asterisk ("$*$") indicates a complex conjugate. Grosse and Shilov [16,17] have proposed a similar mechanism as the explanation for the cofield electrorotation observed in polystyrene microspheres at low frequencies (below 100 Hz).

Another effect of the CP is the induction of a net electrical charge arising from the concentration gradients [18,19]. In fact, current conservation for a symmetrical electrolyte leads to the following equation for the perturbation of the electrical potential: $\nabla^2 \delta\phi = -\nabla\phi_0 \cdot \nabla\delta c/c_0$ (see Appendix A). Since δc and ϕ_0 are oscillating functions with angular frequency ω, $\delta\phi$ has a nonzero time-averaged component satisfying

$$\nabla^2 \langle \delta\phi \rangle = -(1/2)\mathrm{Re}[\nabla\tilde{\phi}_0 \cdot \nabla\delta\tilde{c}^*/c_0], \tag{7}$$

with normal derivative equal zero at the cylinder surface. Figure 2(c) shows a schematic representation of the induced charges associated with the rectified potential ($\delta\rho = -\varepsilon\nabla^2\langle\delta\phi\rangle$) for a cylinder with negative surface charge. The rectified electric field corresponding to these induced charges acts on the intrinsic charges of the diffuse layer, generating an electro-osmotic slip velocity with a nonzero time average given by

$$\langle \mathbf{u}_{\mathrm{slip}} \rangle_B = (\varepsilon/\eta)\zeta_0 \nabla_s \langle \delta\phi \rangle. \tag{8}$$

The evaluation of Eq. (8) requires a solution for $\langle\delta\phi\rangle$. To this end, we write Eq. (7) as

$$\nabla^2 \langle \delta\phi \rangle / \phi_{\mathrm{ther}} = \mathrm{Du}(E_0 a/\phi_{\mathrm{ther}})^2 \mathrm{Re}[f(r) + g(r)\cos(2\theta)], \tag{9}$$

where

$$f(r) = \frac{1}{2K_1'(ka)} \left[K_0(kr) - \frac{K_2(kr)}{(r/a)^2} \right], \tag{10}$$

$$g(r) = \frac{1}{2K_1'(ka)} \left[K_2(kr) - \frac{K_0(kr)}{(r/a)^2} \right]. \tag{11}$$

From this, the solution is of the form $\langle\delta\phi\rangle/\phi_{\mathrm{ther}} = \mathrm{Du}(E_0 a/\phi_{\mathrm{ther}})^2 \mathrm{Re}[F(r) + G(r)\cos(2\theta)]$. $G(r)$ is the only function that contributes to the slip velocity [the derivation of $G(r)$ is outlined in the appendices]. Thus, the

combination of the contributions given by Eqs. (6) and (8) provides the rectified slip velocity for the cylinder. This is of the form $\langle u_{\rm slip}\rangle = U\sin(2\theta)$, where U is the frequency-dependent maximum slip velocity:

$$\frac{U}{(\varepsilon a E_0^2/2\eta)\mathrm{Du}} = |\zeta_0|f_1 + 2\tanh(|\zeta_0|/2)f_2, \tag{12}$$

where we define the functions f_1 and f_2 as

$$f_1(\omega a^2/D) = 4\mathrm{Re}[G(a)], \tag{13}$$

$$f_2(\omega a^2/D) = -\mathrm{Re}[K_1(ka)/(kaK_1'(ka))]. \tag{14}$$

The functions $f_1(x)$ and $f_2(x)$ are plotted in Fig. 3. For zero frequency ($k = 0$), $f_1 = f_2 = 1$ and

$$\frac{U}{(\varepsilon a E_0^2/2\eta)\mathrm{Du}} = |\zeta_0| + 2\tanh(|\zeta_0|/2), \tag{15}$$

while for high frequencies, $f_1 \ll f_2$ and

$$\frac{U}{(\varepsilon a E_0^2/2\eta)\mathrm{Du}} \sim \frac{2}{\sqrt{2\omega a^2/D}}\tanh(|\zeta_0|/2). \tag{16}$$

The rectified slip velocity gives rise to a quadrupolar flow of the liquid around the cylinder, with a velocity field given by

$$\langle \mathbf{u}\rangle = U\left[\frac{1-r^2}{r^3}\cos(2\theta)\hat{r} + \frac{1}{r^3}\sin(2\theta)\hat{\theta}\right]. \tag{17}$$

This expression gives rise to a velocity amplitude that decays approximately as $\sqrt{D/\omega a^2}$ at frequencies larger than D/a^2. ICEO flows around a cylinder are also quadrupolar [they satisfy Eq. (17)] and scale with E_0^2 [20]. However, assuming that the permittivity of the cylinder is much smaller than that of water (true for all experimental cases), the ICEO theory predicts a velocity with a frequency dependence consisting of a plateau followed by a decay around frequencies of the order of the reciprocal of the charge relaxation time of the electrolyte ($\sigma/(2\pi\varepsilon) \approx 0.3 - 3$ MHz for our experimental conditions; this frequency is several orders of magnitude greater than the typical frequencies for the flows observed in our experiments [9,21]). It is also enlightening to compare the slip velocities predicted by both theories. According to the ICEO theory for dielectric objects [20,22], the maximum induced zeta potential for a dc field with amplitude E_0 is $\delta\zeta_{\rm ICEO} = 2(\varepsilon_d/\varepsilon)E_0\lambda_D$, where ε_d is the permittivity of the dielectric object and λ_D is the thickness of the diffuse layer, i.e., the Debye length. Thus, from Eq. (1), the maximum time-averaged slip velocity for an ac field of amplitude E_0 is $v_{\rm slip}^{\rm ICEO} = (\varepsilon_d/\eta)\lambda_D E_0^2$. On the other hand, the maximum slip velocity for the stationary flows is $v_{\rm slip}^{\rm CPEO} = (\varepsilon a E_0^2/2\eta)\mathrm{Du}[|\zeta_0|/\phi_{\rm ther} + 2\tanh(|\zeta_0|/2\phi_{\rm ther})]$, where we introduce the acronym CPEO for CP electroosmosis. Using values of the parameters obtained from our experiments and typical values for the permittivity of polydimethylsiloxane (PDMS) ($\varepsilon_d = 2.8\varepsilon_0$), $\lambda_D \leq 30$ nm and $\mathrm{Du} \in [0.01, 0.1]$, the ratio between the two slip velocities is $v_{\rm slip}^{\rm ICEO}/v_{\rm slip}^{\rm CPEO} \in [0.004, 0.04]$, which demonstrates that CPEO stationary flows completely dominate over ICEO for charged dielectric obstacles.

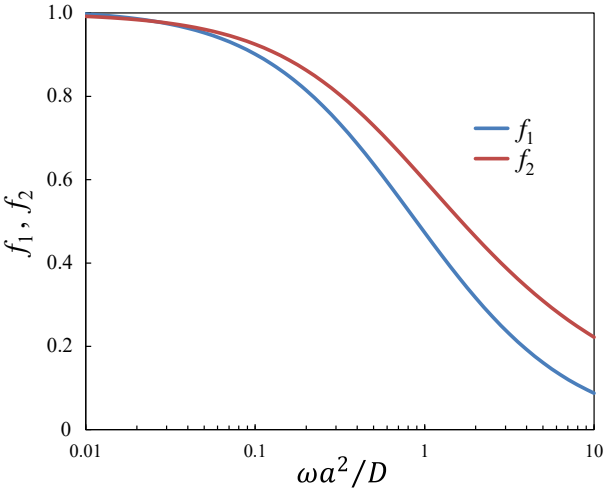

FIG. 3. A plot of the functions f_1 and f_2 versus $\omega a^2/D$. The frequency dependence of the slip velocity is contained within these functions [Eq. (12)].

III. EXPERIMENTAL RESULTS AND COMPARISON WITH THEORY

The CPEO flows were experimentally validated using simple microfluidic devices made using standard soft lithography. Channels (1 cm long, 50 μm tall, and 200 μm wide) containing a periodic square array of cylindrical micropillars (20 μm diameter) are made from PDMS. The separation between the centers of neighboring pillars is 40 μm. The channel is filled with KCl electrolyte with conductivities $\sigma = \{1.75, 5.01, 11.23\}$ mS/m. For flow visualization, fluorescent nanoparticles (500 nm diameter) are dispersed in the electrolyte and imaged with a fluorescence microscope. Before the experiments, the PDMS channels are primed for at least 30 min with a solution of 0.1% Pluronic F-127; a nonionic surfactant that adsorbs onto the PDMS walls to minimize sticking of the tracer particles. Metal needles are inserted at the inlet and outlet of the channel and ac voltages applied, with an amplitude up to 2000 $V_{\rm p.p.}$ and frequencies up to 1 kHz. Videos of the fluorescent particles are analyzed using particle image velocimetry (PIV) [23,24] (described in Sec. S3 of the Supplemental Material [25]).

Figure 4(a) presents the results of the superposition of experimental images, showing the trajectories of the fluorescent particles in an electrolyte. Four symmetrical flow rolls are seen, as predicted from the theory for the rectified electro-osmotic flow field around a cylinder. Figure 4(c) shows the mean value of the velocity magnitude as a function of the applied ac frequency for three electrolyte conductivities. Following convention, the experimental frequency in experiments f is related to the angular frequency by $\omega = 2\pi f$. The data are obtained by averaging the fluid-velocity magnitude within a unit cell of the periodic array of cylinders. The error bars correspond to the dispersion in the measurements within six different unit cells. Importantly, a strong decrease of the stationary velocity is observed for frequencies around and above tens of Hertz, in accordance with $a^2/D \approx 0.1$ s, i.e., the time scale introduced by the diffusion equation, Eq. (3). Additionally, the velocity for a given conductivity approximately decays as $1/\sqrt{f}$, also in agreement with the theoretical predictions. We also performed experiments using a single post (rather than an array). The observed flow is completely analogous to the flow observed with the array of posts. An example of streamlines is shown in Sec. S1 of the Supplemental Material [25].

The stationary electro-osmotic velocity for a periodic array of dielectric cylinders as used experimentally is calculated using the commercial finite-element solver COMSOL Multiphysics. The governing equations for ϕ_0 (the Laplace equation), δc [Eq. (3)] and $\langle \delta\phi \rangle$ [Eq. (7)] are solved in a two-dimensional domain corresponding to a unit cell centered on a cylinder [see Fig. 4(b)]. The boundary conditions on the cylinder surface are $\mathbf{n}\cdot\nabla\phi_0 = 0$, Eq. (4) and $\mathbf{n}\cdot\nabla\langle\delta\phi_0\rangle = 0$. Periodicity is imposed on the boundaries of the unit cell. The velocity field within the unit cell satisfies the Stokes equations, with the slip velocity on the cylinder wall given by the sum of Eqs. (6) and (8). We also impose periodicity for the velocity and pressure fields on the boundaries of the unit cell.

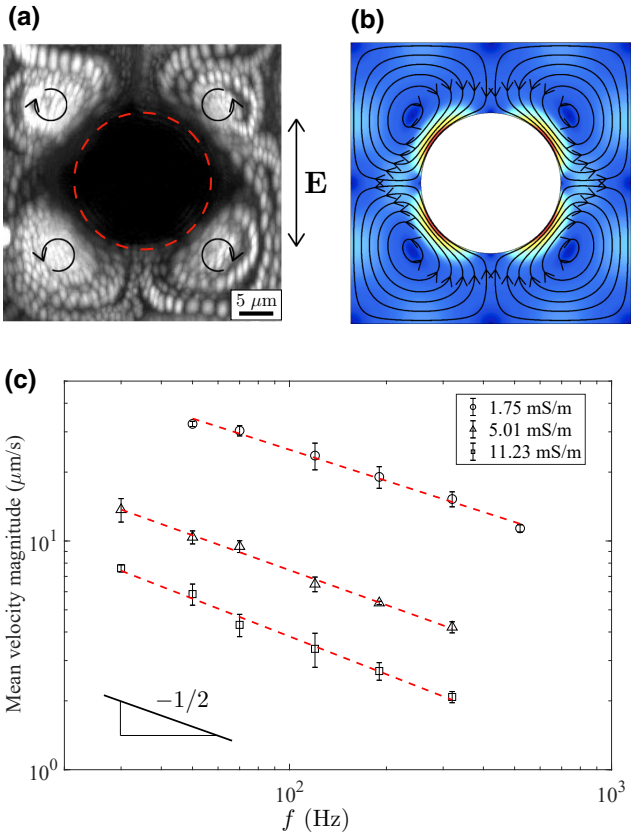

FIG. 4. (a) Experimental streamlines around an insulating pillar of 20 μm diameter. The electrolyte conductivity is 1.75 mS/m and the voltage amplitude and frequency are 1600 $V_{p.p.}$ and 190 Hz, respectively (see the video in the Supplemental Material [25]). (b) Numerically calculated streamlines for the rectified electro-osmotic flow around a dielectric cylinder. The color map represents the magnitude of the fluid-velocity field. (c) Experimental data for the average fluid-velocity magnitude as a function of the signal frequency for three electrolyte conductivities (KCl in water). The amplitude of the applied voltage is 1600 $V_{p.p.}$. The velocity decays approximately as $1/\sqrt{f}$.

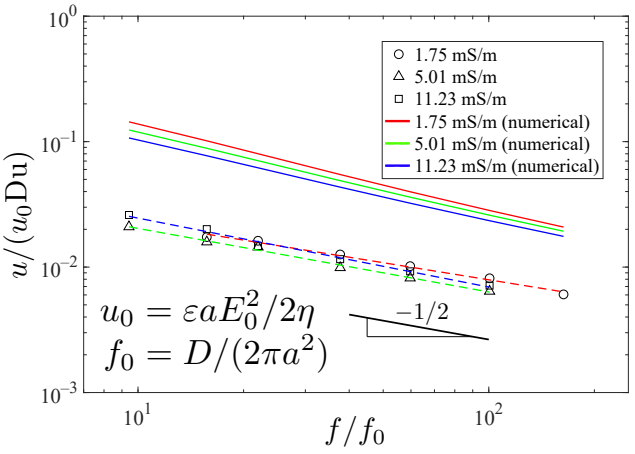

FIG. 5. A comparison between the experimental data in Fig. 4(c) and the numerical calculations for a periodic array of dielectric cylinders. The solid lines correspond to the average velocity magnitude determined from simulations with $E_0 = 96.25$ kV/m and $\zeta_0 = -110$ mV for the lowest conductivities. For the other conductivities, ζ_0 is calculated from the Gouy-Chapman relation for fixed surface charge. The frequencies are nondimensionalized with $f_0 = D/(2\pi a^2)$. The velocities are scaled with the product of a typical velocity ($u_0 = \varepsilon a E_0^2/2\eta$) and the Dukhin number. Note that the numerical curves do not have exactly the same frequency dependence and, therefore, they do not collapse onto a master curve. The reason is that the relative contribution of the two mechanisms to rectified electro-osmosis varies with ζ_0, which in turn decreases with the electrolyte conductivity.

Figure 4(b) shows the streamlines obtained for the rectified electro-osmotic flow around a post in the periodic array. As expected, the time-averaged flow pattern shows four recirculating vortices, as found experimentally. Figure 5 shows a comparison between the experimental data from Fig. 4(c) and the numerical results with the following parameters: $\zeta_0 = -110$ mV (for the lowest conductivity) [26] and $E_0 = 96.25$ kV/m. For the other conductivities, ζ_0 is calculated from the Gouy-Chapman relation for fixed surface charge; these values are in agreement with the measurements in Ref. [27]. The experimental data in Fig. 5 are scaled with u_0Du, where $u_0 = \varepsilon a E_0^2/2\eta$ and Du is calculated by assuming a fixed surface conductance of 1 nS—independent of the electrolyte conductivity. This is a typical value obtained from experimental data for the electrokinetic properties of submicrometer latex particles [28] and it is larger than the estimation obtained for K_s when using the theory of the diffuse layer. The difference is attributed to the contribution to surface conductance arising from a layer of mobile ions adsorbed on the wall [12]—the so-called Stern layer. The experimental trends are correctly described by the theoretical model: the rectified fluid velocity decreases with the electrolyte conductivity and, significantly, its frequency dependence is close to $1/\sqrt{f}$. The magnitude of the velocity is clearly overestimated by the numerical simulations by a factor of around 4.5. It is important to note that the channels are primed with the surfactant Pluronic, which is known to significantly reduce electro-osmotic velocities [29], before each experiment.

IV. CONCLUSIONS

We present a mathematical model that predicts the stationary fluid flow of electrolytes induced by ac electric fields around charged dielectric objects. We show experimental data for the electrolyte flow around micropillars in a microfluidic channel and demonstrate that the experimental trends are in agreement with the numerical calculations for typical values of the surface conductance and the ζ potential for PDMS.

The magnitude of the fluid velocity is overestimated by the numerical calculations, which can be attributed to the fact that adsorption of Pluronic to PDMS significantly reduces electro-osmosis. The theoretical model correctly describes the amplitude and frequency dependence of the rectified flow, in contrast with previous work that attributes the flow around dielectric structures to classical ICEO in an ac field [9,30]. Beyond the fundamental interest in these stationary flows, we anticipate that this model will expand the understanding of the behavior of systems that employ ac electric fields for micro- and nanoparticle manipulation [31,32] and will lead to ways of locally controlling fluid flow using dielectric structures.

ACKNOWLEDGMENTS

P.G.S. and A.R. acknowledge financial support by the European Regional Development Fund (ERDF) and the Spanish Research Agency MCI under Contract No. PGC2018-099217-B-I00.

V. Calero and R. Fernández-Mateo contributed equally to this work.

APPENDIX A: THEORY FOR SURFACE CONDUCTANCE AND ELECTRO-OSMOSIS

We consider a negatively charged dielectric object immersed in a binary electrolyte subjected to an ac electric field and follow the theory developed by Schnitzer and Yariv [14] but extend it to the ac case. This theory is a thin-double-layer analysis of the electrokinetic equations for charged dielectric solids that considers surface-conduction effects. We assume that the frequency ω of the applied electric field is low enough to consider that the electrical double layer (EDL) is in quasiequilibrium ($\omega\varepsilon/\sigma \ll 1$, in which ε and σ are the liquid permittivity and conductivity, respectively). In the following, we use a dimensionless formulation [14]: the length is nondimensionalized with a typical distance a (the radius of the pillar in our experiments), potential with the thermal voltage $\phi_{\text{ther}} = k_B T/e$ (k_B is Boltzmann's constant, T is the absolute temperature, and e is the elementary charge), time with $\eta/\varepsilon E_{\text{ther}}^2$, where $E_{\text{ther}} = \phi_{\text{ther}}/a$, pressure with $\varepsilon E_{\text{ther}}^2$, and concentrations with the typical salt concentration c_0. Thus, the diffusion constants are nondimensionalized with $\varepsilon a^2 E_{\text{ther}}^2/\eta$ and the velocities with $\varepsilon E_{\text{ther}}^2 a/\eta$ and the typical Reynolds number is $\text{Re} = \rho_m \varepsilon E_{\text{ther}}^2 a^2/\eta^2$, in which ρ_m is the liquid mass density. The surface charge on the dielectric is nondimensionalized with $\varepsilon\phi_{\text{ther}}/\lambda_D$, where λ_D is the Debye length.

The nondimensional equations for the conservation of positive and negative ions in the bulk electrolyte (outside the EDL) are, respectively,

$$\nabla \cdot (-c\nabla\phi - \nabla c) + \alpha_+ \mathbf{u} \cdot \nabla c + \alpha_+ \frac{\partial c}{\partial t} = 0, \tag{A1}$$

$$\nabla \cdot (c\nabla\phi - \nabla c) + \alpha_- \mathbf{u} \cdot \nabla c + \alpha_- \frac{\partial c}{\partial t} = 0, \tag{A2}$$

where electroneutrality has been taken into account so that the concentrations of positive and negative ions are equal $c_+ = c_- = c$. The nondimensional parameters α_+ and α_- are the reciprocals of the nondimensional diffusion constants D_+ and D_- of the positive and negative ions, respectively. Adding and subtracting Eqs. (A1) and (A2), we obtain

$$D\nabla^2 c = \mathbf{u} \cdot \nabla c + \frac{\partial c}{\partial t}, \tag{A3}$$

$$\nabla \cdot (c\nabla\phi) = \gamma\left(\frac{\partial c}{\partial t} + \mathbf{u}\cdot\nabla c\right), \tag{A4}$$

where $D = 2/(\alpha_+ + \alpha_-)$ and $\gamma = (\alpha_+ - \alpha_-)/2$. Equation (A3) is the diffusion equation for the salt concentration, in which D is a nondimensional ambipolar diffusion constant. Equation (A4) can be read as the equation for the electrical potential, where γ is a parameter that controls the ion-mobility asymmetry.

The boundary conditions on the surface of the charged dielectric object are as follows [14]. The zero normal flux of co-ions (anions in our case) is given by

$$c\frac{\partial\phi}{\partial n} - \frac{\partial c}{\partial n} = 0. \tag{A5}$$

The normal flux of counter-ions (cations in our case) equates to the surface divergence of the EDL cation fluxes:

$$-c\frac{\partial\phi}{\partial n} - \frac{\partial c}{\partial n} = 2\mathrm{Du}\nabla_s^2(\phi + \ln c), \tag{A6}$$

where Du is the Dukhin number, defined as $\mathrm{Du} = (1 + 2\alpha_+)|q_s|\lambda_D$, in which q_s and λ_D are the nondimensional intrinsic surface charge and the Debye length, respectively. Here, the normal derivative is from the dielectric to the electrolyte. The Dukhin number is defined in the literature [4] as $\mathrm{Du} = K_s/(\sigma a)$, where K_s is the surface conductance. This expression is fully equivalent to the definition $\mathrm{Du} = (1 + 2\alpha_+)|q_s|\lambda_D$ for a symmetrical electrolyte with equal diffusivities and a large zeta potential (the case we deal with in this work). The Supplemental Material contains a detailed derivation of the equivalence of the two definitions [25]. In previous equations, we assume that the particle is nonpolarizable, i.e., the charge induced in the EDL by the external electric field is negligible. This condition will be examined later.

The liquid velocity and pressure satisfy the Navier-Stokes equation for a negligible Reynolds number:

$$\mathrm{Re}\frac{\partial\mathbf{u}}{\partial t} = -\nabla p + \nabla^2\mathbf{u} + \nabla^2\phi\nabla\phi, \quad \nabla\cdot\mathbf{u} = 0, \tag{A7}$$

where the Coulomb term is present because gradients of concentration can lead to induced charge in the bulk, through Eq. (A4), and the time derivative of velocity is present because it may not be negligible for high frequency.

The boundary conditions on the charged dielectric surface are (i) the wall is impermeable, $\mathbf{u}\cdot\mathbf{n} = 0$, and (ii) there is a slip velocity generated at the EDL [33]:

$$\mathbf{u}_s = \zeta\nabla_s\phi - 4\ln[\cosh(\zeta/4)]\nabla_s c, \tag{A8}$$

where the zeta potential ζ is related to the intrinsic charge by [1]

$$q_s = 2\sqrt{c}\sinh(\zeta/2). \tag{A9}$$

Here, we see that perturbations of the salt concentration lead to perturbations of the zeta potential, i.e., $\delta\zeta = -\delta c\tanh(\zeta_0/2)/c_0$.

Following Schnitzer and Yariv [15], we now perform a linear expansion in the parameter Du (which is small in our case): $\phi = \phi_0 + \delta\phi$, $c = c_0 + \delta c$, $\zeta = \zeta_0 + \delta\zeta$, $\mathbf{u} = \mathbf{u}_0 + \delta\mathbf{u}$, in which $\delta\phi$, δc, $\delta\zeta$, and $\delta\mathbf{u}$ are of the order of Du. In addition, the equations will be simplified in order to obtain an analytical solution.

Consider an applied ac electric field of nondimensional angular frequency ω. The solution at order zero ($\mathrm{Du} = 0$) is as follows: (a) the salt concentration is unperturbed, $c_0 = 1$; (b) the zeta potential in the absence of CP is uniform and is given by the relation $q_s = 2\sinh(\zeta_0/2)$; (c) the potential in the liquid bulk is $\phi_0(t) = \mathrm{Re}[\tilde{\phi}_0 e^{i\omega t}]$, where $\tilde{\phi}_0$ is the potential phasor that satisfies Laplace's equation with the boundary condition $\partial\tilde{\phi}_0/\partial n = 0$ at the dielectric surface (the solution for a cylinder is given in Eq. (2)); and (d) the velocity field and pressure are, respectively, $\mathbf{u}_0(t) = \mathrm{Re}[\tilde{\mathbf{u}}_0 e^{i\omega t}]$ and $p_0(t) = \mathrm{Re}[\tilde{p}_0 e^{i\omega t}]$, where $\tilde{\mathbf{u}}_0$ and $\tilde{p}_0$ satisfy

$$i\omega\mathrm{Re}\tilde{\mathbf{u}}_0 = -\nabla\tilde{p}_0 + \nabla^2\tilde{\mathbf{u}}_0, \quad \nabla\cdot\tilde{\mathbf{u}}_0 = 0, \tag{A10}$$

with the boundary condition $\tilde{\mathbf{u}}_0 = \zeta_0\nabla\tilde{\phi}_0$ at the dielectric surface. The analytical solution for the velocity and pressure generated around a cylinder is shown below (Appendix D).

The concentration δc satisfies

$$D\nabla^2\delta c = \mathbf{u}_0\cdot\nabla\delta c + \frac{\partial\delta c}{\partial t}. \tag{A11}$$

Here, we neglect the advection term in order to obtain an analytical solution. For this to be valid, the Péclet number (Pe) must be negligibly small ($\mathrm{Pe} = U_0 L/\bar{D}$, where U_0 is a typical velocity, L is the characteristic length for the concentration gradients, and $\bar{D}$ is the dimensional diffusivity of the ions). For dc, the characteristic length is a, the pillar radius. For ac fields, the characteristic length is the smaller of a or the diffusion penetration depth (the penetration depth is $\sqrt{\bar{D}/\bar{\omega}}$, in which $\bar{D}$ and $\bar{\omega}$ are dimensional quantities). Pe is negligible when either U_0 or L is very small. In our experimental system, this implies that either U_0 is much smaller than 200 $\mu m/s$ or $\omega \gg 2\pi 10$ rad/s. The boundary condition for Eq. (A11) at the dielectric surface is

$$-\frac{\partial\delta c}{\partial n} = \mathrm{Du}\nabla_s^2(\phi_0). \tag{A12}$$

Since ϕ_0 is an oscillating function in time with angular frequency ω and we neglect the advection term, we

find a solution of δc that is of the form $\delta c = \mathrm{Re}[\delta\tilde{c}e^{i\omega t}]$. The complex function $\delta\tilde{c}$ satisfies

$$D\nabla^2\delta\tilde{c} = i\omega\delta\tilde{c}. \tag{A13}$$

with the boundary condition

$$\frac{\partial\delta\tilde{c}}{\partial n} = -\mathrm{Du}\nabla_s^2(\tilde{\phi}_0). \tag{A14}$$

We further assume that positive and negative ions have the same mobility, so that $\gamma = 0$ in Eq. (A4). The potential $\delta\phi$ then satisfies

$$\nabla^2\delta\phi + \nabla\phi_0\cdot\nabla\delta c = 0, \tag{A15}$$

with the following boundary condition on the dielectric surface:

$$\frac{\partial\delta\phi}{\partial n} = \frac{\partial\delta c}{\partial n}. \tag{A16}$$

Equation (A15) and the boundary condition given in Eq. (A16) imply that the general solution for $\delta\phi$ has three Fourier independent frequency components: $\{1, e^{i\omega t}, e^{2i\omega t}\}$. We are interested in the time-independent component, because this contributes to the rectified velocity, as shown below. Thus we solve $\nabla^2\langle\delta\phi\rangle + \langle\nabla\phi_0\cdot\nabla\delta c\rangle = 0$.

The time-averaged velocity and pressure at the first order satisfy

$$\nabla^2\delta\mathbf{u} + \langle\nabla^2\delta\phi\nabla\phi_0\rangle = \nabla\delta p, \quad \nabla\cdot\delta\mathbf{u} = 0. \tag{A17}$$

The Coulomb term has a zero time average, $\langle\nabla^2\delta\phi\nabla\phi_0\rangle = 0$. Effectively, the Laplacian of $\delta\phi$ is equal to $-\nabla\phi_0\cdot\nabla\delta c$ because of Eq. (A15). It has Fourier components $\{1, e^{2i\omega t}\}$ and when multiplied by $\nabla\phi_0$ the Coulomb term has Fourier components $\{e^{i\omega t}, e^{3i\omega t}\}$.

The boundary conditions for the time-averaged velocity on the dielectric surface at the first order are $\delta\mathbf{u}\cdot\mathbf{n} = 0$ and the time-averaged slip velocity is as follows:

$$\delta\mathbf{u}_s = \zeta_0\nabla_s\langle\delta\phi\rangle + \langle\delta\zeta\nabla_s\phi_0\rangle - 4\ln(\cosh(\zeta_0/4))\nabla_s\langle\delta c\rangle = \cdots = \zeta_0\nabla_s\langle\delta\phi\rangle + \langle\delta\zeta\nabla_s\phi_0\rangle, \tag{A18}$$

where the last equality comes from $\langle\delta c\rangle = 0$. Here, $\delta\zeta = -\delta c\tanh(\zeta_0/2)$.

Summary of approximations in the model:

1. Thin EDL and highly charged surface, as required for the Schnitzer-Yariv model.
2. Frequencies much smaller than the electrolyte charge relaxation frequency, ensuring that the EDL is in quasiequilibrium.
3. High frequencies or weak electric fields, so that advection of ions can be neglected.
4. A small Du, to justify the use of a linear expansion.
5. Equal ion diffusivities, so that the charge induced in the bulk due to different diffusivities can be neglected.
6. A negligible induced charge in the EDL (valid for common dielectrics).

APPENDIX B: NEGLIGIBLE INDUCED CHARGE

At this point, we examine the charge induced by the applied field on a dielectric cylinder. First, we compare the maximum induced zeta potential from the induced charge on a dielectric and also from the change in concentration due to surface conduction. Both induced zeta potentials are maximum at zero frequency. According to Ref. [20], the maximum induced zeta potential on a dielectric cylinder due to induced charge is

$$\zeta_{\mathrm{IC}} = 2\frac{\varepsilon_d}{\varepsilon_w}E_0\lambda_D, \tag{B1}$$

where ε_d and ε_w are the dielectric constants of the solid and water, respectively. From $\delta\zeta = -\delta c\tanh(\zeta_0/2)$ with δc given by Eq. (5) in nondimensional form and evaluated on the cylinder surface, the maximum induced zeta potential due to the concentration perturbation is

$$\zeta_{\mathrm{CP}} = 2\mathrm{Du}E_0\tanh(|\zeta_0|/2). \tag{B2}$$

We see that for a thin EDL ($\lambda_D \ll 1$) and a non-negligible Dukhin number (i.e., $\mathrm{Du} > \lambda_D$), $\zeta_{\mathrm{IC}}/\zeta_{\mathrm{CP}} \sim (\varepsilon_d/\varepsilon_w)(\lambda_D/\mathrm{Du}) \ll 1$ for common dielectrics. Thus, it is justifiable to neglect ζ_{IC} compared with ζ_{CP}.

APPENDIX C: FUNCTIONS FOR ANALYTICAL SOLUTION

The functions $F(r)$ and $G(r)$ are obtained from the equations

$$\frac{1}{r}\frac{\partial}{\partial r}\left(r\frac{\partial F}{\partial r}\right) = f, \tag{C1}$$

$$\frac{1}{r}\frac{\partial}{\partial r}\left(r\frac{\partial G}{\partial r}\right) - \frac{4G}{r^2} = g, \tag{C2}$$

with boundary conditions of $\partial F/\partial r = \partial G/\partial r = 0$, both for $r = 1$ and $r \to \infty$. Only the function $G(r)$ contributes to the rectified slip velocity [Eq. (12)]. We solve for G using Green's function, which satisfies Eq. (C2), but with a source equal to the Dirac delta function $\delta(r - r')$ and with boundary conditions of zero radial derivatives at $r = 1$ and

$r \to \infty$. The solution for G is then

$$G(r) = -r^{-2}\int_1^r \frac{g(r')(r'^4+1)}{4r'}dr' - (r^2+r^{-2})\int_r^\infty \frac{g(r')}{4r'}dr'. \quad \text{(C3)}$$

According to Eq. (12), we require the value of G evaluated on the cylinder surface $G(1)$:

$$G(1) = -\int_1^\infty \frac{g(r')}{2r'}dr' = \frac{1}{4K_1'(k)}\int_1^\infty \left(\frac{K_0(kr')}{r'^3} - \frac{K_2(kr')}{r'}\right)dr'. \quad \text{(C4)}$$

The integral shown in Eq. (C4) is evaluated using MATHEMATICA.

APPENDIX D: OSCILLATING VELOCITY AND PRESSURE AROUND A CYLINDER

This appendix derives the oscillating velocity at zero order. This does not affect the stationary electro-osmotic velocity, since we neglect the advection term in Eq. (5). The solution to Eq. (A10) for the case of a cylinder can be found by writing [34]

$$\tilde{\mathbf{u}}_0 = -\frac{\nabla\tilde{p}_0}{i\omega\mathrm{Re}} + \nabla\times(\psi\hat{z}), \quad \text{(D1)}$$

with equations for $\tilde{p}_0$ and ψ given by, respectively,

$$\nabla^2\tilde{p}_0 = 0, \quad \nabla^2\psi = i\omega\mathrm{Re}\psi. \quad \text{(D2)}$$

The imposition of boundary conditions of zero velocity at infinity and a slip velocity on the cylinder surface $\tilde{\mathbf{u}}_0 = 2\zeta E_0 \sin\theta\hat{\theta}$ leads to

$$\tilde{p}_0 = i\omega\mathrm{Re}2\zeta E_0 \frac{K_1(\alpha)}{K_1(\alpha)+\alpha K_1'(\alpha)}\frac{\cos\theta}{r}, \quad \text{(D3)}$$

$$\psi = -2\zeta E_0 \frac{K_1(\alpha r)}{K_1(\alpha)+\alpha K_1'(\alpha)}\sin\theta, \quad \text{(D4)}$$

where $\alpha = \sqrt{i\omega\mathrm{Re}}$.

[1] R. J. Hunter, *Introduction to Modern Colloid Science* (Oxford University Press, New York, 1993).

[2] J. Lyklema, *Fundamentals of Interface and Colloid Science* (Academic Press Limited, London, 1995).

[3] H. A. Stone, A. D. Stroock, and A. Ajdari, Engineering flows in small devices: Microfluidics toward a lab-on-a-chip, Annu. Rev. Fluid Mech. **36**, 381411 (2004).

[4] A. V. Delgado, F. Gonzalez-Caballero, R. J. Hunter, L. K. Koopal, and J. Lyklema, Measurement and interpretation of electrokinetic phenomena (IUPAC technical report), Pure Appl. Chem. **77**, 1753 (2005).

[5] V. Calero, P. Garcia-Sanchez, A. Ramos, and H. Morgan, Electrokinetic biased deterministic lateral displacement: Scaling analysis and simulations, J. Chromatogr. A **1623**, 461151 (2020).

[6] Y. Eckstein, G. Yossifon, A. Seifert, and T. Miloh, Nonlinear electrokinetic phenomena around nearly insulated sharp tips in microflows, J. Colloid Interface Sci. **338**, 243 (2009).

[7] S. K. Thamida and H.-C. Chang, Nonlinear electrokinetic ejection and entrainment due to polarization at nearly insulated wedges, Phys. Fluids **14**, 4315 (2002).

[8] P. Takhistov, K. Duginova, and H.-C. Chang, Electrokinetic mixing vortices due to electrolyte depletion at microchannel junctions, J. Colloid Interface Sci. **263**, 133 (2003).

[9] M. Zehavi, A. Boymelgreen, and G. Yossifon, Competition between Induced-Charge Electro-osmosis and Electrothermal Effects at Low Frequencies around a Weakly Polarizable Microchannel Corner, Phys. Rev. Appl. **5**, 044013 (2016).

[10] M. Z. Bazant and T. M. Squires, Induced-Charge Electrokinetic Phenomena: Theory and Microfluidic Applications, Phys. Rev. Lett. **92**, 066101 (2004).

[11] S. S Dukhin and V. N. Shilov, *Dielectric Phenomena and the Double Layer in Disperse Systems and Polyelectrolytes* (Wiley, New York, 1974).

[12] V. N. Shilov, A. V. Delgado, F. Gonzalez-Caballero, and C. Grosse, Thin double layer theory of the wide-frequency range dielectric dispersion of suspensions of non-conducting spherical particles including surface conductivity of the stagnant layer, Colloids Surf. A: Physicochem. Eng. Aspects **192**, 253 (2001).

[13] N. A. Mishchuk, Concentration polarization of interface and non-linear electrokinetic phenomena, Adv. Colloid Interface Sci. **160**, 16 (2010).

[14] O. Schnitzer and E. Yariv, Macroscale description of electrokinetic flows at large zeta potentials: Nonlinear surface conduction, Phys. Rev. E **86**, 021503 (2012).

[15] O. Schnitzer and E. Yariv, Nonlinear electrophoresis at arbitrary field strengths: Small-Dukhin-number analysis, Phys. Fluids **26**, 122002 (2014).

[16] C. Grosse and V. N. Shilov, Theory of the low-frequency electrorotation of polystyrene particles in electrolyte solution, J. Phys. Chem. **100**, 1771 (1996).

[17] C. Grosse and V. N. Shilov, Theory of the low frequency electrorotation of disperse particles in electrolyte solution, Colloids Surfaces A: Physicochem. Eng. Aspects **140**, 199 (1998).

[18] V. G. Levich, *Physicochemical Hydrodynamics* (Prentice-Hall, Englewood Cliffs, N. J., 1962).

[19] J. S. Newman and K. E. Thomas-Alyea, *Electrochemical Systems* (Wiley-IEEE, Hoboken, N.J., 2004).

[20] T. M. Squires and M. Z. Bazant, Induced-charge electro-osmosis, J. Fluid Mech. **509**, 217 (2004).

[21] G. Yossifon, I. Frankel, and T. Miloh, Macro-scale description of transient electro-kinetic phenomena over polarizable dielectric solids, J. Fluid Mech. **620**, 241 (2009).

[22] C. Zhao and C. Yang, Analysis of induced-charge electroosmotic flow in a microchannel embedded with polarizable dielectric blocks, Phys. Rev. E **80**, 046312 (2009).

[23] W. Thielicke and E. J. Stamhuis, PIVlab towards user-friendly, affordable and accurate digital particle image velocimetry in MATLAB, J. Open Res. Soft. **2**, p.e30 (2014).

[24] C. D. Meinhart, S. T. Wereley, and J. G. Santiago, A PIV algorithm for estimating time-averaged velocity fields, J. Fluids Eng. **122**, 285 (2000).

[25] See the Supplemental Material at http://link.aps.org/supplemental/10.1103/PhysRevApplied.15.014047. Supplementary Material contains a video of the rectified flows around the cylinder array, an image of the streamlines around a single post, a description of the PIV measurements and a derivation of the equivalence between the two definitions of the Dukhin number.

[26] A. Sze, D. Erickson, L. Ren, and D. Li, Zeta-potential measurement using the Smoluchowski equation and the slope of the current-time relationship in electroosmotic flow, J. Colloid Interface Sci. **261**, 402 (2003).

[27] M. A. Saucedo-Espinosa and B. H. Lapizco-Encinas, Refinement of current monitoring methodology for electroosmotic flow assessment under low ionic strength conditions, Biomicrofluidics **10**, 033104 (2016).

[28] I. Ermolina and H. Morgan, The electrokinetic properties of latex particles: Comparison of electrophoresis and dielectrophoresis, J. Colloid Interface Sci. **285**, 419 (2005).

[29] M. Viefhues, S. Manchanda, T.-C. Chao, D. Anselmetti, J. Regtmeier, and A. Ros, Physisorbed surface coatings for poly (dimethylsiloxane) and quartz microfluidic devices, Anal. Bioanal. Chem. **401**, 2113 (2011).

[30] Q. Wang, N. N. Dingari, and C. R. Buie, Nonlinear electrokinetic effects in insulator-based dielectrophoretic systems, Electrophoresis **38**, 2576 (2017).

[31] B. H. Lapizco-Encinas, B. A. Simmons, E. B. Cummings, and Y. Fintschenko, Insulator-based dielectrophoresis for the selective concentration and separation of live bacteria in water, Electrophoresis **25**, 1695 (2004).

[32] V. Calero, P. Garcia-Sanchez, C. Honrado, A. Ramos, and H. Morgan, AC electrokinetic biased deterministic lateral displacement for tunable particle separation, Lab. Chip **19**, 1386 (2019).

[33] D. C. Prieve, J. L. Anderson, J. P. Ebel, and M. E. Lowell, Motion of a particle generated by chemical gradients. Part 2. Electrolytes, J. Fluid Mech. **148**, 247 (1984).

[34] J. M. Andres and U. Ingard, Acoustic streaming at low Reynolds numbers, J. Acoust. Soc. Am. **25**, 932 (1953).

Paper D

Stationary electro-osmotic flow driven by AC fields around charged dielectric spheres

Summary of Results

The theory of CPEO was translated from the geometry of a pillar within a microfluidic channel to a free sphere immersed in an electrolyte. Given the differences in size, the CPEO theory was generalised for arbitrary Dukhin numbers. The model was experimentally validated by measuring the flow of small (500 nm) tracer particles around individual particles with significant slip velocity (3 $\mu\mathrm{m}$).

Contribution Statement

I suggested and proved the idea of using two populations of particles with different sizes to trace the fluid around the bigger particles; and Morgan, Ramos and Garcia-Sanchez saw the necessity of generalizing the CPEO theory for larger values of the Dukhin number. In this work, I did all the experimental work and the data analysis, Ramos and I elaborated the theory. Garcia-Sanchez, Ramos and I wrote the first version of the manuscript. Morgan, Ramos, Garcia-Sanchez and Calero provided supervisory support. All authors contributed to the final version of the manuscript.

J. Fluid Mech. (2021), *vol*. 924, R2, doi:10.1017/jfm.2021.650

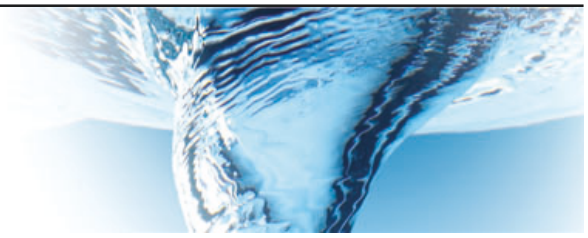

Stationary electro-osmotic flow driven by AC fields around charged dielectric spheres

Raúl Fernández-Mateo[1], Pablo García-Sánchez[2], Víctor Calero[2], Hywel Morgan[1] and Antonio Ramos[2],†

[1]School of Electronics and Computer Science, University of Southampton, Southampton SO17 1BJ, UK

[2]Depto. Electrónica y Electromagnetismo, Facultad de Física, Universidad de Sevilla, Avda. Reina Mercedes s/n, 41012 Sevilla, Spain

(Received 27 May 2021; revised 13 July 2021; accepted 14 July 2021)

We experimentally demonstrate quadrupolar electro-osmotic flows around charged dielectric microspheres immersed in an electrolyte when subjected to an alternating current electric field. We present an electrokinetic model that predicts the flow characteristics based on the phenomena of surface conductance and polarization of the electrolyte concentration around the particles. We refer to these flows as concentration polarization electro-osmosis. We anticipate that these flows may play a major role in the electric-field-induced assembly of colloids and on the electrokinetic manipulation of dielectric micro- and nanoparticles.

Key words: colloids, electrokinetic flows

1. Introduction

Solid particles immersed in aqueous electrolytes usually carry a net surface charge which is screened by a diffuse ionic layer on the electrolyte side of the interface. Relative motion between the solid and liquid can occur when an external electric field acts on these charges, giving rise to particle motion known as electrophoresis (Hunter 1993). For diffuse layers much thinner than the particle size, the electrophoretic velocity is given by the Helmholtz–Smoluchowski formula (Hunter 1993) as $\boldsymbol{U} = (\varepsilon\zeta/\eta)\boldsymbol{E}$, where ε is the medium permittivity and η its viscosity, $\boldsymbol{E}$ the applied electric field and ζ the zeta potential (the electrical potential at the slip plane; Delgado *et al.* 2005). In the presence of an alternating current (AC) field with amplitude $\boldsymbol{E}_0$, electrophoresis manifests

† Email address for correspondence: ramos@us.es

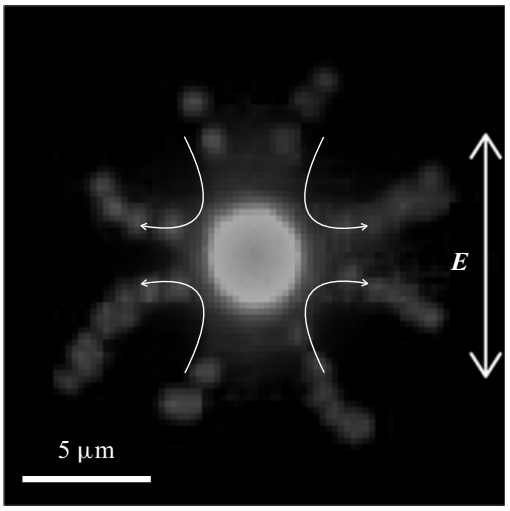

Figure 1. Experimental paths of 500 nm particles around a fluorescent latex sphere of 3 μm diameter along with streamlines predicted by (2.32). The applied field magnitude and frequency are 80 kV m^{-1} and 292 Hz.

itself as an oscillatory motion of the particle at the same frequency as the field, with a displacement amplitude given by $(\varepsilon\zeta/\eta)\boldsymbol{E}_0/\omega$, where ω is the angular frequency of the electric field. Observations of the fluid flow around micron-scale solid dielectric particles in an AC field has revealed a previously unobserved fluid flow pattern. Here we report fluid patterns around 3 μm spheres exposed to low-frequency AC field imaged using fluorescent tracer particles (500 nm diameter). Figure 1 shows an example of these flow patterns. Significantly, the observed quadrupolar flow is not oscillatory. This paper presents a theoretical model that describes these observations by considering the effect of perturbations in the electrolyte concentration on the electro-osmotic flow around the particles. The gradients in electrolyte concentration occur due to particle surface conduction. The model for these phenomena predicts the previously reported stationary flows observed around dielectric micropillars (20 μm diameter) subjected to AC fields (Calero *et al.* 2021). The surface conduction of these micropillars is relatively small, and the model was based on the approximation for small Dukhin number (the ratio of surface to bulk conductance; Delgado *et al.* 2005). However, this is not small for particles with a typical size around 1 μm or smaller. As a first attempt to model stationary flows for arbitrary values of the Dukhin number, we develop a theoretical scheme for weak electric fields. Gamayunov, Murtsovkin & Dukhin (1986) argued that stationary quadrupolar flows may appear around charged dielectric spheres as a consequence of concentration polarization and/or induced charge within the electrical double layer (EDL). The flow pattern due to EDL polarization in a DC field was analysed in detail by Dukhin & Murtsovkin (1986). Here we extend the analysis of Schnitzer & Yariv (2012) to the case of AC electric fields and describe the stationary flow around a charged colloidal sphere as a function of frequency, albeit with the restriction of a binary electrolyte with equal ionic diffusivities. The latter assumption is valid for our experiments with KCl aqueous solutions and greatly simplifies the theoretical treatment of the problem. In this work we focus on the simplest system, in which stationary flows for AC fields arise due to surface conduction, where there is already an asymmetry between counter-ions and co-ions. Experimental data on the stationary electro-osmotic flow around microparticles are in agreement with the predictions of the model. These flows could be important in controlling the interaction between microscopic particles subjected to low-frequency AC electric fields (around 1 kHz or less) and in general for any technique relying on AC fields for electrical manipulation of dielectric particles.

2. Theory

Schnitzer & Yariv (2012) derived a mathematical model for the electrokinetic flows of symmetric electrolytes at large zeta potentials in the limit of thin EDL, including surface conduction effects. Building on this work, we modelled the stationary flows induced by AC fields around charged cylinders with small Dukhin number (Calero *et al.* 2021). We now explore the case of finite Dukhin number and weak electric fields (Schnitzer *et al.* 2013). To this end, we consider a negatively charged dielectric sphere immersed in a binary electrolyte and subjected to an AC electric field with amplitude E_0 and angular frequency ω. We assume that this frequency is low enough so that the EDL is in quasi-equilibrium ($\omega \ll \sigma/\varepsilon$, with ε and σ denoting the liquid permittivity and conductivity, respectively). We use a dimensionless formulation where length is scaled with the radius of the particle a, electric potential with the thermal voltage $\phi_{ther} = k_B T/ze$ (where k_B is Boltzmann's constant, T absolute temperature, z ionic valence and e elementary charge), time with $\eta/\varepsilon E_{ther}^2$ (where $E_{ther} = \phi_{ther}/a$ is the thermal electric field), pressure with εE_{ther}^2, and ion concentrations with typical salt concentration c_0. Thus, diffusion constants are non-dimensionalized with $\varepsilon a^2 E_{ther}^2/\eta$, velocities with $\varepsilon E_{ther}^2 a/\eta$, and the typical Reynolds number is $Re = \rho_m \varepsilon E_{ther}^2 a^2/\eta^2$, with ρ_m the liquid mass density. The surface charge on the dielectric is non-dimensionalized with $\varepsilon\phi_{ther}/\lambda_D$, where λ_D is the Debye length.

The conservation equations for the concentration of positive (c_+) and negative (c_-) ions are, respectively,

$$\boldsymbol{\nabla}\cdot(-c_+\boldsymbol{\nabla}\phi - \boldsymbol{\nabla}c_+) + \alpha_+\boldsymbol{u}\cdot\boldsymbol{\nabla}c_+ + \alpha_+\frac{\partial c_+}{\partial t} = 0, \tag{2.1}$$

$$\boldsymbol{\nabla}\cdot(c_-\boldsymbol{\nabla}\phi - \boldsymbol{\nabla}c_-) + \alpha_-\boldsymbol{u}\cdot\boldsymbol{\nabla}c_- + \alpha_-\frac{\partial c_-}{\partial t} = 0, \tag{2.2}$$

where α_+ and α_- are the reciprocals of the non-dimensional diffusion constants D_+ and D_- for positive and negative ions, respectively, and the liquid velocity is $\boldsymbol{u}$. In the bulk electrolyte outside the EDL, electro-neutrality ($c_+ = c_- = c$) means that these equations can be combined to give

$$D\nabla^2 c = \boldsymbol{u}\cdot\boldsymbol{\nabla}c + \frac{\partial c}{\partial t}, \tag{2.3}$$

$$\boldsymbol{\nabla}\cdot(c\boldsymbol{\nabla}\phi) = \gamma\left(\frac{\partial c}{\partial t} + \boldsymbol{u}\cdot\boldsymbol{\nabla}c\right), \tag{2.4}$$

where $D = 2/(\alpha_+ + \alpha_-)$ and $\gamma = (\alpha_+ - \alpha_-)/2$. Equation (2.3) is the diffusion equation for the ion concentration. Equation (2.4) is essentially the equation for the electric potential, where γ is a parameter that is related to the asymmetry in ion mobility.

The boundary conditions on the surface of the charged dielectric sphere are as follows (Schnitzer & Yariv 2012). The normal flux of co-ions (anions in our case) is zero:

$$c\frac{\partial\phi}{\partial n} - \frac{\partial c}{\partial n} = 0. \tag{2.5}$$

The normal flux of counter-ions (cations in our case) equals the surface divergence of EDL cation flux:

$$-c\frac{\partial\phi}{\partial n} - \frac{\partial c}{\partial n} = 2\,Du\nabla_s^2(\phi + \ln c), \tag{2.6}$$

where Du is a Dukhin number defined as $Du = (1 + 2\alpha_+)|q_s|\lambda_D$, with q_s denoting the non-dimensional intrinsic surface charge. Here the normal derivative is from the dielectric

to the electrolyte. In the literature (Delgado *et al.* 2005), the Dukhin number is defined as $Du_o = K_s/(\sigma a)$, where K_s is the surface conductance. For large negative zeta potential (the case in this work), the relation between these two definitions is $Du_o \approx Du\, 2D_+/(D_+ + D_-)$. Here Du can be considered a fixed quantity if the surface charge is fixed. In this work we assume this to be the case, i.e. variations in salt concentration do not lead to variations in the intrinsic surface charge. Also, note that the boundary conditions (2.5) and (2.6) neglect the charging of the EDL at the particle surface, in contrast to the modelling of induced-charge electro-osmosis (ICEO) phenomena with AC fields (Squires & Bazant 2004). As shown in Schnitzer & Yariv (2014) for dielectric particles and moderate fields, the induced zeta potential associated with induced charges in the EDL is negligibly small compared with the thermal voltage.

The liquid velocity and pressure satisfy the Navier–Stokes equations for negligible Reynolds number:

$$0 = -\boldsymbol{\nabla} p + \nabla^2 \boldsymbol{u} + \nabla^2 \phi \boldsymbol{\nabla}\phi, \quad \boldsymbol{\nabla}\cdot\boldsymbol{u} = 0, \tag{2.7a,b}$$

where the Coulomb term is present because gradients in ion concentration can lead to induced charge in the bulk, through (2.4). In these equations we neglect the term $Re\partial \boldsymbol{u}/\partial t$ because it is negligible for particles with radii of the order of microns and frequencies less than 100 kHz. In other words (using dimensional quantities), this is negligible when $\rho_m \omega a^2/\eta \ll 1$. Thus, (2.7*a*,*b*) are quasi-static in the sense that time is implicit. The boundary condition at the particle surface is $\boldsymbol{u} = \boldsymbol{U} + \boldsymbol{u}_s$, where $\boldsymbol{U}$ is the translational velocity of the particle centre and $\boldsymbol{u}_s$ is the slip velocity generated at the EDL (Prieve *et al.* 1984):

$$\boldsymbol{u}_s = \zeta \boldsymbol{\nabla}_s \phi - 4 \ln\left(\cosh(\zeta/4)\right) \boldsymbol{\nabla}_s \ln c. \tag{2.8}$$

The zeta potential ζ is related to the intrinsic charge by the following (Hunter 1993):

$$q_s = 2\sqrt{c}\sinh(\zeta/2). \tag{2.9}$$

The translational velocity $\boldsymbol{U}$ is determined by the condition that the total hydrodynamic stress equals zero at the surface of the sphere (Schnitzer *et al.* 2013). Far from the particle, at infinity, the fluid velocity is zero. At this point, the reference frame can be changed to one that is attached to the particle. The quasi-static equations for velocity and pressure are the same, and the new boundary conditions are $\boldsymbol{u} = \boldsymbol{u}_s$ at the particle surface, $\boldsymbol{u} = -\boldsymbol{U}$ at infinity. Under an applied AC electric field, the sphere velocity $\boldsymbol{U}$ is an oscillating function of time, with zero time average (from symmetry).

Following Schnitzer *et al.* (2013), we now perform a power expansion of the amplitude of the applied AC electric field $\beta \equiv E_0/E_{ther}$: $c = 1 + \beta c_1 + \beta^2 c_2 + \ldots$, $\phi = \beta\phi_1 + \beta^2\phi_2 + \ldots$, $\boldsymbol{u} = \beta\boldsymbol{u}_1 + \beta^2\boldsymbol{u}_2 + \ldots$, $p = \beta p_1 + \beta^2 p_2 + \ldots$ The linear approximation provides a fluid velocity that is oscillatory in time, while the stationary electro-osmotic flow around the sphere is found at second order in β.

2.1. *Linear response*

Salt concentration and potential satisfy

$$D\nabla^2 c_1 = \frac{\partial c_1}{\partial t}, \quad \nabla^2\phi_1 = \gamma\frac{\partial c_1}{\partial t}, \tag{2.10a,b}$$

with boundary conditions as follows: at $r = 1$,

$$\frac{\partial c_1}{\partial r} + Du\,\nabla_s^2(\phi_1 + c_1) = 0, \quad \frac{\partial c_1}{\partial r} - \frac{\partial \phi_1}{\partial r} = 0, \tag{2.11a,b}$$

where ∇_s^2 is the surface Laplacian, and at $r \to \infty$,

$$c_1 = 0, \quad \phi_1 = -\cos(\omega t) r \cos\theta. \tag{2.12a,b}$$

Assume that positive and negative ions have the same mobility, so that $\gamma = 0$. Since the applied field is an oscillating function in time with angular frequency ω, we write c_1 and ϕ_1 as $c_1 = Re[\tilde{c}_1 \mathrm{e}^{\mathrm{i}\omega t}]$, $\phi_1 = Re[\tilde{\phi}_1 \mathrm{e}^{\mathrm{i}\omega t}]$. The complex functions satisfy

$$D\nabla^2 \tilde{c}_1 = \mathrm{i}\omega \tilde{c}_1, \quad \nabla^2 \tilde{\phi}_1 = 0. \tag{2.13a,b}$$

Given that both $\tilde{c}_1$ and $\tilde{\phi}_1$ are of the form $f(r)\cos\theta$, the solutions are found as

$$\tilde{c}_1 = C\mathrm{e}^{-k(r-1)} \frac{1+kr}{r^2} \cos\theta, \quad \tilde{\phi}_1 = -r\cos\theta + F\frac{\cos\theta}{2r^2}, \tag{2.14a,b}$$

where $k = \sqrt{\mathrm{i}\omega/D}$, and

$$C = \frac{3\,Du}{2+2k+k^2+Du(k+2)^2}, \quad F = \frac{2\,Du(1+k+k^2)-(2+2k+k^2)}{2+2k+k^2+Du(k+2)^2}. \tag{2.15a,b}$$

The limit of zero frequency ($k = 0$)

$$\tilde{c}_1 = \frac{3\,Du}{2+4\,Du}\frac{\cos\theta}{r^2}, \quad \tilde{\phi}_1 = -r\cos\theta + \frac{Du-1}{2+4\,Du}\frac{\cos\theta}{r^2} \tag{2.16a,b}$$

is coincident with that given by Schnitzer & Yariv (2012), and by Hunter (1993) for thin double layers and a highly charged surface. At infinite frequency ($k \to \infty$),

$$\tilde{c}_1 = 0, \quad \tilde{\phi}_1 = -r\cos\theta + \frac{2\,Du-1}{2+2\,Du}\frac{\cos\theta}{r^2}. \tag{2.17a,b}$$

Here it can be seen that $F/2 = (2\,Du-1)/(2\,Du+2)$ is the low-frequency value of the Maxwell–Wagner–O'Konski dipole coefficient (O'Konski 1960). The frequency dependence of the dipole coefficient $F/2$ is coincident with that given in Shilov *et al.* (2001) for a highly charged surface, with thin double layer and equal ion mobilities, because $\gamma = 0$ is set in (2.10*a*,*b*).

The fluid flow is oscillatory in time and governed by the equations

$$\nabla^2 \boldsymbol{u}_1 = \nabla p_1, \quad \nabla \cdot \boldsymbol{u}_1 = 0, \tag{2.18a,b}$$

with slip velocity at $r = 1$ given by

$$\boldsymbol{u}_{s1} = \zeta_0 \nabla_s \phi_1 - 4\log\left(\cosh(\zeta_0/4)\right) \nabla_s c_1. \tag{2.19}$$

At infinity the fluid velocity goes to $\boldsymbol{u}_1 \to -Re[U_1 \mathrm{e}^{\mathrm{i}\omega t}]\hat{\boldsymbol{z}}$. Here U_1 is determined by the condition that the total hydrodynamic stress is zero on the sphere, which leads to

$$U_1 = \zeta_0 \frac{2+2k+k^2+2\,Du(1+k)}{2+2k+k^2+Du(k+2)^2} + 8\log\left(\cosh(\zeta_0/4)\right)\frac{Du(1+k)}{2+2k+k^2+Du(k+2)^2}. \tag{2.20}$$

The slip velocity is then $\boldsymbol{u}_{s1} = \frac{3}{2}Re[U_1 \mathrm{e}^{\mathrm{i}\omega t}]\sin\theta\hat{\theta}$. At the limit of zero frequency,

$$U_1 = \frac{\zeta_0(1+Du)+4\,Du\log\left(\cosh(\zeta_0/4)\right)}{1+2\,Du}; \tag{2.21}$$

taking into account that ζ_0 is negative, this agrees with the expression given by Schnitzer *et al.* (2013). The latter was shown to be equivalent to the expression provided by O'Brien (1983) for large absolute zeta potential.

2.2. *Quadratic response*

The equations for salt concentration and potential at second order in β are

$$D\nabla^2 c_2 = \frac{\partial c_2}{\partial t} + \boldsymbol{u}_1 \cdot \boldsymbol{\nabla} c_1, \quad \nabla^2 \phi_2 = -\boldsymbol{\nabla}\phi_1 \cdot \boldsymbol{\nabla} c_1, \tag{2.22a,b}$$

with boundary conditions at $r = 1$ given by

$$\frac{\partial c_2}{\partial r} + Du\, \boldsymbol{\nabla}_s^2(\phi_2 + c_2) = \frac{Du}{2}\boldsymbol{\nabla}_s^2 c_1^2, \quad \frac{\partial c_2}{\partial r} - \frac{\partial \phi_2}{\partial r} = c_1 \frac{\partial \phi_1}{\partial r}, \tag{2.23a,b}$$

while at $r \to \infty$ both c_2 and ϕ_2 go to zero.

The time-averaged velocity and pressure satisfy

$$\nabla^2 \langle \boldsymbol{u}_2 \rangle = \boldsymbol{\nabla} \langle p_2 \rangle, \quad \boldsymbol{\nabla} \cdot \langle \boldsymbol{u}_2 \rangle = 0. \tag{2.24a,b}$$

Here the body force is zero since $\nabla^2 \phi_1 = 0$. The boundary condition at $r = 1$ is a time-averaged slip velocity,

$$\langle \boldsymbol{u}_{2s} \rangle = \zeta_0 \boldsymbol{\nabla}_s \langle \phi_2 \rangle + \langle \zeta_1 \boldsymbol{\nabla}_s \phi_1 \rangle - 4 \ln\left(\cosh\left(\frac{\zeta_0}{4}\right)\right) \boldsymbol{\nabla}_s \left\langle c_2 - \frac{c_1^2}{2} \right\rangle - \tanh\left(\frac{\zeta_0}{4}\right) \langle \zeta_1 \boldsymbol{\nabla}_s \phi_1 \rangle, \tag{2.25}$$

with $\zeta_1 = -c_1 \tanh(\zeta_0/2)$ from (2.9) and fixed q_s. From symmetry, at infinity $\boldsymbol{u}_2 \to 0$. Therefore, the time-averaged velocity can be derived from the time averages $\langle c_2 \rangle$ and $\langle \phi_2 \rangle$. The equations for $\langle c_2 \rangle$ and $\langle \phi_2 \rangle$ are

$$\nabla^2 \langle c_2 \rangle = \frac{1}{2D} Re\left[\boldsymbol{\nabla} \tilde{c}_1 \cdot \tilde{\boldsymbol{u}}_1^*\right], \quad \nabla^2 \langle \phi_2 \rangle = -\frac{1}{2} Re\left[\boldsymbol{\nabla} \tilde{\phi}_1 \cdot \boldsymbol{\nabla} \tilde{c}_1^*\right], \tag{2.26a,b}$$

where the time-averaged product of two oscillating functions satisfies $\langle f(t) g(t) \rangle = \frac{1}{2} Re[f g^*]$. The boundary conditions at $r = 1$ are now written as

$$\left.\begin{aligned} \frac{\partial \langle c_2 \rangle}{\partial r} + Du\, \boldsymbol{\nabla}_s^2 \langle \phi_2 + c_2 \rangle = \frac{Du}{4} \boldsymbol{\nabla}_s^2 |\tilde{c}_1|^2, \\ \frac{\partial \langle c_2 \rangle}{\partial r} - \frac{\partial \langle \phi_2 \rangle}{\partial r} = \frac{1}{2} Re\left[\tilde{c}_1 \frac{\partial \tilde{\phi}_1}{\partial r}\right]. \end{aligned}\right\} \tag{2.27}$$

The source terms in the equations (2.26*a*,*b*) and the independent terms in the boundary conditions (2.27) are linear combinations of $P_0(\cos\theta)$ and $P_2(\cos\theta)$, where $P_n(x)$ is the Legendre polynomial of degree n. Therefore, $\langle c_2 \rangle$ and $\langle \phi_2 \rangle$ can be written as $\langle c_2 \rangle = c_{20}(r) + c_{22}(r) P_2(\cos\theta)$ and $\langle \phi_2 \rangle = \phi_{20}(r) + \phi_{22}(r) P_2(\cos\theta)$. Only the terms proportional to $P_2(\cos\theta)$ are important for the slip velocity (2.25). The general solutions of (2.26*a*,*b*) for these terms that decay at infinity are of the form

$$c_{22} = \frac{A}{r^3} + Re[G_c(r)], \quad \phi_{22} = \frac{B}{r^3} + Re[G_\phi(r)], \tag{2.28a,b}$$

where A and B are constants that are determined from the boundary conditions, and G_c and G_ϕ are particular solutions of the equations

$$\left.\begin{aligned} \frac{1}{x^2}\frac{\partial}{\partial x}\left(x^2 \frac{\partial G_c}{\partial x}\right) - \frac{6 G_c}{x^2} = \frac{C U_1^* k \mathrm{e}^k}{2D} \mathrm{e}^{-x} g_c(x), \\ \frac{1}{x^2}\frac{\partial}{\partial x}\left(x^2 \frac{\partial G_\phi}{\partial x}\right) - \frac{6 G_\phi}{x^2} = -\frac{C k \mathrm{e}^k}{2} \mathrm{e}^{-x} g_\phi(x), \end{aligned}\right\} \tag{2.29}$$

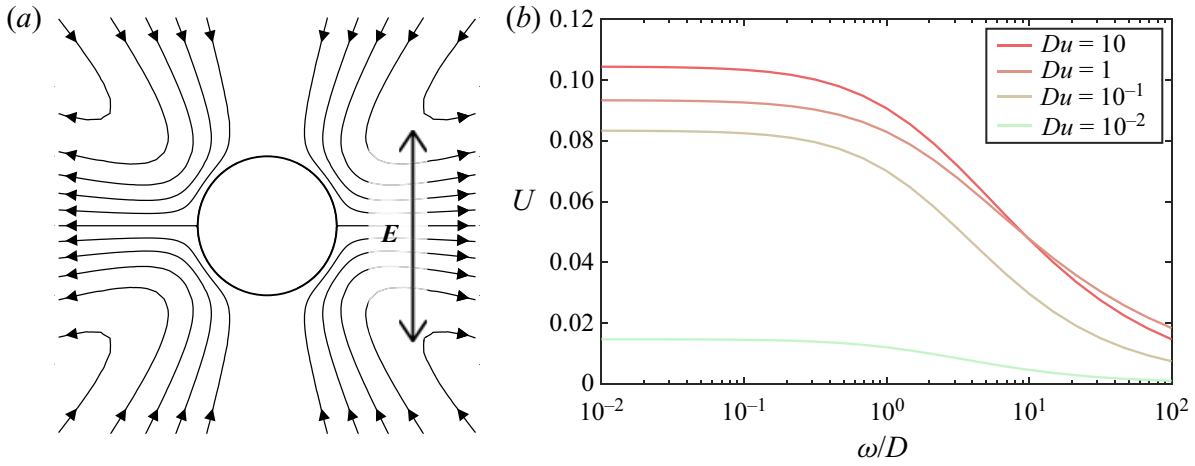

Figure 2. (*a*) Streamlines of the field represented by (2.32). (*b*) Slip velocity U as a function of ω/D. Here $\zeta = -4$, $D = 4.5$.

where $x = kr$, and

$$\left.\begin{aligned} g_c(x) &= 2x^{-3} + 2x^{-2} + \tfrac{2}{3}x^{-1} - k^3(x^{-6} + x^{-5} + \tfrac{2}{3}x^{-4}), \\ g_\phi(x) &= 2x^{-3} + 2x^{-2} + \tfrac{2}{3}x^{-1} + k^3F^*(x^{-6} + x^{-5} + \tfrac{2}{3}x^{-4}). \end{aligned}\right\} \tag{2.30}$$

Note that the operator $D_r^2 \equiv (1/r^2)\,\mathrm{d}/\mathrm{d}r(r^2(\mathrm{d}/\mathrm{d}r)) - 6/r^2$ comes from the Laplacian operator in spherical coordinates when using solutions of the form $f(r)P_2(\cos\theta)$. The right-hand sides in (2.29) are linear combinations of terms like $x^m\mathrm{e}^{-x}$. A solution of the equation $D_x^2 G = x^m\mathrm{e}^{-x}$ that decays at infinity is

$$G(m, x) = \tfrac{1}{5}(\Gamma(m + 5, x)x^{-3} - \Gamma(m, x)x^2), \tag{2.31}$$

where $\Gamma(m, x)$ is the incomplete Gamma function. Therefore, we construct G_c and G_ϕ as linear combinations of $G(m, x)$ with $m = -6, -5, \ldots, -1$, and from here we obtain c_{22} and ϕ_{22}.

Finally, the time-averaged slip velocity (2.25) is obtained as $\langle \boldsymbol{u}_{2s}\rangle = U\sin(2\theta)\hat{\theta}$, where U is given in Appendix A. With this slip velocity on the sphere, the time-averaged velocity field is as follows (Gamayunov *et al.* 1986; Squires & Bazant 2004):

$$\langle \boldsymbol{u}_2\rangle = U\left(\frac{(1 - r^2)(1 + 3\cos 2\theta)}{2r^4}\hat{r} + \frac{\sin 2\theta}{r^4}\hat{\theta}\right). \tag{2.32}$$

The streamlines of this velocity field are shown in figure 2(*a*).

Figure 2(b) shows U as a function of ω/D ($\omega a^2/D$ with dimensions) for different values of the Dukhin number. While the theory for small Dukhin number leads to a velocity that scales linearly with Du, the current model predicts a saturation. For example, figure 2(*b*) shows that the slip velocities for $Du = 0.1$ and $Du = 1$ differ by around 10 %. It is clear that the intensity of the flow around the particle decreases beyond the characteristic dimensional frequency $\omega_c = D/a^2$, which is the reciprocal of the ion diffusion time for the radius a. For frequencies much greater than this, U decays as $\omega^{-1/2}$, and this frequency-dependent behaviour stems from the diffusion equation for the salt (2.13*a*,*b*). The mechanism that produces the quadratic flow is a consequence of the polarization of ion concentration, which decreases as $\omega^{-1/2}$.

3. Experiments

The flows around single particles were imaged using a simple microfluidic channel. This consists of a straight polydimethylsiloxane (PDMS) channel 1 cm long with inlet and outlet reservoirs, fabricated using standard soft lithography. The channel cross-section is 50 μm $\times$ 50 μm. The inlet and outlet reservoirs are sealed with metal cylinders that serve as the electrodes for the electric field. Fluorescent (500 nm and 3 μm) carboxylate particles were suspended in an aqueous solution of potassium chloride (KCl) with a conductivity of $\sigma = 1.7$ mS m^{-1}. The 3 μm particle concentration was very low (no more than three or four particles in the channel at any one time). In order to prevent particles from sticking to the channel walls, these were pretreated with a solution of 0.1 % (w/v) Pluronic F-127 in deionized water (a non-ionic surfactant that adsorbs onto the PDMS) for at least 30 min. The peak-to-peak amplitude of the AC applied voltages was 1600 V over the frequency range from 100 Hz to 5 kHz. Below 100 Hz, the 3 μm particle oscillations due to the combination of electro-osmosis and zero-order electrophoresis are too large in amplitude to allow accurate measurement of the steady flows around the particles. For frequencies above 5 kHz, the magnitude of the quadrupolar flow is too weak compared to the Brownian motion of the tracer particles.

The trajectories of the 500 nm tracers were imaged using fluorescent microscopy. These tracers describe a three-dimensional flow pattern around the 3 μm particles. The microscope objective was focused at approximately a horizontal plane at the centre of the large particle. Out of all the tracer trajectories, only those that were approximately within the focal plane were used (as shown in figure 1).

The 3 μm particles oscillate due to electrophoresis, but also have a small drift due to small pressure fluctuations within the microchannel. Thus, in order to measure the fluid velocity around these particles with respect to them, a MATLAB program was developed to track the position of single 3 μm particles and to place this large particle in the centre of a reference frame. This process is described in the supplementary movie available at https://doi.org/10.1017/jfm.2021.650. The videos of fluid flow thus have the large particle at a fixed position in the centre of the image, with the smaller tracer particles flowing around it. Particle tracking velocimetry of the tracers provides a set of velocities at given positions in the plane that are then compared with the theoretical flow field (2.32) through a least-squares fitting analysis with a single fitting parameter, U, the maximum slip velocity. Finally, the slip velocity and the experimental error are estimated from the average and dispersion of the values determined from analysis of each streamline.

Figure 3 shows experimental data on the slip velocity as a function of frequency, along with the predictions of the model. Typical parameters for carboxylated latex beads are $\zeta = -75$ mV and $K_s = 1$ nS (Ermolina & Morgan 2005). The figure shows that for the expected Dukhin number ($Du = 0.392$), the theoretical prediction overestimates the velocity by a factor of between 2 and 3.

4. Discussion and conclusions

This paper describes observations of stationary flows around dielectric spheres. Quadrupolar fluid flows driven by electro-osmosis have been predicted around metal spheres (Squires & Bazant 2004). However, in this case the slip velocity has a different origin, namely, ICEO. In the case of a charged dielectric sphere, the rectified fluid flow arises from the polarization of electrolyte concentration (concentration-polarization electro-osmosis, CPEO) that results from the surface conductance around the sphere. As shown in Calero *et al.* (2021), the induced charge on a dielectric sphere leads to an

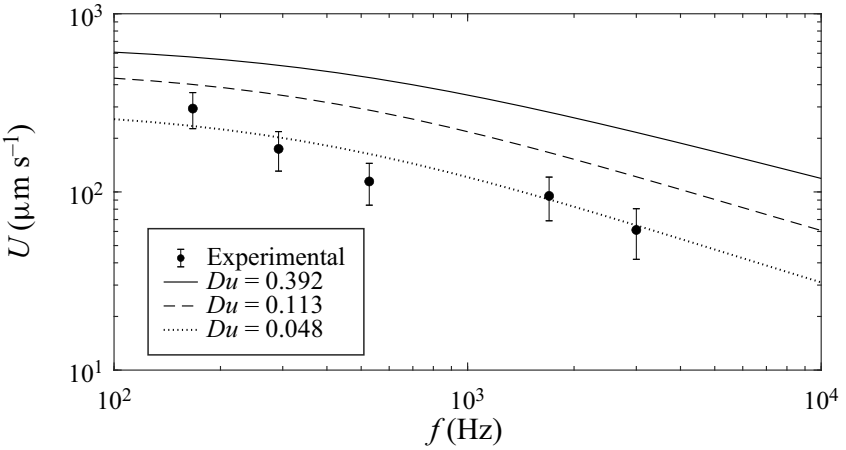

Figure 3. Experimental slip velocity U versus frequency of the applied field ($E_0 = 80$ kV m^{-1}, $\sigma = 1.7$ mS m^{-1}, $a = 1.5$ μm and zeta potential is set to $\zeta_0 = -75$ mV). Theoretical curves are shown for different values of Du: $Du_o = K_s/(\sigma a)$ with $K_s = 1$ nS (——); $Du = (1 + 2\alpha_+)|q_s|\lambda_D$ (- - - -); $Du_o = K_s/(\sigma a)$ with $K_s = 0.12$ nS as obtained by a least-squares fitting (· · · · · ·).

associated induced zeta potential that is much smaller than the variation in zeta potential due to concentration polarization. This implies that CPEO velocities are much higher than ICEO velocities for the case of dielectric surfaces.

Our mathematical model predicts quadrupolar flows with a velocity magnitude that vanishes for frequencies higher than $\omega_c = D/a^2$, in agreement with experimental observations. A quantitative comparison between theory and experiment shows that the velocity magnitude is overestimated by the present model for typical values of Du measured for latex spheres. The nonlinear model assumes weak electric fields ($E_0 a < k_B T/e$), but in the experiments $E_0 a \approx 120$ mV $\approx 5 k_B T/e$. However, for AC fields the characteristic scale of the ion diffusion equation is the smaller of a or the diffusion penetration depth $\sqrt{D/\omega}$. This suggests that the condition of weak fields could be relaxed for high frequencies and rewritten as $E_0 \ell < k_B T/e$, with ℓ the smaller of the two scales. For example, for $f \approx 3$ kHz, the characteristic length is $\ell \sim a/5$ and $E_0 \ell \sim k_B T/e$.

The effects of this flow pattern on the pair interactions between particles have been theoretically studied in the context of induced-charge electrophoresis and compared to that of dielectrophoresis (DEP) (Saintillan 2008). Interestingly, the induced motion between particles decays for large distances as $(a/r)^2$ due to the hydrodynamic interaction, and as $(a/r)^4$ due to the DEP interaction (with r the distance between particle centres). Clearly, the hydrodynamic interaction is more important than the DEP interaction when the particles are separated by distances of several diameters. From our experiments and theory for CPEO around dielectric spheres, we expect hydrodynamic interactions between particles to decrease with ionic strength and vanish for frequencies much greater than D/a^2. Curiously, these trends have been found by Mittal *et al.* (2008) in experiments with latex microparticles subjected to AC fields, although they attributed this behaviour to the interaction between induced dipoles on the particles.

Supplementary movie. Supplementary movie is available at https://doi.org/10.1017/jfm.2021.650.

Funding. P.G.-S. and A.R. acknowledge financial support from the European Regional Development Fund and the Spanish State Research Agency (MCI) under contract PGC2018-099217-B-I00.

Declaration of interests. The authors report no conflict of interest.

Data availability statement. The data that support the findings of this study are openly available in the University of Southampton repository at https://doi.org/10.52.58/SOTON/D1898.

Author ORCIDs.
Raúl Fernández-Mateo https://orcid.org/0000-0003-1413-8046;
Pablo García-Sánchez https://orcid.org/0000-0003-3538-2590;
Víctor Calero https://orcid.org/0000-0002-8971-7301;
Hywel Morgan https://orcid.org/0000-0003-4850-5676;
Antonio Ramos https://orcid.org/0000-0002-2190-1188.

Appendix A. Expression for U

In this appendix we provide the expression for the maximum stationary slip velocity on the sphere, U (see (2.32)). We have checked that U coincides with the expression of Schnitzer *et al.* (2013) for $k = 0$. It is given by

$$\begin{aligned} U = &-\frac{3}{2}\zeta_0 Re\left[B_1 + B_2 + G_\phi(k)\right] - \frac{1}{4}\tanh\left(\zeta_0/2\right) Re\left[(1+k)C(1 - F^*/2)\right] \\ &+ 6\log\left(\cosh(\zeta_0/4)\right) Re\left[A_1 + A_2 + G_c(k)\right] \\ &- \left(4\log\left(\cosh\left(\frac{\zeta_0}{4}\right)\right) + \tanh\left(\frac{\zeta_0}{4}\right)\tanh\left(\frac{\zeta_0}{2}\right)\right)\frac{|C(1+k)|^2}{4}, \end{aligned} \tag{A1}$$

where

$$\left.\begin{aligned} A_1 = -2\,Du\frac{3G_\phi(k) + kG'_\phi(k)}{3 + 12\,Du} + \frac{2}{3}Du\frac{(1+k)(1+F^*)C}{3+12\,Du} + Du\frac{|C(1+k)|^2}{3+12\,Du}, \\ B_1 = A_1 + \frac{3kG'_\phi(k) - (1+k)(1+F^*)C}{9}, \end{aligned}\right\} \tag{A2}$$

$$A_2 = \frac{(1+2\,Du)kG'_c(k) - 6\,DuG_c(k)}{3+12\,Du}, \quad B_2 = \frac{-2\,DukG'_c(k) - 6\,DuG_c(k)}{3+12\,Du}, \tag{A3a,b}$$

$$\begin{aligned} G_c(x) = &\frac{CU_1^* k\mathrm{e}^k}{2D}[2G(-1,x)/3 + 2G(-2,x) + 2G(-3,x) \\ &- k^3(2G(-4,x)/3 + G(-5,x) + G(-6,x))], \end{aligned} \tag{A4}$$

$$\begin{aligned} G_\phi(x) = &-\frac{Ck\mathrm{e}^k}{2}[2G(-1,x)/3 + 2G(-2,x) + 2G(-3,x) \\ &+ k^3F^*(2G(-4,x)/3 + G(-5,x) + G(-6,x))]. \end{aligned} \tag{A5}$$

References

Calero, V., Fernández-Mateo, R., Morgan, H., García-Sánchez, P. & Ramos, A. 2021 Stationary electro-osmotic flow driven by AC fields around insulators. *Phys. Rev. Appl.* **15** (1), 014047.

Delgado, A.V., Gonzalez-Caballero, F., Hunter, R.J., Koopal, L.K. & Lyklema, J. 2005 Measurement and interpretation of electrokinetic phenomena (IUPAC technical report). *Pure Appl. Chem.* **77**, 1753–1802.

Dukhin, A.S. & Murtsovkin, V.A. 1986 Pair interaction of particles in electric field. 2. Influence of polarization of double layer of dielectric particles on their hydrodynamic interaction in a stationary electric field. *Colloid J. USSR* **48** (2), 203–211.

ERMOLINA, I. & MORGAN, H. 2005 The electrokinetic properties of latex particles: comparison of electrophoresis and dielectrophoresis. *J. Colloid Interface Sci.* **285** (1), 419–428.

GAMAYUNOV, N.I., MURTSOVKIN, V.A. & DUKHIN, A.S. 1986 Pair interaction of particles in electric field. 1. Features of hydrodynamic interaction of polarized particles. *Colloid J. USSR* **48** (2), 197–203.

HUNTER, R.J. 1993 *Introduction to Modern Colloid Science*. Oxford University Press.

MITTAL, M., LELE, P.P., KALER, E.W. & FURST, E.M. 2008 Polarization and interactions of colloidal particles in AC electric fields. *J. Chem. Phys.* **129** (6), 064513.

O'BRIEN, R.W. 1983 The solution of the electrokinetic equations for colloidal particles with thin double layers. *J. Colloid Interface Sci.* **92** (1), 204–216.

O'KONSKI, C.T. 1960 Electric properties of macromolecules. V. Theory of ionic polarization in polyelectrolytes. *J. Phys. Chem.* **64** (5), 605–619.

PRIEVE, D.C., ANDERSON, J.L., EBEL, J.P. & LOWELL, M.E. 1984 Motion of a particle generated by chemical gradients. Part 2. Electrolytes. *J. Fluid Mech.* **148**, 247–269.

SAINTILLAN, D. 2008 Nonlinear interactions in electrophoresis of ideally polarizable particles. *Phys. Fluids* **20** (6), 067104.

SCHNITZER, O. & YARIV, E. 2012 Macroscale description of electrokinetic flows at large zeta potentials: nonlinear surface conduction. *Phys. Rev.* E **86** (2), 021503.

SCHNITZER, O. & YARIV, E. 2014 Strong electro-osmotic flows about dielectric surfaces of zero surface charge. *Phys. Rev.* E **89**, 043005.

SCHNITZER, O., ZEYDE, R., YAVNEH, I. & YARIV, E. 2013 Weakly nonlinear electrophoresis of a highly charged colloidal particle. *Phys. Fluids* **25** (5), 052004.

SHILOV, V.N., DELGADO, A.V., GONZALEZ-CABALLERO, F. & GROSSE, C. 2001 Thin double layer theory of the wide-frequency range dielectric dispersion of suspensions of non-conducting spherical particles including surface conductivity of the stagnant layer. *Colloids Surf.* A **192** (1–3), 253–265.

SQUIRES, T.M. & BAZANT, M.Z. 2004 Induced-charge electro-osmosis. *J. Fluid Mech.* **509** (1), 217–252.

Paper E

Concentration-Polarization Electroosmosis Near Insulating Constrictions within Microfluidic Channels

Summary of Results

In this paper, the generality of CPEO flows was tested by quantifying the fluid velocity field around constrictions in microfluidic channels. Results were compared against numerical simulations of the CPEO theory. Importantly, CPEO and not insulating dielectrophoresis (iDEP) was proven to be the driving phenomenon for microfluidic constrictions at low electric field frequencies.

Contribution Statement

Garcia-Sanchez, Morgan and Ramos had long suspected that many works in the literature wrongly attributed iDEP to the phenomena around insulating microstructures at low frequency AC electric fields. Given the satisfactory explanation of CPEO for the case of the pillars, they encouraged the study CPEO around corners. In this work, Calero and I did the experimental work, Garcia-Sanchez and I did the numerical work, and Calero and I analysed the experimental data and compared these with simulations. Garcia-Sanchez, Ramos and I wrote the first version of the manuscript. Morgan, Ramos and Garcia-Sanchez provided supervisory support. All authors contributed to the final version of the manuscript.

analytical chemistry

pubs.acs.org/ac Article

Concentration–Polarization Electroosmosis near Insulating Constrictions within Microfluidic Channels

Raúl Fernández-Mateo, Víctor Calero, Hywel Morgan, Antonio Ramos, and Pablo García-Sánchez*

Cite This: *Anal. Chem.* 2021, 93, 14667–14674 Read Online

ACCESS | Metrics & More | Article Recommendations

ABSTRACT: Electric fields are commonly used to trap and separate micro- and nanoparticles near channel constrictions in microfluidic devices. The trapping mechanism is attributed to the electrical forces arising from the nonhomogeneous electric field caused by the constrictions, and the phenomenon is known as insulator-based-dielectrophoresis (iDEP). In this paper, we describe stationary electroosmotic flows of electrolytes around insulating constrictions induced by low frequency AC electric fields (below 10 kHz). Experimental characterization of the flows is described for two different channel heights (50 and 10 μm), together with numerical simulations based on an electrokinetic model that considers the modification of the local ionic concentration due to surface conductance on charged insulating walls. We term this phenomenon concentration–polarization electroosmosis (CPEO). The observed flow characteristics are in qualitative agreement with the predictions of this model. However, for shallow channels (10 μm), trapping of the particles on both sides of the constrictions is also observed. This particle and fluid behavior could play a major role in iDEP and could be easily misinterpreted as a dielectrophoretic force.

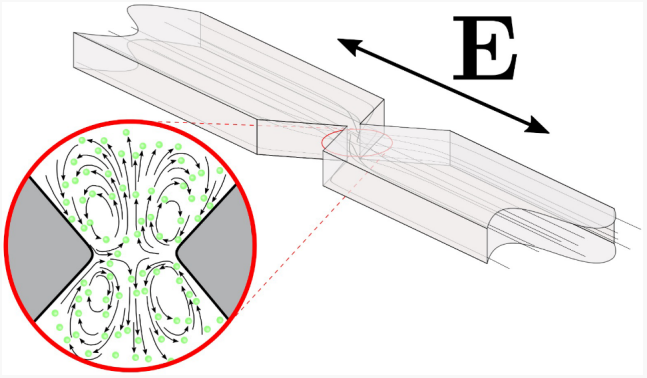

Electric fields have been widely used to manipulate small particles dispersed in aqueous solutions.[1,2] Many research groups have demonstrated electric-field induced trapping of particles and molecules within constrictions in microfluidic channels.[3] For example, early work by Chou et al.[4] showed that DNA could be trapped and enriched between insulating obstacles fabricated in a quartz wafer. Electrical manipulation and trapping of latex colloids within arrays of glass posts was demonstrated by Cummings and Sigh.[5] Liao et al.[6] used nanoconstrictions and a combination of AC and DC fields for protein enrichment in physiological media. Lapizco-Encinas et al. reported concentration and separation of live and dead bacteria[7] and concentration of proteins in low conductivity electrolytes using DC fields in an array of cylindrical insulating posts etched in glass.[8] Physher and Hayes demonstrated separation of bacteria populations using a series of constrictions with decreasing width along a channel subject to a DC field.[9]

All these results are based on the application of an electric field along constrictions and/or obstacles in a channel where the electric current is squeezed, giving rise to a spatially nonuniform electric field. In this situation, when a polarizable particle is in the presence of a nonhomogeneous electric field, a net electrical force is exerted on it and the resulting particle motion is known as dielectrophoresis (DEP).[10,11] Because the field distortion is created by insulating objects, the technique is called insulating-DEP (iDEP) or electrodeless-DEP (eDEP), although the term eDEP is more commonly used to denote electrode-based DEP.

In this paper we study fluid flows generated in the vicinity of insulating constrictions due to the presence of a low frequency (<10 kHz) AC electric field, similar to those used in iDEP. The study is motivated by recent observations of quadrupolar fluid flow induced by AC fields around insulating micropillars[12,13] and charged dielectric microspheres.[14] The constriction consists of a simple triangular shaped insulator within a long microchannel with a square cross-section, similar to the geometry used for particle trapping in the work of Chou et al.[4] and Su et al.[15] The fluid flow profile is measured using 500 nm diameter tracer particles. Figure 1(a) shows a diagram of the channel and the constriction, together with the inlet and outlet reservoirs within which electrodes are placed. The flow characteristics are described as a function of different experimental parameters (frequency, amplitude, and electrolyte

Received: July 7, 2021
Accepted: October 11, 2021
Published: October 27, 2021

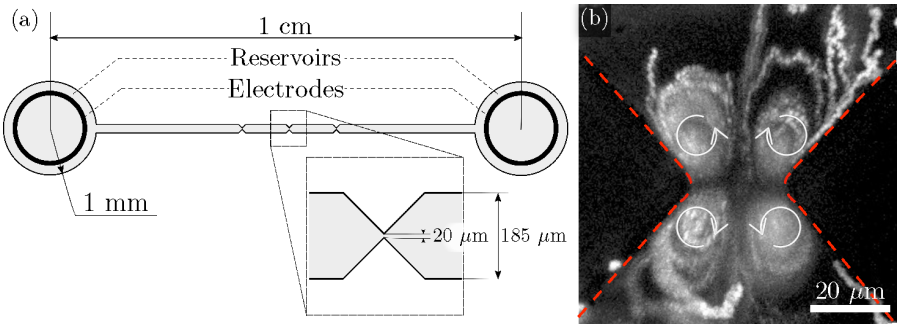

Figure 1. (a) Diagram of the microfluidic channel showing three constrictions (top view). A voltage is applied using metal needle electrodes inserted into the reservoirs. Two channel heights were used: 10 and 50 μm. (b) An image demonstrating an example of quadrupolar fluid vortices observed around a constriction.

conductivity). We also demonstrate that the extent and influence of the fluid rolls depends on the height of the channel.

Experimental measurements of the fluid velocity are in qualitative agreement with predictions of our recent theory of concentration−polarization electroosmosis (CPEO).[13] Stationary flow vortices induced by AC fields, similar to those shown in Figure 1(b), arise from gradients in electrolyte concentration caused by the surface conductance on the charged walls of insulating objects such as glass or polydimethylsiloxane (PDMS). The flow patterns are seen in relatively low conductivity electrolytes; they are not electrothermal in origin[16] although such flows may occur in higher conductivity electrolytes.[17] In addition to being of fundamental interest, these flows are likely to influence the behavior of iDEP devices and provide further insights into the operation and application of techniques such as iDEP and electrokinetic deterministic lateral displacement (DLD) where AC fields modify particle behavior.[18−21]

EXPERIMENTAL SECTION

Experimental Setup and Methods. The microfluidic devices (Figure 1) were made of PDMS using standard soft lithography. The constrictions are 20 μm wide, and channels with two different heights were made: 50 and 10 μm. Aqueous solutions of KCl with conductivities σ = {1.7, 6.1, 12.2} mS/m and pH approximately 5.5 were seeded with polystyrene fluorescent nanoparticles (500 nm diameter, zeta-potential in KCl 6.6 mS/m is ζ=−63 ± 6 mV) which act as tracers to map the fluid flow. These were imaged with a fluorescence microscope with a 100× objective. Prior to experiments, the PDMS channels were primed with a solution of 0.1% (w/v) Pluronic F-127, which is a nonionic surfactanct that adsorbs onto the PDMS walls and minimizes adhesion of the tracer particles. AC voltages of an amplitude up to 1600 V peak-to-peak were applied along the channel with two metal needles placed 1 cm apart at the inlet and outlet of the channel. Videos of the tracer particles were analyzed with "PIV lab", a software for particle image velocimetry (PIV).[22] The liquid in the channel was renewed after each measurement to minimize any changes in electrical properties caused by Faradaic reactions due to the low-frequency field. A pressure controller (Elveflow OB1MK3+) was used to refresh the liquid in the channel and to stop the flow for the measurements.

Experimental Results with Tall Channels. Figure 2 shows a set of diagrams describing the behavior of the fluorescent tracer beads near the constriction in a 50 μm tall

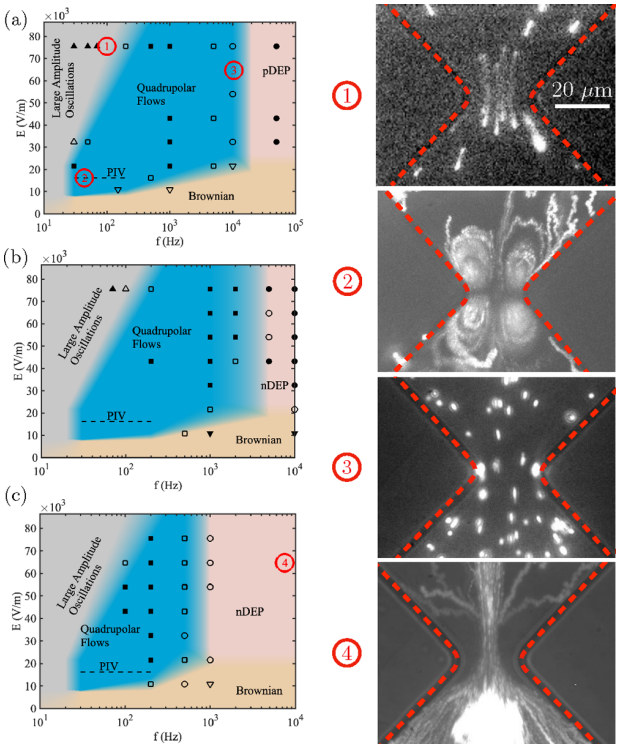

Figure 2. Maps showing the general behavior of the colloidal particles (500 nm diameter) near a channel constriction as a function of amplitude and frequency of the AC electric field. Three different conductivities of electrolyte were used, and a map is shown for each of these: (a) 1.7 mS/m, (b) 6.1 mS/m, (c) 12.2 mS/m. The dashed lines for each electrolyte conductivity indicate the frequency range within which fluid velocities were measured by PIV. The channels are 50 μm tall, and the constriction is 20 μm wide. The experimental points used to construct the maps are shown, and the predominant behavior is highlighted as (■) quadrupolar flows, (●) DEP, (▲) large amplitude oscillations, (▼) Brownian motion. Solid symbols indicate that a single behavior dominated. Open symbols indicate a mix of behaviors.

channel as a function of the electric field amplitude **E** and frequency *f*. In these plots, **E** is the amplitude of the electric field far from the constriction. The figure has a diagram for each electrolyte conductivity, and the symbols indicate the points on the map where experimental observations were recorded.

The maps show that particle electrophoresis dominates at low frequencies, manifesting as an oscillatory motion that

https://doi.org/10.1021/acs.analchem.1c02849
Anal. Chem. 2021, 93, 14667−14674

drives the particle from one side of the constriction to the other and back (see image in Figure 2(a)). The amplitude of the oscillating electrophoresis decreases with increasing frequency and eventually vanishes for frequencies larger than tens of Hertz depending on the amplitude of the electric field. In this situation, when the electrophoresis becomes relatively small, four steady flow vortices were observed at the microfluidic constriction. This regime corresponds to the blue regions in the maps of Figure 2, and example images of the quadrupolar flows are shown in the figure. These images were obtained by superimposing several video frames of particle motion. Figure 3(a) shows a larger image of one of

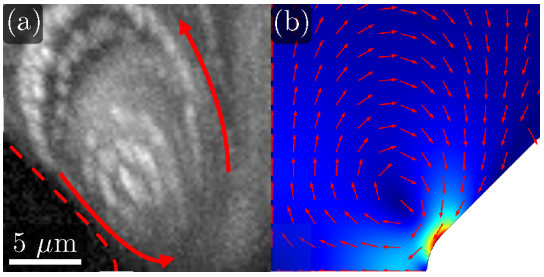

Figure 3. (a) Experimental streamlines in the constriction for KCl with a conductivity of 1.7 mS/m, an applied field amplitude of 15 kV/m, and frequency of 65 Hz. (b) COMSOL simulations reproducing the experimental system. The surface plot depicts the solution of the velocity field magnitude, while the arrow plot corresponds to the fluid velocity direction.

these rolls. As discussed below, we hypothesize that concentration polarization drives these quadrupolar flows which we refer to as concentration−polarization electro-osmosis (CPEO).[13]

Further increasing the frequency of the AC signal leads to a decrease in the velocity of the flow vortices. For the lowest electrolyte conductivity (1.7 mS/m), the fluorescent beads accumulate at the tip of the triangular constrictions at frequencies of approximately 20 kHz and above. This frequency effectively establishes the boundary or transition between the quadrupolar flows and positive dielectrophoresis (pDEP) of the particles. This transition frequency is marked on Figure 2(a). At high frequencies, pDEP drives particle accumulation to regions of maximum field gradient at the tip of the constriction. To determine the transition frequency, the field was applied and the particle behavior was observed after approximately 2 min to allow the beads to accumulate at the tip of the constriction. Neither particle motion nor accumulation were observed for low values of electric field amplitude (≈10 kV/m and below). This is labeled on the map as "Brownian". The absolute limits of this region are somehow arbitrary because they depend on experimental factors including the time-window of observation. Furthermore, the boundaries between the different regimes (Figures 2) will vary depending on particle size. For example, the DEP force varies with particle volume and is expected to dominate over a wider frequency range for larger particles.

Increasing the electrolyte conductivity to 6.1 mS/m reduces the transition frequency to 5 kHz (Figure 2(b)), while for a higher electrolyte conductivity of 12.2 mS/m, the transition frequency is around 1 kHz (Figure 2(c)). However, at these higher conductivities, the beads do not accumulate at the tip of the constriction but are expelled from the vicinity of the tip, as expected if the particles undergo negative dielectrophoresis (nDEP). This change from positive to negative DEP can be understood if the particle effective conductivity is evaluated from the O'Konski model[1] as $\sigma_p = 2K_s/a$, where K_s is the surface conductance of the particle. A typical value for K_s of latex beads is 0.5 nS[2,3] and $\sigma_p = 4$ mS/m. This is in accordance with the observation of pDEP for 1.7 mS/m and nDEP for the two other conductivities.

Quantitative characterization of the quadrupolar flows was performed by measuring the average magnitude of the fluid velocity using PIV analysis in an area near the constriction containing a single vortex (see Figure 7 for an example area). Each of the four symmetric vortices were analyzed independently, and the mean magnitude of the velocity field was averaged across all four. The peak-to-peak voltage amplitude was kept constant at 300 V, corresponding to a field amplitude of 15 kV/m. The position in the map of these detailed measurements within the quadrupolar flow is indicated with the dashed lines in Figure 2. The data in Figure 4 gives the mean velocity as a function of frequency for

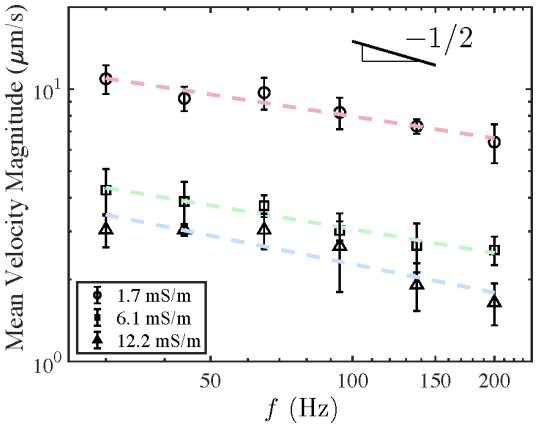

Figure 4. Results of PIV measurements for the average velocity magnitude as a function of frequency of the applied electric field. The amplitude of the applied field was 15 kV/m. Two trends can be clearly observed: the decay of the velocity magnitude with frequency ($f^{-1/2}$ trend line shown) and with electrolyte conductivity.

each electrolyte conductivity. This velocity approximately decreases as $\sqrt{f}$, in agreement with our previous findings for the trend in CPEO velocity around a micropillar.[13]

Experimental Results with Shallow Channels. Many iDEP devices use constrictions within microchannels that are shallower than those used in the previous section, typically around 10 μm tall or less.[4,5] Therefore, the flow patterns were also measured for constrictions in channels with a reduced height of 10 μm. As for the taller channels, large-amplitude oscillations of the fluorescent beads were observed at low AC frequencies. Quadrupolar flows were also observed, but they only extended a short distance from the constrictions walls and dominated within a much smaller region of the map, namely for electric fields smaller than 30 kV/m and a frequency range from 30 Hz to 1 kHz (see blue region in Figure 5). For sufficiently high electric field magnitude and frequency (green region in Figure 5), beads were observed to accumulate on both sides of the constriction tips (see image in Figure 5). A similar behavior was also found around insulating pillars subjected to AC fields in a shallow channel (8 μm).[20] This

https://doi.org/10.1021/acs.analchem.1c02849
Anal. Chem. 2021, 93, 14667−14674

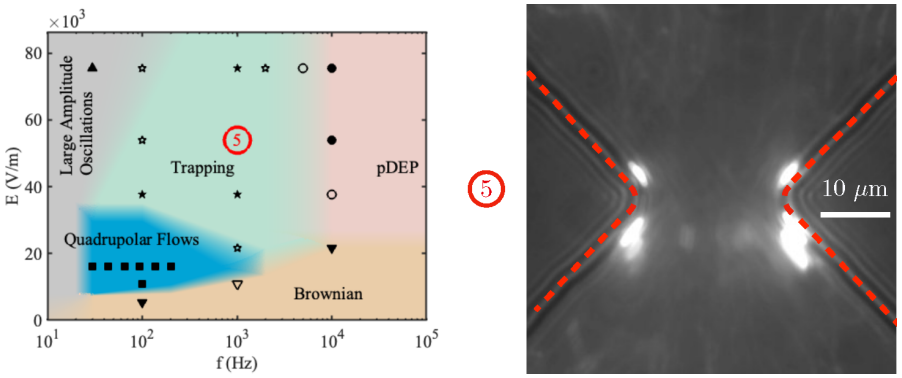

Figure 5. Particle behavior in shallow (10 μm) channels for a conductivity of σ = 1.7 mS/m. A trapping region emerges, where particles are concentrated at the sides of the constriction tips. This is shown in the image on the right, obtained by averaging the intensity of single image frames from a video over 2 min. Experimental points used to construct the maps are included to highlight the dominant behavior: (■) Quadrupolar flows, (★) trapping, (●) DEP, (▲) large amplitude oscillations, (▼) Brownian motion. Filled symbols indicate a single behavior dominated; open symbols indicate a mixture of behaviors.

trapping is notably different from DEP trapping because the particles accumulate in different positions than those expected from nDEP or pDEP. Significantly, the trapping occurs in the same positions regardless of whether the particles experience pDEP or nDEP at higher frequencies. This phenomenon disappears for increasing frequency, and classical DEP behavior is observed if the magnitude of the electric field is large enough to overcome Brownian motion and diffusion. At present the theoretical basis for this "trapping" regime is not clear, but it is likely to play an important role in the behavior of iDEP devices.

Experimental Results with Larger Particles. To check the influence of particle size on fluid flow traceability, some experiments were performed using 1 μm diameter fluorescent particles (zeta-potential in KCl 6.6 mS/m is $\zeta = -71 \pm 4$ mV). Figure 6(a) shows the map for these particles in the tall channels and a conductivity of 1.7 mS/m. The following differences with respect to the 500 nm particles (Figure 2(a)) are found: (i) Positive DEP appears at slightly lower frequencies (10 kHz for 1 μm particles whereas for the 500 nm particles this frequency was 20 kHz), and (ii) most of the region of quadrupolar flows for the 500 nm particles is now occupied by the trapping region.

Figure 6(b) shows the map for the 1 μm particles in the shallow channel at a conductivity of 1.7 mS/m. Comparing this with the 500 nm particle map (Figure 5) shows that quadrupolar flows are not observed. Instead, trapping is observed in that region of the map.

The 1 μm particles were also used to measure the fluid velocity within the region of quadrupolar flows in Figure 6(a). The measured velocities are very close to the previous results with 500 nm particles (Figure 4). This confirms that the larger particles can be used as fluid flow tracers. In summary, the maps depend on particle size, but the 500 nm tracers can be used to trace and measure the flows over a wider range of velocities.

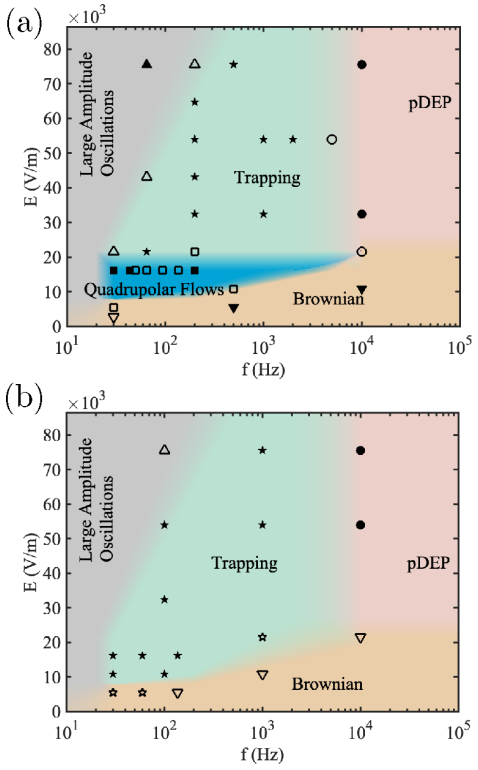

Figure 6. Behavior of 1 μm particles suspended in 1.7 mS/m KCl. (a) 50 μm tall channel and (b) 10 μm tall channel. (■) Quadrupolar flows, (★) trapping, (●) DEP, (▲) large amplitude oscillations, (▼) Brownian motion. Filled symbols indicate a single behavior dominated; open symbols indicate a mixture of behaviors.

■ THEORETICAL ANALYSIS OF THE QUADRUPOLAR FLOWS

Electroosmosis refers to the fluid motion induced by an electric field acting on the diffuse electrical layer of electrolytes close to the surface of a charged solid.[24,25] This motion is commonly described via an effective slip velocity tangential to the solid wall, $\mathbf{u}_{slip}$, given by the Helmholtz−Smoluchowski formula:[24]

$$\mathbf{u}_{slip} = -\frac{\varepsilon\zeta}{\eta}\mathbf{E} \quad (1)$$

where ε and η are, respectively, the electrolyte permittivity and viscosity. $\mathbf{E}$ is the amplitude of the applied electric field, and ζ (zeta-potential) is commonly defined as the electrical potential at the slip plane with the bulk solution.[26]

https://doi.org/10.1021/acs.analchem.1c02849
Anal. Chem. 2021, 93, 14667−14674

Equation 1 predicts an oscillatory slip velocity with a zero time-average value for the case of AC electric fields. Therefore, electroosmosis cannot account for our recent observations of a nonzero time-average electroosmostic velocity around dielectric microposts[12] and corners[27] in the presence of an AC field. In a recent paper,[13] we showed that these flows can be explained by a model that considers the polarization of a modified electrolyte concentration (i.e., concentration polarization) that occurs due to surface conductance on the charged surface.[25] Thus, we refer to this phenomenon as concentration−polarization electroosmosis (CPEO). In this section we compare the predictions of this theory with the experimental data presented in the previous section.

Our theoretical analysis[13] follows the works of Schnitzer and Yariv[28,29] that considered the electrophoresis of charged particles immersed in a symmetrical electrolyte. We extended the analysis to the case of AC signals and performed a linear expansion of the governing equations for a small Dukhin number (Du), the ratio of surface to bulk conductance.[25] In this approximation, the electrical potential can be written as $\phi = \phi_0 + \delta\phi$, where ϕ_0 is the potential within the electrolyte for Du = 0, and $\delta\phi$ is the perturbation as a consequence of surface conductance. In the present case, the electrolyte is subject to an AC field with magnitude E_0 and angular frequency ω. Thus, ϕ_0 in the electrolyte can be written as $\phi_0(t) = \mathcal{R}e[\tilde{\phi}_0 \exp(i\omega t)]$, where $\tilde{\phi}_0$ is the potential phasor and $\mathcal{R}e[\cdots]$ indicates the real part of the argument between the brackets. The phasor ϕ_0 is found by solving Laplace's equation with boundary conditions of zero normal derivative on the channel walls (see Figure 7).

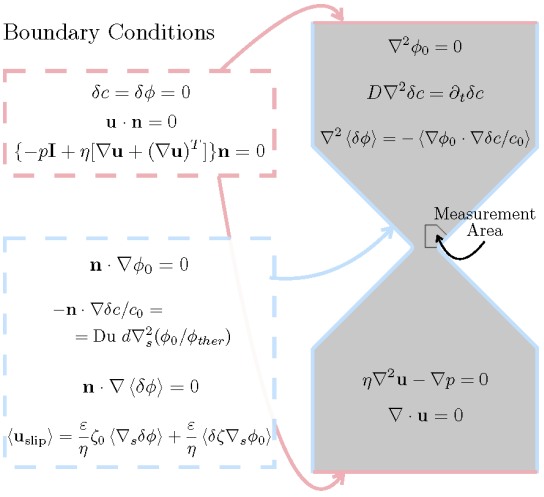

Figure 7. Summary of equations and boundary conditions for the electric potential, electrolyte concentration, and fluid velocity.

The electrolyte concentration is also written as $c = c_0 + \delta c$, where c_0 is the bulk concentration and δc is the perturbation due to the applied field. Neglecting advection, c satisfies the diffusion equation which implies that the phasor $\delta\tilde{c}$ is a solution of $D\nabla^2\delta\tilde{c} = i\omega\delta\tilde{c}$, where D is the diffusion coefficient of the ions in the electrolyte. We calculate $\delta\tilde{c}$ in the domain of Figure 7 with the following boundary condition on the walls:

$$-\mathbf{n}\cdot\nabla\delta c/c_0 = \mathrm{Du}\, d\nabla_s^2(\phi_0/\phi_{\mathrm{ther}}) \tag{2}$$

where $\mathbf{n}$ is a unit vector normal to the wall and d is the characteristic length scale of the problem (constriction width in our case). ∇_s^2 is the Laplacian operator tangential to the wall surface. $\phi_{\mathrm{ther}} = k_B T/e \approx 25$ mV and used as the scale for electric potential. The Dukhin number, Du, is the ratio of surface to bulk conductance (Du = $K_s/\sigma d$, with K_s the surface conductance and σ the electrolyte conductivity). Equation 2 was derived[29] for the case of thin diffuse layers. It assumes that the surface current is only due to counterions (co-ions are expelled from the diffuse layer), and it describes the balance of this current with the flux of ions coming from the bulk electrolyte (see also our previous paper[13]).

Changes in local concentration δc near the walls result in variations of the zeta-potential $\delta\zeta$. Using the Gouy−Chapman relation,[24] $\delta\zeta/\phi_{\mathrm{ther}} = -\delta c \tanh(\zeta_0/2\phi_{\mathrm{ther}})/c_0$. For the case of an AC voltage, $\delta\zeta$ is also an oscillating function with the same angular frequency ω. From eq 1 it is found that this oscillating zeta-potential gives rise to a net time averaged electroosmotic velocity given by

$$\langle\mathbf{u}_{\mathrm{slip}}\rangle_A = (\varepsilon/2\eta)\mathcal{R}e[\delta\tilde{\zeta}\nabla_s\tilde{\phi}_0^*] \tag{3}$$

where * indicates complex conjugate.

As shown in our previous work,[13] gradients in electrolyte concentration lead to a rectified (nonzero time-average) electric field. This can be seen from the equation of current conservation for a symmetrical electrolyte that yields the following equation for the time-averaged component of the perturbation of the electrical potential:

$$\nabla^2\langle\delta\phi\rangle = -(1/2)\mathcal{R}e[\nabla\tilde{\phi}_0\cdot\nabla\delta\tilde{c}^*/c_0] \tag{4}$$

This rectified electric field acts on the charges in the intrinsic diffuse layer of the channel walls and generates a nonzero time average electroosmotic velocity given by

$$\langle\mathbf{u}_{\mathrm{slip}}\rangle_B = (\varepsilon/\eta)\zeta_0\nabla_s\langle\delta\phi\rangle \tag{5}$$

From the solutions of $\delta\phi$ and δc, eqs 3 and 5 are evaluated on the channel walls and used as boundary conditions to determine the time-averaged fluid velocity ($\mathbf{u}$) within the channel, which satisfies the Stokes equation:

$$\eta\nabla^2\mathbf{u} - \nabla p = 0 \tag{6}$$

$$\nabla\cdot\mathbf{u} = 0 \tag{7}$$

NUMERICAL RESULTS AND COMPARISON WITH EXPERIMENTS

The finite element software Comsol Multiphysics was used to solve the above equations in the domain of Figure 7. Geometrical dimensions are scaled with constriction width d, and angular frequencies are scaled with the reciprocal of the diffusion time associated with d, d^2/D (frequencies are scaled with $D/2\pi d^2$). The electric potential is scaled with ϕ_{ther}, and the scale for fluid velocities results in $u_0 = \varepsilon d E_0^2/2\eta$. Figure 3(b) shows the solution of the fluid velocity field near the constriction for $f = 65$ Hz. The figure shows one of the four flow vortices generated by the slip velocity on the channel wall. The arrow field indicates the velocity direction, which gives rise to a circulating flow vortex as observed experimentally. The surface plot shows the velocity magnitude, which reaches a maximum near the tip of the constriction. To compare with experiments, the mean velocity magnitude was calculated within the boundary indicated in Figure 7, i.e., the area where the experimental velocity magnitude was measured. Figure 8(a) shows numerical results for the mean velocity magnitude

https://doi.org/10.1021/acs.analchem.1c02849
Anal. Chem. 2021, 93, 14667−14674

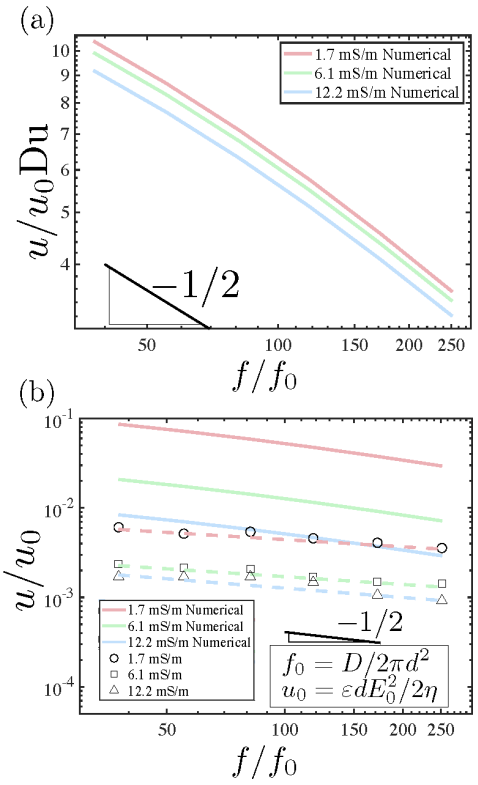

Figure 8. (a) Results of simulations for the measured zeta-potential of PDMS without surface treatment. (b) Comparison between experimental and simulation data. Du is determined as Du = $K_s/\sigma d$, with a typical surface conductance of K_s = 1 nS. The results of the simulations have been reduced to account for the effect of Pluronic on electroosmotic mobility.

scaled with u_0Du as a function of frequency determined for three values of the zeta-potential of PDMS: −89.0 ± 1.2 mV for 1.7 mS/m, −83.2 mV for 6.1 mS/m, and −74.3 mV for 12.2 mS/m. These zeta-potential values were determined experimentally for a PDMS channel using the current-monitoring method, first reported by Huang et al.[30] The velocity approximately decays with the square root of the frequency, as expected.

Figure 8(b) also shows experimental measurements of the velocity from Figure 4 scaled with u_0Du. For each conductivity, Du is estimated from Du = $K_s/\sigma d$ with K_s = 1 nS, a widely used value for the surface conductance and a value that was used in our previous work on insulating PDMS posts.[13] According to Viefhues et al.,[31] the addition of Pluronic reduces the electroosmotic velocity. We have used the current-monitoring method for measuring electroosmotic mobility of PDMS surfaces primed with Pluronic and we have observed a mobility reduction factor around 4. Specifically, the theoretical values in Figure 8(b) correspond to the data in Figure 8(a) divided by the following factors: 3.5 for 1.7 mS/m, 3.9 for 6.1 mS/m, and 4.5 for 12.2 mS/m, to take into account the reduction of surface mobility. In general, the theoretical results systematically overpredict the measured velocities by a factor ranging between 2 and 10. Three possible explanations for this discrepancy include the following: (1) The actual value for K_s is smaller than assumed; a least-square fit to the data gave a value of K_s = 0.16 nS. The Bikerman equation[25] for the surface conductance in the diffuse layer predicts a value of K_s = 0.29 nS for our experimental parameters, closer to the result of our fitting. However, this result does not necessarily reflect that the Bikerman model for a bare surface describes our experimental situation, which corresponds to a surface treated with Pluronic. (2) A linear model for CPEO flows was used, which is valid as long as the amplitude of the electric field remains small, $E_0 d \lesssim k_B T/e$. This assumption might not be satisfied within the constriction, where the electric field is high. (3) The model is valid for a small Du, which means that surface conduction is much smaller than in the bulk. This might not be the case at the tips of the constrictions.

Analysis of the Influence of Electrothermal Flows and Induced-Charge Electroosmosis. Electrical currents produce Joule heating within electrolytes, and this can lead to gradients in temperature that create nonhomogeneous regions of conductivity and permittivity in the liquid. The electric field acting on these conductivity and permittivity gradients gives rise to a bulk fluid motion known as electrothermal flow.[16,32] Electrothermal flows in iDEP constrictions were first reported using high conductivity phosphate buffer solutions.[33] Wang et al.[17] reported electrothermal flow in constrictions using 10 mM KCl and AC fields with a frequency of 1 kHz. Also, electrothermal flows were used to enrich submicron particles suspended in PBS.[34] However, electrothermal flows do not play a role in our experiments because the electrolyte conductivity is not high enough for Joule heating to produce significant changes in temperature. In addition, the effect of electrothermal flows is found for frequencies of the order of the reciprocal of the charge relaxation time of the electrolyte (around hundreds of kHz), while the flows studied here vanish for frequencies much larger than $D/(2\pi d^2)$ (around 1 Hz for our experimental conditions).

Recent works have discussed the appearance of induced-charge electroosmosis (ICEO[35]) within microfluidic constrictions[17] and corners.[27] ICEO flows typically occur on metal surfaces in contact with electrolytes subjected to DC or AC electric fields, and its origin is the interaction of the field with the electrical charges induced at the metal−electrolyte interface. The most important difference between the mechanisms for ICEO and CPEO flows is that, in the latter case, the surface charge is not modified by the applied electric field. ICEO theory for insulating objects[36,37] predicts a slip velocity that decays around frequencies of the order of the reciprocal of the charge relaxation time of the electrolyte ($\sigma/2\pi\varepsilon$, ≈0.3−3 MHz for our experimental parameters). This frequency is orders of magnitude higher than the typical frequency in our experiments (below 10 kHz). Additionally, it can be shown that ICEO velocities on insulating walls are negligibly small compared to CPEO.[13]

CONCLUSIONS

We have experimentally demonstrated the presence of quadrupolar fluid flows induced by AC electric fields around constrictions in microfluidic channels for low conductivity electrolytes. The flow pattern and magnitude was determined using fluorescent tracer beads (500 nm diameter). The flow patterns are visible for frequencies above 10 Hz because particle electrophoresis dominates for lower frequencies. The magnitude of the fluid velocity decreases with the conductivity of the electrolyte and approximately scales with the reciprocal of the square root of the frequency of the AC field. Also, the fluid velocity vanishes for frequencies much higher than the reciprocal of the electrolyte concentration diffusion time ($D/$

https://doi.org/10.1021/acs.analchem.1c02849
Anal. Chem. 2021, 93, 14667−14674

d^2, with D the diffusion coefficient of the electrolyte and d a typical length, for example, the constriction width). Particle dielectrophoresis occurs for frequencies higher than the latter. Significantly, the height of the channel has a major influence on the particle behavior and fluid patterns. Specifically, for shallow channels (10 μm high), trapping of the particles occurs on both sides of the constrictions. Further work is needed to clarify the mechanism responsible for this trapping. In comparison with the tall channels, the weakening of the CPEO flows may be due to the proximity of the top and bottom walls. Surface conduction leads to concentration polarization and a rectified electric field that probably persist in these shallow channels. Therefore, these phenomena should be taken into account in the theoretical explanation of the trapping, which is clearly different from classical DEP. Previous work on iDEP devices describes particle behavior as a competition between DEP forces, that scale with the square of the electric field, and the particle motion arising by the combined effect of electrophoresis and liquid electroosmosis, that scale linearly with the electric field. However, large discrepancies between theory and experimental data have been reported.[38] Given the strength and structure of these quadrupolar flows, they must be considered as an additional mechanism affecting the force balance on particles, especially at low frequencies and conductivities. For example, trapping by pDEP will be distorted by these flows (as observed for the 500 nm particle which are only trapped when the flows vanish). Also, particles experiencing nDEP could be subjected to an apparent larger DEP force because flow recirculation at the constriction moves the particles away from it. Future work should focus on the influence of these flows and trapping regime to improve the understanding and application of iDEP and other techniques such as DLD.

The experimental trends for the fluid flows are in agreement with the rectified electroosmosis that arises from the concentration−polarization due to surface conductance on the channel walls,[13] a mechanism that we named concentration−polarization electroosmosis (CPEO). We compared the experimental data with the predictions of an electrokinetic model based on the approximations of a small Du number and amplitude of electric fields. The results of the model qualitatively agree with observed trends, although the velocities are systematically overestimated if a typical value of 1 nS is assumed for the surface conductance. The assumptions of a small Du and E_0 might not be correct for this system, and more theoretical and experimental characterization is required along with an accurate determination of the surface conductance of these surfaces.

AUTHOR INFORMATION

Corresponding Author

Pablo García-Sánchez − *Departamento de Electrónica y Electromagnetismo, Facultad de Física, Universidad de Sevilla, 41012 Sevilla, Spain;* orcid.org/0000-0003-3538-2590; Email: pablogarcia@us.es

Authors

Raúl Fernández-Mateo − *School of Electronics and Computer Science, University of Southampton, Southampton SO17 1BJ, United Kingdom*

Víctor Calero − *Departamento de Electrónica y Electromagnetismo, Facultad de Física, Universidad de Sevilla, 41012 Sevilla, Spain*

Hywel Morgan − *School of Electronics and Computer Science, University of Southampton, Southampton SO17 1BJ, United Kingdom;* orcid.org/0000-0003-4850-5676

Antonio Ramos − *Departamento de Electrónica y Electromagnetismo, Facultad de Física, Universidad de Sevilla, 41012 Sevilla, Spain;* orcid.org/0000-0002-2190-1188

Complete contact information is available at: https://pubs.acs.org/10.1021/acs.analchem.1c02849

Notes

The authors declare no competing financial interest.

ACKNOWLEDGMENTS

P.G.S. and A.R. acknowledge financial support by ERDF and Spanish Research Agency MCI under contract PGC2018-099217-B-I00. We also thank Katie Chamberlain for making the PDMS masters.

REFERENCES

(1) Morgan, H.; Green, N. G. *AC Electrokinetics: Colloids and nanoparticles*; Research Studies Press Ltd., 2003.
(2) Stone, H.; Stroock, A.; Ajdari, A. *Annu. Rev. Fluid Mech.* **2004**, *36*, 381−411.
(3) Lapizco-Encinas, B. H. *Electrophoresis* **2019**, *40*, 358−375.
(4) Chou, C.-F.; Tegenfeldt, J. O.; Bakajin, O.; Chan, S. S.; Cox, E. C.; Darnton, N.; Duke, T.; Austin, R. H. *Biophys. J.* **2002**, *83*, 2170−2179.
(5) Cummings, E. B.; Singh, A. K. *Anal. Chem.* **2003**, *75*, 4724−4731.
(6) Liao, K.-T.; Chou, C.-F. *J. Am. Chem. Soc.* **2012**, *134*, 8742−8745.
(7) Lapizco-Encinas, B. H.; Simmons, B. A.; Cummings, E. B.; Fintschenko, Y. *Electrophoresis* **2004**, *25*, 1695−1704.
(8) Lapizco-Encinas, B. H.; Ozuna-Chacón, S.; Rito-Palomares, M. *J. Chrom. A* **2008**, *1206*, 45−51.
(9) Pysher, M. D.; Hayes, M. A. *Anal. Chem.* **2007**, *79*, 4552−4557.
(10) Jones, T. B. *Electromechanics of Particles*; Cambridge University Press, 1995.
(11) Pohl, H. A. *Dielectrophoresis*; Cambridge University Press, 1978.
(12) Calero, V.; Garcia-Sanchez, P.; Ramos, A.; Morgan, H. *J. Chrom. A* **2020**, *1623*, 461151.
(13) Calero, V.; Fernández-Mateo, R.; Morgan, H.; García-Sánchez, P.; Ramos, A. *Phys. Rev. Appl.* **2021**, *15*, 014047.
(14) Fernández-Mateo, R.; García-Sánchez, P.; Calero, V.; Morgan, H.; Ramos, A. Stationary electro-osmotic ow driven by ac fields around charged dielectric spheres. *J. Fluid Mech.* **2021**, *924*, 650
(15) Su, Y.-H.; Tsegaye, M.; Varhue, W.; Liao, K.-T.; Abebe, L. S.; Smith, J. A.; Guerrant, R. L.; Swami, N. S. *Analyst* **2014**, *139*, 66−73.
(16) Green, N. G.; Ramos, A.; González, A.; Castellanos, A.; Morgan, H. *J. Electrost.* **2001**, *53*, 71−87.
(17) Wang, Q.; Dingari, N. N.; Buie, C. R. *Electrophoresis* **2017**, *38*, 2576−2586.
(18) Beech, J. P.; Jönsson, P.; Tegenfeldt, J. O. *Lab Chip* **2009**, *9*, 2698−2706.
(19) Ho, B. D.; Beech, J. P.; Tegenfeldt, J. O. *Micromachines* **2020**, *11*, 1014.
(20) Calero, V.; Garcia-Sanchez, P.; Honrado, C.; Ramos, A.; Morgan, H. *Lab Chip* **2019**, *19*, 1386−1396.
(21) Calero, V.; Garcia-Sanchez, P.; Ramos, A.; Morgan, H. *Biomicrofluidics* **2019**, *13*, 054110.
(22) Thielicke, W.; Stamhuis, E. J. PIVlab Towards User-friendly, Affordable and Accurate Digital Particle Image Velocimetry in MATLAB. *J. Open Research Soft.* **2014**, *2* (1), e30
(23) Ermolina, I.; Morgan, H. *J. Colloid Interface Sci.* **2005**, *285*, 419−428.

(24) Hunter, R. *Introduction to Modern Colloid Science*; Oxford University Press, 1993.
(25) Lyklema, J. *Fundamentals of Interface and Colloid Science*; Academic Press Limited, 1995.
(26) Delgado, A. V.; Gonzalez-Caballero, F.; Hunter, R.; Koopal, L.; Lyklema, J. *Pure Appl. Chem.* **2005**, *77*, 1753−1802.
(27) Zehavi, M.; Boymelgreen, A.; Yossifon, G. *Phys. Rev. Appl.* **2016**, *5*, 044013.
(28) Schnitzer, O.; Yariv, E. *Phys. Rev. E* **2012**, *86*, 021503.
(29) Schnitzer, O.; Yariv, E. *Phys. Fluids* **2014**, *26*, 122002.
(30) Huang, X.; Gordon, M. J.; Zare, R. N. *Anal. Chem.* **1988**, *60*, 1837−1838.
(31) Viefhues, M.; Manchanda, S.; Chao, T.-C.; Anselmetti, D.; Regtmeier, J.; Ros, A. *Anal. Bioanal. Chem.* **2011**, *401*, 2113.
(32) González, A.; Ramos, A.; Morgan, H.; Green, N. G.; Castellanos, A. *J. Fluid Mech.* **2006**, *564*, 415−433.
(33) Sridharan, S.; Zhu, J.; Hu, G.; Xuan, X. *Electrophoresis* **2011**, *32*, 2274−2281.
(34) Kale, A.; Song, L.; Lu, X.; Yu, L.; Hu, G.; Xuan, X. *Electrophoresis* **2018**, *39*, 887−896.
(35) Bazant, M. Z.; Squires, T. M. *Phys. Rev. Lett.* **2004**, *92*, 066101.
(36) Squires, T. M.; Bazant, M. Z. *J. Fluid Mech.* **1999**, *509*, 217−252.
(37) Zhao, C.; Yang, C. *Phys. Rev. E* **2009**, *80*, 046312.
(38) Hill, N.; Lapizco-Encinas, B. H. *Electrophoresis* **2019**, *40*, 2541−2552.

https://doi.org/10.1021/acs.analchem.1c02849
Anal. Chem. 2021, 93, 14667−14674

Paper F

Wall Repulsion of Charged Colloidal Particles during Electrophoresis in Microfluidic Channels

Summary of Results

This paper demonstrated that the quadrupolar fluid flow arising around particles subjected to low frequency electric fields induces a dominant repulsion form the walls of a microfluidic channel, regardless of the origin of the flows. Previously, the particle-wall repulsion was attributed to dipole-dipole interaction with a large mismatch between theory and experiments.

Contribution Statement

The idea of testing the influence of the flow vortices in the particle-wall repulsion using particles undergoing electrophoresis in a microfluidic channel was envisioned by Garcia-Sanchez and Calero before the results of Paper D. Then, Ramos and I related these experiments to the measurements of the fluid vortices around the particles after the successful measurements achieved in Paper D. For this paper, Calero and I did the experimental work; Ramos, Garcia-Sanchez and I developed the theory; I analysed the experimental data and compared it to the theoretical predictions; Garcia-Sanchez, Ramos, Calero and I wrote the first version of the manuscript. Morgan, Ramos and Garcia-Sanchez provided supervisory support. All authors contributed to the final version of the manuscript.

Wall Repulsion of Charged Colloidal Particles during Electrophoresis in Microfluidic Channels

Raúl Fernández-Mateo,[1] Víctor Calero,[2] Hywel Morgan,[1] Pablo García-Sánchez,[2] and Antonio Ramos[2,*]
[1]School of Electronics and Computer Science, University of Southampton, Southampton SO17 1BJ, United Kingdom
[2]Departamento Electrónica y Electromagnetismo, Facultad de Física, Universidad de Sevilla, Avenida Reina Mercedes s/n, 41012 Sevilla, Spain

(Received 31 August 2021; revised 26 November 2021; accepted 18 January 2022; published 16 February 2022)

Electrophoresis describes the motion of charged particles suspended in electrolytes when subjected to an external electric field. Previous experiments have shown that particles undergoing electrophoresis are repelled from nearby channel walls, contrary to the standard description of electrophoresis that predicts no hydrodynamic repulsion. Dielectrophoretic (DEP) repulsive forces have been commonly invoked as the cause of this wall repulsion. We show that DEP forces can only account for this wall repulsion at high frequencies of applied electric field. In the presence of a low-frequency field, quadrupolar electro-osmotic flows are observed around the particles. We experimentally demonstrate that these hydrodynamic flows are the cause of the widely observed particle-wall interaction. This hydrodynamic wall repulsion should be considered in the design and application of electric-field-driven manipulation of particles in microfluidic devices.

DOI: 10.1103/PhysRevLett.128.074501

Electrophoresis is the motion of colloidal particles suspended in an aqueous electrolyte under the influence of spatially uniform electric fields [1]. The mechanism has been extensively exploited for analysis and separation of colloids and macromolecules such as DNA, RNA, and proteins [2,3]. Particles suspended in an electrolyte carry a net surface charge that is screened by a diffuse ionic layer on the electrolyte side of the interface. The action of an external electric field leads to a relative motion between the liquid and particle. The relation between the applied field $\mathbf{E}$ and the particle velocity $\mathbf{u}$ when the diffuse ionic layer is thin compared to the particle dimension was obtained by Smoluchowski [4]

$$\mathbf{u} = \frac{\varepsilon\zeta}{\eta}\mathbf{E}, \tag{1}$$

where ε and η are the electrolyte permittivity and viscosity, respectively, and ζ is the zeta potential of the particle-electrolyte interface. The latter is usually considered to be the electrical potential at the inner edge of the diffuse ionic layer surrounding the particle [1].

Combining electrokinetic forces with microfluidics has led to new methods for precise control of particles and liquids on the microscale [5,6]. In many of these electrically assisted microfluidic techniques, the interaction between the particles and the channel walls plays a significant role. In particular, multiple studies have shown that spherical particles undergoing electrophoresis are repelled from nearby dielectric walls [7,8]. However, the classical theory of electrophoresis does not predict such repulsion (nor attraction) from the walls [9,10]. According to theory, the velocity field around the particle scales linearly with the electric-field amplitude. A simple symmetry argument leads to the conclusion that the particle velocity perpendicular to the wall is zero. Assuming that for a given electric field the particle is repelled from the wall, then upon a change of direction of the field, the velocity field will change direction and attraction to the wall is predicted. This leads to a paradox since both situations are equivalent.

Wall repulsion in electrophoresis has been explained in terms of a dielectrophoretic (DEP) repulsion [11], a force that scales quadratically with the electric field, and thus the symmetry argument above does not apply. DEP repulsion can be described in terms of the image charges associated with the insulating walls.

In this Letter, we provide experimental evidence for wall-particle interaction in an ac electric field of different frequencies and demonstrate that DEP forces cannot account for the repulsion observed at low frequencies, which is much larger than predicted. We demonstrate that the main contribution to wall repulsion in electrophoresis arises from a stationary fluid flow around the particles.

We recently reported that ac electric fields induce stationary fluid flows around insulating charged cylinders [12,13] and spheres [14]. These flows are referred to as concentration polarization electro-osmosis (CPEO) since their origin is attributed to the perturbation of the slip velocity due to local variations in electrolyte concentrations arising from surface conduction. These CPEO flows are quadratic with the electric field and therefore have a nonzero time average, which is observed experimentally

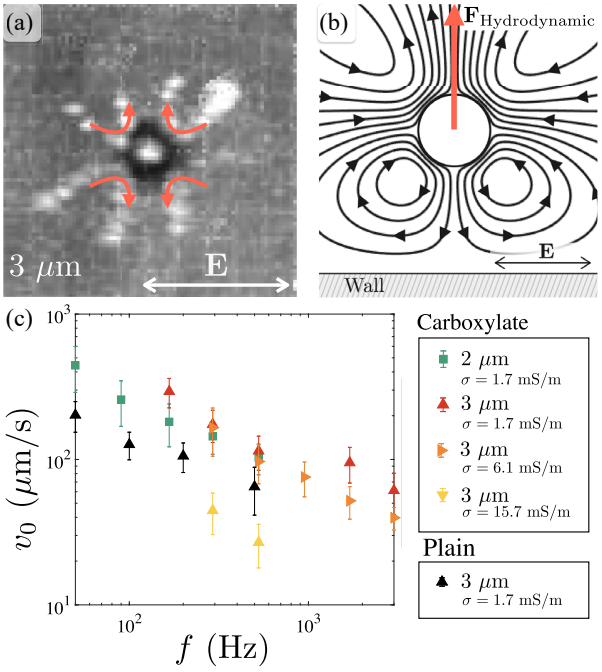

FIG. 1. (a) Experimental images of fluid flow around a single 3 μm diameter particle far from the wall. Flow was observed using 500 nm diameter tracer particles. The final image was created from a superposition of a stack of images and the arrows indicate the flow direction. The particle is suspended in KCl of $\sigma = 1.7$ mS/m and an ac field with a frequency of 200 Hz and amplitude of 80 kV/m. (b) Schematic diagram showing how this flow leads to particle-wall repulsion. (c) Experimental data of slip velocity (v_0) on the particles versus frequency for an applied field with a magnitude of 80 kV/m.

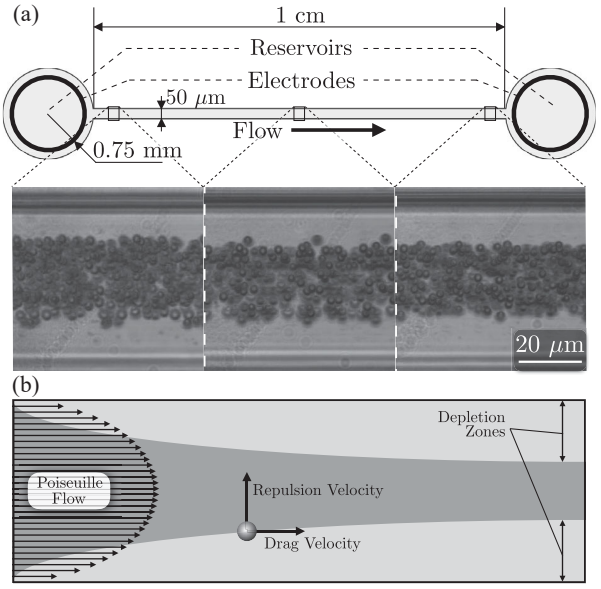

FIG. 2. (a) Schematic diagram of the experimental device (not to scale) and images of the observed particle-wall repulsion at three different positions along the channel (3 μm plain particles, ac field at a frequency of 90 Hz and amplitude 80 kV/m, KCl electrolyte conductivity 6.1 mS/m). The images are obtained by superimposing frames of single particles. (b) Sketch of the expected behavior of the particles subjected to both a Poiseuille flow and a hydrodynamic wall repulsion.

as a stationary flow. It therefore follows that particle repulsion from nearby walls must occur.

Figure 1(a) shows an example of the observed stationary flow around a 3 μm diameter microsphere suspended in KCl (1.7 mS/m) in the presence of an ac electric field with a frequency of 200 Hz and amplitude of 80 kV/m. The fluid patterns were observed using 500 nm diameter fluorescent beads that act as flow tracers. Taking the direction of the electric field as the polar axis, the liquid flows toward the particle at both poles and away from the particle at the equator. Figure 1(b) depicts how the liquid flow is driven from the particle toward the wall leading to a hydrodynamic repulsion. Figure 1(c) shows experimental data of the slip velocity on the particles versus frequency for an applied field with a magnitude of 80 kV/m (see Supplemental Material [15] for details).

The experimental devices were made from polydimethylsiloxane using standard soft lithography and bonded to a glass wafer. They consisted of a 1 cm long channel with a 50×50 μm square cross section, see Fig. 2(a). Voltages were applied along the channel using two metal needles inserted into the reservoirs at each end. Electric fields were generated with an amplitude of 80 kV/m and frequencies ranging from 50 Hz to 10 kHz. The wall repulsion was measured for fluorescent carboxylate particles of 1–3 μm diameter, along with 3 μm diameter plain polystyrene particles; these have a lower surface charge than the carboxylate particles. All particles were suspended in KCl solutions at conductivities of 1.7, 6.1, and 15.7 mS/m. Before the experiments, the channels were pretreated with a nonionic surfactant (Pluronic F-127) to avoid nonspecific particle adhesion to the channel walls. A side effect of this treatment is that electro-osmosis on the channel walls is very much reduced [16,17].

To begin with, particle-wall separation was investigated following the application of an ac electric field along the microchannel together with a pressure-driven flow with a maximum velocity of approximately 1.56 mm/s. The particle concentration was kept low so that particles flowed through the channel one by one, eliminating particle-particle interaction. When no electric field was applied, the particles were randomly distributed across the channel.

Figure 2(a) shows the repulsion from the wall at three different locations along the channel: immediately after the channel inlet, the center, and end of the channel. The images were obtained from the superimposition of more than 600 frames of single particles in the pressure-driven flow. The applied field frequency was 90 Hz and the electrolyte conductivity was 6.1 mS/m. Particles enter the channel randomly distributed and the effect of the

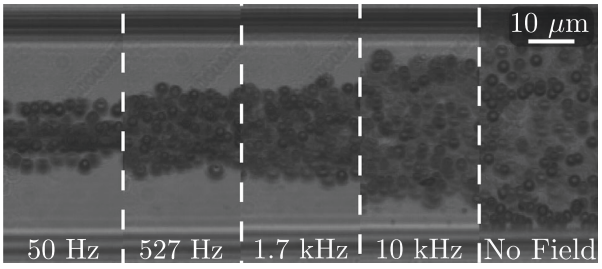

FIG. 3. Superimposed images at the end of the channel of 3 μm carboxylate particles suspended in 1.7 mS/m KCl solution for different frequencies. The electric-field amplitude is 80 kV/m.

particle-wall repulsion leads to a particle-free region near the walls, as schematically shown in Fig. 2(b). The width of the depleted region grows with distance downstream but at a decreasing rate, indicating that the repulsion decays with distance from the wall.

The particle-wall repulsion dataset is summarized in Fig. 3. This shows the extent of the depletion region at the end of the microchannel as a function of electric-field frequency. The wall repulsion is most significant at low frequencies. To determine this separation, a custom software was used to plot a histogram of the transverse coordinates of each particle, i.e., the coordinate perpendicular to the channel wall z_i, $i \in (1, \ldots, N)$ where N is the total number of particles counted. The mean particle-wall separation was determined as half the difference between the channel width and the width of the distribution of z_i (this width Δz is defined as the range that contains 95% of all particle positions). Further details are provided in the Supplemental Material [15].

Figure 4 shows the particle-wall separation at the end of the channel as a function of electric-field frequency. In all cases, wall separation decays with frequency. Figure 4(a) shows that this separation increases with particle size. It also shows that the separation for two particles with equal diameters is larger for the most charged, i.e., carboxylate spheres experience the greatest repulsion. Figure 4(b) shows that, for a given particle size, the separation decreases with electrolyte conductivity. The dashed lines in these figures indicate the calculated maximum particle-wall separation predicted by DEP repulsion according to Eq. (7). The experimental data clearly show that the calculated DEP force significantly underestimates the separation. However, for experimental conditions where CPEO flows vanish, a very good agreement with prediction due to DEP repulsion is found [see data at high frequencies in Fig. 4(b) for the highest conductivity and in Fig. 4(a) for plain particles].

As mentioned previously, we recently reported the presence of stationary CPEO flows around charged dielectric microspheres in the presence of an ac electric field [14]. The general trends observed for particle-wall separation in these experiments reported in Fig. 4 mirror the characteristics of CPEO flows, which also decrease with

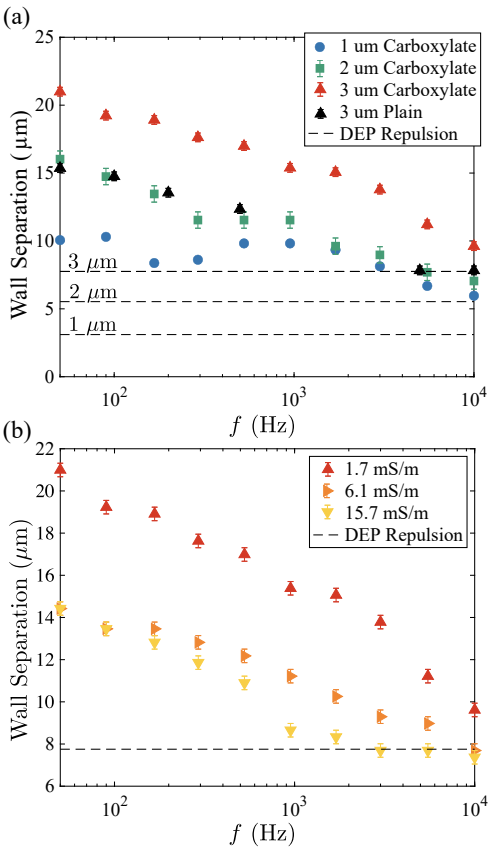

FIG. 4. Wall separation measured at the end of the channel for (a) different particles in an electrolyte of 1.7 mS/m conductivity and (b) different electrolyte conductivities for the 3 μm carboxylate beads. The wall separation represents the size of the depletion zones in Fig. 3. Dashed lines represent the maximum separation predicted by dielectrophoresis, Eq. (7) with $\alpha = -0.5$.

electrolyte conductivity and frequency [13,14]. In addition, a reduced concentration polarization and associated CPEO flow is expected for plain spheres, since particles with lower surface charge have a lower surface conductance. We propose that CPEO flows around individual particles are responsible for the observed particle-wall separation. To validate this hypothesis, a second set of experiments was conducted to quantify the strength of the quadrupolar flow velocity shown in Fig. 1(a). Fluorescent colloids (500 nm) were used as tracers to observe the flow around particles far from the channel walls and in the absence of pressure-driven flow. Flow tracing was performed for three different populations of particles (2 μm carboxylate, 3 μm plain, and 3 μm carboxylate) suspended in the same 1.7 mS/m conductivity electrolyte, and also for the 3 μm carboxylate in three different electrolyte conductivities (1.7, 6.1, and 15.7 mS/m KCl). Fluid flow was measured using computer-assisted particle image velocimetry.

Theoretically, an axisymmetric flow is expected with the axis defined by the electric-field direction, as in the flow pattern first predicted by Gamayunov *et al.* [18],

$$\mathbf{v} = v_0\left(\frac{[1-(r/a)^2](1+3\cos 2\theta)}{2(r/a)^4}\hat{r} + \frac{\sin 2\theta}{(r/a)^4}\hat{\theta}\right), \quad (2)$$

where r and θ are, respectively, the radial distance and polar angle, a is the sphere radius, and v_0 is the maximum time-averaged slip velocity at the particle surface. Thus, v_0 can be obtained as a single parameter from a least-squares fit of Eq. (2) to the experimental velocity fields. As expected, v_0 decreases with electrolyte conductivity and frequency of electric field, see Fig. 1(c).

The distortion of this flow pattern by the presence of a wall can be calculated by the method of reflections [19]. In this case, the reflected flow leads to a net particle motion perpendicular to the wall. If the particle is far from the wall, this velocity is given by

$$\mathbf{u} = v_0\frac{3a^2}{8h^2}\hat{z}, \quad (3)$$

where h is the distance of the particle center to the wall. This expression was obtained by Yariv [20] in the context of induced charge electro-osmotic flows around conducting spheres [21]. Equation (3) is the leading-order term in the method of reflections for small values of a/h. Equation (3) can also be found from the image system of the fundamental singularities of Stokes' equations [22]. The expression by Gamayunov *et al.* (2) reduces to a stresslet [23] with velocity field $\mathbf{v} = -v_0(1+3\cos 2\theta)/[2(r/a)^2]\hat{r}$ for $a/r \ll 1$. In the Supplemental Material [15], the velocity field of this stresslet is calculated in the vicinity of a nonslip wall, and the velocity that is induced on the particle is given by Eq. (3).

An analytical expression for the particle-wall distance was obtained as follows. The fluid velocity in the middle horizontal plane of the channel (where the particles are imaged) is approximated by a parabolic profile,

$$\mathbf{v} = 4\mathcal{V}\left[\frac{z}{W} - \left(\frac{z}{W}\right)^2\right]\hat{x}, \quad (4)$$

where $\mathcal{V}$ is the maximum fluid velocity and W is the width of the channel. If the particle velocity perpendicular to the wall u_z is given by (3) and the longitudinal velocity u_x by (4), $dz/dx = u_z/u_x$ can be integrated to obtain the following expression that links the particle-wall separation h with the time-averaged slip velocity at the particle surface v_0 after covering a distance L along the channel:

$$\frac{v_0 a^2 L}{\mathcal{V}W^3} = \frac{8}{15}\left[5\left(\frac{h}{W}\right)^4 - 4\left(\frac{h}{W}\right)^5\right]. \quad (5)$$

Use of Eq. (5) assumes that the remote-wall approximation that leads to Eq. (3) is valid; i.e., higher-order terms are neglected. To confirm this assumption, we have numerically calculated the velocity component perpendicular to the wall of a sphere, with a slip velocity given by $\mathbf{v}_s = v_0 \sin 2\theta\hat{\theta}$. By integrating this velocity, the particle-wall separation is found, and comparison with the prediction of (5) shows a negligible difference for $h \gg a$ (see Supplemental Material [15]).

The wall repulsion due to DEP forces was calculated using the method of images for an insulating wall. The repulsion velocity due to this mechanism far from the wall is

$$u_{\mathrm{DEP}} = \frac{\varepsilon a^5(\alpha E_0)^2}{16\eta h^4}, \quad (6)$$

where α is the real part of the nondimensional polarizability, which for a sphere ranges between -0.5 and 1 [24]. The wall separation due to DEP repulsion satisfies

$$\frac{\varepsilon a^5 L(\alpha E_0)^2}{\mathcal{V}W^5\eta} = \frac{32}{21}\left[7\left(\frac{h}{W}\right)^6 - 6\left(\frac{h}{W}\right)^7\right]. \quad (7)$$

For comparison with the experimental wall separation, a nondimensional polarizability $\alpha = -0.5$ was used, which corresponds to the maximum polarizability in absolute value for a particle that is less polarizable than the medium. Note that the repulsion velocity generated by DEP forces decays as $(a/h)^4$, while the repulsion generated by the CPEO flow decays as $(a/h)^2$. Thus, DEP repulsion is a much shorter range effect.

Figure 5 shows the wall separation (data in Fig. 4) for a given particle versus its slip velocity v_0 [data in Fig. 1(c)] measured under the same experimental conditions (i.e., electrolyte conductivity, amplitude, and frequency of electric field). Wall separations and v_0 are, respectively, scaled with channel width W and $a^2L/\mathcal{V}W^3$. The figure shows how the

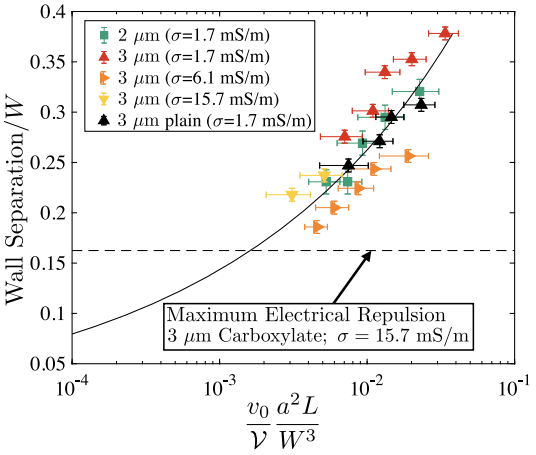

FIG. 5. Nondimensional wall separation versus nondimensional slip velocity. The figure shows experimental values of wall separation versus experimental values of slip velocity. They follow the trend predicted by Eq. (5). The dashed horizontal line represents the maximum electrical repulsion calculated from Eq. (7).

experimental data collapse onto a single (solid) line, which corresponds to the prediction given by Eq. (5). This result means that, irrespective of liquid conductivity, ac electric field, zeta potential, or particle diameter, the separation is only determined by the product of $v_0 a^2$, i.e., the intensity of the stresslet. The dashed line depicts the separation for the case of maximum DEP repulsion as calculated from Eq. (7).

Liang *et al.* [7] reported lateral migration of particles in a rectangular channel with electrophoresis and attributed this to DEP wall repulsion. However, their experimental data show separation that was systematically greater than that predicted by dielectrophoresis. Kazoe and Yoda [25] also reported wall separation induced by dc electric fields for submicron particles (100–900 nm diameter) and concluded that the particle-wall force was around 40 times larger than DEP force. Experiments with dc electrophoresis show that wall repulsion decreases with electrolyte conductivity [8], and the importance of zeta potential and surface conductance has been emphasized [8,26,27] in agreement with our findings. It is also important to note that inertial lift in shear flows is affected by electrophoresis, as demonstrated by Lochab and Prakash [28]. However, the Reynolds number in our experiments is around 0.05 so that inertial effects can be safely neglected.

In conclusion, experimental data demonstrate that wall repulsion in ac electrophoresis is due to the presence of a stationary fluid flow around microparticles that is induced by an applied electric field. The origin of these flows is attributed to the perturbation of the electro-osmotic slip velocity due to concentration polarization arising from surface conductance. Consequently, and in contrast to the widely reported common hypothesis, our analysis demonstrates that DEP repulsion is not the main contribution to particle-wall repulsion for electrophoresis at low frequencies (below 10 kHz for our experimental conditions). This phenomenon will have consequences for the design of microfluidic technologies that use electric fields for particle manipulation and separation [27]. For example, particle manipulation by deterministic lateral displacement [29], insulating DEP [30], and colloidal assembly [31] all make use of low-frequency electric fields and the behavior will be unavoidably influenced by the CPEO flows.

The data that support this study are openly available in the University of Southampton repository at [32].

V. C., P. G. S., and A. R. acknowledge Grant PGC2018-099217-B-I00 funded by MCIN/AEI/10.13039/501100011033 and by "ERDF A way of making Europe."

*Corresponding author.
ramos@us.es

[1] R. Hunter, *Introduction to Modern Colloid Science* (Oxford University Press, New York, 1993).
[2] J.-L. Viovy, Rev. Mod. Phys. **72**, 813 (2000).
[3] P. H. O'Farrell, J. Biol. Chem. **250**, 4007 (1975).
[4] M. von Smoluchowski, Bull. Int. Acad. Sci. Cracovie **8**, 182 (1903).
[5] H. Morgan and N. G. Green, *AC Electrokinetics: Colloids and Nanoparticles* (Research Studies Press Ltd., Baldock, 2003).
[6] D. J. Harrison, K. Fluri, K. Seiler, Z. Fan, C. S. Effenhauser, and A. Manz, Science **261**, 895 (1993).
[7] L. Liang, Y. Ai, J. Zhu, S. Qian, and X. Xuan, J. Colloid Interface Sci. **347**, 142 (2010).
[8] Z. Liu, D. Li, Y. Song, X. Pan, D. Li, and X. Xuan, Phys. Fluids **29**, 102001 (2017).
[9] H. J. Keh and J. L. Anderson, J. Fluid Mech. **153**, 417 (1985).
[10] H. J. Keh and S. B. Chen, J. Fluid Mech. **194**, 377 (1988).
[11] E. Yariv, Soft Matter **12**, 6277 (2016).
[12] V. Calero, P. Garcia-Sanchez, A. Ramos, and H. Morgan, J. Chromatogr. A **1263**, 461151 (2020).
[13] V. Calero, R. Fernández-Mateo, H. Morgan, P. García-Sánchez, and A. Ramos, Phys. Rev. Applied **15**, 014047 (2021).
[14] R. Fernández-Mateo, P. García-Sánchez, V. Calero, H. Morgan, and A. Ramos, J. Fluid Mech. **924**, R2 (2021).
[15] See Supplemental Material at http://link.aps.org/supplemental/10.1103/PhysRevLett.128.074501 for analytical and numerical calculations of hydrodynamic wall repulsion, a description of the analysis of experimental data, and a comparison between experimental wall repulsion and CPEO predictions.
[16] M. Viefhues, S. Manchanda, T.-C. Chao, D. Anselmetti, J. Regtmeier, and A. Ros, Anal. Bioanal. Chem. **401**, 2113 (2011).
[17] R. Fernández-Mateo, P. García-Sánchez, V. Calero, A. Ramos, and H. Morgan, Electrophoresis (2021), 10.1002/elps.202100267.
[18] N. I. Gamayunov, V. A. Murtsovkin, and A. S. Dukhin, Colloid J. USSR **48**, 197 (1986).
[19] J. Happel and H. Brenner, *Low Reynolds Number Hydrodynamics: With Special Applications to Particulate Media* (Springer Science & Business Media, Dordrecht, 2012), Vol. 1.
[20] E. Yariv, Proc. R. Soc. A **465**, 709 (2009).
[21] Induced charge electro-osmotic flows are negligible for dielectric particles [12] and, therefore, the origin of the quadrupolar flows is attributed to CPEO.
[22] J. Blake and A. Chwang, J. Eng. Math. **8**, 23 (1974).
[23] G. Batchelor, J. Fluid Mech. **44**, 419 (1970).
[24] T. B. Jones, *Electromechanics of Particles* (Cambridge University Press, Cambridge, England, 1995).
[25] Y. Kazoe and M. Yoda, Langmuir **27**, 11481 (2011).
[26] Z. Liu, D. Li, M. Saffarian, T.-R. Tzeng, Y. Song, X. Pan, and X. Xuan, Electrophoresis **40**, 955 (2019).
[27] C. Thomas, X. Lu, A. Todd, Y. Raval, T.-R. Tzeng, Y. Song, J. Wang, D. Li, and X. Xuan, Electrophoresis **38**, 320 (2017).
[28] V. Lochab and S. Prakash, Soft Matter **17**, 611 (2021).
[29] V. Calero, P. Garcia-Sanchez, C. Honrado, A. Ramos, and H. Morgan, Lab Chip **19**, 1386 (2019).
[30] E. B. Cummings and A. K. Singh, Anal. Chem. **75**, 4724 (2003).
[31] M. Trau, D. A. Saville, and I. A. Aksay, Langmuir **13**, 6375 (1997).
[32] 10.5258/SOTON/D2120.

Paper G

Wall repulsion during electrophoresis: Testing the theory of concentration-polarization electro-osmosis

Summary of Results

We took the previous work a step further and demonstrated that CPEO was the origin of the observed particle- wall repulsion. Also, given the simplicity and reproducibility of the experiments, we were able to (i) test the limits of validity of the CPEO theory for the most intense fields and (ii) infer experimental CPEO slip velocities for a wide range of particle sizes and electric field parameters.

Contribution Statement

I observed that for lower-intensity fields, CPEO could predict the observed particle-wall separation in the experiments of Paper F. Consequently, Garcia-Sanchez and I decided to try voltage sweeps, instead of frequency sweeps, to test the range in which CPEO could correctly predict the separation. For this paper, I did the experimental work and the analysis of the experimental data, I and Garcia-Sanchez further developed the theory and wrote the first version of the manuscript. I made the comparison between the theoretical predictions and the experimental results. Morgan, Ramos and Garcia-Sanchez provided supervisory support. All authors contributed to the final version of the manuscript.

Physics of Fluids ARTICLE scitation.org/journal/phf

Wall repulsion during electrophoresis: Testing the theory of concentration-polarization electro-osmosis

Cite as: Phys. Fluids **35**, 012019 (2023); doi: 10.1063/5.0134307
Submitted: 9 November 2022 · Accepted: 8 January 2023 ·
Published Online: 30 January 2023

Raúl Fernández-Mateo,[1,a)] Hywel Morgan,[1] Antonio Ramos,[2] and Pablo García-Sánchez[2]

AFFILIATIONS

[1]School of Electronics and Computer Science, University of Southampton, Southampton SO17 1BJ, United Kingdom
[2]Depto. Electrónica y Electromagnetismo, Facultad de Física, Universidad de Sevilla, Avda. Reina Mercedes s/n, 41012 Sevilla, Spain

[a)]Author to whom correspondence should be addressed: r.fernandez-mateo@soton.ac.uk

ABSTRACT

We experimentally study the repulsion of charged microscopic particles with the channel walls during electrophoresis in microfluidic devices. For low frequencies of the electric fields (<10 kHz), this repulsion is mainly due to the hydrodynamic interaction caused by the flow vortices that arise from the slip velocity induced by the electric field on the particle surface, as shown in a recent publication [Fernandez-Mateo *et al.*, Phys. Rev. Lett. **128**, 074501 (2022)]. The maximum slip velocity on the particle surface is inferred from measurements of wall-particle separation. Importantly, this procedure allows us to infer very small slip velocities that, otherwise, are too weak to be measured directly. Data at small electric field amplitudes (E_0) agree with theoretical predictions using the model of Concentration Polarization Electro-osmosis (CPEO), which has recently been proposed as the mechanism behind the flow vortices on the surface of the particles. Data for higher electric fields show that the predictions of the CPEO theory for weak electric fields are not valid beyond $E_0 \sim 60$ kV/m. Additionally, we also show that, for sufficiently strong electric fields, the quadrupolar flow structures become disrupted, leading to a weaker wall repulsion.

I. INTRODUCTION

Electrophoresis is the motion of charged colloidal particles suspended in an aqueous electrolyte when subjected to a uniform electric field.[1] Particles are usually suspended in an aqueous electrolyte so that the surface charge is screened by a diffuse ionic layer, giving rise to an electrical double layer (EDL). The action of an external electric field **E** on the EDL leads to a relative motion between the liquid and the particle. When the diffuse ionic layer is thin compared to particle size, the velocity of the particles **u** is given by the Helmholtz–Smoluchowski formula,[2]

$$\mathbf{u} = \frac{\varepsilon\zeta}{\eta}\mathbf{E}, \tag{1}$$

where ε and η are the electrolyte permittivity and viscosity, respectively, and ζ is the zeta potential of the particle-electrolyte interface. The latter is generally considered to be the electrical potential at the inner edge of the diffuse ionic layer surrounding the particle.[1]

Practical applications of electrophoresis typically make use of capillaries and/or microchannels that contain the liquid and suspended particles. Several studies have shown that particles undergoing electrophoresis are repelled from the neighboring dielectric walls of the channel.[3,4] These early studies reported the lateral migration of particles in dc electric fields. However, a simple symmetry argument[5] leads to the conclusion that the effect cannot be due to classical electrophoresis, meaning that particle-wall repulsion is independent of the orientation of the field. Thus, the use of ac electric fields to examine the particle-wall interaction provides a simpler scenario to test experimental results against theoretical predictions given that it provides a decoupling from the two phenomena of particle electrophoresis and electro-osmosis.

Recently, we have shown that for the case of a low-frequency ac electric field (<10 kHz), repulsion is due to the hydrodynamic wall-particle interaction that arises from the fluid flow induced by the electric field around the particle.[5] This contrasts with previous publications that explain the origin of the particle-wall repulsion as the electrostatic interaction between the electrical dipole induced on the particle and its image dipole in the wall.[6] The measured particle-wall separation was in agreement with the observed quadrupolar flow structures around charged microspheres when suspended in low-

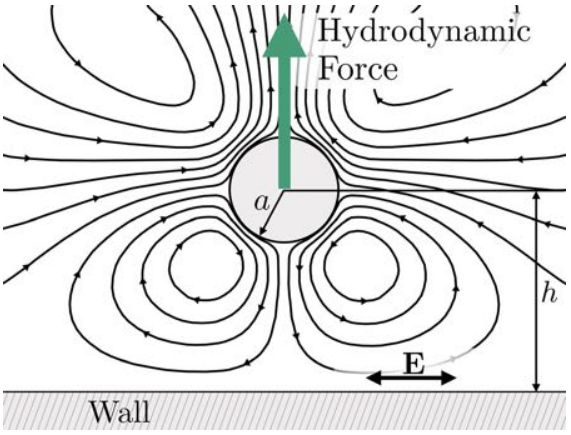

FIG. 1. Schematic representation of the streamlines for the stationary quadrupolar fluid flow around a spherical particle near a flat wall when an ac electric field is applied in the direction parallel to the wall. The resulting force appearing on the particle is marked by the green arrow.

conductivity electrolytes and could be satisfactorily explained by classical dipole-dipole repulsion in the case of higher frequencies and electrolyte conductivities.[5]

The quadrupolar flows shown in Fig. 1 are caused by Concentration-Polarization Electro-Osmosis (CPEO),[7] i.e., stationary electrosmotic flow arising from variations in the electrolyte concentration around dielectric particles that occurs because of surface conduction.[8] The results in Ref. 5 demonstrated a correlation between measurements of the velocity magnitude of the quadrupolar flows around the particles and measurements of the particle-wall separation, regardless of the physical origin of the flows. The goal of this paper is to compare experimental data of particle-wall separation with theoretical predictions from the CPEO theory.

The general theory for CPEO flows is only valid in the limit of weak electric fields.[9] In other words, the product of the electric field magnitude (E_0) and particle radius (a) must be of the order or smaller than the thermal voltage[10] ($E_0 a < k_B T/e \approx 25$ mV, where k_B is the Boltzmann's constant, T is the absolute temperature, and e is the proton charge). This criterion was not met in our previous experiments in Ref. 5, where we used particles with diameters between 1 and 3 μm subjected to ac fields with an amplitude of $E_0 = 80$ kV/m. In this paper, we present experimental data of wall-particle separation for a wide range of electric field amplitudes. Specifically, particle-wall repulsion data at small electric fields provide a quantitative comparison with the theoretical model, whilst data at higher electric fields define the limits of applicability of the current CPEO theory. In the range of electric field magnitudes where the effect of wall repulsion during electrophoresis is dominant, i.e., from ~10 to ~100 kV/m, particles between 1 and 3 μm provide a good range for $\beta = eE_0 a/(k_B T)$: from $\beta = 0.2$ (in the linear regime) up to $\beta > 6$, where deviations from CPEO are expected. In order to compare with the theory, the experimental data for particle-wall separation was used to extract the slip velocity on the surface of the particle, and these velocities were then compared to theoretical prediction. Remarkably, this procedure allows us to deduce very small slip velocities on particles that are otherwise, too small to be measured directly. We also show that for sufficiently strong electric fields, the quadrupolar flows become disrupted, leading to weaker wall repulsion.

II. EXPERIMENTAL DETAILS

Electrophoresis experiments were performed with microchannels 1 cm long and 50 × 50 μm square cross section—see Fig. 2. Channels were made from polydimethylsiloxane (PDMS) using standard soft-lithography and bonded to a glass wafer. They were pretreated with a nonionic surfactant (Pluronic F-127) to avoid nonspecific particle adhesion to the walls. A side effect of this treatment is that electro-osmosis on the channel walls is very much reduced.[11,12] The following particles were used: fluorescent carboxylate particles of 1, 2, and 3 μm diameter, along with plain polystyrene particles of 3 μm diameter. The latter particles have a lower surface charge than that of the carboxylate particles. The zeta-potentials of the particles were measured using a Malvern Zetasizer, resulting in −62 mV for the 1 μm particles, −72 mV for the 2 μm particles, −81 mV for the 3 μm carboxylate particles, and −27 mV for the 3 μm plain particles. All particles were suspended in KCl solutions at 1.7 mS/m conductivity.

The electric field along the channel was applied to two metal needles inserted into the reservoirs at each end. Electric fields were

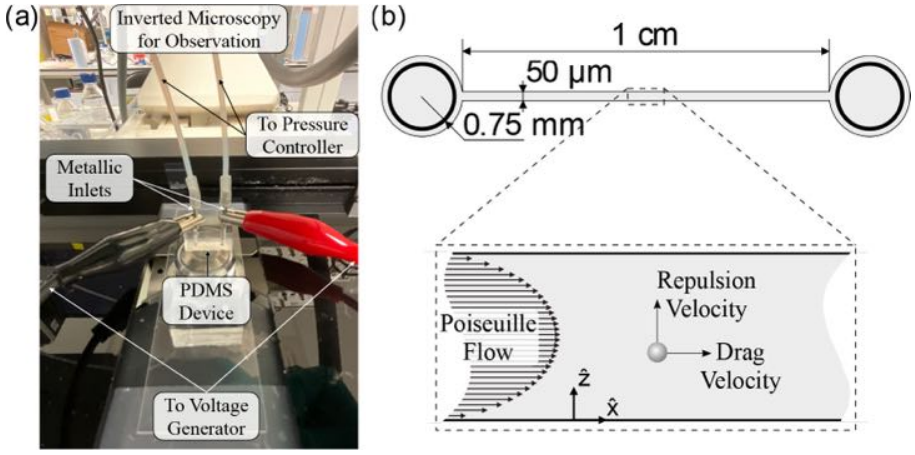

FIG. 2. (a) Photograph of the experimental setup with the microfluidic device made of PDMS and plasma-bonded to a glass slide. The metallic inlets of the device are connected to a pressure controller and clips to apply the voltage signal. Particle movement was measured with an inverted microscope. (b) Drawing of the microfluidic channel (not to scale) and a diagram showing the particles flowing in a Poiseuille profile while being repelled from the channel walls.

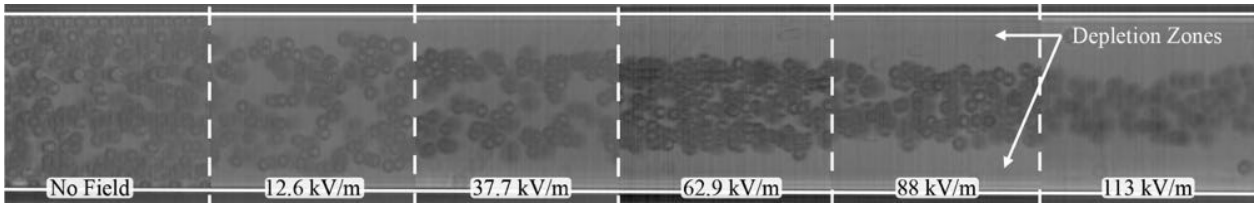

FIG. 3. Sequence of composite images from video recordings taken at the end of the channel showing 3 μm carboxylate particles flowing in a 1.7 mS/m KCl electrolyte for different electric field amplitudes, with $f = 90$ Hz. Particle-depleted regions are created near the channel walls because of particle-wall repulsion. As the field intensity increases, so does the repulsion and therefore the wall separation at the end of the channel. The apparently high concentration of particles in this image is due to image post-processing (stacking of the frames) and does not show the actual particle concentration. The channel walls are marked by the horizontal white lines, separated by 50 μm.

generated with amplitudes from 10 up to 100 kV/m and frequencies ranging from 50 Hz to 10 kHz. In a typical experiment, the particle suspension is pumped into the channel through one of the needles using a pressure generator to maintain a constant flow with an average velocity of 1.56 mm/s. The particle concentration was kept very low to avoid particle–particle interactions so that they flow through the channel one by one. Videos of particle motion were captured with a camera connected to the microscope and the particle positions in the transverse direction to the fluid flow were determined using a custom-written MATLAB code.[5]

III. EXPERIMENTAL RESULTS

In order to visualize the particle distribution across the channel, we recorded movies containing more than 600 frames which were later stacked, resulting in composite images showing all the particles that appeared throughout the full duration of the video at once. This clearly shows the depletion regions near the channel walls, which is not related to the particle concentration in the electrolyte. Figure 3 shows the example of 3 μm carboxylate particles driven by a Poiseuille flow and subjected to an electric field of multiple amplitudes and 90 Hz of frequency. It shows that prior to the application of the electric field, particles were randomly distributed in the channel (left-most image). As shown in the figure, the stream of particles becomes focused as the electric field intensity increases, leading to the regions devoid of particles near the channel walls.

Particle separation was characterized by measuring the regions devoid of particles. This was quantified by making a histogram of the transverse coordinates of the particles, i.e., the distance of a particle to one of the channel walls $z_i, i \in (1, \ldots, N)$, where N is the total number of particles. The wall separation is then defined as the width of the depletion zone, calculated as half the difference between the channel width and the width of the z_i histogram (this width is defined as the range that contains 95% of all positions).

Figure 4 shows the wall separation for carboxylate particles (3 μm diameter) as a function of the frequency of applied voltage for an electrolyte conductivity of 1.7 mS/m. In Fig. 4(a), the electric field amplitude was 60 kV/m, and particles show a monotonous decrease in wall separation with the frequency of the electric field, as predicted by the linear model (described in Sec. IV). However, experimental data for higher electric fields (100 kV/m) presented in Fig. 4(b) clearly show a minimum in the wall separation at around 2 kHz. This result is not predicted by the CPEO theory, where the slip velocity (and wall repulsion) varies monotonically with the frequency of the electric field.

In order to clarify this result, small fluorescent tracer particles (500 nm diameter) were used to visualize the quadrupolar flow structure around individual 3 μm spheres. The insets in Fig. 4(b) show example images of flow created by superimposing approximately ten

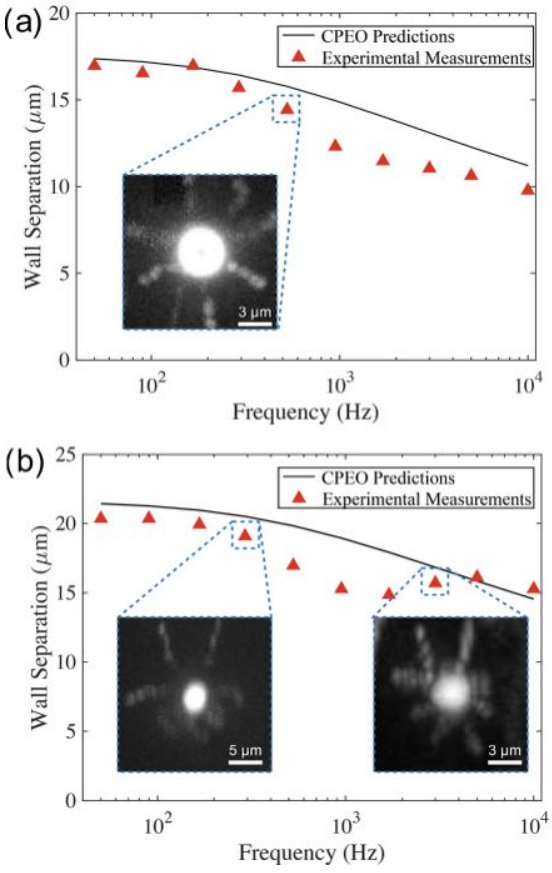

FIG. 4. Experimental data for wall repulsion at an electric field of (a) 60 kV/m and (b) 100 kV/m. 3 μm carboxylate particles were suspended in a 1.7 mS/m KCl electrolyte. The symmetrical flow vortices are destroyed at high electric fields as shown by the left-hand side inset image (292 Hz) in (b). The flow patterns are partially recovered at higher frequencies as seen in the right-hand side inset image taken at 3 kHz, or lower-intense fields as shown in the inset image of (a) taken at 527 Hz. Flows were traced with 500 nm fluorescent polystyrene particles.

frames. These show that flow field below ~1 kHz is distorted, while at higher frequencies, the fluid flow patterns around the sphere tend to recover the expected structure.

Figure 5(a) shows the wall separation for four different particles as a function of the amplitude of the electric field for a fixed frequency of 90 Hz, while Fig. 5(b) shows wall separation for the same conditions but a higher frequency of 527 Hz.

IV. THEORY AND COMPARISON WITH EXPERIMENTAL DATA

As mentioned above, the application of an ac field to a dispersion of charged dielectric particles leads to a well-defined pattern of electro-osmotic flows driven by CPEO.[9] The time-averaged slip velocity on spherical particles can be written as $v_{slip} = v_0 \sin(2\theta)$, where θ is the polar angle with respect to an axis given by the direction of the electric field and v_0 was derived for a sphere with arbitrary Dukhin number in a previous publication.[9] The Dukhin number, Du, is the ratio of surface conductance on the particle K_s to the bulk conductance: Du $= K_s/(a\sigma)$, where a is the particle radius and σ is the electrical conductivity of the electrolyte.[8] A MATLAB script for computing the value of v_0 can be found in the Supplementary Material. This slip velocity leads to an axisymmetric flow pattern structure around the spherical particles with the symmetry axis given by the direction of the applied electric field.[13]

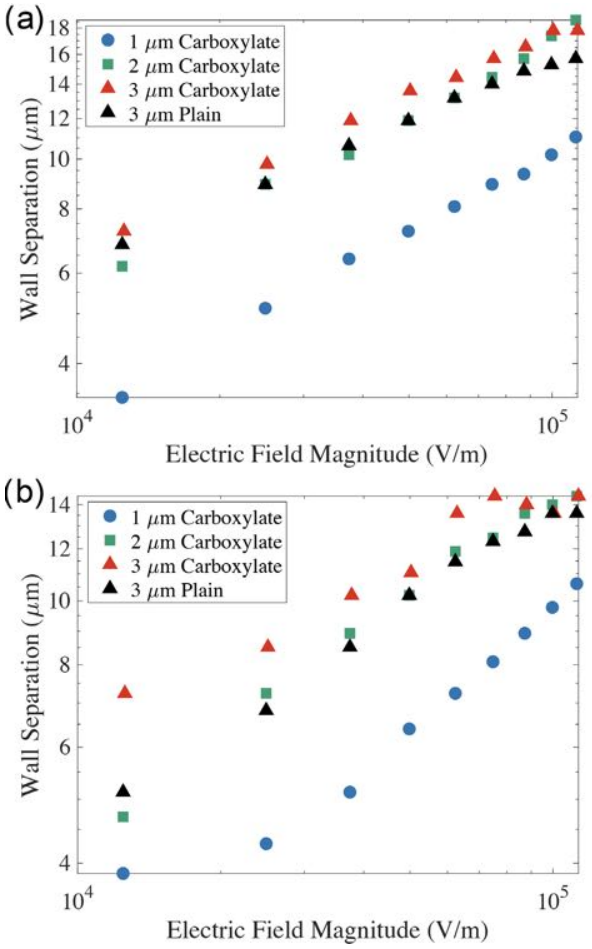

FIG. 5. Experimentally measured wall repulsion at different electric field amplitudes and two different frequencies: (a) 90 Hz and (b) 527 Hz. Four different populations of polystyrene particles suspended in a 1.7 mS/m KCl electrolyte were used: 1, 2, and 3 μm carboxylate and 3 μm plain particles.

$$\mathbf{v}_{\mathrm{CPEO}} = v_0 \left(\frac{(1-(r/a)^2)(1+3\cos 2\theta)}{2(r/a)^4} \hat{r} + \frac{\sin 2\theta}{(r/a)^4} \hat{\theta} \right), \quad (2)$$

where r is the radial distance. Conducting spheres suspended in electrolytes also develop quadrupolar flows as given by Eq. (2) when subjected to electric fields. In this case, the slip velocity on the particle arises because of induced-charge electro-osmosis (ICEO).[14] ICEO flows are negligible for dielectric particles;[7] therefore, only CPEO is considered as the origin of the quadrupolar flows.

The flow patterns are distorted by the presence of nearby walls; the resulting flow structure is described by the superposition of Eq. (2) and the flow field reflected from the wall (see Fig. 1). Importantly, the action of the reflected flow on the particle leads to motion away from the wall. If the particle is far from the wall, its drift velocity is given by

$$u = v_0 \frac{3a^2}{8h^2}, \quad (3)$$

where h is the distance of the particle center to the wall. This equation is a particular case of the expression derived by Smart and Leighton[15] for the drift of a stresslet due to the presence of a plane. In the context of electrokinetics, Yariv[16] obtained this expression for the case of repulsion of conducting spheres from a wall due to ICEO quadrupolar flows.

Taking into account the expression for the repulsion velocity given in Eq. (3), we obtain an analytical expression for the particle-wall separation at the end of the channel. First, consider the mid-horizontal plane of the channel. This corresponds to the focal plane measured in the experiments where particles are imaged. The velocity component of the particles along the channel u_x is given by the fluid velocity on this plane, which can be approximated by a parabolic profile,

$$\mathbf{v}_{\mathrm{Poiseuille}} = 4\mathcal{V}\left[\frac{z}{W} - \left(\frac{z}{W}\right)^2\right]\hat{x}, \quad (4)$$

where $\mathcal{V}$ is the maximum fluid velocity in the channel, z is the transverse position to the direction of the flow measured from one of the walls, and W is the channel width. This approximation (4) differs by less than 4% from the exact solution for the fully developed Poiseuille flow in the mid-plane of a channel with a square cross-section.[17] Since there are two side walls, the component of particle velocity perpendicular to the channel u_z results from applying Eq. (3) to both walls and adding the contributions.

$$\mathbf{u_z} = v_0 \frac{3a^2}{8}\left[\frac{1}{z^2} - \frac{1}{(W-z)^2}\right]\hat{z}. \quad (5)$$

Thus, $dz/dx = u_z/u_x$ can be integrated to obtain the following expression that relates the particle-wall separation h after covering a

distance L along the channel with the slip velocity on the particle surface v_0,

$$v_0 = \frac{32}{3}\frac{\mathscr{V}W^3}{a^2L}[f(h/W) - f(z_0/W)], \tag{6}$$

where z_0 is the initial separation from the wall and $f(\xi) = (18(1-2\xi)^2 - 9(1-2\xi)^4 + 2(1-2\xi)^6 - 12\log|1-2\xi|)/1536$. The width of the depletion region after a distance L along the channel can be estimated from Eq. (6) with z_0 equal to the particle radius.

Since Eq. (6) is derived from Eq. (3), it assumes that the remote-wall approximation is valid, i.e., higher-order terms are neglected in the calculation of the velocity field reflected by the wall. The validity of this approximation was already tested in our previous work.[5]

In order to compare the experimental results shown in Fig. 5 with the CPEO theory, a theoretical value for v_0 is determined using the experimental zeta-potential values (Sec. II) and the Dukhin number obtained from a typical value for surface conductance of colloids ($K_s = 1$ nS) independently of their size and surface functionalisation. This is a typical value obtained from experimental data for the electrokinetic properties of submicrometer latex particles[18–20] and is larger than the estimate obtained for K_s when using the theory of the diffuse layer.[21] The difference is attributed to the contribution to surface conductance arising from a layer of mobile ions adsorbed on the wall[19]—the so-called Stern layer. Figure 6 shows the non-dimensional wall separation h/W numerically obtained from Eq. (6) together with the measured values vs the reduced electric field $\beta = E_0ae/(k_BT)$.

The β parameter was used in Ref. 9 to develop the theoretical predictions of the slip velocity in the limit of the small electric field, $\beta < 1$. However, Fig. 6 shows how the theoretical predictions are in good agreement with the experimental data of wall separation for values of β well above 1. Interestingly, comparing results for cases (a) and (b) in the figure, we note that the deviation from the theoretical predictions depends on the frequency of the applied electric field. This is in agreement with the data in Fig. 4 which shows that the experimental data are farther from the CPEO predictions at 527 Hz than at 90 Hz. Further research will focus on understanding the upper limits of high intensity electric fields in the theory of CPEO.

V. SLIP VELOCITY ESTIMATIONS

With respect to Fig. 6, it is of interest to analyze the low β regime. The agreement between theoretical predictions and experimental measurements found for low electric field amplitudes means that the slip velocity can still be related to the wall separation in this regime, as argued in Ref. 5. This is significant because we are able to infer slip velocities at $\beta < 1$, something that was previously not possible using the direct measurement procedure presented in Ref. 9. The reason for this is the necessity of measuring over a minimum space around the particle to trace the fluid flow. Experimentally, it was found that at least five radii away from the target particle is needed for consistency of measurements. However, as the CPEO flows decay rapidly with distance to the particle surface [$\sim(a/r)^2$], together with the fact that due to Brownian motion the velocity of 500 nm tracer particles could not be measured with velocities $<$ 2–3 μm/s, gives an approximate limit of 50 μm/s below which direct experimental measurements break down.

The first reported measurements of slip velocity in Ref. 9 were made using an electric field magnitude of 80 kV/m and particles of 3 μm diameter, resulting in $\beta = 4.8$. Later in Ref. 5, 2 μm particles were used at the same electric field magnitude reducing β to 3.2, still far from $\beta < 1$. Although the results presented here demonstrate a good agreement for β values up to $\beta \sim 4$, thus confirming the validity of results presented previously, Eq. (6) means that it is now possible to estimate the slip velocity for smaller particles and lower electric fields, where the reduced electric field is as low as $\beta = 0.2$. These results, presented in Fig. 7, show a wide parametric range (electric field amplitude, frequency, and particle size) of slip velocity indirect estimations.

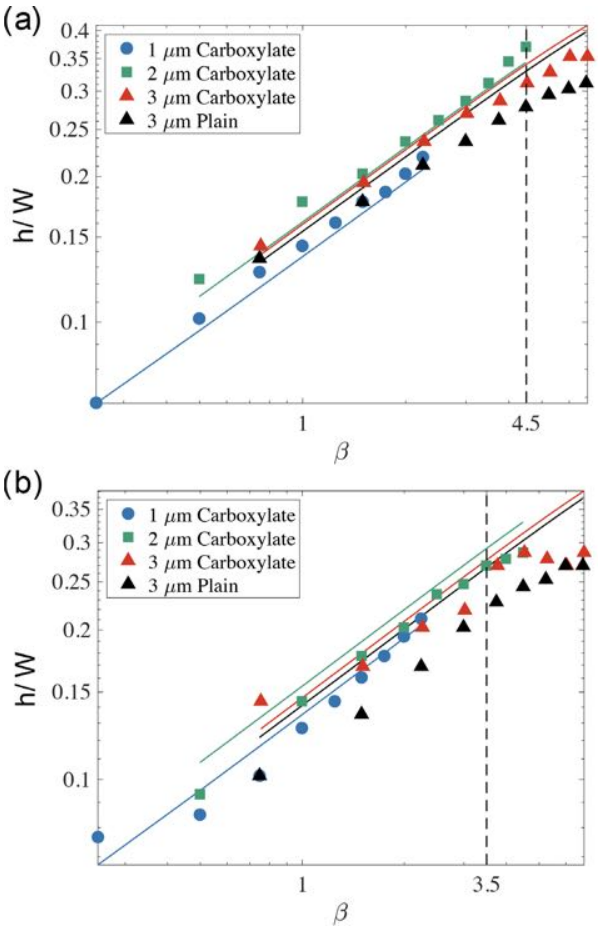

FIG. 6. Comparison of the experimental values shown in Fig. 5 with the theoretical predictions of wall repulsion from Eq. (6), based on the slip velocity from CPEO theory.[9] Good agreement is seen for lower values of $\beta = E_0ae/(k_BT)$ up to values over 1. Zeta-potential values shown in Sec. II, $K_s = 1$ nS, with $\mathrm{Du} = K_s/(\sigma a)$. Two different frequencies are compared: (a) 90 Hz and (b) 527 Hz.

There are several advantages to determining the slip velocity from wall repulsion measurements rather than with tracer particles. The experimental setup is much simpler, and the measurements are automated. In other words, the position of the particles in the channel is determined automatically using a custom-written software. This means that a large number of particles can be measured in a short time window, and particle-particle interaction is avoided by using low-particle concentrations.

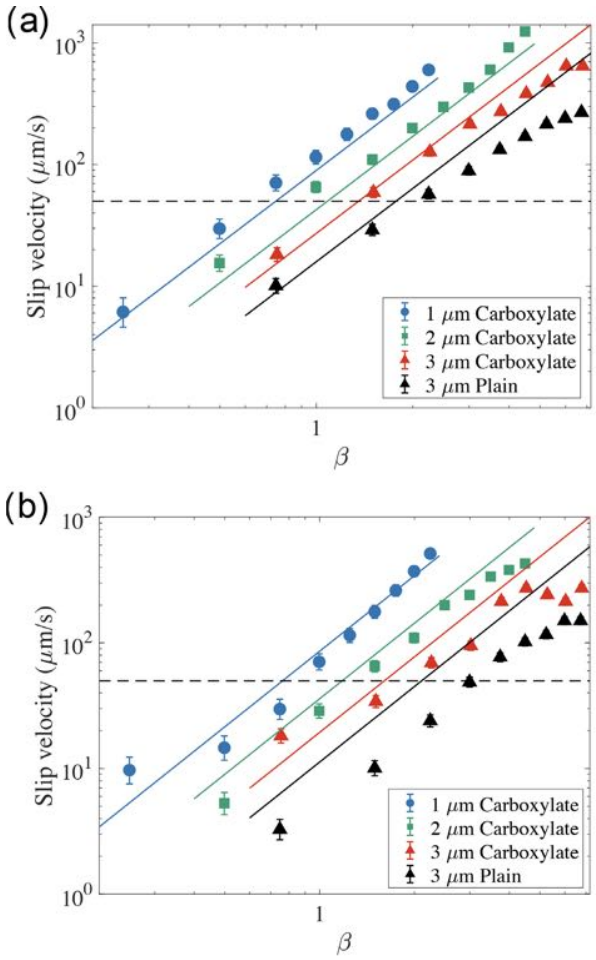

FIG. 7. Estimated slip velocity from the experimental results of wall repulsion presented in Fig. 5 for the same frequencies: (a) 90 Hz and (b) 527 Hz. The horizontal dashed line marks a rough limit for the direct measurements at 50 μm/s.

VI. DISCUSSION AND CONCLUSIONS

This paper has shown that experimental data of wall separation for dielectric microparticles undergoing electrophoresis in small electric fields ($E_0 < 60$ kV/m) agrees with theoretical predictions of the hydrodynamic interaction arising from Concentration-Polarization Electro-osmosis (CPEO) around the particles. This result supports the fact that hydrodynamic forces are responsible for particle-wall separation[5] and confirms that CPEO is the mechanism behind these observed flows. Since CPEO flows around the particles are weak at small electric fields and cannot be directly measured, comparison between theory and experiments provides a further means of validating the CPEO theory. Likewise, CPEO flows for small particles (less than 1 μm diameter) are very difficult to measure. Thus, this method also allows comparison between theory and experiments for colloids. Furthermore, the influence of inertial lift on electrophoresis[22] is negligible since the Reynolds number is very small in our experiments (around 0.08). This is in contrast with the experiments by Yoda *et al.*[23,24] where dc electrophoresis experiments combined with Pouiseuille flows show the formation of bands of colloidal particles along the direction of the flow. In those experiments, inertial lift seems to play a major role in the band formation.[25] Nevertheless, CPEO flows might also influence the band formation as in the case of the patterns of colloidal particles reported in Ref. 26.

In this work, the electric field can reach 100 kV/m; therefore, electrothermal effects could occur in the device because temperature changes cause variations in fluid properties such as viscosity, permittivity, and conductivity, and large temperature gradients can give rise to electrothermal flows.[27,28] We consider the energy balance in our system which is given by the integral form of the convection–diffusion equation with a source coming from Joule heating

$$\rho C_p \int_V dV(\mathrm{v}\cdot\nabla T) - \kappa \oint_S d\mathrm{S}\cdot\nabla T = \int_V dV \sigma E^2. \tag{7}$$

Here, ρ is the mass density, C_p is the heat capacity at constant pressure, T is the temperature field, and κ is the thermal conductivity.

For simplicity, consider a cylindrical channel of radius $R = 25$ μm, length $L = 1$ cm surrounded by a PDMS wall with a thickness of $W = 5$ mm. The reason for considering the PDMS and not the glass side is because glass has a higher thermal conductivity (see Table S2 of the supplementary material) and a smaller thickness. The heat flux from the convection term leads to a temperature rise of the order of $\Delta T = \sigma E_{\mathrm{rms}}^2 L/(\rho C_p v) \sim 25$ K. However, the temperature rise given by the conduction term leads to $\Delta T = \sigma E_{\mathrm{rms}}^2 R^2 \ln(W/R)/(2\kappa) \sim 0.1$ K, estimated by solving the conduction contribution of Eq. (7) in cylindrical coordinates for the highest field of $E_0 = 100$ kV/m. Therefore, the heat loss due to conduction dominates as usual in microfluidics. Moreover, this is the temperature increase with respect to the environment and not within the electrolyte in the channel, meaning that any temperature gradients in the electrolyte that could give rise to electrothermal effects are negligible. A detailed COMSOL simulation of the system is provided in the supplementary material. The fully coupled fluid dynamic, electric, and heat transfer problems were solved demonstrating an even lower temperature increase in just 35 mK.

Data for wall repulsion of particles at higher electric fields show that the predictions of the CPEO theory for weak electric fields are valid up to $E_0 a \approx 4k_B T/e$ although the original framework assumed validity up to the thermal voltage $k_B T/e$. For higher electric field magnitudes, wall repulsion deviates from the expected behavior and does not monotonously decrease with the frequency. The origin of these unexpected trends was clarified by visualizing the streamlines around the particles indicating that the quadrupolar flow structures become disrupted at higher electric fields, leading to a weaker wall repulsion. Finally, the influence of wall repulsion during particle electrophoresis is critical in the design of microfluidic devices that use electric fields for particle manipulation and separation.[29] Examples of use of low-frequency electric fields for particle manipulation are deterministic lateral displacement,[30] insulating DEP,[31,32] and colloidal assembly.[33]

SUPPLEMENTARY MATERIAL

See the supplementary material for a detailed description of how to compute the maximum slip velocity on the surface of a sphere based on the CPEO model described in Ref. 9. We also provide simulations to estimate any possible heating that might occur for the worst-case

scenario, with highest electric field demonstrating that any thermal effects are negligible.

ACKNOWLEDGMENTS

P.G.S. and A.R. acknowledge Grant No. PGC2018–099217-B-I00 funded by No. MCIN/AEI/10.13039/501100011033 and by "ERDF A way of making Europe."

AUTHOR DECLARATIONS

Conflict of Interest

The authors have no conflicts to disclose.

Author Contributions

Raul Fernandez-Mateo: Conceptualization (equal); Formal analysis (equal); Methodology (equal); Software (equal); Validation (equal); Writing – original draft (equal); Writing – review & editing (equal). **Hywel Morgan:** Conceptualization (equal); Formal analysis (equal); Funding acquisition (equal); Methodology (equal); Software (equal); Validation (equal); Writing – original draft (equal); Writing – review & editing (equal). **Antonio Ramos:** Conceptualization (equal); Formal analysis (equal); Funding acquisition (equal); Validation (equal); Writing – review & editing (equal). **Pablo Garcia-Sanchez:** Conceptualization (equal); Formal analysis (equal); Funding acquisition (equal); Validation (equal); Writing – original draft (equal); Writing – review & editing (equal).

DATA AVAILABILITY

The data that support the findings of this study are openly accessible in the University of Southampton repository available at https://doi.org/10.5258/SOTON/D2491.[34]

REFERENCES

[1]R. Hunter, *Introduction to Modern Colloid Science* (Oxford University Press, 1993).
[2]M. von Smoluchowski, "Contribution à la théorie de l'endosmose électrique et de quelques phénomènes corrélatifs," Bull. Akad. Sci. Cracov. **8**, 182–200 (1903).
[3]L. Liang, Y. Ai, J. Zhu, S. Qian, and X. Xuan, "Wall-induced lateral migration in particle electrophoresis through a rectangular microchannel," J. Colloid Interface Sci. **347**, 142–146 (2010).
[4]Z. Liu, D. Li, Y. Song, X. Pan, D. Li, and X. Xuan, "Surface-conduction enhanced dielectrophoretic-like particle migration in electric-field driven fluid flow through a straight rectangular microchannel," Phys. Fluids **29**, 102001 (2017).
[5]R. Fernández-Mateo, V. Calero, H. Morgan, P. García-Sánchez, and A. Ramos, "Wall repulsion of charged colloidal particles during electrophoresis in microfluidic channels," Phys. Rev. Lett. **128**, 074501 (2022).
[6]E. Yariv, "'Force-free' electrophoresis?," Phys. fluids **18**, 031702 (2006).
[7]V. Calero, R. Fernández-Mateo, H. Morgan, P. García-Sánchez, and A. Ramos, "Stationary electro-osmotic flow driven by ac fields around insulators," Phys. Rev. Appl. **15**, 014047 (2021).
[8]J. Lyklema, *Fundamentals of Interface and Colloid Science* (Academic Press Limited, 1995).
[9]R. Fernández-Mateo, P. García-Sánchez, V. Calero, H. Morgan, and A. Ramos, "Stationary electro-osmotic flow driven by AC fields around charged dielectric spheres," J. Fluid Mech. **924**, R2 (2021).
[10]O. Schnitzer and E. Yariv, "Macroscale description of electrokinetic flows at large zeta potentials: Nonlinear surface conduction," Phys. Rev. E **86**, 021503 (2012).
[11]M. Viefhues, S. Manchanda, T.-C. Chao, D. Anselmetti, J. Regtmeier, and A. Ros, "Physisorbed surface coatings for poly (dimethylsiloxane) and quartz microfluidic devices," Anal. Bioanal. Chem. **401**, 2113 (2011).
[12]R. Fernández-Mateo, P. García-Sánchez, V. Calero, A. Ramos, and H. Morgan, "A simple and accurate method of measuring the zeta-potential of microfluidic channels," Electrophoresis **43**, 1259–1262 (2022).
[13]N. I. Gamayunov, V. A. Murtsovkin, and A. S. Dukhin, "Pair interaction of particles in electric field. 1. Features of hydrodynamic interaction of polarized particles," Colloid J. USSR **48**, 197–203 (1986).
[14]M. Z. Bazant and T. M. Squires, "Induced-charge electrokinetic phenomena: Theory and microfluidic applications," Phys. Rev. Lett. **92**, 066101 (2004).
[15]J. R. Smart and D. T. Leighton, Jr., "Measurement of the drift of a droplet due to the presence of a plane," Phys. Fluids A **3**, 21–28 (1991).
[16]E. Yariv, "Boundary-induced electrophoresis of uncharged conducting particles: Remote wall approximations," Proc. R. Soc. A **465**, 709–723 (2009).
[17]H. Bruus, *Theoretical Microfluidics* (Oxford University Press, 2007), Vol. 18.
[18]W. Arnold, H. Schwan, and U. Zimmermann, "Surface conductance and other properties of latex particles measured by electrorotation," J. Phys. Chem. **91**, 5093–5098 (1987).
[19]V. Shilov, A. Delgado, F. Gonzalez-Caballero, and C. Grosse, "Thin double layer theory of the wide-frequency range dielectric dispersion of suspensions of non-conducting spherical particles including surface conductivity of the stagnant layer," Colloids Surf. A **192**, 253–265 (2001).
[20]I. Ermolina and H. Morgan, "The electrokinetic properties of latex particles: Comparison of electrophoresis and dielectrophoresis," J. Colloid Interface Sci. **285**, 419–428 (2005).
[21]A. V. Delgado, F. Gonzalez-Caballero, R. Hunter, L. Koopal, and J. Lyklema, "Measurement and interpretation of electrokinetic phenomena (IUPAC technical report)," Pure Appl. Chem. **77**, 1753–1802 (2005).
[22]V. Lochab and S. Prakash, "Combined electrokinetic and shear flows control colloidal particle distribution across microchannel cross-sections," Soft Matter **17**, 611–620 (2021).
[23]N. Cevheri and M. Yoda, "Electrokinetically driven reversible banding of colloidal particles near the wall," Lab Chip **14**, 1391–1394 (2014).
[24]M. Rossi, A. Marin, N. Cevheri, C. J. Kähler, and M. Yoda, "Particle distribution and velocity in electrokinetically induced banding," Microfluid. Nanofluid. **23**, 1–9 (2019).
[25]A. J. Yee and M. Yoda, "Observations of the near-wall accumulation of suspended particles due to shear and electroosmotic flow in opposite directions," Electrophoresis **42**, 2215–2222 (2021).
[26]F. Katzmeier, B. Altaner, J. List, U. Gerland, and F. C. Simmel, "Emergence of colloidal patterns in ac electric fields," Phys. Rev. Lett. **128**, 058002 (2022).
[27]A. Castellanos, A. Ramos, A. González, N. G. Green, and H. Morgan, "Electrohydrodynamics and dielectrophoresis in microsystems: Scaling laws," J. Phys. D **36**, 2584–2597 (2003).
[28]Q. Wang, N. N. Dingari, and C. R. Buie, "Nonlinear electrokinetic effects in insulator-based dielectrophoretic systems," Electrophoresis **38**, 2576–2586 (2017).
[29]C. Thomas, X. Lu, A. Todd, Y. Raval, T.-R. Tzeng, Y. Song, J. Wang, D. Li, and X. Xuan, "Charge-based separation of particles and cells with similar sizes via the wall-induced electrical lift," Electrophoresis **38**, 320–326 (2017).
[30]V. Calero, P. Garcia-Sanchez, C. Honrado, A. Ramos, and H. Morgan, "AC electrokinetic biased deterministic lateral displacement for tunable particle separation," Lab Chip **19**, 1386–1396 (2019).
[31]E. B. Cummings and A. K. Singh, "Dielectrophoresis in microchips containing arrays of insulating posts: Theoretical and experimental results," Anal. Chem. **75**, 4724–4731 (2003).
[32]R. Fernández-Mateo, V. Calero, H. Morgan, A. Ramos, and P. García-Sánchez, "Concentration-polarization electroosmosis near insulating constrictions within microfluidic channels," Anal. Chem. **93**, 14667–14674 (2021).
[33]M. Trau, D. A. Saville, and I. A. Aksay, "Assembly of colloidal crystals at electrode interfaces," Langmuir **13**, 6375–6381 (1997).
[34]Dataset: R. Fernandez-Mateo, 1997 "Dataset supporting the article: Wall repulsion during electrophoresis: Testing the theory of concentration-polarization electroosmosis," University of Southampton Institutional Repository.

Paper H

Concentration-Polarization Electroosmosis for Particle Fractionation

Summary of Results

After the particle-wall repulsion was tested and shown to be explained by CPEO, we were able to estimate and tune deflection of particles undergoing electrophoresis based on size and surface charge. Using simple flow-focusing channels, it was possible to separate mixtures of polystyrene particles of sizes ranging from 500 nm to 3 $\mu\mathrm{m}$ in diameter, and particles having the same size and different surface charge. Also a population of *S. Aureus* bacteria was separated from a mixture with 3 $\mu\mathrm{m}$ polystyrene particles.

Contribution Statement

Morgan, after the large particle-wall separation observed in the experiments for Paper F, had the idea of using co-flow channels to fractionate particles using CPEO, and its possible application to bacteria. I did the experimental work and data analysis; I made the comparison of the experimental data with the CPEO predictions and wrote the first version of the manuscript. Morgan, Garcia-Sanchez and Ramos provided supervisory support. Final version of the manuscript is in progress.

Concentration-Polarization Electroosmosis for particle fractionation

Raúl Fernández-Mateo,[1] Pablo García-Sánchez,[2] Antonio Ramos,[2] and Hywel Morgan[1,*]

[1] *School of Electronics and Computer Science, University of Southampton, Southampton SO17 1BJ, United Kingdom.*
[2] *Depto. Electrónica y Electromagnetismo. Facultad de Física. Universidad de Sevilla. Avda. Reina Mercedes s/n, 41012. Sevilla (Spain).*

Low-frequency AC electric fields induce steady-state electroosmotic flows around charged dielectric micro-particles, this phenomenon has been termed Concentration-Polarization Electroosmosis (CPEO). Recently, these flows were proven to cause particle-wall repulsion of colloids flowing in a microfluidic channel when the electric field is applied along the channel. In this work, we exploit this phenomenon to fractionate micron-sized polystyrene particles and bacteria in a flow-focusing device. The results are in agreement with the prediction of the CPEO theory. CPEO-based fractionation can be implemented in current devices commonly used for particle lifting, such as inertial or viscoelastic focusing, with no additional fabrication process other than inserting a couple of electrodes.

I. INTRODUCTION

Isolation of bacteria from a complex sample is a major challenge in microfluidics. It requi efficiency separation and a low detection limit for the early detection of blood-stream infectio may be triggered by an extremely low pathogen tration, below 100 cfu/mL [1, 2]. Microfluidics c vide the fast point-of-care diagnostics which is c anticipate the generalised immune response of s

Common microfluidic approaches for the iso bacteria from whole blood include acoustophore inertial focusing [6] or dielectrophoresis (DEP) [ever, given the size range similarities between and components in the blood stream, specially r cells (RBCs) and platelets, size-based separatic anisms such as inertial microfluidics [6] fail t between both populations. Similar problems are faced with mechanical properties used in acoustophoresis, and electrical properties in DEP.

Microfluidic techniques also include lysing of blood cells [8, 9], i.e. sudden decrease in salt concentration producing osmotic imbalances in the blood cells, causing them to explode into smaller debris. Due to the stronger membrane of bacterial cells, they have been proven to survive the shock and be 100% viable after the blood lysate [8]. At the expense of sample dilution, lysing facilitates the isolation using the techniques mentioned above, e.g. acoustophoresis [9].

In short, an isolation technique for the high efficiency enrichment and isolation of bacteria in clinical samples is still missing. Nonetheless, combination of microscale forces have often succeeded in microfluidics for improving the resolution of particle fractionation. An excellent example is the use of deterministic lateral displacement (DLD), a size-based separation method, in combination with DEP [10, 11], allowing almost a ten-fold enhancement of size resolution from the initial technologies [12].

* Corresponding author: hm@ecs.soton.ac.uk

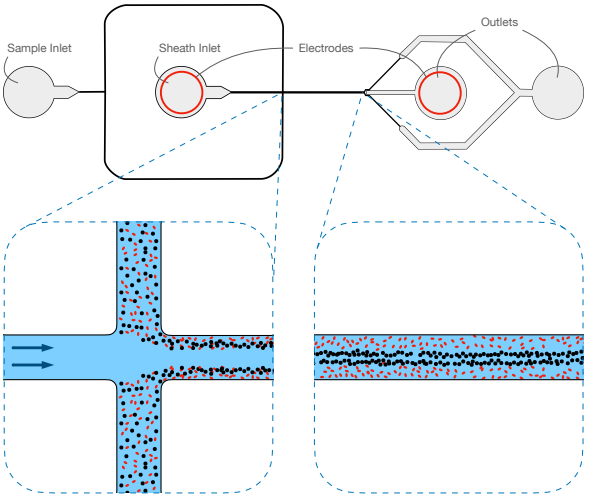

FIG. 1. Schematics of the flow-focusing channels used for particle separation. Bottom left inset show the junction where the sheath flow joins the sample flow, pushing it to the channel walls. On the right, it is shown how at the end of the channel fractionation of the sample components is achieved by differences in wall separation.

In this work, we propose a proof-of-concept device capable of discerning populations of polystyrene microparticles based on size and surface charge exploiting novel observations of hydrodynamic particle-wall interactions [13], and apply the technology to isolate a bacterial population from polystyrene particles. The origin of this interaction is the Concentration Polarization Electroosmosis (CPEO) flows around the micro-particles subjected to low-frequency ($\lesssim 10^4$ Hz) AC electric fields in low-conductivity electrolytes ($\lesssim 0.1$ S/m) [14, 15]. We exploit the CPEO particle-wall interaction to achieve particle fractionation based on size and/or surface charge. With this purpose, we use flow-focusing channels as shown in Figure 1 to first push a sample mixture close to the channel walls. Then, as the particles flow through the channel, they migrate towards the centre of the cross-section with a rate that depends upon their size and surface charge,

achieving fractionation at the end of the channel.

Flow-focusing channels have been used in the past for various fractionation techniques which rely on particle wall repulsion, such as inertial focusing [16], viscoelastic lifting [17, 18], pinched-flow fractionation [19, 20], or combinations of phenomena [21] which have allowed high-purity fractionation of biological compounds. Thus, CPEO introduces a new dimension to these existing methods exploiting tunable wall repulsion through the application of an external AC electric field in a simple configuration requiring no additional complexity in device fabrication.

Here, we report fractionation of combinations of polystyrene particles with sizes ranging from 500 nm to 3 μm in diameter, and particle populations of 3 μm with different surface charge. The observed separations are in good agreement with CPEO predictions. We also achieved high-efficiency separation of *S. Aureus 9144* bacteria from 3 μm Carboxylate beads.

II. METHODS

A. Device design and preparation

Devices are fabricated using standard soft-lithography procedures for creating the molds –SU8 on a silicon wafer substrate. Then, PDMS (in a 10% (w/w) mixture with curing agent) is casted in the molds, cured at 60°C and oxygen plasma-bonded to glass for obtaining the devices.

Co-flow channels from two different inlets intersect in a cross junction with three inlet channels having the same 50 μm×50 μm square cross-section –two channels containing the electrolyte solution and the sample mixture coming from one inlet, and one sheath channel with the same solution but no sample coming from the other inlet (see Figure 1). The outlet channel has the same cross-section of 50 μm×50 μm and 5 mm in length. After that, the channel expands into a gated exit for final separation.

B. Bacteria culture

A strain of *S. Aureus 9144* was incubated overnight to the saturation concentration. The resulting population, with a concentration of around 10^8 cells/mL, was later harvested by washing 5 times in the desired conductivity media. For our experiments, we used 1.7 mS/m KCl together with 280 mM D-Mannitol, a non-metabolising sugar, to compensate the osmotic pressure.

As the *S. Aureus* Bacteria are of a spherical shape, we used Dynamic Light Scattering (DLS) (Malvern Zetasizer Nano) to obtain the size distribution of the population. The results, presented in Figure 2(a), show a median diameter of (1.09 ± 0.12) μm. We have also measured the zeta-potential of the population using DLS, shown in Figure 2(b): resulting in (-31.1 ± 4.0) mV in accordance with literature [22–24]. These measurements were done

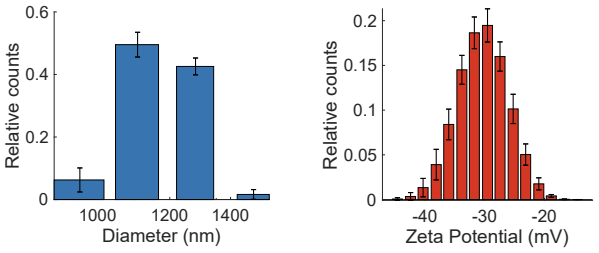

FIG. 2. (a) Size and (b) zeta potential distribution using DLS (Malvern Zetasizer) of *S.Aureus 9144* Bacteria suspended in 1.7 mS/m KCl and 280 mM D-Mannitol. We obtained a diameter of (1.09±0.12) μm and a zeta-potential of (−31.1±4.0) mV.

C. Sample preparation

We first tested the separation capabilities of the device by introducing mixtures of 500 nm, 1 μm, 2 μm and 3 μm carboxylate microbeads, having different fluorescence emission wavelengths in order to distinguish them at the end of the device. The zeta potential ζ was obtained from previous measurements: −63 mV, −71 mV, −74 mV and −78 mV, respectively. We also used plain 3 μm beads ($\zeta = -15$ mV) to demonstrate fractionation based on surface charge.

For each experiment, we mixed two population samples having an approximate concentration of 10^6 particles/mL. The medium was a KCl electrolyte at a conductivity of 1.7 mS/m. We also mixed the 3 μm carboxylate particles (10^6 particles/mL) with bacteria using the media described above (section II B). In all cases, the sheath fluid was the same as the sample fluid but completely depleted of particles.

D. Device operation

Devices are run at a constant flow rate using two independent syringe pumps to modulate the sample pinch into the channel walls after the junction. The electric field is applied by inserting two metallic cylinders in the two closest inlet reservoirs of the device, while the remaining inlets to the device are left floating. The metallic needles are connected to a voltage amplifier which magnifies the sinusoidal signals provided by a signal generator. The flow rate, channel length, voltage and frequency applied between the electrodes were chosen for optimal particle fractionation based on experimental observations and the CPEO particle-wall repulsion theory validated in a previous work [15]. The optimisation is described in the Appendix, and resulted in a flow rate of 2.5 μL/hour imposed in the sample inlet and 5 μL/hour in the sheath

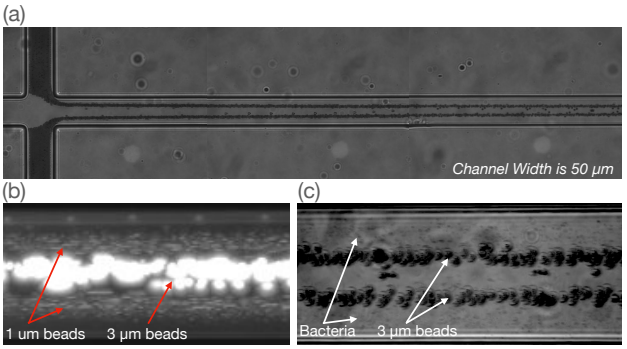

FIG. 3. Image stack compositions of different particle populations flowing in the devices. (a) 3 μm plain particles flowing through the junction, pushed to the wall and beginning of separation from the wall. (b) 1 μm and 3 μm carboxylate particles at the end of the channel separated in two different streams. Electric field is 100 kV/m, with a frequency of 50 Hz. (c) *S. Aureus* separated from 3 μm carboxylate particles at the end of the channel. Electric field is 100 kV/m, with a frequency of 1.7 kHz.

inlet. The electric field inside the channel had an amplitude of approximately 100 kV/m with a frequency that was tuned between 50 Hz and 2 kHz.

Figure 3 shows image compositions consisting in stacks of frames recorded during a time-span of 30 seconds at a frame-rate of 16 fps, meaning that the particle concentration observed in the images does not resemble the actual concentration in the media. Part (a) of the figure shows 3 μm Plain particles entering the main channel of the device after the junction when subjected to an electric field of around 100 kV/m and a frequency of 50 Hz. It is shown how the particle stream is initially pinched to the lateral channel walls due to the sheath flow. Then, as the hydrodynamic particle-wall interaction is most intense when the particles are closer to the wall and decay with the square of the separation distance (4), a sudden repulsion from the wall is observed right after the particles go through the corner. After this, the particles keep repelling from the walls at a lower rate.

E. Particle detection

The evaluation of the fractionation efficiency of the device was made by determining the particle distribution across the channel right before any outlet split using the Particle Finder software [25]. When the sample mixture is composed of particles having different sizes and surface charges, each population will separate to a different extent from the wall, leading to fractionation. By applying different detection filters, Particle Finder is able to discern between different particle populations flowing in the channel. An example is represented in Figure 3(b), where we can observe 1 μm particles at different cross-sectional positions of the channel from 3 μm particles. This is also shown in the case of 3 μm carboxylate particles and the *S. Aureus* population in Figure 3(c). These images are elaborated through the stacking of approximately 1000 frames of video recordings. The frames used to elaborate these stacks were individually analysed by the Particle Finder software to obtain the relative particle concentration across the channel section.

We use the concepts of sample recovery and waste removal for the quantification of the fractionation efficiency. Sample recovery is defined as the ratio of the targeted sample population exiting the device through the desired outlet with respect to the total targeted population sample flowing in the device. Analogously, the waste removal is defined as the ratio of the population we want to eliminate from our sample which is deflected towards the waste outlet with respect to the total undesired population flowing in the device. The optimal fractionation efficiency was obtained maximising the product of sample recovery and waste removal.

III. RESULTS

In Figure 4 we show the cross-sectional relative concentration of each population's species at the end of the channel of all the experiments performed with different population pairs of polystyrene beads, as well as the 3 μm Carboxylate particles with the *S. Aureus* sample.

We define the relative concentration of particles i at position z as $\rho_i(z) = (1/N_i)\Delta N_i/\Delta z$, where ΔN_i is the number of particles within the range $[z, z+\Delta z]$ and N_i is the total number of particles i.

The wall interaction and channel design imply a symmetrical distribution of the concentration at all times with respect to the central section of the channel. For this reason, the concentration profiles represented in Figure 4 are the average of the concentration from both sides of the symmetry plane. As a consequence, wall separation is represented from one of the walls to the symmetry plane, i.e. 25 μm.

A. Fractionation of polystyrene particles by size

Reading from left to right, the first four plots in Figure 4 represent the different population mixtures containing two different particle sizes and approximately the same surface charge. The experiments were performed with an applied electric field of 100 kV/m of amplitude and frequency of 50 Hz.

First, we fractionated 500 nm particles from 2 μm particles with an optimal recovery of the 500 nm population of 86.2% while removing 89.7% of the 2 μm particles, resulting in an overall 77.2% separation efficiency. Likewise, an optimisation of the device outlet distribution could be made to achieve a 71.9% separation efficiency when mixing 1 μm and 2 μm beads (83.4% recovery of the 1 μm's and 86.3% removal of the 2 μm's); 96.9% efficiency

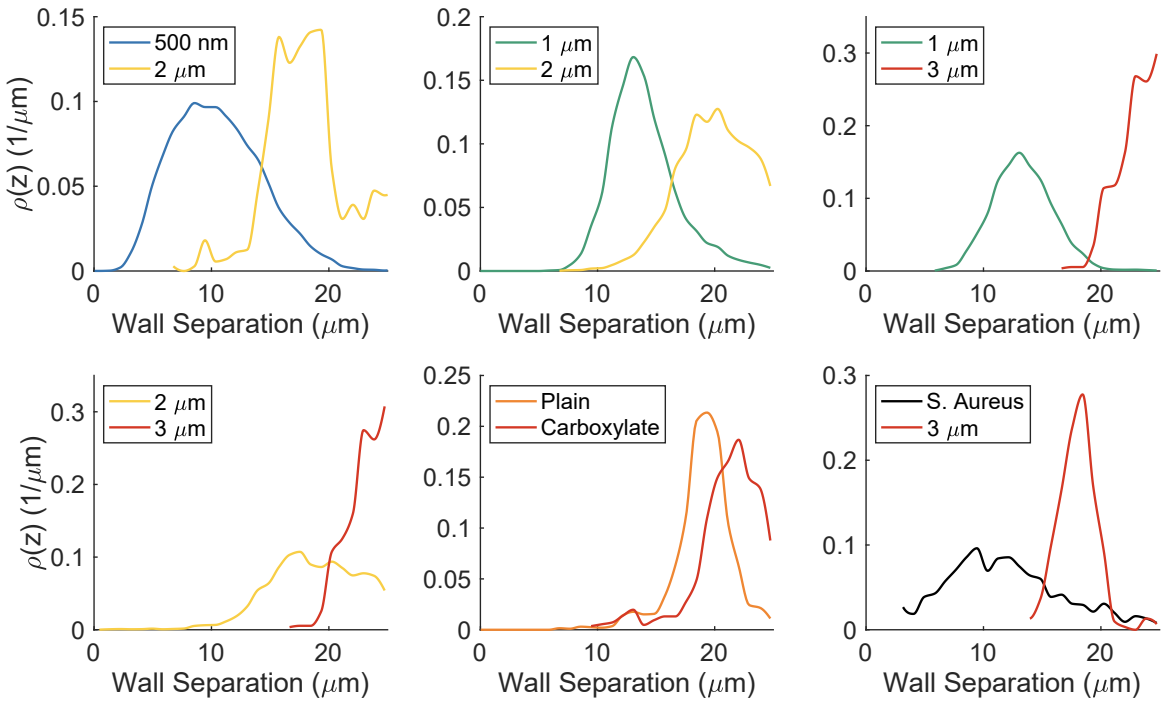

FIG. 4. Relative concentrations of particle populations in a mixture at the end of the channel. Each plot represents a different experiment where combinations of two different populations were mixed at the inlet of the device. The applied electric field was 100 kV/m in all cases, with a frequency of 50 Hz for the case of the polystyrene particles, and 1.7 kHz for the combined case of 3 μm carboxylate particles with *S. Aureus* bacteria. The concentrations were computed using $\Delta z = 0.9$ μm.

when mixing 1 μm and 3 μm beads (98.1% recovery of the 1 μm's and 98.8% removal of the 3 μm's); and 60.4% efficiency when mixing 2 μm and 3 μm beads, recovering 69.2% of the population of 2 μm while removing 87.3% of the bigger particles.

B. Fractionation of polystyrene particles by charge

One of the main features of CPEO particle separation is that it not only allows to fractionate by size, but also based on surface charge. We have separated particles having the same 3 μm diameter, but different zeta potential. The relative concentration at the end of the channel is presented in the central bottom plot of Figure 4. Again, particles were experiencing an electric field of 100 kV/m of amplitude and 50 Hz of frequency.

An optimised outlet distribution for this case could result in a 51.4% separation efficiency, achieving 79.1% recovery of the plain particles (less charged population) while removing 64.5% of the carboxylate particles.

C. Fractionation of bacterial population from polystyrene particles

We exploit the measurements of bacterial surface conductance found in the literature [26] and our size and zeta potential measurements presented in Figure 2 to predict their migration towards the centre of the channel using CPEO.

In this case, sample was subjected to an electric field of an amplitude of 100 kV/m and a frequency of 1.7 kHz. We used these predictions to achieve fractionation of the *S. Aureus* bacterial population from 3 μm carboxylate particles with an overall 74.1% efficiency, recovering 77.1% of the bacteria while removing 96.2% of the polystyrene particles.

IV. DISCUSSION

A. Origin of the CPEO flows

CPEO flows are time-averaged electroosmotic flows arising from the phenomenon of surface conductance on dielectrics immersed in low-conductivity electrolytes and in the presence of low-frequency AC electric fields. For a spherical particle, these flows are described by the velocity field below, whose streamlines are represented in

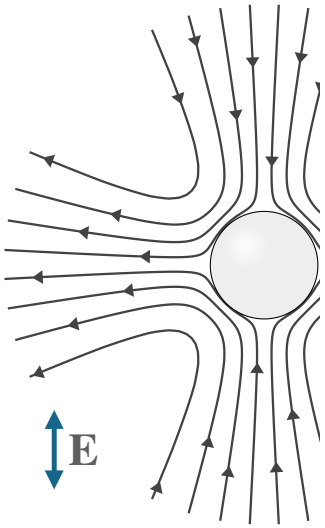

FIG. 5. Fluid velocity field streamlines due to CPEO around a spherical particle. The streamlines are axially symmetric with respect to the direction of the electric field.

Figure 5:

$$\mathbf{v}(r,\theta) = \mathcal{V}\left[\frac{1-r^2}{2r^4}(1+3\cos 2\theta)\ \hat{r} + \frac{1}{r^4}\sin 2\theta\ \hat{\theta}\right]. \quad (1)$$

We refer to this flow field as the Gamayunov field. Gamayuvov et al. [27] were the first to describe the flow pattern around a particle arising from an electroosmotic slip velocity of the form $\sim \sin 2\theta$. In the above equation, r is the distance to the particle centre expressed in units of the particle radius a and θ is the angle with respect to the direction of the electric field. $\mathcal{V}$ is maximum slip velocity at the particle surface,

$$\mathcal{V} = \frac{\varepsilon a E_0^2}{\eta} v_0(f, \zeta, \mathrm{Du}, a, D), \quad (2)$$

where E_0 is the electric field magnitude, ε is the electrolyte permittivity and η its viscosity. The reduced slip velocity v_0 is a non-dimensional function of the electric field frequency f, the zeta potential of the particle ζ, the Dukhin number Du (i.e. the ratio of surface to bulk conductance), the particle radius a and the electrolyte diffusivity D.

The function v_0 is represented in Figure 6 for the polystyrene particles and experimental conditions used in this work. In the plots we can observe how the velocity decays for frequencies beyond the reciprocal of the diffusion time,

$$f_{CP} = \frac{D}{2\pi a^2}. \quad (3)$$

This is a consequence of the diffusion equation governing the concentration of the electrolyte. The qualitative analysis and mathematical description of CPEO based on the power expansion on the electric field amplitude can be found in Ref. [14].

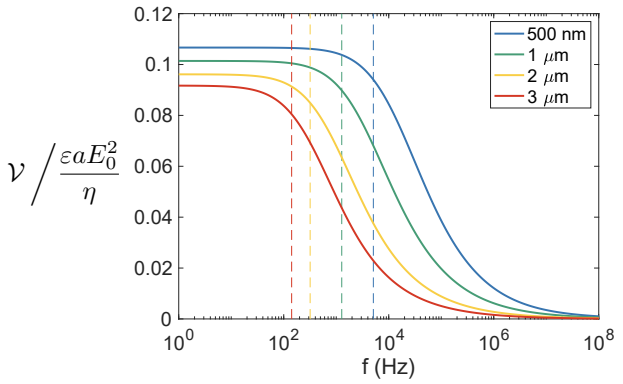

FIG. 6. Reduced slip velocity as a function of the electric field frequency for the particle range used in this work. For the calculation, we supposed a KCl electrolyte ($D = 2 \times 10^{-9}$ m^2/s) having a conductivity of 1.7 mS/m and a particle zeta potential of -60 mV.

B. Hydrodynamic particle-wall interaction

The CPEO flows become distorted when in the vicinity of a domain boundary, such as the walls in a microfluidic channel as shown in Figure 7. The distortion causes a hydrodynamic force leading to particle-wall interaction. Depending on the relative direction of the applied electric field with respect to the channel wall, the interaction could be either attractive, repulsive or have tangential components to the wall [28, 29]. In our case the electric field is parallel to the channel wall, meaning that the interaction is repulsive (Figure 7). The repulsion velocity can be described in the limit of large separation $a/z \ll 1$ by equation (4)

$$u = \mathcal{V}\frac{3a^2}{8z^2}. \quad (4)$$

This expression was obtained by Yariv [30] in the context of induced-charge electroosmosis (ICEO).

We demonstrated in a previous publication [13] that CPEO repulsion mechanism is dominant for low conductivity electrolytes (up to $\sim$ 15 mS/m) and low electric field frequencies (up to $\sim$ 10 kHz). Other repulsion mechanisms such as the resulting from DEP interaction [31, 32] can only account for the interaction at larger frequencies and conductivities. Also, this interaction decays with the fourth power of the separation distance, $u_{DEP} \sim 1/z^4$, meaning that the hydrodynamic interaction is effective at a longer range than DEP. In the case of ICEO, although this phenomenon produces similar flow patterns [33], we showed that appreciable surface conductances (i.e. Dukhin numbers) imply negligible induced charge in dielectrics [34], and thus cannot be responsible for the interaction.

We use CPEO theory to predict the concentration distribution at the end of the channel of the bacterial cells. For this purpose, we compute the trajectories of

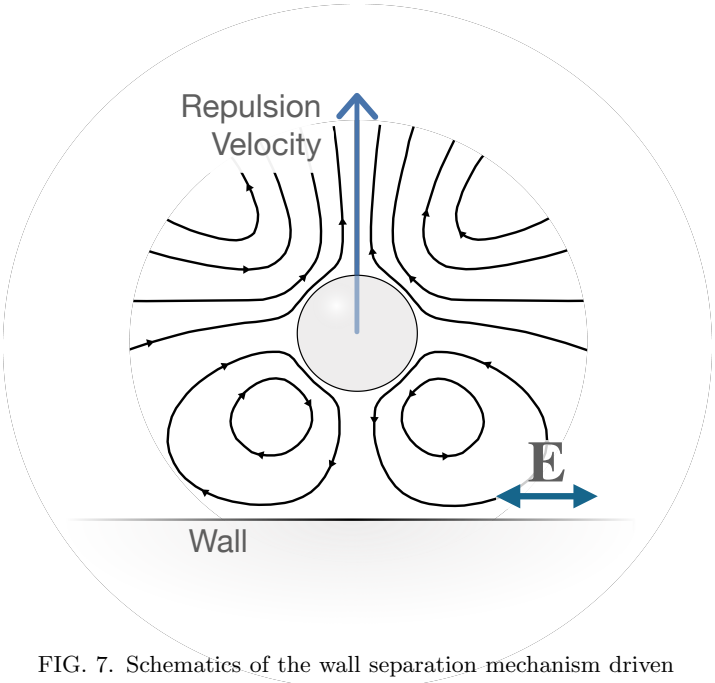

FIG. 7. Schematics of the wall separation mechanism driven by the CPEO flows around particles when the electric field is applied parallel to the wall.

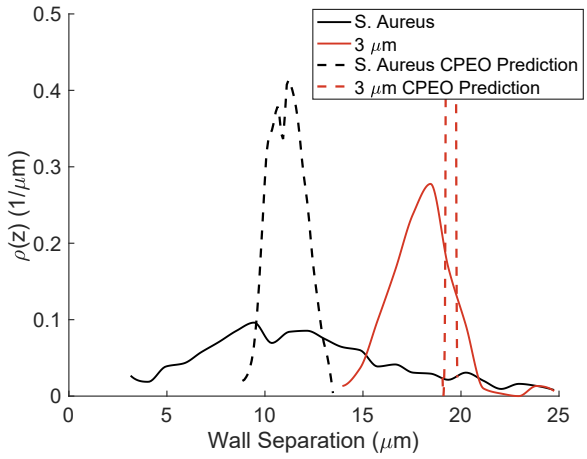

FIG. 8. Comparison of the bacteria concentration distribution at the end of the channel as measured at the end of the channel (solid black line) and predicted by the CPEO theory (dashed black curve). CPEO concentration profile was obtained simulating 10^3 particles with a size and zeta-potential distribution according to Fig. 2, $K_s = 1$ nS and an initial distribution according to the observations.

a $N = 10^3$ particle population whose size and zeta potential distributions correspond to those shown in Figure 2. Additionally, the surface conductance of the particles was set to $K_s = 1$ nS [26] with a 20% dispersion; and the initial separation from the wall was a uniform distribution based on experimental observations of the initial width of the particle stream. The numerical results are presented in Figure 8. We can observe in this Figure that the maximum of the distribution can be predicted by CPEO. However, we obtain a wider distribution in the experiment. This could be attributed to cell-cell adhesion and particle-particle interaction while flowing in the channel given the high concentration used in the experiments. Future work will focus in elucidating the origin of this observed dispersion.

We also include in the figure a prediction of the separation induced by CPEO of a particle with the same experimental features of the 3 μm carboxylate particles including the experimental distribution found in the zeta potential measurements. The initial separation was also based on experimental observations. The predicted separation exceeds the experimental observations, in agreement with previous studies [15] given the electric field magnitude range in which the experiments were performed.

V. CONCLUSIONS

We have demonstrated that the hydrodynamic particle-wall interaction caused by the CPEO flows around particles in the micro-scale can be used to fractionate population mixtures based on size and surface charge. For this purpose, we used five different populations of polystyrene particles having different sizes, ranging from 500 nm to 3 μm in diameter, and surface charges (with zeta-potentials from -15 mV to -78 mV).

Previous experimental work demonstrating Charge-based separation in microfluidic devices actuated with electric fields [35, 36] could be explained by the CPEO particle-wall interaction.

We have also shown that this separation technique can also be applied to a bacterial population, which we have isolated from 3 μm polystyrene beads, in reasonable accordance with CPEO predictions.

ACKNOWLEDGEMENTS

We acknowledge Xiang Wang from University of Southampton and Prof. Mark Sutton from UKHSA for providing the bacteria culture.

Appendix A: Optimisation of fractionation efficiency

We used the particle-wall separation predictions from CPEO theory to find the optimal parameters and maximise the fractionation capabilities of the device. Our purpose is to find the maximum wall separation for the biggest possible flow rate. The strategy is to find these parameters for the case of the particle population most susceptible to the CPEO effects (i.e. the 3 μm carboxylate particles). In that way, we will maximise the resolution of the fractionation inside the channel as these particles will migrate towards the centre-most sections of the channel, leaving room for the rest of populations.

The particle-wall separation at the end of the channel h and the slip velocity at the particle surface $\mathcal{V}$ were related for the CPEO interaction in a previous publication [15]:

$$\mathcal{V} = \frac{32}{3}\frac{V_{max}W^3}{a^2L}[f(h/W) - f(h_0/W)] \tag{A1}$$

where V_{max} is the maximum velocity of the pressure-driven flow, L and W are the length and width of the channel, respectively; h_0 is the particle-wall separation at the beginning of the channel and $f(\xi) = (18(1-2\xi)^2 - 9(1-2\xi)^4 + 2(1-2\xi)^6 - 12\log|1-2\xi|)/1536$.

In this equation, the electrical parameters and the particle properties are enclosed in the slip velocity as presented in equation (2). Additionally, maximum pressure-driven flow velocity V_{max} and flow rate Q are related in a planar Poiseuille flow by $Q = 2WV_{max}/3$. This means that for particles with a given set of properties (size, zeta potential and surface conductance) in a channel with a given dimensions (width and length in our two-dimensional model), to maintain the particle-wall separation at the end of the channel with an increasing flow rate, we must increase the electric field magnitude as $E_0 \sim \sqrt{Q}$.

However, we obviously cannot keep increasing the electric field indefinitely. In fact, the analysis of the CPEO performed in our previous work [15] concludes that for electric field magnitudes above ~ 100 kV/m the CPEO flows become severely disrupted and the experimental repulsion falls below the theory predictions, making the phenomenon inefficient for particle separation. This limitation turns the optimisation process to acting on the channel design: increasing the flow rate while achieving the same wall separation at the end of the channel in a capped electric field magnitude leads to an increasing channel length as $L \sim Q$.

That is, longer channels will balance the flight time of particles flowing at a bigger flow rate, $\tau \sim L/V_{max}$. The electrical design of our setup brings yet another limitation to the optimisation, this time to the maximum length of our channel. The design presented in Figure 1 shows that the electric field is applied through electrodes positioned at two opposite inlets, meaning that the electric field magnitude is affected by the channel length – if we apply a voltage ϕ_0 at the electrodes, the electric field in the channel will scale as $E_0 \sim \phi_0/L$. The maximum electric field voltage that we can apply to the electrodes within reason (≈ 900 Volts of amplitude) sets an upper limit for the channel length which maintains the electric field magnitude.

In short, the optimisation process translates into a trade-off in deciding the channel length: it should be long enough for allowing sufficient flight time of the particles, but this length is restricted by the electric field magnitude we want to achieve. In Figure 9 we show this compromise for a fixed particle population (3 μm carboxylate particles), applied voltage (900 Volts of amplitude), and flow rate ($Q = 7.5$ μL/h). As different

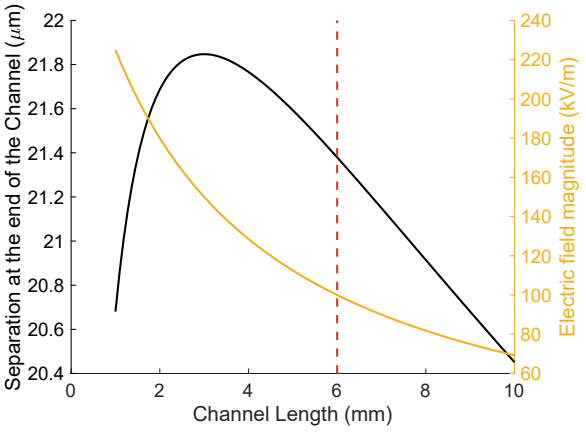

FIG. 9. Separation at the end of the channel h as a function of the channel length L as given by equation (A1). Slip velocities are computed for a 3 μm carboxylate particle, $f = 50$ Hz, $Q = 7.5\mu$L/h, and a KCl electrolyte with a conductivity of 1.7 mS/m. The red vertical line marks the channel length for which the electric field in the channel is 100 kV/m.

flow rates will only displace the plot vertically, we find that we are interested in channel lengths to be as close to $L = 3$ mm as possible. We conclude that if we stretch the field magnitude to the upper limits of the CPEO description, the most satisfactory channel length should be around $L = 5$ mm. Further optimisation of the channel design with an electrode rearrangement will allow higher throughputs achieving similar separation capabilities.

[1] N. Leggieri, A. Rida, P. Francois, and J. Schrenzel, Current opinion in infectious diseases **23**, 311 (2010).
[2] S. Narayana Iyengar, T. Kumar, G. Mårtensson, and A. Russom, Electrophoresis **42**, 2538 (2021).
[3] Y. Zhang, Y. Zhou, Y. Yang, and D. Pappas, Analyst **146**, 2110 (2021).
[4] P. Ohlsson, K. Petersson, P. Augustsson, and T. Laurell, Scientific reports **8**, 1 (2018).
[5] J. Rufo, F. Cai, J. Friend, M. Wiklund, and T. J. Huang, Nature Reviews Methods Primers **2**, 1 (2022).
[6] H. W. Hou, R. P. Bhattacharyya, D. T. Hung, and J. Han, Lab on a Chip **15**, 2297 (2015).
[7] S. Park, Y. Zhang, T.-H. Wang, and S. Yang, Lab on a Chip **11**, 2893 (2011).
[8] S. Zelenin, J. Hansson, S. Ardabili, H. Ramachandraiah, H. Brismar, and A. Russom, Biotechnology letters **37**, 825 (2015).
[9] D. Van Assche, E. Reithuber, W. Qiu, T. Laurell, B. Henriques-Normark, P. Mellroth, P. Ohlsson, and P. Augustsson, Scientific reports **10**, 1 (2020).

[10] J. P. Beech, P. Jönsson, and J. O. Tegenfeldt, Lab on a Chip **9**, 2698 (2009).

[11] V. Calero, P. Garcia-Sanchez, C. Honrado, A. Ramos, and H. Morgan, Lab on a Chip **19**, 1386 (2019).

[12] R. J. Gillams, V. Calero, R. Fernandez-Mateo, and H. Morgan, Lab on a Chip **22**, 3869 (2022).

[13] R. Fernandez-Mateo, V. Calero, H. Morgan, P. Garcia-Sanchez, and A. Ramos, Physical Review Letters **128**, 074501 (2022).

[14] R. Fernández-Mateo, P. García-Sánchez, V. Calero, H. Morgan, and A. Ramos, Journal of Fluid Mechanics **924** (2021).

[15] R. Fernandez-Mateo, H. Morgan, A. Ramos, and P. Garcia-Sanchez, Physics of Fluids (2023).

[16] J. M. Martel and M. Toner, Annual review of biomedical engineering **16**, 371 (2014).

[17] C. Liu, J. Guo, F. Tian, N. Yang, F. Yan, Y. Ding, J. Wei, G. Hu, G. Nie, and J. Sun, ACS nano **11**, 6968 (2017).

[18] F. Tian, W. Zhang, L. Cai, S. Li, G. Hu, Y. Cong, C. Liu, T. Li, and J. Sun, Lab on a Chip **17**, 3078 (2017).

[19] M. Yamada, M. Nakashima, and M. Seki, Analytical chemistry **76**, 5465 (2004).

[20] M. Pødenphant, N. Ashley, K. Koprowska, K. U. Mir, M. Zalkovskij, B. Bilenberg, W. Bodmer, A. Kristensen, and R. Marie, Lab on a Chip **15**, 4598 (2015).

[21] X. Lu and X. Xuan, Analytical chemistry **87**, 6389 (2015).

[22] E. Kłodzińska, M. Szumski, K. Hrynkiewicz, E. Dziubakiewicz, M. Jackowski, and B. Buszewski, Electrophoresis **30**, 3086 (2009).

[23] E. Kłodzińska, M. Szumski, E. Dziubakiewicz, K. Hrynkiewicz, E. Skwarek, W. Janusz, and B. Buszewski, Electrophoresis **31**, 1590 (2010).

[24] S. Halder, K. K. Yadav, R. Sarkar, S. Mukherjee, P. Saha, S. Haldar, S. Karmakar, and T. Sen, SpringerPlus **4**, 1 (2015).

[25] R. Fernández-Mateo, V. Calero, P. García-Sánchez, A. Ramos, and H. Morgan, Microfluidics and Nanofluidics **27**, 19 (2023).

[26] A. van der Wal, M. Minor, W. Norde, A. J. Zehnder, and J. Lyklema, Journal of Colloid and Interface Science **186**, 71 (1997).

[27] N. Gamayunov, V. Murtsovkin, and A. Dukhin, Colloid J. USSR (Engl. Transl.);(United States) **48** (1986).

[28] J. R. Smart and D. T. Leighton Jr, Physics of Fluids A: Fluid Dynamics **3**, 21 (1991).

[29] J. Blake and A. Chwang, Journal of Engineering Mathematics **8**, 23 (1974).

[30] E. Yariv, Proceedings of the Royal Society A: Mathematical, Physical and Engineering Sciences **465**, 709 (2009).

[31] E. Yariv, Physics of fluids **18**, 031702 (2006).

[32] E. Yariv, Soft Matter **12**, 6277 (2016).

[33] M. Z. Bazant and T. M. Squires, Physical Review Letters **92**, 066101 (2004).

[34] V. Calero, R. Fernández-Mateo, H. Morgan, P. García-Sánchez, and A. Ramos, Physical Review Applied **15**, 014047 (2021).

[35] C. Thomas, X. Lu, A. Todd, Y. Raval, T.-R. Tzeng, Y. Song, J. Wang, D. Li, and X. Xuan, Electrophoresis **18**, 320 (2017).

[36] B. D. Ho, J. P. Beech, and J. O. Tegenfeldt, Micromachines **11**, 1014 (2020).

Paper I

Low-frequency electrokinetics in a periodic pillar array for particle separation

Summary of Results

The success of CPEO in predicting particle-wall separation finally explains the behaviour of electrokinetic-biased DLD fractionation at low electric field frequencies and low electrolyte conductivities. In this work, a procedure was developed to numerically simulate particle-wall interaction predicted by CPEO in a DLD pillar array, and to compare the results with the previously published observations [35]. For this purpose, the fields were solved using COMSOL and then the results transferred to MATLAB to simulate the particle trajectories.

Contribution Statement

Garcia-Sanchez, Calero, Ramos and Morgan had the original idea of checking the effects of the CPEO particle-wall repulsion between the polystyrene particles and the walls of the pillars in the array. I wrote the code for translating the COMSOL fields into MATLAB for particle simulation, and Calero performed the simulations. Calero and I contributed to the enhancement of the code while performing the simulations. Calero wrote the first version of the manuscript. Morgan, Ramos and Garcia-Sanchez provided supervisory support. All authors contributed to the final version of the manuscript, which is under review in the *Journal of Chromatography A* as of July 2023.

Low-frequency electrokinetics in a periodic pillar array for particle separation

Víctor Calero,[1,2] Raúl Fernández-Mateo,[3] Hywel Morgan,[3] Pablo García-Sánchez,[1,*] and Antonio Ramos[1]

[1] *Depto. Electrónica y Electromagnetismo. Facultad de Física. Universidad de Sevilla. Avda. Reina Mercedes s/n, 41012. Sevilla (Spain).*

[2] *International Iberian Nanotechnology Laboratory (INL), Braga 4715-330, Portugal.*

[3] *School of Electronics and Computer Science, University of Southampton, Southampton SO17 1BJ, United Kingdom.*

Deterministic Lateral Displacement (DLD) exploits periodic arrays of pillars inside microfluidic channels for high-precision sorting of micro- and nano-particles. Previously we demonstrated how DLD separation can be significantly improved by the addition of AC electrokinetic forces, increasing the tunability of the technique and expanding the range of applications. At high frequencies of the electric field (>1kHz) the behaviour of such systems is dominated by Dielectrophoresis (DEP), whereas at low frequencies the particle behaviour is much richer and more complex. In this article, we present a detailed numerical analysis of the mechanisms governing particle motion in a DLD micropillar array in the presence of a low-frequency AC electric field. We show how a combination of Electrophoresis (EP) and Concentration-Polarisation Electroosmosis (CPEO) driven wall-particle repulsion account for the observed experimental behaviour of particles, and demonstrate how this complete model can predict conditions that lead to electrically induced deviation of particles much smaller than the critical size of the DLD array.

I. INTRODUCTION

Over the last decades, there has been an increased interest in the development of microfluidic particle separation techniques. Low-volume high-precision fractionation methods are important for the development of devices capable of performing full analytical processes on a single platform. Examples include the isolation, detection and monitoring of a wide range of bioparticles (such as circulating tumour cells (CTCs), bacteria or extracellular vesicles [1–4]) from complex samples that ultimately enable early diagnosis and monitoring of disease.

Deterministic Lateral Displacement (DLD) is a promising microfluidic separation approach that delivers high-resolution continuous-flow size-based separation of particles over a wide range of sizes, from nanoparticles to cells that are tens of micrometers in size [5, 6]. DLD devices take advantage of laminar flow on the microscale to sort particles in a deterministic way based on a specific geometry of an array of micro-pillars. In the DLD geometry each row of posts is displaced a given distance ($\Delta\lambda$) from the previous, defining a periodicity N given by:

$$N = \frac{\lambda}{\Delta\lambda} \tag{1}$$

where λ is the distance between consecutive rows of pillars. Figure 1 shows a diagram of the typical DLD pillar array geometry and the physical mechanism responsible for size-based separation. The shift in the consecutive rows gives rise to a separatrix streamline which divides the fluid flow into portions passing above and below the next post. If a particle is bigger than the minimum distance from the separatrix to the nearest post, upon interaction with this post, it will be displaced towards the portion of fluid passing above the following post. As a result, particles follow the deviation angle defined by the array geometry ($\theta_D = \arctan(1/N)$), bumping on the posts and displacing laterally (dark particles in Figure 1). If on the contrary, the particle is smaller than the distance from the separatrix to the post, it is not displaced by the posts and will remain in the fluid passing below the next post, following an overall straight trajectory with zero net lateral displacement, zigzagging around the pillars (light particles in Figure 1). The critical diameter (D_c) is thus defined as the diameter above which the particles follow deviating trajectories and is therefore determined by the width of the separatrix near the posts. For a more detailed description of this mechanism see [7].

Since first reported by Huang *et al.* [8], DLD separation has been extensively studied and enhanced. A particularly interesting and promising approach consists of coupling DLD with external fields, turning passive DLD size-based separation into active and tunable sorting that can target additional physical properties of the particles rather than size. Amongst the many options, coupling DLD with electric fields has proven to be a very useful approach with a rich number of physical mechanisms leading to enhanced particle separation. This approach was first reported by Beech *et al.* [9], applying an AC electric field along the DLD channels in the direction parallel to the fluid flow. They showed tunable separation of 3 μm and 5 μm diameter particles inside a DLD device with 6 μm critical diameter, and attributed the induced deviation to Dielectrophoresis (DEP). Later [10] they showed that the particle behaviour is much richer than first claimed and explored how the deviation depended on the suspending electrolyte conductivity, the particle charge and the electric field frequency.

* Corresponding author: pablogarcia@us.es

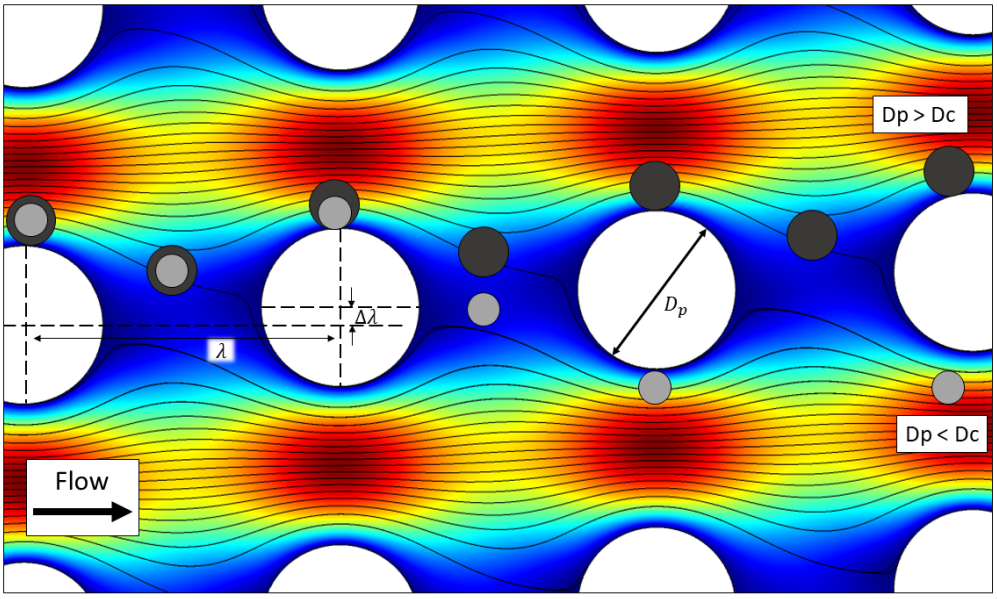

FIG. 1. Diagram representing a typical DLD cylindrical pillar array geometry. The passive size-based separation mechanism relies on the separatrix streamline which divides the flow passing above and below the following post. Particles bigger than a critical diameter D_c are displaced by the posts periodically while particles smaller follow the streamlines in an overall straight trajectory. The colour map represent the magnitude of the fluid velocity.

In recent articles, we explored the induced deviation of particles smaller than the D_c when an AC electric field is applied orthogonal to the fluid flow [11, 12]. We first characterised the particle behaviour and induced separation of 500 nm, 1 μm and 3 μm in a DLD with a D_c of 6.3 μm as a function of the electric field frequency. Two different regimes were identified. At high frequencies ($>$ 1 kHz), particle behaviour was dominated by DEP whereas at low frequencies other mechanisms came into play. The scaling laws governing the electrokinetic induced behaviour at both, high and low frequencies were explored. It was demonstrated that negative DEP (nDEP) drove the separation at high frequencies, and good agreement was found between the experimental results and numerical simulations. At low frequencies dependence of the separation was characterised as a function of the magnitude of the electric field, particle size and fluid velocity. A full theoretical model was not available at the time to account for the observations.

In this paper, we present a thorough and detailed numerical study of the low-frequency AC electrokinetic behaviour of the particles within a DLD pillar array. The model considers the low-frequency oscillating Electrophoresis (EP) along the electric field lines around the pillars together with wall-particle repulsion that occurs during EP [13–15]. We recently described the latter mechanism as driven by stationary electroosomotic (EO) flows around the particles due to Concentration-Polarization (CP) of the electrolyte surrounding the particle, termed CPEO [16, 17]. The results are in excellent agreement with the observed experimental trends. This last analysis completes the understanding of the electrokinetic behaviour of particles inside the DLD devices and provides a full theoretical framework to explain the electrokinetic biased DLD particle separation.

II. THEORY

A. High frequency regime ($f \gtrsim 1$kHz)

Figure 2 shows a diagram of the two different regimes of AC electrokinetic induced deviation in a DLD channel for high and low frequencies of the electric field. At high frequencies, the DEP force dominates the particle behaviour. The force arises from the spatial gradient in the electric field due to the insulating pillars (see Figure 2a). The time average DEP acting on a particle subjected to an AC field [18, 19] $\mathbf{E} = \mathrm{Re}[\mathbf{E}_0(\mathbf{r})e^{i\omega t}]$ is given by:

$$\mathbf{F}_{\mathrm{DEP}} = \pi a^3 \varepsilon \mathrm{Re}[\tilde{f}_{CM}] \nabla |\mathbf{E}_0|^2 \qquad (2)$$

where a is the particle radius, ε the medium permittivity, $\tilde{f}_{CM}$ is the Clausius-Mossotti factor and Re[...] denotes the real part of the function between brackets. The parameter $\tilde{f}_{CM}$ relates the polarisabilities of the particle and the surrounding medium. When a particle is less polarisable than the medium, $\mathrm{Re}[\tilde{f}_{CM}] < 0$ it experiences

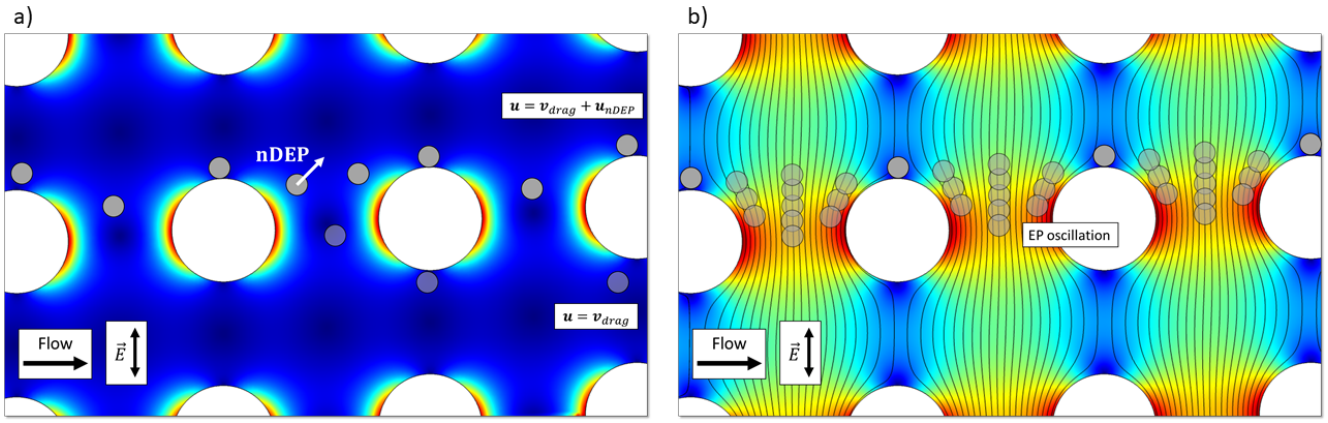

FIG. 2. Diagram of electrically tuned DLD separation. (a) Negative DEP induced separation - Colour map represents the intensity of the nDEP force. (b) Low frequency separation - Colour map represents the magnitude of the electric field.

nDEP, i.e. it is repelled from high electric field gradients. When this occurs in the DLD shown in Figure 2a, the particles are repelled from the downstream gaps between the posts. If the nDEP repulsion is strong enough to disrupt the particle trajectories and make them cross the separatrix streamline, the particles are therefore prevented from zigzagging between the posts and are forced to follow a deviating trajectory. Under the influence of a DEP force and a fluid velocity field $\mathbf{v}_f$, the particle velocity $\mathbf{u}$ is given by:

$$\mathbf{u} = \mathbf{v}_f + \mathbf{u}_{\mathrm{DEP}} \tag{3}$$

with $\mathbf{u}_{\mathrm{DEP}} = \frac{a^2 \varepsilon \mathrm{Re}[\tilde{f}_{CM}]}{6\eta} \nabla |\mathbf{E}_0|^2$, where η is the dynamic viscosity of the fluid. Following the analysis in Calero *et al.* [12], a dimensionless expression of equation (3) can be derived using the post radius R, a typical fluid velocity U, and a typical electric field magnitude E_0:

$$\tilde{\mathbf{u}} = \tilde{\mathbf{v}}_f + \mathrm{sgn}(\mathrm{Re}[\tilde{f}_{CM}]) N \tilde{\nabla} |\tilde{\mathbf{E}}_0|^2 \tag{4}$$

In this equation, the dimensionless parameter $N = \frac{\varepsilon E_0^2 a^2}{6\eta R U} |\mathrm{Re}[\tilde{f}_{CM}]|$ quantifies the relative contribution of the DEP force to the net particle velocity, and therefore the deviation induced by this force scales with the magnitude of this parameter.

B. Low frequency regime ($f \lesssim 1$kHz)

For frequencies below ∼1 kHz, other forces come into play. Although the oscillating EP has a zero time-average displacement, it leads to an oscillation of the particle along the electric field lines with a velocity $\mathbf{u}_{\mathrm{ep}}$ given by the Helmholtz-Smoluchowski equation:

$$\mathbf{u}_{\mathrm{ep}} = \frac{\varepsilon \zeta}{\eta} \mathbf{E} \tag{5}$$

where ζ is the zeta potential of the particle [20]. We hypothesise that this oscillation leads to a pronounced interaction between the walls of the DLD posts and the finite-sized rigid particles as they flow along the microchannels, creating an induced deflection.

However, low-frequency EP is not the only phenomenon that is present at low frequencies. We recently reported the presence of Concentration-Polarization Electroosmotic (CPEO) flows around charged dielectric particles subjected to low-frequency AC electric fields [16]. The particle surface conductance leads to a perturbation in the local electrolyte concentration, and therefore in the electroosmotic slip velocity at the particle surface, creating a stationary quadrupolar flow pattern, as shown in Figure 3a. The CPEO flows have a non-zero time average velocity with a quadratic dependence on the electric field magnitude. Their magnitude decreases with electrolyte conductivity and AC field frequency and increases with the particle surface charge. A complete theoretical description of this mechanism can be found in [16].

In a previous publication [15] we demonstrated that CPEO flow is the dominant mechanism that creates the observed particle-wall repulsion during Electrophoresis of charged dielectric particles. Our results show that the hydrodynamic interaction due to CPEO flows overcomes the DEP forces in the low frequency regime and that the latter can only explain the observed particle-wall separation at high frequencies. In the presence of a low frequency AC electric field and with the particle situated in the vicinity of a wall, the CPEO flow patterns become distorted, as shown in Figure 3b. This hydrodynamic interaction gives rise to a net particle velocity with respect to the nearby wall which can be calculated following the method of reflections [21]. For the case of an electric field parallel to the wall, there is a net particle repulsion perpendicular to the wall given by [22, 23]:

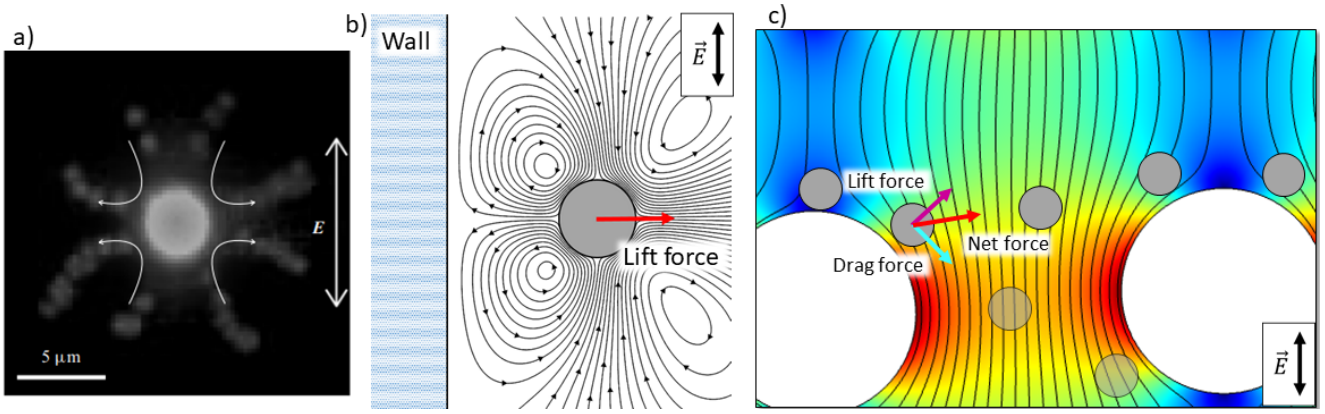

FIG. 3. Principles of CPEO assisted particle deviation in DLD arrays. (a) Experimentally observed CPEO flows around a 3 μm carboxylate particle ($f = 282$ Hz and $E = 80$ kV/m) using 500 nm fluorescent spheres as flow tracers. Reproduced from Fernández-Mateo *et al.* [16] (with permission from Cambridge University Press 2021). (b) Particle repulsion from a flat wall induced by CPEO flows around the particles. (c) Deviation inside DLD post array induced by CPEO wall repulsion - Colour map represents the magnitude of the electric field.

$$\mathbf{u}_{\text{rep}} = v_0 \frac{3a^2}{8h^2}\hat{z}, \tag{6}$$

where h is the distance from the particle center to the wall and $\hat{z}$ the unit vector which is perpendicular to the wall. The constant v_0 is the CPEO slip velocity at the surface of the particle [16]. This is the leading-order term in the method of reflections for small values of a/h. A similar analysis can be used to predict the particle velocity perpendicular to the wall for the case of an electric field perpendicular to the wall. In this case, the CPEO flow leads to wall-particle attraction with a velocity given by [23]:

$$\mathbf{u}_{\text{at}} = -v_0 \frac{3a^2}{4h^2}\hat{z}, \tag{7}$$

Smart and Leighton [23] also showed that, when the field is at an angle to the surface of the flat wall ($0 < \varphi < \pi/2$), there is an extra component to the particle velocity, that is tangential to the wall given by:

$$\mathbf{u}_{\text{tan}} = -v_0 \frac{3a^2}{4h^2} \sin\varphi\cos\varphi\hat{x}, \tag{8}$$

In this paper, we describe the role of this mechanism in a DLD array as particles are repelled from the posts. We hypothesize that the CPEO particle-wall repulsion plays a mayor role in the low-frequency electrokinetic-induced deviation. Every time a particle approaches a DLD pillar, the hydrodynamic interaction leads to particle repulsion from the pillar. If this repulsion is strong enough, then particles are forced to switch from a zigzagging trajectory to the displacement mode, following the array deviation angle (see Figure 3c).

III. NUMERICAL METHODS

A. High frequency regime simulations

At high electric field frequencies, the only forces acting on the particles are the hydrodynamic drag force from the net fluid flow along the microfluidic channels and DEP. To simulate this situation we followed the exact same methods previously described by Calero *et al.* [12]. The spatial distribution of the electric field and fluid flow velocity is first calculated inside a DLD unit cell (see Figure 4a) using Finite Element Analysis and the software COMSOL Multiphysics v5.4. To calculate the fluid flow, the 2D Stokes equation ($Re \sim 10^{-3}$) was solved with periodic boundary conditions in the perpendicular and longitudinal directions, enforcing a zero net velocity in the direction perpendicular to the flow and mean fluid velocity magnitude of $U = 100$ μm/s in the longitudinal direction. A no-slip boundary condition was used at the surface of the posts. The electric field $\mathbf{E}$ was calculated from the perturbation $\mathbf{E}'$ of a uniform field $E_0\hat{y}$. For the case of an electric field in the direction y (perpendicular to the fluid flow):

$$\mathbf{E} = \mathbf{E}' + E_0\hat{y} \rightarrow \phi = \phi' - E_0 y \tag{9}$$

Thus, to calculate $\mathbf{E}'$ the Laplace equation was solved for the electrical potential ϕ' with periodic boundary conditions at the boundaries of the unit cell. To model the pillars as insulators the following condition was used at the surface of the posts:

$$\frac{\partial\phi}{\partial n} = 0 \rightarrow \frac{\partial\phi'}{\partial n} = E_0 n_y \tag{10}$$

where n_y is the y-component of a unit vector normal to the boundary.

Figure 4a shows the spatial dependence of the fluid velocity and electric field magnitude in the DLD unit cell. The trajectories of $n > 2000$ particles inside a DLD unit cell are simulated for different initial positions equally distributed and covering the entire possible range, with the velocity given by equation (3).

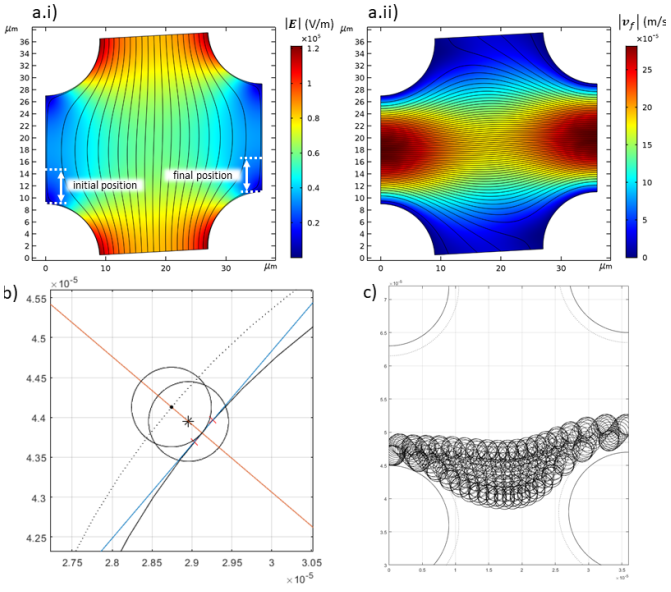

FIG. 4. (a.i) Electric field distribution calculated in the DLD unit cell, marking the initial and final position of the particles. (a.ii) Fluid flow profile inside the DLD unit cell. (b) Hard wall inelastic-collision correction. The initial position (marked with an asterisk in the particle centre) is corrected for the distance of the overlap between particle and post, to the position marked with a dot in the particle centre. (c) Example trajectory of the deviation of a 3 μm particle at low frequencies induced by CPEO and EP oscillations.

The initial and final positions (as defined in Figure 4a.i) are related by a transfer function which can then be used to calculate, using linear interpolation, the final position of any particle entering the unit cell for any value of initial position [12, 24]. The transfer function will thus depend on the ratio between the fluid drag force and the DEP force and can be used to estimate the deviation angle after a particle crosses a large number of unit cells. In every iteration, a particle in deviation mode exits the unit cell at the same distance from the nearest post at which it entered. This is then reflected in the transfer function by crossing the line of slope 1 that passes through the origin, i.e. in the trajectory across the unit cell the initial and final positions (as defined in Figure 4a.i) are equal.

In this study we used parameters that enabled comparison with the experimental results [12]: $U = 100\mu$m/s, $\mathrm{Re}[\tilde{f}_{CM}] = -0.5$, $a = 0.5, 1.5\mu$m and $|\mathbf{E}_0| < 80$kV/m and with a symmetric DLD geometry with $D_p = \lambda/2$ and $N = 18$ ($\theta = 3.18°$). The particle-wall interaction was modeled as a non-elastic hard wall collision as described by Kim *et al.* [24] and in our previous work [12]. Briefly, we considered an exclusion zone of one particle radius around the posts. Thus particles with an initial/final position closer than a to a post were considered to enter/exit the unit cell at a distance a from that post. In the transfer function, this translates into removing the prohibited initial and final (exit) positions from this function [12].

B. Low-frequency regime simulations

In the low-frequency regime, the approach used for high frequencies is not valid because of the significant electrophoretic oscillation of particles. This introduces an extra degree of complexity through the addition of a new parameter, the phase of the electric field. This is because the phase of the field with which the particle enters the unit cell differs from the exiting phase, depending on the time the particle takes to cover the distance of the unit cell. This adds an extra dimension to the numerical simulations and turns the 1D-1D transfer function into a 2D-2D function.

To circumvent this complexity, a different approach was taken by simply simulating the trajectories of a single particle after it has crossed a large number of unit cells. To realise this the electric and fluid fields were exported to MATLAB R2022b and the particle trajectories were calculated across a large number of unit cells (360 unit cells, i.e. 20 periods of the DLD array), until the trajectory converged into either a zig-zag or displacement mode. The components of the particle velocity are:

$$\mathbf{u} = \mathbf{v}_f + \mathbf{u}_{\mathrm{ep}} + \mathbf{u}_{\mathrm{rep}} + \mathbf{u}_{\mathrm{at}} \tag{11}$$

For simplicity the tangential component $\mathbf{u}_{\mathrm{tan}}$ (given by equation (8)) was not considered in the simulations since this component is much smaller than the electrophoretic velocity ($\mathbf{u}_{\mathrm{ep}} \gg \mathbf{u}_{\mathrm{tan}}$). The EP velocity $\mathbf{u}_{\mathrm{ep}}$ is given by equation (5), which for an oscillating field with angular frequency ω and phase φ, $\mathbf{E} = \mathbf{E}_0 \cos(\omega t + \varphi)$, produces an oscillating motion along the electric field lines, only relevant for low values of ω. The values for ζ were measured experimentally and used as input to the model: $\zeta = -70$ mV and $\zeta = -78$ mV for the 1 μm and 3 μm diameter particles, respectively. Since in this case the electric field is neither tangential nor perpendicular to the pillar wall, to calculate the contribution of the CPEO hydrodynamic interaction $\mathbf{u}_{\mathrm{rep}}$ and $\mathbf{u}_{\mathrm{at}}$ were calculated at each point of the unit cell as:

$$\mathbf{u}_{\mathrm{rep}} = v_0 \frac{3a^2}{8h^2} \frac{|E_t|^2}{|E_0|^2} \hat{n}, \tag{12}$$

$$\mathbf{u}_{\mathrm{at}} = -v_0 \frac{3a^2}{4h^2} \frac{|E_n|^2}{|E_0|^2} \hat{n}, \tag{13}$$

where E_t and E_n are, respectively the tangential and normal components of the electric field to the pillar wall at the particle position and $\hat{n}$ a unit vector perpendicular to the wall [25]. The value for v_0 is the only input to the model and was estimated experimentally following the methods described by Fernandez-Mateo *et al.* [15], where the wall-repulsion was measured along a straight channel with the electric field applied parallel to the fluid flow. This was done in conditions that allowed comparison to published experimental data [12] (at an electrolyte conductivity of 2.8 mS/m, an electric field of 50 Hz and 60 kV/m, and particle diameters of 1 and 3 μm): $v_0 = (109.4 \pm 18.6)$ μm/s for 1 μm particles and $v_0 = (324.5 \pm 25.0)$ μm/s for 3 μm particles. In order to estimate v_0 for other electric field magnitudes the measurements at 60 kV/m were used together with the quadratic dependence with $|E|$ predicted by the CPEO model [16].

Finally, the particle-wall interaction was modelled as a hard-wall inelastic collision. At each time step, if a particle approached the post boundary at a distance smaller than a particle radius, the particle position was corrected the same distance in the direction perpendicular to the wall. An example of this correction is given in Figure 4b. A typical trajectory of a 3 μm particle across a DLD unit cell under the influence of a low-frequency electric field ($E_0 = 20$ kV/m and $f = 50$ Hz), i.e. EP and CPEO wall interaction is shown in Figure 4c.

With this model we are replicating the experimental design described in Calero et al. [12] where the devices were pretreated with a surfactant (Pluronic F-127) to avoid particle adhesion and minimize electroosmotic flow [26–28]. Consequently, in the simulations the low frequency is solely caused by electrophoresis.

Note that CPEO flows around the insulating posts are not considered ([12, 29]) due to the fact that the post diameter is larger than the height of the microchannels. Since the upper and lower walls are very close, the no-slip condition significantly reduces the magnitude of these flows.

Also, for simplicity, we have assumed in this regime that the DEP contribution is negligible with respect to the contributions of EP and CPEO. This assumption is supported by experimental data where the low-frequency deviation is demonstrated regardless of the DEP behavior of the particles: induced deviation was observed not only for nDEP particles but, also, for particles with positive DEP (pDEP) or with $\mathrm{Re}[\tilde{f}_{CM}] \sim 0$. Numerical data in the results section validate this simplification.

IV. RESULTS

A. Simulation results and comparison with experimental data

To test the model, the dependence of the deviation angle for 1 μm and 3 μm diameter rigid spheres was analysed as a function of the applied electric field magnitude, at high and low frequencies for an electric field applied perpendicular to the fluid flow. We then compared the results with the experimental data previously reported [12]. The results are summarised in Figure 5. The deviation angle is directly calculated from the net lateral displacement given by the simulations, and is plotted against the ratio $E_0 a/\sqrt{U}$, to enable a direct comparison between all data sets (with different values of U and particle sizes). This is valid since it is the ratio between the quadratic electric forces and the hydrodynamic drag from the fluid flow. This leads to an overlapping set of curves for the nDEP induced deviation. Note that the simulations at high frequencies assume $\mathrm{Re}[\tilde{f}_{CM}] = -0.5$, i.e. the nDEP magnitude is maximum and therefore nDEP induced deviation is also maximum. For the experimental conditions at which the deviation and the parameter v_0 were measured, the nDEP is even weaker for the 3 μm particles with $\mathrm{Re}[\tilde{f}_{CM}] = -0.21$ or is even positive DEP for the 1 μm particles with $\mathrm{Re}[\tilde{f}_{CM}] = 0.12$.

The figure shows that at low frequencies the results from the model (including contributions from EP oscillation and CPEO) match the experimental trends. It predicts a clear difference in the critical electric field, i.e. the value of $|E_0|$ at which the particles switch to the displacement mode, for the two different particle sizes as observed experimentally. Furthermore, the model predicts a critical field lower than that given by the nDEP mechanism and much closer to the experimental results. This is particularly noticeable for the smallest particle size. Importantly, experiments show a much smoother transition from zero lateral displacement to the maximum deviation angle, mainly for the smaller particles. This is not predicted by the simulations, which show an abrupt transition between displacement or zig-zag. This sharp transition is expected from a fully deterministic behaviour of the particles. The smoothness observed experimentally is attributed to experimental artifacts not accounted for in the simulations, mostly the non-uniformity of the electric field magnitude across the channel caused by changes in the local conductivity near the electrodes[30].

Although the deviation angle defined by the DLD array is equal in both experiments and simulations, there is an observed difference in the maximum value of the deviation angle. This is simply due to the specific design of the experimental DLD devices (explained in [12]). The devices have a region near the electrode with zero pillar array offset where fully deflected particles concentrate. Particles in a displacement trajectory reach this region before they arrive at the end of the channel, and

travel in a straight line with zero deviation. Since the experimental deviation angle is estimated from the total displacement at the end of the channel and the channel length, this leads to a smaller angle than that defined by the array geometry.

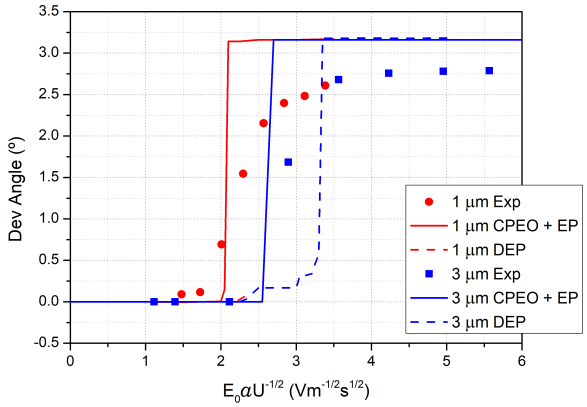

FIG. 5. Comparison of experimental data for 1 μm and 3 μm particles with simulations results: (electrolyte conductivity of 2.8 mS/m and field frequency of 50 Hz) at low frequencies including EP oscillation and CPEO wall interaction (solid lines) and high frequencies with nDEP (dashed lines). Note that the simulation results for the high-frequency deviation of 1 μm and 3 μm collapse and overlap.

B. Low frequency behaviour: contributions of EP and CPEO

The numerical model was then used to analyse the contribution of the CPEO particle-wall interaction to the deviation with a low frequency electric field perpendicular to the flow. For this purpose, particle trajectories were simulated taking into account solely the influence of the EP oscillation or the influence of combination of EP and CPEO. Figure 6 summarises the results for the deviation of 1 μm and 3 μm particles at 50 Hz and a v_0 measured at this frequency and 2.8 mS/m. It shows that the EP oscillation alone can induce deviation of particles via inelastic collision with the pillar walls. We hypothesise that the collisions limits the oscillating motion towards the posts giving a non-zero time average lateral displacement that is magnified after interaction with several posts. The symmetry of this mechanism is broken by the tilt angle of the DLD array, leading to a preferential direction in the post-particle interaction driven by the EP oscillation.

However, as shown in Figure 6, the critical field is significantly reduced when the CPEO wall interaction is included in the simulations. Importantly, there was no deviation when only the CPEO wall-interaction is considered (ignoring the EP oscillation) for any of the two particles sizes, in the range of field amplitudes explored. Figure 6a shows the low frequency deviation for two different particle sizes, demonstrating that the reduction in the critical field is more noticeable for the smallest particles. Figure 6b shows how the deviation of the 3 μm diameter spheres depends on the frequency of the applied electric field. It shows that, as the frequency increases, the influence of the CPEO interaction becomes more prominent. At 50 Hz, the addition of CPEO decreases the critical field magnitude by $\sim 5\%$ whereas for 167 Hz the reduction is more than 30%. This implies that as frequency increases, the contribution of the EP oscillations decreases faster than the CPEO wall interaction.

Figure 7 shows an example of how this mechanism works. It shows the trajectory of a 1 μm diameter rigid sphere in a DLD array under the influence of a 50 Hz field perpendicular to the flow for: (a) the EP force, (b) the CPEO wall-interaction and (c) combination of both. These simulations were done at a field of 43 kV/m, corresponding to the regime where the EP oscillation alone does not induce deviation, but only when combined with CPEO. Figure 7a depicts how, when only the EP force is considered, the particles barely interact with the posts because of the distortion of the electric field lines around the insulating posts. When the CPEO wall interaction is the only mechanism (Figure 7b), particles only pass near the posts for a small portion of their trajectories. Since the CPEO decays with distance to the wall squared, this interaction does not lead to a large change in the particle trajectory. When both mechanisms are combined (Figure 7c), the particle oscillations along the field lines drives the particles near the post walls, maximising the effect of the CPEO particle-wall interaction leading to the induced particle deviation. These results lead to the conclusion that only when both mechanisms are combined, there is an accurate prediction of the observed experimental trends. Thus there is a non-linear dependence of the induced deviation with the electric field magnitude, a decline with the electric field frequency and the electrolyte conductivity and the lack of a direct relationship between the oscillation amplitude and the induced deviation.

C. Comparison between a parallel and a perpendicular field

Finally the particle trajectories were examined with the electric field applied parallel to the fluid flow. This configuration has been experimentally characterised by Tegenfeldt *et al.* [9, 10, 31]. They found very similar trends with nDEP dominating at high frequencies and/or high medium conductivities; the high frequency deviation can be fully explained by DEP. However, deviation at low frequencies is different, with the effect decreasing with the field frequency and electrolyte conductivity. Interestingly, they also showed that the particle surface charge was directly linked to the low frequency induced

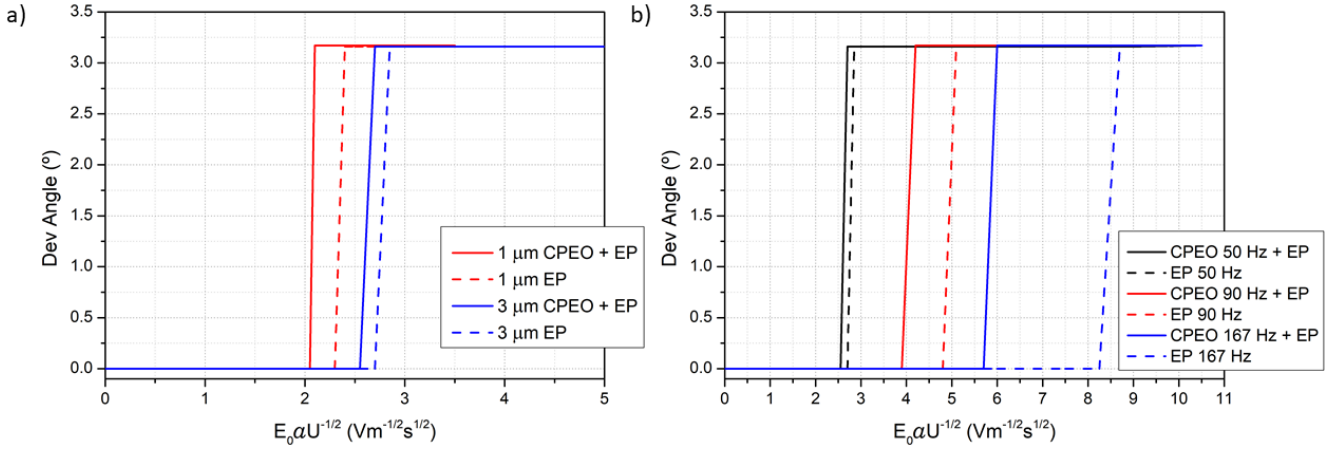

FIG. 6. Comparison of the deviation induced by EP oscillation only and EP oscillation combined with CPEO induced deviation. (a) Two different particle sizes at 50 Hz. (b) 3 μm diameter particles at different field frequencies.

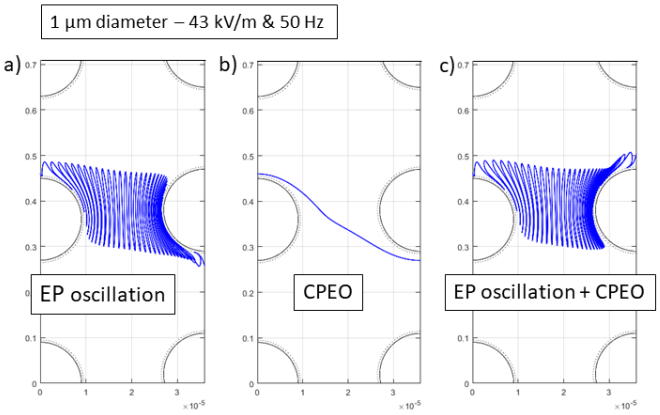

FIG. 7. Example of simulated trajectories of 1 μm diameter particle inside DLD devices with a low (50 Hz) frequency electric field perpendicular to the fluid flow. (a) Contribution only from electrophoretic oscillation. (b) Only CPEO contribution. (c) Combination of CPEO and EP oscillation.

deviation [10]. Under the same conditions, particles with a higher surface charge had a reduced critical electric field magnitude, i.e. they deviated for lower values of field strength. This matches the hypothesis that the low frequency deviation is dominated by a combination of CPEO and EP oscillation, since both mechanisms are stronger for a higher surface charge density. Also, in this case, the EP oscillation occurs in the direction of the fluid flow (along the field lines), so that this mechanism alone could not lead to an increased wall-particle interaction.

The simulations show that when the field is applied in the direction of fluid flow, there is no induced deviation when any of the two mechanisms, CPEO wall interaction or EP oscillation, is considered independently. Only when the two are combined does the electric field force the particles to switch to the displacement mode. In contrast to the perpendicular field, with the field parallel to the fluid flow, the EP oscillation takes place in the direction of the fluid streamlines and so does the inelastic post-particle interaction. As a result, the oscillations alone cannot produce the net displacement required to push particles across the separatrix streamline. Similar to the perpendicular case, when the CPEO acts independently, particles only spend a small fraction of time near the posts, so that the effects of the CPEO wall interaction are largely reduced. Only when the oscillating trajectories drive the particles back and forth near the post wall, does the CPEO effect accumulate forcing the particles to deviate.

Figure 8 shows the simulation results at 50 Hz with the field applied in the direction of the fluid flow (as a function of electric field magnitude). The figure shows a comparison with the maximum nDEP induced deviation. For the 1 μm particles, there is a negligible difference between the critical field magnitude given by the nDEP mechanism and the low frequency induced deviation. However, for the bigger particles of 3 μm, there is a significant reduction in critical field magnitude for the low frequency mechanism. This figure also provides a comparison between the predicted low frequency deviation for an electric field applied perpendicular ($\perp$) and parallel ($\parallel$) to the fluid flow. The predicted deviation of the 3 μm spheres is approximately equal for both field orientations. Nevertheless, the critical field magnitude for the smaller 1 μm diameter particles is significantly lower for the perpendicular field. This result suggests that a perpendicular field is the optimal configuration to maximise the deviation of particles that are substantially smaller than the critical diameter [32].

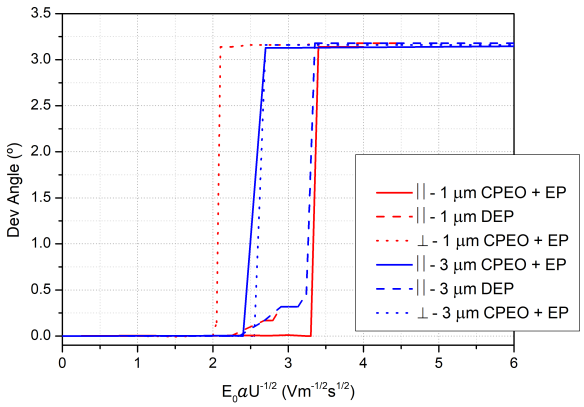

FIG. 8. Comparison between nDEP and low-frequency induced deviation for an electric field applied parallel to the fluid flow (||) and the low-frequency deviation induced by an electric field perpendicular to the fluid flow (⊥). Note that, as in Figure 5, the simulation results for the high-frequency deviation of 1 μm and 3 μm overlap.

V. CONCLUSIONS

In conclusion, these numerical simulations have provided a comprehensive understanding of the factors that govern the low-frequency electrokinetic-induced sorting of particles inside a microfluidic DLD channel. We have demonstrated that the CPEO wall-particle interaction combined with EP oscillation fully explains the deflection induced by low-frequency electric fields, with the simulations matching the experimentally observed trends. Note that electrothermal flows have been neglected, given that this phenomenon occurs at higher electrolyte conductivities.

By establishing a link between the recently reported CPEO mechanism and the low-frequency electrokinetic separation of particles in DLD devices, our model consolidates previous experimental and numerical results, completing the theoretical framework for a full understanding of the behaviour of electrokinetic-biased DLD particle separation systems. The implications of our findings are significant in the design and optimization of DLD devices for particle sorting and fractionation, when combined with electric fields, enabling particles significantly smaller than the critical diameter to be deflected and sorted. The simulations can be used to tailor the physical and electrical properties of the particles to achieve specific separation outcomes, and to optimize the post-array geometry, field frequency and conductivity of the solution to enhance separation efficiency.

ACKNOWLEDGMENTS

P.G.S. and A.R. acknowledge Grant P20-00534 funded by "Consejería de Economía, Conocimiento, Empresas y Universidad (Junta de Andalucía)".

[1] H. Cho, J. Kim, H. Song, K. Y. Sohn, M. Jeon, and K.-H. Han, Analyst **143**, 2936 (2018).
[2] H. W. Hou, M. E. Warkiani, B. L. Khoo, Z. R. Li, R. A. Soo, D. S.-W. Tan, W.-T. Lim, J. Han, A. A. S. Bhagat, and C. T. Lim, Scientific reports **3**, 1259 (2013).
[3] P. Ohlsson, M. Evander, K. Petersson, L. Mellhammar, A. Lehmusvuori, U. Karhunen, M. Soikkeli, T. Seppa, E. Tuunainen, A. Spangar, et al., Analytical chemistry **88**, 9403 (2016).
[4] J. C. Contreras-Naranjo, H.-J. Wu, and V. M. Ugaz, Lab on a Chip **17**, 3558 (2017).
[5] K. Loutherback, J. D'Silva, L. Liu, A. Wu, R. H. Austin, and J. C. Sturm, AIP advances **2**, 042107 (2012).
[6] B. H. Wunsch, J. T. Smith, S. M. Gifford, C. Wang, M. Brink, R. L. Bruce, R. H. Austin, G. Stolovitzky, and Y. Astier, Nature nanotechnology **11**, 936 (2016).
[7] J. McGrath, M. Jimenez, and H. Bridle, Lab on a Chip **14**, 4139 (2014).
[8] L. R. Huang, E. C. Cox, R. H. Austin, and J. C. Sturm, Science **304**, 987 (2004).
[9] J. P. Beech, P. Jönsson, and J. O. Tegenfeldt, Lab on a Chip **9**, 2698 (2009).
[10] B. D. Ho, J. P. Beech, and J. O. Tegenfeldt, Micromachines **11**, 1014 (2020).
[11] V. Calero, P. Garcia-Sanchez, C. Honrado, A. Ramos, and H. Morgan, Lab on a Chip **19**, 1386 (2019).
[12] V. Calero, P. Garcia-Sanchez, A. Ramos, and H. Morgan, Journal of Chromatography A p. 461151 (2020).
[13] L. Liang, Y. Ai, J. Zhu, S. Qian, and X. Xuan, Journal of colloid and interface science **347**, 142 (2010).
[14] L. Liang, S. Qian, and X. Xuan, Journal of colloid and interface science **350**, 377 (2010).
[15] R. Fernandez-Mateo, V. Calero, H. Morgan, P. Garcia-Sanchez, and A. Ramos, Physical Review Letters **128**, 074501 (2022).
[16] R. Fernández-Mateo, P. García-Sánchez, V. Calero, H. Morgan, and A. Ramos, Journal of Fluid Mechanics **924** (2021).
[17] V. Calero, R. Fernández-Mateo, H. Morgan, P. García-Sánchez, and A. Ramos, Physical Review Applied **15**, 014047 (2021).
[18] J. Lyklema, *Fundamentals of Interface and Colloid Science* (Academic Press Limited, 1995).
[19] H. Morgan and N. G. Green, *AC Electrokinetics: colloids and nanoparticles.* (Research Studies Press Ltd., 2003).
[20] M. von Smoluchowski, Bull. Akad. Sci. Cracovie. **8**, 182 (1903).
[21] J. Happel and H. Brenner, *Low Reynolds number hydrodynamics: with special applications to particulate media*, vol. 1 (Springer Science & Business Media, 2012).
[22] E. Yariv, Proceedings of the Royal Society A: Mathematical, Physical and Engineering Sciences **465**, 709 (2009).
[23] J. R. Smart and D. T. Leighton Jr, Physics of Fluids A: Fluid Dynamics **3**, 21 (1991).

[24] S.-C. Kim, B. H. Wunsch, H. Hu, J. T. Smith, R. H. Austin, and G. Stolovitzky, Proceedings of the National Academy of Sciences **114**, E5034 (2017).
[25] J. E. Flores-Mena, P. García-Sánchez, and A. Ramos, Micromachines **14**, 23 (2022).
[26] R. V. Davalos, G. J. McGraw, T. I. Wallow, A. M. Morales, K. L. Krafcik, Y. Fintschenko, E. B. Cummings, and B. A. Simmons, Analytical and bioanalytical chemistry **390**, 847 (2008).
[27] M. Viefhues, S. Manchanda, T.-C. Chao, D. Anselmetti, J. Regtmeier, and A. Ros, Analytical and bioanalytical chemistry **401**, 2113 (2011).
[28] R. Fernández-Mateo, P. García-Sánchez, V. Calero, A. Ramos, and H. Morgan, Electrophoresis **43**, 1259 (2022).
[29] R. Fernández-Mateo, P. García-Sánchez, V. Calero, A. Ramos, and H. Morgan, Electrophoresis **43**, 1259–1262 (2022).
[30] V. Calero, P. Garcia-Sanchez, A. Ramos, and H. Morgan, Biomicrofluidics **13**, 054110 (2019).
[31] B. D. Ho, J. P. Beech, and J. O. Tegenfeldt, Micromachines **12** (2021).
[32] R. J. Gillams, V. Calero, R. Fernandez-Mateo, and H. Morgan, Lab on a Chip **22**, 3869 (2022).

Paper J

InsulatingTravelling-WaveElectrophoresis

Summary of Results

This describes a travelling-wave electrophoresis (TWE) microfluidic device that can drive the rotation of particles around a central axis. Traditionally, TWE is created with a linear array of electrodes within a channel. Each electrode is driven with a sinusoidal voltage with a phase delay between neighbours, producing a travelling wave electric field. This phenomenon has been used for transporting particles undergoing electrophoresis, or fractionating particle populations based on their electrophoretic mobility. Our device consists of a single insulating pillar positioned in the centre of an array of four electrodes, each electrode driven by an ac signal with a 90° phase shift. The dielectric pillar distorts the electric field producing a rotating travelling-wave. An asynchronous stationary electrophoretic motion of the particles is observed, moving concentric to the insulating micro-post. An analytical framework was developed providing excellent agreement with experimental observations. The presence of the dielectric pillar ultimately governs the effect, so this phenomenon is refereed to as insulating TWE (iTWE), to differentiate it from standard TWE that uses a linear array of microelectrodes. The simple design means that the electrodes are far from the particles, reducing the influence of any Faradaic reactions on the particle suspension.

Contribution Statement

This work was first suggested by Ramos and Garcia-Sanchez as a way of testing the frequency behaviour of the CPEO theory. However, the experimental results suggested that CPEO was not playing any significant role in the observed flow behaviour. Ramos first proposed that TWE was the origin of the experimental observations. I, Ramos, Morgan and Garcia-Sanchez designed the devices; I and Calero did the experimental work. I did the experimental data analysis. Ramos, Garcia-Sanchez and I elaborated the theory. I and Garcia-Sanchez did the comparison between the experiments and the theory. Garcia-Sanchez, I and Ramos wrote the first version of the manuscript. Morgan, Ramos and Garcia-Sanchez provided supervisory support. All authors contributed to elaborate the final version of the manuscript, which is in press in the *Physical Review E* as of July 2023.

Insulating Travelling-Wave Electrophoresis

Raúl Fernández-Mateo,[1] Víctor Calero,[2] Hywel Morgan,[1] Pablo García-Sánchez,[2] and Antonio Ramos[2,*]

[1] *School of Electronics and Computer Science, University of Southampton, Southampton SO17 1BJ, United Kingdom.*
[2] *Depto. Electrónica y Electromagnetismo. Facultad de Física. Universidad de Sevilla. Avda. Reina Mercedes s/n, 41012. Sevilla (Spain).*

Travelling-wave electrophoresis (TWE) is a method for transporting charged colloidal particles used in many microfluidic techniques for particle manipulation and fractionation. This method exploits the travelling-wave components of the electric field generated by an array of electrodes subjected to ac voltages with a phase delay between neighboring electrodes. In this article, we propose an alternative way of generating travelling-wave electric fields in microchannels. We apply a rotating electric field around a cylindrical insulating micropillar and the resulting travelling-wave modes induce particle drift around the cylinder. We termed this phenomenon as insulating travelling-wave electrophoresis (i-TWE) to distinguish it from standard TWE performed with arrays of microelectrodes. We characterised the particle drift experimentally and show a quantitative comparison of the particle velocity with theoretical predictions. Excellent agreement is found when the influence of electroosmosis on the channel walls is also considered.

I. INTRODUCTION

Electrophoresis is widely used to manipulate and separate charged particles (colloids, molecules) suspended in electrolytes, and capillary electrophoresis [1] is the standard for high-efficiency separation of molecules. Electrophoresis describes the motion of a particle due to the action of an electric field on the electrical double layer (EDL) at the particle-electrolyte interface [2]. When the EDL is thin with respect to the particle size, the electrophoretic velocity of the particle $\mathbf{u}_{\mathrm{ep}}$ is given by the Helmholtz-Smoluchowski formula [3],

$$\mathbf{u}_{\mathrm{ep}} = \frac{\varepsilon\zeta}{\eta}\mathbf{E} \tag{1}$$

where $\mathbf{E}$ is the applied electric field, ε and η are the electrolyte permittivity and viscosity respectively, and ζ is the zeta potential. The latter is usually defined as the electrical potential at the inner edge of the diffuse ionic layer surrounding the particle [2].

Recent papers have shown that Travelling-Wave (TW) electric fields can be used to achieve electrophoretic motion of charged particles with a controlled direction and velocity magnitude, a phenomenon known as Travelling-Wave Electrophoresis (TWE) [4]. TW electric fields are conventionally generated using arrays of microelectrodes connected to oscillating potentials of the same frequency but with a fixed phase lag between neighboring electrodes (see Figure 1). In TWE, there are fundamentally two different modes depending on the relative value of electrophoretic velocity to the phase velocity of the wave, which is $v = \omega/k$, where ω is the angular frequency of the ac voltage on the electrodes and k is the wave number of the TW electric field, $k = 2\pi/L$, where L is the spatial periodicity (see Figure 1). If

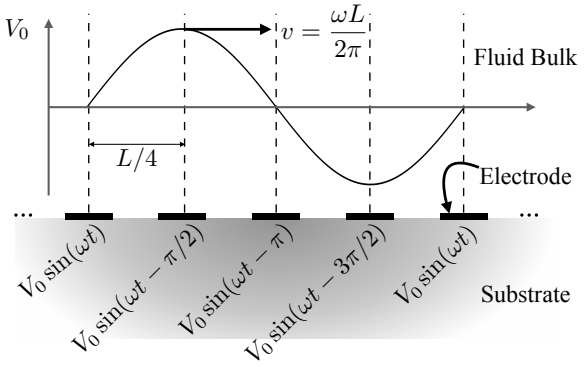

FIG. 1. Diagram showing a classical TWE electrode configuration where an array of electrodes is connected to an oscillating electric potential of the same frequency ω but a different phase. This produces an approximate harmonic wave in the fluid bulk with a spatial periodicity L.

$v \leq u_{\mathrm{ep}}$, the particles "surf" the travelling wave and their motion is synchronous, i.e. their velocity is that of the wave phase. However, if the travelling wave is faster ($v > u_{\mathrm{ep}}$), the particles cannot follow and migrate by partially following each successive wave crest, this is called asynchronous motion. For this reason, the ratio v/u_{ep} has been defined as the responsiveness of the particles to the wave [4].

In 2007, Wei [5] proposed the use of TWE for mobility-based particle fractionation inside microfluidic channels. Edwards et al. [4] showed good agreement between theory and velocity measurements of TWE experiments in microfluidics. They also showed that chaotic behavior is theoretically expected for intermediate values of the particle mobility. Jo et al. [6] used TWE in a microchannel and demonstrated efficient separation of fluorescent dyes and proteins with relatively narrow sample bandwidths.

* Corresponding author: ramos@us.es

In this work, we show how TW fields can be created around insulating objects and how these fields can be used to control particle migration in a similar manner to "classical" TWE with microelectrode arrays. This is achieved by applying a rotating electric field around an insulating micropillar placed in a microfluidic chamber. The rotating electric field is generated by four electrodes placed far from the chamber. This arrangement is simpler than using an array of microelectrodes, which requires a complicated wiring scheme to address each electrode with the appropriate electrical signal. Creation of the travelling-wave electric fields far from the electrodes also avoids other undesired effects such as Faradaic reactions [7], which usually cause electrode degradation and modification of liquid conductivity and pH, and the generation of AC electroosmotic flows on microelectrode in contact with the electrolyte [8].

We use the term insulating travelling-wave electrophoresis (iTWE) to distinguish this approach from the standard TWE with arrays of microelectrodes. In this work, we experimentally measured the particle velocity of particles undergoing iTWE and performed a quantitative comparison with both numerical simulations and an analytical model that is derived in the limit of high electric field frequency. Excellent agreement is found with experimental data provided that electroosmosis on the channel walls is included in the model.

II. THEORY

Consider the application of an harmonic electrical potential with angular frequency ω in an electrolyte liquid given by the following expression in polar coordinates (r, θ):

$$\bar{\phi}(\bar{r}, \theta, \bar{t}) = \mathcal{R}e[-E_0 \bar{r} e^{i(\theta - \omega \bar{t})}] \tag{2}$$

where E_0 is a constant, $\mathcal{R}e[\cdots]$ means the real part of the expression between brackets and the bar indicates a dimensional variable. As shown in the experimental section, an approximation to this electric potential can be achieved using a quadrupolar array of electrodes driven by ac voltages with a relative phase lag of 90°. The electric field associated with (2) corresponds to a counterclockwise rotating field within the XY plane and with magnitude E_0.

If an insulating obstacle is placed within the electrolyte, the electrical current cannot penetrate it and therefore the field lines are distorted around the surface. The zero current condition at the surface, S, transforms into the following boundary condition for the potential: $\mathbf{n} \cdot \nabla \phi|_S = 0$, where $\mathbf{n}$ is a unit vector normal to S. In the case of a cylindrical object of radius R, with the axis perpendicular to the rotation plane and containing the point $r = 0$, the electrical potential in the liquid is:

$$\bar{\phi}(\bar{r}, \theta, \bar{t}) = -E_0 \left(\bar{r} + \frac{R^2}{\bar{r}} \right) \mathcal{R}e[e^{i(\theta - \omega \bar{t})}] \tag{3}$$

For convenience, the potential is scaled by $E_0 R$. The length scale is chosen to be the radius of the post R, and the time scale the inverse of the electric field angular frequency $1/\omega$. Using these scaling parameters, the expression (3) can be rewritten in a non-dimensional form as

$$\phi(r, \theta, t) = -\left(r + \frac{1}{r} \right) \mathcal{R}e[e^{i(\theta - t)}] \tag{4}$$

and therefore the electric field is

$$\mathbf{E} = \left(1 - \frac{1}{r^2} \right) \cos(\theta - t) \hat{r} - \left(1 + \frac{1}{r^2} \right) \sin(\theta - t) \hat{\theta}. \tag{5}$$

The components of the electric field at a given distance $r = r_0$ from the centre of the pillar can be seen as waves travelling in the angular direction with wavenumber $k = 1/r_0$. Thus, the phase velocity of these waves corresponds to $v = \omega r_0$. Following on from the description of TWE in the introduction, we expect a synchronous drift for particles with $u_{\mathrm{ep}} \geq \omega r_0$. In our experiments we used colloidal particles suspended in electrolytes, with $\zeta \approx -60$ mV and a field magnitude of $E_0 = 10^4$ V/m. The asynchronous regime occurs if $r > 1.01R$ for the lowest frequency applied ($f = 13$ Hz). This means that, in practice, the asynchronous regime is to be expected for all experimental conditions. Figure 2(a) shows the asynchronous trajectory of a particle undergoing electrophoretic motion due to this electric field. In this regime, the particle drifts in the angular direction while it oscillates in the radial direction.

In order to develop an analytical expression for the drift velocity, we follow the high frequency asynchronous (HFA) approximation employed by J.R. Melcher *et al.* [9], where the spatial variables were decomposed into one oscillating component and a time-averaged drift velocity. In our case,

$$r = r_0 + r', \quad \theta = \omega_p t + \theta', \tag{6}$$

where the primed variables denote purely oscillating terms and are assumed to be $r', \theta' \ll 1$. That is, the radial component is expected to have small oscillations around a fixed position r_0, and the angular component is expected to grow linearly over time with a time-averaged angular drift ω_p plus small oscillations around this linear growth.

The electrophoretic response of the particles given by eq. (1) leads to the following nondimensional equations of motion:

$$\frac{dr'}{dt} = \tilde{u} \left(1 - \frac{1}{(r_0 + r')^2} \right) \cos[\theta' - (1 - \omega_p)t] \tag{7}$$

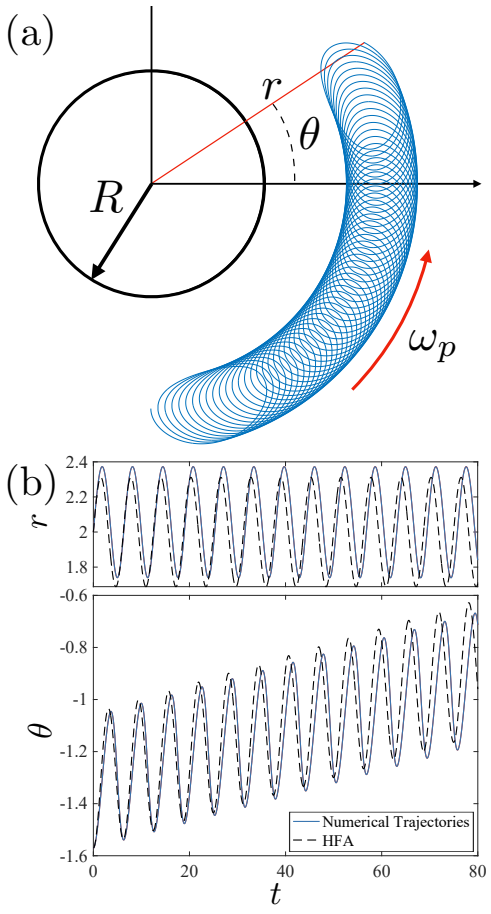

FIG. 2. Analysis of the Rotating TWE system. (a) Sketch of the system showing the trajectory of a single particle ($\tilde{u} = 0.418$, $r_0 = 2$) obtained by direct numerical integration of the equations. The particle describes loops with an overall drift angular velocity ω_p. (b) Radial and angular coordinates representing the same case as (a) described by simulation of trajectories (blue) and by the high-frequency asynchronous approximation (HFA, dashed black).

$$\omega_p + \frac{d\theta'}{dt} = -\tilde{u}\left(\frac{1}{r_0 + r'} + \frac{1}{(r_0 + r')^3}\right)\sin[\theta' - (1-\omega_p)t] \tag{8}$$

where $\tilde{u} = \mu E_0/\omega R$ is the scaled velocity, and $\mu = \varepsilon\zeta/\eta$ the electrophoretic mobility. Since the oscillating components are much smaller than 1 the equations for r' and θ' can be written as:

$$\frac{dr'}{dt} = \tilde{u}\left(1 - \frac{1}{r_0^2}\right)\cos[(1-\omega_p)t] \tag{9}$$

$$\frac{d\theta'}{dt} = \tilde{u}\left(\frac{1}{r_0} + \frac{1}{r_0^3}\right)\sin[(1-\omega_p)t] \tag{10}$$

Note that this approximation is valid as long as $\tilde{u} \ll 1$. With the expressions for r' and θ', the time average of the equation (8) at the lowest order in the expansion gives an expression for the average of the angular drift velocity,

$$\omega_p = \tilde{u}\left(\frac{1}{r_0^2} + \frac{3}{r_0^4}\right)\langle r'\sin[(1-\omega_p)t]\rangle - \tilde{u}\left(\frac{1}{r_0} + \frac{1}{r_0^3}\right)\langle\theta'\cos[(1-\omega_p)t]\rangle \tag{11}$$

where $\langle ...\rangle$ stands for time average. After some algebra, in the limit of $\omega_p \ll 1$, we obtain the following expression for the time-averaged drift velocity of the particles around the cylinder:

$$\omega_p = \frac{1}{2} - \sqrt{\frac{1}{4} - \frac{2\tilde{u}^2}{r_0^6}} \approx \frac{2\tilde{u}^2}{r_0^6}. \tag{12}$$

Figure 2 shows a calculation for the case of $\tilde{u} = 0.418$ and $r_0 = 2$. Figures 2(b) and 3 show a comparison between the HFA approximation and numerical simulations using the full electrophoretic velocity corresponding to the field in equation (5). In this case, the drift velocity ω_p obtained from the HFA approximation differs from the average displacement given by the numerical trajectories by 8%.

Figure 3 shows ω_p as a function of the initial radial distance to the centre of the post r_0 in Fig. 3(a) and also as a function of the reduced velocity $\tilde{u}$ in Fig. 3(b). The range of $\tilde{u}$ corresponds to typical experimental conditions (ζ of the order of tens of mV, $E_0 \approx 10$ kV/m and ω ranging from 10 to 100 rad/s). A good agreement is found for low drift velocity conditions, i.e. positions far from the pillar and/or high electric field frequency, in which $\tilde{u} \ll 1$. However, deviations from the analytical solution are found if, for example, $\tilde{u} \leq 0.5$ for $r_0 = 2$.

III. EXPERIMENTS

In order to experimentally validate the description given above for a TWE rotating around an insulating cylinder a simple 4-electrode device was constructed. A quadrupolar array of planar platinum micro-electrodes was fabricated within a microfluidic channel, as shown in Figure 4(a). A 20 μm diameter post was constructed in the centre of the electrodes [see Fig. 4(b)]. These channels were fabricated from PDMS using standard soft lithography. The channels are 37 μm high and the width of each arm is 200 μm.

Experiments were performed with a KCl electrolyte at three different conductivities: $\sigma = 1.5$ mS/m, 3 mS/m and 6 mS/m seeded with 500 nm polystyrene fluorescent particles to act as fluid tracers. The PDMS channels were bonded to the glass substrate (with electrodes) using O_2 plasma bonding. Prior to experiments, devices were primed with a surfactant solution (0.1% (w/v) Pluronic F-127) for at least 30 minutes in order to avoid particle clogging and adhesion to channel walls.

The fluid is introduced in the channel through two reservoirs located at both ends of the channel, as seen

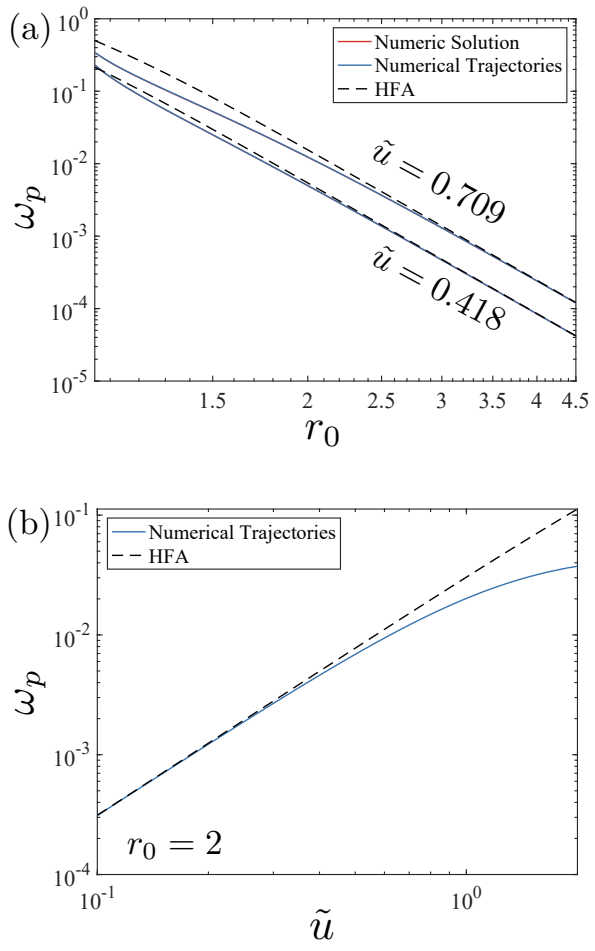

FIG. 3. Dependence of the drift angular velocity ω_p on (a) the initial radius r_0 and (b) the reduced velocity $\tilde{u}$ given by direct numerical integration (solid curves) and HFA approximation (dashed lines). Typical experimental parameters are $\zeta = -63$ mV and $E_0 = 10$ kV/m.

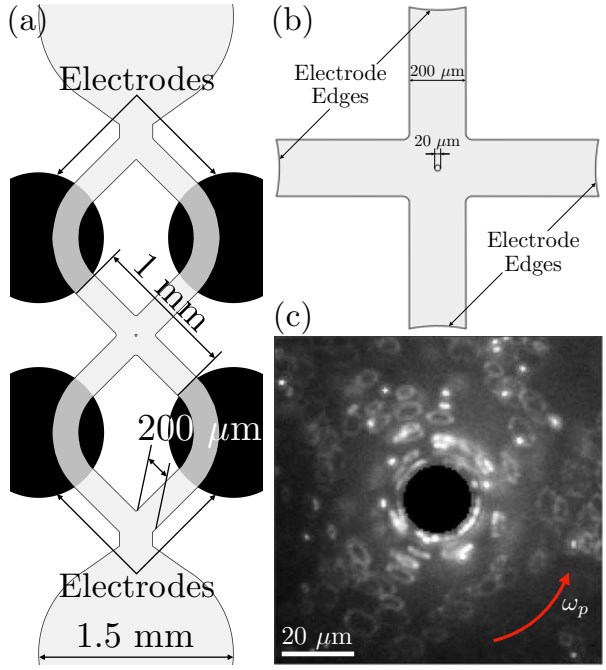

FIG. 4. Experimental set-up for observing Rotating TWE (a) Top view of the microfluidic channel and the electrodes with the pillar in the centre. (b) Detail of the channel showing the pillar. (c) Frame from one of the recordings showing the flow around the pillar ($\sigma = 1.5$ mS/m, $E_0 = 10$ kV/m, $f = 17$ Hz).

in Figure 4(a). Both reservoir inlets were connected to a pressure controller to control the fluid flow and eventually stop it to perform the rotation TWE experiments. Each of the four electrodes is connected to a signal generator which provides a sinusoidal signal of 10 Volts peak-to-peak, with frequencies ranging from 10 Hz to 100 Hz and a 90° phase delay between contiguous electrodes to produce the rotating field.

To analyse the flow, videos containing of approximately 1000 frames were recorded and processed using particle image velocimetry (PIV) software [10]. Frames are taken at a constant rate of 16 fps, which is lower or of the order of the electric field frequency and, therefore, of the electrophoretic rotation. For that reason, tracer particles describe a full loop in each frame for most cases, as shown in Figure 4(c). Far from the pillar, loops are approximately circular allowing an estimate of the experimental mobility based on a linear regression from amplitude $\mathcal{A}$ measurements at different frequencies; where $\mathcal{A} = 2|\mu|E_0/\omega$. For the case of the lowest conductivity of 1.5 mS/m, the mobility $|\mu| = 4.35 \times 10^{-8}$ m^2/(V·s); zeta-potential measurements of the tracer particles gives a similar value with $|\mu| = \varepsilon|\zeta|/\eta = 4.46 \times 10^{-8}$ m^2/(V·s). From the PIV measurements, the centre of the loops was traced, giving an estimate of the drift angular velocity ω_p.

Figure 5(a) shows PIV analysis of the experimental videos for an applied voltage with a frequency of 17 Hz ($\tilde{u} = 0.418$), as a function of the distance to the post. Figure 5(b) shows data for a frequency sweep and an initial separation of $r_0 = 2R$ from the surface of the post. The reduced mobilities in this case range from $\tilde{u} = 0.154$ to 0.546. It was not possible to obtain reliable measurements for distances to the surface of the post for less than 5 μm because it was not possible to trace the loops with the PIV software.

IV. COMPARISON BETWEEN THEORY AND EXPERIMENTS

Figure 5 shows experimental data for $f = 17$ Hz together with the predictions of the theoretical model for $\tilde{u} = 0.418$, which corresponds to the expected reduced velocity for that frequency. There is a clear mismatch between theory and experiment, not only in the magni-

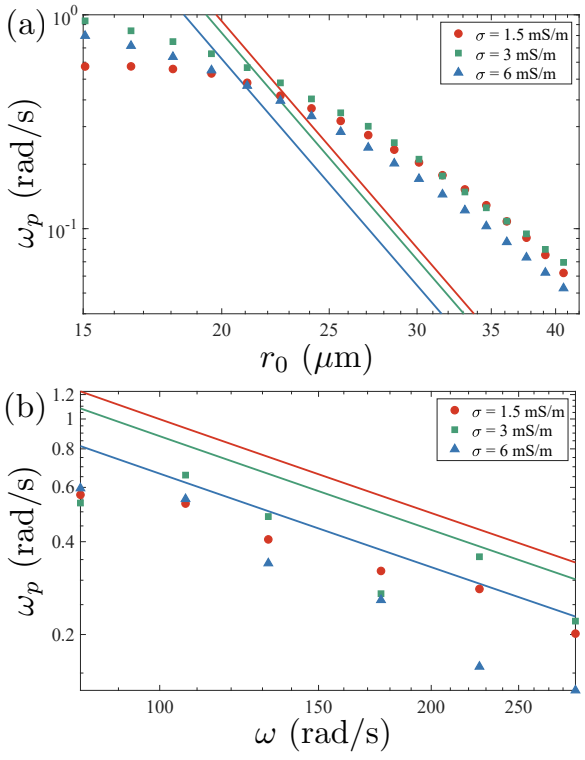

FIG. 5. PIV measurements determined from the experimental results. (a) Drift velocity ω_p as a function of the radial distance to the centre of the post for an electric field frequency of $f = 17$ Hz, i.e. $\tilde{u} = 0.418$ (b) Drift for a fixed distance to the post of $r_0 = 2R$ as a function of the frequency, with reduced mobilities ranging from $\tilde{u} = 0.154$ ($f = 46$ Hz) to $\tilde{u} = 0.546$ ($f = 13$ Hz). Solid lines represent predictions from the HFA approximation given by eq. (12).

tude of ω_p, but also in the trend with distance to the cylinder. This indicates there are contributions to the motion of the particles that are omitted. For this reason, we will now analyze the influence of the following on the particle trajectories: (i) The difference between the electric field described so far and the electric field generated by the four electrodes and (ii) the contribution to particle rotation from the electroosmosis generated on the channel walls.

A. Electric field in the device

In order to accurately determine the electric field in the experimental device, the electric potential was calculated numerically in the 2D domain of Figure 4(b) with the commercial software COMSOL Multiphysics. The electric potential is written as $\phi(\mathbf{r}, t) = \phi_0(r, \theta)\cos(\omega t)$, where $\phi_0(r, \theta)$ is the solution of the Laplace equation ($\nabla^2\phi_0 = 0$) with the following boundary conditions: zero current on the surface of the post and the channel walls ($\mathbf{n} \cdot \nabla\phi_0|_S = 0$), $\phi_0 = 0$ on the upper and lower

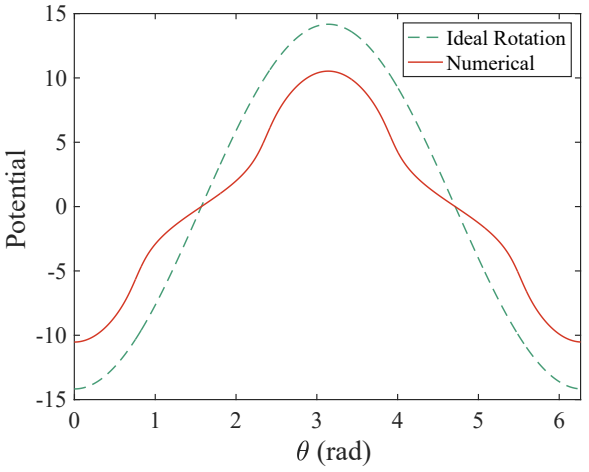

FIG. 6. Electric potential for the ideal rotating field (dashed green) and the numerical simulation (solid red) for the largest concentric circumference allowed by our geometry.

electrodes, $\phi_0 = 1$ on the left electrode and $\phi_0 = -1$ on the right electrode.

Figure 6 shows the value of ϕ_0 along a circumference of radius $r_0 = \sqrt{2 \times 200^2}/(2R)$ with its center on the post axis; this is the largest circumference concentric with the pillar allowed by the geometry. For comparison, we also show the electric potential calculated with equation 4 at $t = 0$. The difference between the maxima of the two curves is around 30%, which suggests that a more realistic simulation of the particle trajectories might require the exact numerical solution of the electric field in order to calculate the electrophoretic velocity. Simulations were also performed with COMSOL confirming that the trajectories of the particles are different for both situations. For example, Figure 7 shows the trajectories of particles at several initial distances from the post for the ideal electric field (eq. (5), red circles) and for the numerically calculated electric field (green circles). The arrows in that figure show the direction of the net particle motion (i.e. particle drift). Remarkably, the latter case shows that particles beyond a critical distance reverse their net motion; this never occurs with the ideal electric field. This finding motivated us to perform an analysis of the contributions to the particle motion of the angular modes of the electric field in the experimental device (see Appendix A).

Although reversal of particle motion was observed in experiments, the results of the simulations using the numerically calculated field do not agree with the measured dependence on radial distance. In particular, the simulations predict the crossover for the particle direction at a different radial position, i.e. the radius from the post at which the particle trajectory changes direction. This implies that there is some other mechanism missing the analysis of particle velocity.

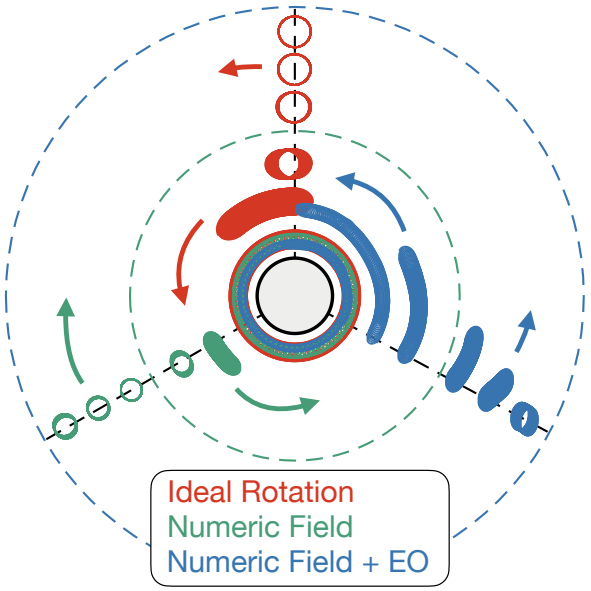

FIG. 7. Representation of the trajectories as predicted by the different approaches. Red: Ideal rotation with drift velocity following eq. (12). Green: Trajectories determined from the numerically calculated electric field. Blue: Numerically calculated trajectories given by the numerical field with the electroosmotic back-pressure. The green concentric circle describes the crossover radius of zero drift velocity in the simulation with the numeric electric field $r_C = 4.37$. The blue circumference represents the crossover radius found with the combination of the numeric field and electroosmotic flow $r_C = 7.66$, which reproduces the experimental crossover radius (see Supplementary movie [13]). These trajectories were computed for a typical experimental condition: $\sigma = 6$ mS/m, $f = 17$ Hz ($\tilde{u} = 0.418$) and a fixed timespan of $\omega\bar{t} = 500$.

B. Electroosmosis in the channel

Recent publications have shown that the use of Pluronic drastically reduces the electroosmotic mobility of the walls [11, 12]. However, the residual electroosmotic flow induced on the channel walls might still contribute to the particle motion. In this section we describe simulations of particle trajectories including the drag on the particles due to the electroosmotic flow in the device.

Prior to the simulation of the trajectories, a numerical solution to the velocity field in the device is required. For this purpose, the Stokes equations ($\nabla p = \eta\nabla^2\mathbf{u}$ and $\nabla\cdot\mathbf{u} = 0$) for the fluid velocity was included in the COMSOL model. Boundary conditions of electroosmotic slip velocity ($\mathbf{u} = -\varepsilon\zeta_w\mathbf{E}/\eta$) on the channel and post walls were used. In addition, a no flow conditions $\mathbf{u} = 0$ was set on the electrode boundaries. To compute the electroosmotic mobility, the zeta potential was set $\zeta_w = -25$ mV, as determined from previous measurements of surfactant-treated PDMS [12].

C. Comparison with experimental results

Figure 7 shows simulations of particle trajectories for the original description of the ideal rotation (section II) along with the two major corrections presented above. The trajectory in red is the ideal condition where rotation is driven by the field given by equation (5) at different initial separation distances. Plotted in green are the trajectories of particles when using the numerically calculated field, and in blue the trajectories are for particles undergoing electrophoresis together with a drag force from the electroosmotic flow created by the channel walls, with the electric field and fluid velocity field numerically computed.

All particle trajectories are computed for a fixed amount of time ($t = 500$) in order to illustrate the dependence of velocity with initial separation from the post, for three different models. Simulations were made for typical experimental conditions: a conductivity of 6 mS/m, an electric field of magnitude $E_0 = 10$ kV/m and frequency of $f = 17$ Hz, giving a reduced velocity of $\tilde{u} = 0.418$. The concentric dashed circumferences represent the radius of zero drift velocity predicted by the numerical electric field (green circumference), and the crossover radius predicted by a combination of numerical electric field and electroosmotic flow (blue). Note that the amplitude of the loops described by the particles resemble the experimental conditions for the green and blue trajectories, but only the complete numerical approach (blue) describes the radial dependence of drift velocity that realistically describes the change in direction at $r_C^{\mathrm{Num}} = 7.66$. The Supplementary movie shows the change in the drift velocity at this radial this distance.

Finally, Figure 8 shows a comparison between the experimental drift velocities obtained by PIV measurements of the video recordings and the results from the numerical simulations obtained by averaging the angular displacement of particle trajectories such as those shown in Figure 7 (blue). Figure 8(a) shows results for an electric field amplitude $E_0 = 10$ kV/m and frequency $f = 17$ Hz, for all experimental conductivities, as a function of distance to the centre of the post. This shows that the numerically calculated electric field and fluid flow field ultimately results in a better description of the dependence of ω_p with r. Figure 8(b) shows a frequency sweep between 13 Hz and 46 Hz for a fixed initial radius at $r_0 = 2R$ and the same electric field amplitude $E_0 = 10$ kV/m. The comparison shows that the dependence with frequency is well predicted by the model.

To summarise for the TWE, the inclusion of the corrections presented above provide an explanation of both the magnitude of the observed drift velocity and the trend with frequency and distance to the pillar.

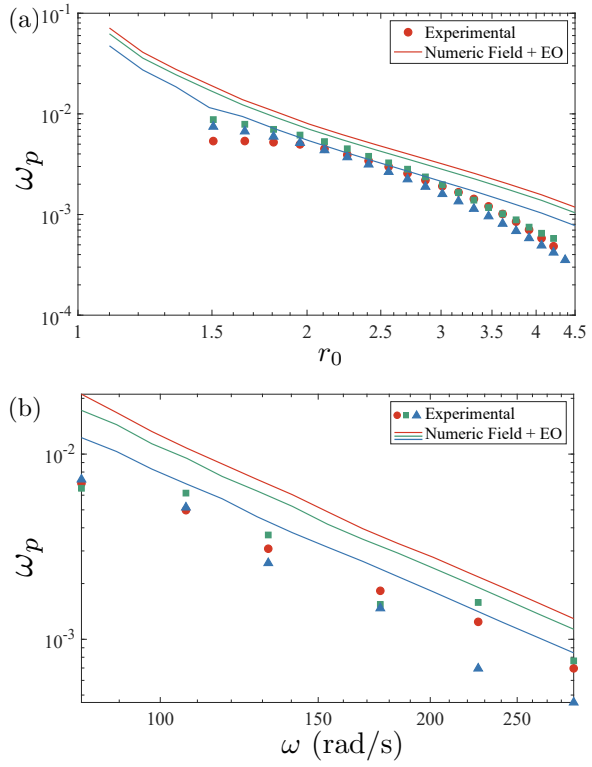

FIG. 8. Comparison between the experimental results and the numerically calculated trajectories when including the numerical electric field and the electroosmotic flow (solid lines). The plots show the drift velocity as a function of (a) the distance to the post for a fixed electric field frequency of $f = 17$ Hz and (b) the frequency for a fixed distance to the post $r_0 = 2R$. Data is plotted for different condutivities: 1.5 mS/m (red), 3 mS/m (green) and 6 mS/m (blue). Data for zeta potential was determined from the experimental results in [12, 14] and the Gouy-Chapmann equation when needed for an extrapolation to different conductivities.

V. CONCLUSIONS

We have demonstrated that the disturbance in a rotating field caused by the presence of a dielectric cylinder produces a travelling wave around the obstacle. This phenomenon occurs because of the presence of the dielectric object in the system, therefore we term it insulating travelling-wave electrophoresis (iTWE), analogous to the phenomenon of insulator-based dielectrophoresis (iDEP) [15–17].

A simple two-dimensional extension of the published TWE theory provides a qualitative description of the time-averaged drift velocity that matches the observed dependence with frequency of applied electric field and the decay with the distance from the post. A more detailed description of the experimental geometry that takes into account the electrosmotic flows generated in the channels provides a good agreement with the experimental observations.

Additional effects such as electrothermal flows can be discounted since the frequency-dependent behaviour is not the same, and the light illumination did not influence the experimental observations [18]. Furthermore, the frequencies of the ac voltages are too low to cause travelling-wave dielectrophoresis (twDEP) [19].

The observed phenomenon provides a new way for manipulation of colloidal particles far from the electrodes – a major problem in the field of microfluidics and electrokinetics, as discussed in the introduction. An optimised geometry that exploits these fundamental forces could be used to fractionate a suspension of particles based on different mobilities.

ACKNOWLEDGMENTS

P.G.S. and A.R. acknowledge Grant P20-00534 funded by "Consejería de Economía, Conocimiento, Empresas y Universidad (Junta de Andalucía)".

Appendix A: Electric field analysis

In order to understand the effect of the experimental electric field on particle trajectories, an analytical expression for the electric potential in the neighbourhood of the pillars is required. This was performed based on separation of variables in polar cylindrical coordinates. First write a general solution for the potential at time $t = 0$ that satisfies the boundary condition on the pillar surface ($\mathbf{n} \cdot \nabla\phi|_S = 0$ at $r = 1$), while preserving the vertical and horizontal symmetry axes of the geometry [see Figure 4(b)]:

$$\phi^M(r,\theta) = \sum_{n=0}^{\infty} A_n \left(r^{2n+1} + \frac{1}{r^{2n+1}} \right) \cos[(2n+1)\theta]. \tag{A1}$$

Note that $n = 0$ represents the ideal electric potential, the most relevant contribution.

To obtain the coefficients A_n, we equate the series expansion to the numerical solution of the potential at a certain radius r_{comp} far from the post. We choose $r_{\text{comp}} = \sqrt{2 \times 200^2}/(2R)$. The first two coefficients are found to be $A_0 = -0.6452$ and $A_1 = -6.077 \times 10^{-4}$. With only these two modes, ϕ^M differs from the numerically calculated potential by less than 3%.

We now proceed to write the full time-dependent electrical potential. The experimental electric field is generated by two sinusoidal AC signals which are out of phase by 90 degrees and are applied to two pairs of electrodes rotated by 90 degrees. That is, the time-dependent po-

tential can be expressed as

$$\phi(r,\theta,t) = \phi^M(r,\theta)\cos t + \phi^M(r,\theta-\pi/2)\sin t$$
$$= \sum_{n=0}^{\infty} A_n \left(r^{2n+1} + \frac{1}{r^{2n+1}}\right) \times$$
$$\left(\cos[(2n+1)\theta]\cos t + \cos\left[(2n+1)\left(\theta - \frac{\pi}{2}\right)\right]\sin t\right). \quad \text{(A2)}$$

Using the identity $\cos[(2n+1)(\theta-\pi/2)] = (-1)^n \sin[(2n+1)\theta]$, the above expression can be rewritten as

$$\phi = \sum_{n=0}^{\infty} A_n \left(r^{2n+1} + \frac{1}{r^{2n+1}}\right) \cos[(2n+1)\theta - (-1)^n t]. \quad \text{(A3)}$$

This shows that the potential is the superposition of modes rotating alternately clockwise or anticlockwise depending on whether n is odd or even, respectively. This is the origin of the reversal in the drift velocity with radius shown in Fig. 7 when the rotation is calculated from the numerical field.

Using the HFA method, we now arrive at an analytical expression for the particle drift angular velocity ω_p,

$$\omega_p = \frac{\sum_n (-1)^n (2n+1) G_n}{2/\tilde{u}^2 - \sum_n (2n+1)^2 G_n}, \quad \text{(A4)}$$

where G_n are radial functions for each mode. This expression and the first modes are derived in Appendix B. Interestingly, the expression predicts a change of sign in drift angular velocity as a function of r. Using just the first two modes of the potential $n = 0, 1$ in (A4) and with G_0 and G_1 shown in eq. (B11) and (B12), respectively, the crossover radius r_C of zero drift velocity given by

$$r_C \approx \left(\frac{A_0}{3A_1}\right)^{1/4} \approx 4.37. \quad \text{(A5)}$$

Appendix B: HFA approximation for the complete electrical problem

We write the expression (A3) as

$$\phi(r,\theta,t) = \sum_{n=0}^{\infty} F_n(r)\cos[k_n\theta - (-1)^n t]. \quad \text{(B1)}$$

The equations for particle motion become

$$\frac{dr}{dt} = -\tilde{u}\sum_{n=0}^{\infty} f_n(r)\cos[k_n\theta - (-1)^n t], \quad \text{(B2)}$$

$$\frac{d\theta}{dt} = \tilde{u}\sum_{n=0}^{\infty} k_n \frac{F_n(r)}{r^2}\sin[k_n\theta - (-1)^n t], \quad \text{(B3)}$$

where we define $f_n(r) = F_n'(r)$. As in equation (6), section II we write r and θ as the sum of time-averaged and oscillating components, leading to:

$$\frac{dr'}{dt} = -\tilde{u}\sum_{n=0}^{\infty} f_n(r'+r_0)\cos(k_n\theta' - \Omega_n t),$$

$$\omega_p + \frac{d\theta'}{dt} = \tilde{u}\sum_{n=0}^{\infty} k_n \frac{F_n(r'+r_0)}{(r'+r_0)^2}\sin(k_n\theta' - \Omega_n t),$$

where we define $\Omega_n = (-1)^n - k_n\omega_p$. Suppose now that $r', \theta' \ll 1$, meaning that to first order we can write

$$\frac{dr'}{dt} = -\tilde{u}\sum_{n=0}^{\infty}[f_n(r_0)\cos(\Omega_n t) +$$
$$f_n'(r_0)\cos(\Omega_n t)r' + k_n f_n(r_0)\sin(\Omega_n t)\theta' + ...], \quad \text{(B4)}$$

$$\omega_p + \frac{d\theta'}{dt} = \tilde{u}\sum_{n=0}^{\infty} k_n \left[-\frac{F_n(r_0)}{r_0^2}\sin(\Omega_n t) - \right.$$
$$\left(\frac{f_n(r_0)}{r_0^2} - \frac{2F_n(r_0)}{r_0^3}\right)\sin(\Omega_n t)r' +$$
$$\left. k_n\frac{F_n(r_0)}{r_0^2}\cos(\Omega_n t)\theta' + ...\right]. \quad \text{(B5)}$$

It can be observed from the above equations that the oscillating functions not only have the frequency modes $\{\Omega_n\}$, $n \in \{0, \mathbb{N}\}$ but also cross terms with frequencies $\{|\Omega_i \pm \Omega_j|\}$, $i \neq j \in \{0, \mathbb{N}\}$. However, as we are only interested in the time-averaged part of (B5), then only the first terms (and not all of them) in (B4) and the oscillating part of (B5) survive:

$$\frac{dr'}{dt} = -\tilde{u}\sum_{n=0}^{\infty} f_n(r_0)\cos(\Omega_n t), \quad \text{(B6)}$$

$$\frac{d\theta'}{dt} = -\tilde{u}\sum_{n=0}^{\infty} k_n \frac{F_n(r_0)}{r_0^2}\sin(\Omega_n t). \quad \text{(B7)}$$

These can be readily integrated and substituted into (B5). Taking the time-average yields terms of the form

$$\langle \sin(\Omega_n t)\sin(\Omega_m t)\rangle = \frac{\delta_{n,m}}{2}, \quad \langle \cos(\Omega_n t)\cos(\Omega_l t)\rangle = \frac{\delta_{n,l}}{2}$$

where $\delta_{i,j}$ is the Kronecker delta, whose value is 1 if $i = j$ and 0 otherwise. We can finally write

$$\omega_p = \frac{\tilde{u}^2}{2R^2}\sum_{n=0}^{\infty}\frac{k_n}{\Omega_n}\times$$
$$\left[f_n^2(r_0) - \frac{2}{r_0}F_n(r_0)f_n(r_0) + \frac{k_n^2}{r_0^2}F_n^2(r_0)\right]. \quad \text{(B8)}$$

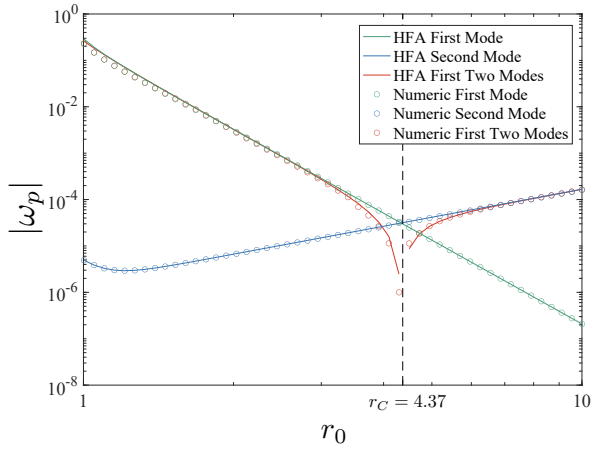

FIG. 9. Comparison between the HFA approximation results and direct numerical simulations of particle trajectories. Drift velocities corresponding to the first and second modes are shown in green and blue, respectively. The combination of the first two modes is represented in red, where the reversal in velocity can be observed at r_C. $A_0 = -0.6452$, $A_1 = -6.077 \times 10^{-4}$, $\tilde{u} = 0.5$.

Defining the generatrix function

$$G_j = G\{F_j(r_0)\} = \frac{1}{r_0^2}\left[f_j^2(r_0) - \frac{2}{r_0}F_j(r_0)f_j(r_0) + \frac{k_j^2}{r_0^2}F_j^2(r_0)\right] \quad \text{(B9)}$$

and noting that $\Omega_n = (-1)^n - k_n\omega_p$, we can express the drift velocity in the limit $\omega_p \ll 1$ as

$$\omega_p = \frac{\sum_n (-1)^n k_n G_n}{2/\tilde{u}^2 - \sum_n k_n^2 G_n}, \quad \text{(B10)}$$

which is the equation presented in (A4).

For the first two modes we have

$$F_0(r) = A_0\left(r + \frac{1}{r}\right), \quad F_1(r) = A_1\left(r^3 + \frac{1}{r^3}\right),$$

together with $k_0 = 1$ and $k_1 = 3$, so that

$$G\{F_0(r_0)\} = \frac{4A_0^2}{r_0^6}, \quad \text{(B11)}$$

$$G\{F_1(r_0)\} = 12A_1^2\left[\frac{2}{r_0^{10}} + r_0^2\right]. \quad \text{(B12)}$$

To test the validity of the average drift velocity obtained from the HFA approximation, Figure 9 compares the resulting ω_p with the numerical simulations for the same electric field, using the first two modes. The absolute value is used to allow comparison with the second mode.

[1] J. W. Jorgenson and K. D. Lukacs, Science **222**, 266 (1983).
[2] R. Hunter, *Introduction to Modern Colloid Science* (Oxford University Press, 1993).
[3] M. von Smoluchowski, Bull. Akad. Sci. Cracovie. **8**, 182 (1903).
[4] B. F. Edwards, A. T. Timperman, R. L. Carroll, K. Jo, J. M. Mease, and J. E. Schiffbauer, Physical review letters **102**, 076103 (2009).
[5] H.-H. Wei, Applied physics letters **90**, 204103 (2007).
[6] K. D. Jo, J. E. Schiffbauer, B. E. Edwards, R. L. Carroll, and A. T. Timperman, Analyst **137**, 875 (2012).
[7] P. García-Sánchez, A. Ramos, A. González, N. G. Green, and H. Morgan, Langmuir **25**, 4988 (2009).
[8] A. Ramos, A. González, P. García-Sánchez, and A. Castellanos, J. Colloid Interface Sci. **309**, 323 (2007).
[9] J. R. Melcher, E. Warren, and R. H. Kotwal, Particulate science and technology **7**, 1 (1989).
[10] W. Thielicke and E. J. Stamhuis, Journal of Open Research Software **2** (2014).
[11] M. Viefhues, S. Manchanda, T.-C. Chao, D. Anselmetti, J. Regtmeier, and A. Ros, Analytical and bioanalytical chemistry **401**, 2113 (2011).
[12] R. Fernández-Mateo, P. García-Sánchez, V. Calero, A. Ramos, and H. Morgan, Electrophoresis **43**, 1259–1262 (2022).
[13] See the Supplemental Material at (...), which contains a video showing particles undergoing iTWE around a microfluidic pillar when a 10 kV/m, 21 Hz rotating field is applied. (????).
[14] V. Calero, P. Garcia-Sanchez, A. Ramos, and H. Morgan, Biomicrofluidics **13**, 054110 (2019).
[15] B. H. Lapizco-Encinas, B. A. Simmons, E. B. Cummings, and Y. Fintschenko, Analytical chemistry **76**, 1571 (2004).
[16] N. Hill and B. H. Lapizco-Encinas, Electrophoresis **40**, 2541 (2019).
[17] B. H. Lapizco-Encinas, Analytical and Bioanalytical Chemistry **414**, 885 (2022).
[18] A. González, A. Ramos, H. Morgan, N. G. Green, and A. Castellanos, Journal of Fluid Mechanics **564**, 415 (2006).
[19] H. Morgan and N. G. Green, *AC Electrokinetics: colloids and nanoparticles.* (Research Studies Press Ltd., 2003).

Part III

Conclusions

Conclusions

This thesis introduces a new AC electrokinetic phenomenon termed Concentration Polarization Electroosmosis or CPEO. It describes steady-state electroosmotic flow around insulating particles and structures in microfluidic channels (pillars, corners, constrictions, etc.) in the presence of low-frequency AC electric fields in low-conductivity electrolytes. A thorough experimental and theoretical analysis of the phenomenon is described, with potential applications for particle manipulation. This framework also explains previous experimental results from the literature which remained unidentified or wrongly attributed to other electrokinetic phenomena. The phenomenon arises from surface conductance which creates Concentration Polarization around micrometric and sub-micrometric particles, as well as dielectric structures and features in microfluidic channels.

The steady-state electroosmotic flows generated by low-frequency AC fields around insulators observed in the literature have fluid flow patterns that resemble the flows predicted by Induced-Charge Electroosmosis (ICEO) for conducting surfaces [44, 45]. This led to many authors using the idea that the induced charge on the surface of dielectrics was responsible for the fluid flow, which resulted in contradictions when trying to match experimental observations with theory. It was not possible to predict the behaviour of the flows with the magnitude of the electric field or frequency. Another unexplained and apparently unrelated behaviour reported in the literature is the unexpectedly large particle-wall separation of dielectric particles undergoing electrophoresis in low-conductivity electrolytes [55, 56]. These were attributed to the DEP force generated by the disturbances in the electric field created by the particle in the vicinity of the channel walls. Electroosmotic flows were also reported for the case of Deterministic Lateral Displacement (DLD) devices when coupled with AC electric fields at low frequencies [35, 47], leading to unpredictable particle fractionation in the regions where CPEO flows were observed.

The CPEO theory was developed to describe the reported steady-state electroosmotic flows around dielectrics. It satisfactorily predicts the magnitude of the flows around dielectric pillars, and their dependency on the frequency and magnitude of the applied electric field. The theory also explains the flows observed around microfluidic corners, constrictions and channel entrances. Furthermore, the ability to describe the fluid flow around micro-particles predicts the hydrodynamic interactions between particles and channel walls. This explains for the first time the observed behaviour of particles in electrokinetic biased DLD at low conductivities and low

electric field frequencies. The CPEO-based particle-wall repulsion also explains the lateral migration of particles undergoing electrophoresis in microfluidic channels. As a result, CPEO theory unifies these apparently unrelated AC electrokinetic phenomena.

Paper C described the first mathematical model of CPEO that predicts stationary flow of low-conductivity electrolytes induced by low-frequency AC electric fields around charged dielectric objects. This is presented with experimental data of the electrolyte flow around insulating micropillars in a microfluidic channel, validating the theory through numerical calculations. The model correctly describes the amplitude and frequency dependence of the rectified flow, in contrast with previous work that attributes the flow around dielectric structures to classical ICEO in AC fields [44]. In Paper D this theoretical model was further refined to describe the electroosmotic flows at a smaller scale assuming weak fields $E_0 a < kT/e$, predicting CPEO flows around dielectric micro-particles. Development of image analysis procedures allowed experimental validation of the CPEO model for 3 μm polystyrene particles. A further verification of the CPEO theory was provided in Paper E, where the presence of CPEO fluid flows around constrictions in microfluidic channels was experimentally demonstrated for low conductivity electrolytes.

Interestingly, in examining the fluid behaviour around constrictions for shallow channels (10 μm high), the particles which were intended to be used as tracers of the fluid flow become trapped on both sides of the constrictions. This phenomenon cannot be explained solely by the CPEO flows around the constrictions, and further work is needed to clarify the mechanism responsible for this trapping. In comparison with the tall channels, for shallow channels the weakening of the CPEO flows may be due to the proximity of the top and bottom walls. A rectified electric field should persist in the channel given that surface conduction is not affected to any large extent. Therefore, these phenomena should be considered in further theoretical analysis of the trapping, which is clearly different from classical DEP.

The next part of the work consisted of a group of four papers (F-I), demonstrating that wall repulsion in low-frequency AC electrophoresis is due to the presence of CPEO flows around micro-particles. This finding has consequences for microfluidic technologies that use electric fields for particle manipulation and separation. First, Paper F demonstrates that the hydrodynamic fluid flows around the particles, regardless of their origin, are responsible for the wall-particle separation observed in AC electrophoresis in microfluidic channels. Consequently, and in contrast to the widely reported common hypothesis [55, 56], the analysis demonstrated that DEP is not the main contribution to the repulsion at low frequencies (below 10 kHz for our experimental conditions). The following paper (Paper G) further demonstrated that the CPEO theory can account for the observed repulsion within the weak-field limit ($\lesssim 60\ \mathrm{kV/m}$). Once CPEO was successfully tested, the accuracy of wall separation measurements provided a means to infer slip velocities for even smaller micro-particles, which meant that the CPEO theory could be tested at smaller scales.

The practical application of CPEO-based particle-wall separation was exploited in the following two papers (Papers H and I) to achieve micron-sized particle fractionation and to explain the reported fractionation of particle for DLD biased with electric fields, something not previously understood [35, 47]. Paper H demonstrates proof of principle fractionation of particles according

to size and surface charge using flow-focusing microfluidic devices. CPEO was used to guide and optimize the device design and operation. Numerical simulations were developed to model the wall-particle CPEO interaction in geometries other than straight walls, and to provide a comprehensive understanding of the factors that govern the low-frequency electrokinetic-induced sorting of particles inside a microfluidic DLD channel. Paper I demonstrated that the CPEO wall-particle interaction combined with EP oscillation fully explains the deflection induced by low-frequency electric fields, with the simulations matching the experimentally observed trends. Therefore, the CPEO model completes the understanding of these microfluidic systems. This will have consequences for the design of microfluidic technologies that use electric fields for particle manipulation and separation.

In the last part of the thesis, Papers 3.4.1 and 3.4.2 describe methods that were developed to deliver the main results in the thesis. Specifically, Paper 3.4.1 described an improved method for measuring the electroosmotic mobility of surfaces based on a current-monitoring method. The technique streamlines the state of the art allowing a simplification of microfluidic devices used in the measurements . The material Zeta potential is determined from the measurements, which were done for native PDMS surfaces and surfaces treated with a non-ionic surfactant (Pluronic F-127) in low-conductivity electrolytes. Paper 3.4.2 described a computational graphical user interface (GUI) tool that provides users with no expertise in image analysis with a user-friendly software for detection and analysis of particles in a flow, with applications in microfluidics.

An additional contribution to the field is Paper J, which describes how the disturbance in a rotating electric field caused by the presence of a dielectric cylinder in a microfluidic channel produces a travelling wave around the obstacle. This travelling wave acts on particles suspended in the electrolyte, producing a time-averaged electrophoretic drift, i.e. travelling-wave electrophoresis or TWE. This work demonstrated how a simple two-dimensional extension of the published TWE theory provides a qualitative description of the time-averaged drift velocity that matches the observed dependence with frequency of applied electric field, and the decay with distance from the post. This new TWE design means that the electrodes can be moved far from the particles because the travelling wave is created by the insulating pillar. This reduces the influence of Faradaic reactions on the particle suspension. For this reason, the phenomenon is referred as insulating-TWE or iTWE. It provides a new way of manipulating/fractionating colloidal particles based on electrical mobility.

In summary, this thesis describes a new AC electrokinetic model (CPEO) that satisfactorily describes previously unexplained experimental observations in the literature of steady-state electroosmotic flows around charged insulating surfaces in microfluidic devices. The theory predicts the dominance of the flows for low conductivity electrolytes ($\lesssim 0.1\ \mathrm{S/m}$) and low electric field frequencies ($\lesssim 10\ \mathrm{kHz}$). It also predicts the appearance of hydrodynamic forces on particles undergoing AC electrophoresis in microfluidic channels, with implications for microfluidic techniques of particle fractionation.

The thesis also leaves open questions arising from the CPEO description and observations. The reason for he observed trapping of particles in or near constrictions within shallow microfluidic

channels remains unclear. Experiments show that this effect, appearing for the same electric field conditions as for CPEO, is also observed for taller channels (50 μm) and larger particles (1 μm and 2 μm). Future experiments should experimentally characterise this trapping phenomenon coupled with numerical simulations to elucidate whether it can be explained by a combination of known phenomena, or whether new descriptions are needed.

The effects of the electroosmotic flow patterns on interactions between particle pairs is an immediate consequence of the CPEO theory. Future experimental and theoretical work should focus on describing this phenomenon, which has been already observed in the literature. These have been theoretically studied in the context of induced-charge electrophoresis and compared to DEP [112]. Interestingly, the induced motion between particles decays for large distances as $(a/r)^2$ due to the hydrodynamic interaction, and as $(a/r)^4$ due to the DEP interaction (with r the distance between particle centres). Clearly, the hydrodynamic interaction dominates over the DEP interaction when the particles are separated by distances of several diameters. From experiments and CPEO theory for dielectric spheres, the hydrodynamic interactions between particles will decrease with increasing ionic strength and vanish for frequencies much greater than D/a^2. These trends were found by Mittal *et al.* [113] in experiments with latex microparticles in to AC fields, although they attributed the behaviour to the interaction between induced dipoles on the particles (i.e. DEP).

From a longer term, this new AC electrokinetic phenomenon could lead to new approaches for particle manipulation at the micron and sub-micron scale. Optimisation of microfluidic devices should allow enhanced fractionation of particles based on CPEO. As discussed in Paper H, the effect can be coupled with existing methods without significantly impacting on designs and fabrication. Future research should be directed towards exploiting new non-linear microfluidics and electrokinetics techniques capable of manipulating nano-scale particles overcoming Brownian forces.

Understanding the physical foundations underlying the experimental observations provide often unexpected new insights into phenomena. With adequate background knowledge, resources and experimental know-how it is possible to design and execute the key theoretical analyses and proof of principle experiments necessary to acquire an in-depth understanding of the phenomenon. This should provide an optimal path for exploiting any new effects leading to new applications. When the "fluid flow rolls" (as referred to initially) were first observed around DLD array pillars (in low-frequency AC electric fields) it was not anticipated their relation with the fractionation observed. Now it is known that those electroosmotic flows were responsible for the fractionation: not around the pillars but around the particles flowing past those posts in the electrolyte instead. These have the same origin, i.e. surface conductance and concentration polarization. To arrive to this finding, this thesis has gone through the description of a whole new AC electrokinetic phenomenon containing very rich physics (still needed to be further developed and exploited), Concentration Polarization Electroosmosis.

Appendix A

Supplementary Material for Paper C

Supplementary material for:

On the Origin of Stationary Electroosmotic Flow Driven by AC Fields Around Insulators

Víctor Calero[1], Raúl Fernández-Mateo[1], Hywel Morgan[1], Pablo García-Sánchez[2], and Antonio Ramos[2]

[1]School of Electronics and Computer Science, University of Southampton, United Kingdom.
[2]Depto. Electrónica y Electromagnetismo. Facultad de Física. Universidad de Sevilla. Avda. Reina Mercedes s/n, 41012. Sevilla, Spain.

Contents:

S1 Image of streamlines using a single post

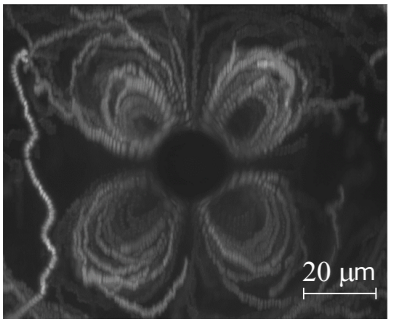

Figure S1: CPEO streamlines around a single post (radius=10 μm). The image is obtained by superimposing 200 frames. The peak-to-peak amplitude of the applied signal is 800 V at 100 Hz.

S2 Definitions of the Dukhin number

According to the Schnitzer-Yariv model, the Dukhin number is $\mathrm{Du} = \mathrm{Bi}(1 + 2\alpha^+)$, where Bi is the Bikerman number $\mathrm{Bi} = |q_s|\lambda_D$ (q_s and λ_D are, respectively, the non-dimensional surface charge and Debye length). With dimensional quantities, Bi is written as

$$\mathrm{Bi} = \left(\frac{|q_s| ze\lambda_D}{\varepsilon k_\mathrm{B}T}\right)\left(\frac{\lambda_D}{a}\right) = \left(\frac{|q_s|/ze}{2ca}\right) \tag{1}$$

That is, surface ion density divided by volume ion density and particle radius. The parameter α^+ is given by

$$\alpha^+ = \left(\frac{\varepsilon(k_\mathrm{B}T)^2}{(ze)^2\eta D^+}\right) \tag{2}$$

In the literature about colloids, the Dukhin number is the ratio $K_s/(\sigma a)$. The diffuse part contribution is [4]:

$$K_s = \frac{2(ze)^2 c\lambda_D}{k_\mathrm{B}T}\left(D^+(e^{-ze\zeta/k_\mathrm{B}T} - 1)\left(1 + \frac{3m^+}{z^2}\right) + D^-(e^{ze\zeta/k_\mathrm{B}T} - 1)\left(1 + \frac{3m^-}{z^2}\right)\right) \tag{3}$$

where $m_\pm = \frac{2}{3}\frac{(k_\mathrm{B}T)^2\varepsilon}{e^2\eta D^\pm}$. We remind that the Schnitzer-Yariv model is obtained for a highly charged surface with large zeta potential (negative in our case) so that $e^{-ze\zeta/k_\mathrm{B}T} \gg 1$,

$$K_s \approx \frac{2(ze)^2 c\lambda_D}{k_\mathrm{B}T} D^+ e^{-ze\zeta/2k_\mathrm{B}T}\left(1 + \frac{3m^+}{z^2}\right) = \frac{2(ze)^2 c\lambda_D}{k_\mathrm{B}T} D^+ e^{-ze\zeta/2k_\mathrm{B}T}\left(1 + \frac{2\varepsilon(k_\mathrm{B}T)^2}{z^2e^2\eta D^+}\right) \tag{4}$$

The volume conductivity is $\sigma = \frac{(ze)^2}{k_\mathrm{B}T}c(D^+ + D^-)$, and the ratio $\mathrm{Du} = K_s/(\sigma a)$ can be written as:

$$\mathrm{Du} \approx \frac{2\lambda_D}{a}\frac{D^+}{D^+ + D^-}e^{-ze\zeta/2k_\mathrm{B}T}\left(1 + \frac{2\varepsilon(k_\mathrm{B}T)^2}{z^2e^2\eta D^+}\right) \tag{5}$$

For equal diffusivities $D^+ = D^-$,

$$\mathrm{Du} \approx \frac{\lambda_D}{a}e^{-ze\zeta/2k_\mathrm{B}T}\left(1 + \frac{2\varepsilon(k_\mathrm{B}T)^2}{z^2e^2\eta D^+}\right) \tag{6}$$

Using eq. (1) and for a symmetric electrolyte $q_s = \sqrt{8c\varepsilon k_\mathrm{B}T}\sinh(ze\zeta/2k_\mathrm{B}T)$,

$$\mathrm{Bi} = \frac{2\lambda_D}{a}\sinh(ze|\zeta|/2k_\mathrm{B}T) \approx \frac{\lambda_D}{a}e^{ze|\zeta|/2k_\mathrm{B}T} \tag{7}$$

Finally,

$$\mathrm{Du} = \mathrm{Bi}(1 + 2\alpha^+) \approx \frac{\lambda_D}{a}e^{ze|\zeta|/2k_\mathrm{B}T}(1 + 2\alpha^+) \tag{8}$$

Thus, they are coincident, for a symmetrical electrolyte with equal diffusion coefficients and high absolute zeta potential, which is the case we are dealing with.

S3 Particle Tracking Velocimetry

In order to compare this theory with experimental results, quantitative measurements of the velocity fields are needed. For this purpose microparticle image velocimetry (μ-PIV) was used.

μ-PIV is a technique based on the evaluation of image pairs separated apart by a known time interval, where the positions of the particles in the two frames are cross-correlated. The basic concept is that if the distance in pixels is calibrated, it is possible to build a velocity field for that image-pair [33].

It is commonly accepted [34, 35] that the algorithms used in regular PIV can be applied at the micro-scale. Therefore, we made use of a widely-known open-source tool for PIV, named PIVlab [36, 37]. PIVlab divides the region of interest (ROI) into an uniform grid of interrogation windows (IWs), whose sizes are chosen such that the displacement of a particle between a pair of images is uniform for each ROI and that each has enough information [33]. This last assertion is important in μ-PIV since the density of seeding particles is low in order to avoid clogging. Furthermore, as the velocities involved in these experiments are extremely low in some of the cases, Brownian motion can be a problem. However, given that the flow is stationary, these problems are bypassed [38] by evaluating a large number of image pairs (correlation averaging). For this work we chose between 400 and 500 pairs.The elemental steps to obtain the velocity field are as follows:

The depth of correlation δ_{DOC} is the maximum distance from the focal plane at which correlation peaks produced by particles can be computed successfully. Following the expression given by Olsen and Adrian [39], for the present study (500 nm fluorescent microspheres) $\delta_{\mathrm{DOC}} = 3.24\,\mu$m. Thus, the velocity measurements carried out by μ-PIV are an average of the velocity field over δ_{DOC} around the focal plane, which is located at the half-width of the channel.

Prior to analysis with PIVlab, the images were preprocessed. First, the ROI was adjusted to create unit cells for the periodic array of posts. The centers of the posts were taken as the nodes of the lattices. Next, with the aid of a calibration image, a mask is created for the areas occupied by the posts. Contrast and particle enhancements were performed using the preprocessing tools available in the software (see [37] for details). The process is shown schematically in Figure S2.

Finally, a multi-pass analysis method was used, where the software analyses the sample in four different passes, using in each case IWs of different sizes. Two different grid sequences were chosen. The selection mainly depended on the average particle velocity, and was done in order for the displacement between a pair of frames to be similar across a set of experiments, given that the framerate was kept constant. As the ROI consisted of squares of the order of two hundred pixels, the two implemented sequences of IWs

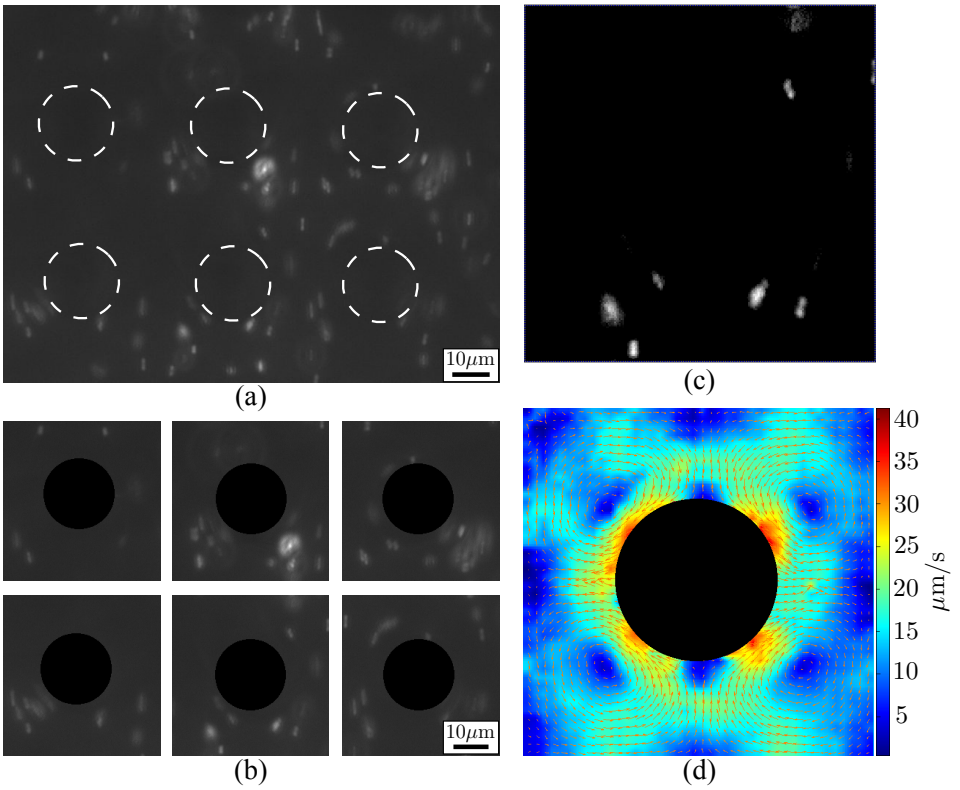

Figure S2: Image processing of the experimental videos for the case of the 1.75 mS/m electrolyte with a 70 Hz, 1000 Vpp applied field (20-micron posts). **(a)** Original image. **(b)** Partition of (a) into six unit cells with the posts covered by masks. **(c)** Example of contrast-enhanced image. **(d)** Velocity field after analysis of a sequence of images showing magnitudes as a color map.

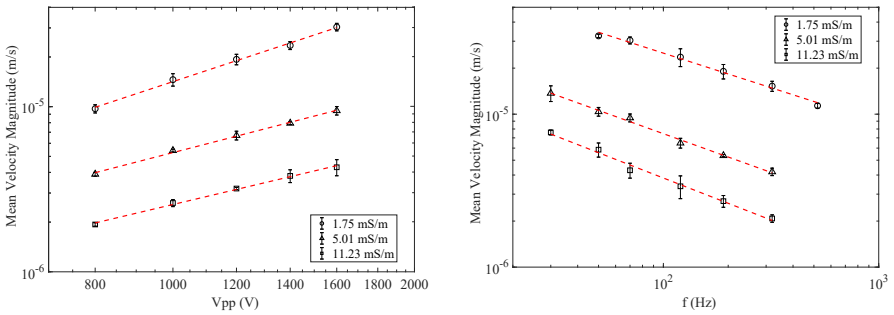

Figure S3: μ-PIV results for the mean velocity magnitude around a post. **(a)** Velocity as a function of imposed voltage for a fixed frequency of 70 Hz. The corresponding fitting slopes are: 1.6035 for the 1.75 mS/m electrolyte, 1.2558 for the 5.01 mS/m electrolyte, and 1.1531 for the 11.23 mS/m electrolyte. **(b)** Mean fluid roll velocity magnitude vs. frequency of the applied signal for a fixed voltage of 1600 Vpp. The slope for the 1.75 mS/m is -0.4526, -0.5066 for the 5.01 mS/m electrolyte, and -0.5494 for the 11.23 mS/m electrolyte.

were squares of 64, 32, 16 and 10 pixels, and 32, 16, 8 and 4 pixels for the lower velocities. To ensure the μ-PIV measurements were as robust as possible, we decided to evaluate the area mean velocity magnitude of the unit cells showed in Figure S2. The results are shown in Figure S3.

References

[4] Angel V. Delgado, Fernando Gonzalez-Caballero, R.J. Hunter, L.K. Koopal, and J. Lyklema, "Measurement and interpretation of electrokinetic phenomena (IUPAC technical report)," Pure and Applied Chemistry **77**, 1753–1802 (2005).

[33] R. Lindken, M. Rossi, S. Große, and J. Westerweel, "Micro-particle image velocimetry (PIV): Recent developments, applications and guidelines," Lab on a Chip **9**, 2551–2567 (2009).

[34] M. Raffel, C. E. Willert, F. Scarano, C. J. Kähler, S. T. Wereley, and J. Kompenhans, *Particle Image Velocimetry: A Practical Guide*, 3rd ed. (Springer International Publishing AG, 2018).

[35] C. E. Willert and M. Gharib, "Digital particle image velocimetry," Experiments in Fluids **10**, 181–193 (1991).

[36] W. Thielicke, "PIVlab - particle image velocimetry (PIV) tool, matlab central file exchange".

[37] W. Thielicke and E. J. Stamhuis, "PIVlab towards user-friendly, affordable and accurate digital particle image velocimetry in MATLAB," Journal of Open Research Software **2** (2014).

[38] C. D. Meinhart, S. T. Wereley, and J. G. Santiago, "A PIV algorithm for estimating time-averaged velocity fields," Journal of Fluids Engineering **122**, 285–289 (2000).

[39] M. G. Olsen and R. J. Adrian, "Out-of-focus effects on particle image visibility and correlation in microscopic particle image velocimetry," Experiments in Fluids **29**, S166–S174 (2000).

Appendix B

Supplementary Material for Paper F

Supplementary material for:

Wall Repulsion in Electrophoresis

Raúl Fernández-Mateo[1], Víctor Calero[2], Hywel Morgan[1], Pablo García-Sánchez[2], and Antonio Ramos[2]

[1]School of Electronics and Computer Science, University of Southampton, Southampton SO17 1BJ, United Kingdom.
[2]Depto. Electrónica y Electromagnetismo. Facultad de Física. Universidad de Sevilla. Avda. Reina Mercedes s/n, 41012. Sevilla, Spain.

Contents:

S1 Wall repulsion of a sphere with a prescribed slip velocity

Consider a sphere of radius a near a flat wall and freely suspended in a viscous fluid with viscosity η (see figure S1). We assume that there is a slip velocity on the surface of the sphere given by the following expression:

$$\mathbf{v}_s = v_0 \sin(2\theta)\mathbf{u}_\theta \tag{1}$$

where v_0 is a constant. In our experiments, this slip velocity is induced by a phenomenon termed Concentration Polarization Electroosmosis (CPEO). However, irrespective of its origin, such slip velocity gives rise to a flow field around the sphere that leads to a net motion of the freely suspended sphere in a direction perpendicular to the wall. Therefore, the velocity on the sphere surface is written as $\mathbf{v} = \mathbf{U} + \mathbf{v}_s$, where $\mathbf{U}$ is the velocity of the center of mass of the sphere w.r.t. the wall. The hydrodynamic stress tensor in the liquid can be written as $\mathbb{T}_{\mathrm{H}} = \mathbb{T}_{\mathrm{H1}} + \mathbb{T}_{\mathrm{H2}}$:

- $\mathbb{T}_{\mathrm{H1}}$ is the stress tensor associated to the Stokes problem of a particle translating with velocity $\mathbf{U}$ perpendicular to the wall. The slip velocity is zero on the sphere surface and on the wall.

-$\mathbb{T}_{\mathrm{H2}}$ is the stress tensor associated to the Stokes problem of a non-moving (U=0) sphere with slip velocity given by $\mathbf{v}_s$ on its surface and no slip on the wall.

Since this is a force-free problem, the following condition applies:

$$\int_S \mathbf{n} \cdot (\mathbb{T}_{\mathrm{H1}} + \mathbb{T}_{\mathrm{H2}}) \mathrm{d}S = 0 \tag{2}$$

where S is any surface that encloses the sphere and $\mathbf{n}$ a unit vector perpendicular to that surface. The two integral terms can be interpreted as follows:

- $\int_S (\mathbf{n} \cdot \mathbb{T}_{\mathrm{H2}}) \mathrm{d}S$ is the force exerted by the liquid on the sphere if it is hold at a fixed position. In our experiments, we name it the **CPEO force** on the sphere ($\mathbf{F}_{\mathrm{CPEO}}$).

- $\int_S (\mathbf{n} \cdot \mathbb{T}_{\mathrm{H1}}) \mathrm{d}S$ is the **viscous drag** ($\mathbf{F}_{\mathrm{drag}}$) on a sphere moving with velocity $\mathbf{U}$. This force can be written as $\mathbf{F}_{\mathrm{drag}} = -\gamma \mathbf{U}$.

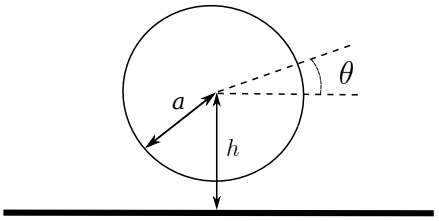

Figure S1: Sphere of radius a near a flat wall. The angle θ is defined with respect the direction of the electric field (parallel to the wall).

In our problem of a sphere moving perpendicular to a wall, the friction coefficient is $\gamma = 6\pi\eta a\lambda$, with λ a correction factor to the Stokes formula given by the following expression [1]:

$$\lambda = \frac{4}{3}\sinh\alpha \sum_{n=1}^{\infty} \frac{n(n+1)}{(2n-1)(2n+3)} \left[\frac{2\sinh(2n+1)\alpha + (2n+1)\sinh 2\alpha}{4\sinh^2(n+1/2)\alpha - (2n+1)^2\sinh^2\alpha} - 1 \right] \tag{3}$$

where $\alpha = \cosh^{-1}(h/a)$. We calculated γ by adding 100 terms in the series of eq. (3). Comsol Multiphysics was used to calculate $\mathbf{F}_{\mathrm{CPEO}}$ as a function of the distance to the wall. The particle velocity is then calculated as $\mathbf{U}_{\mathrm{CPEO}} = \mathbf{F}_{\mathrm{CPEO}}/\gamma$. Figure S2 shows the numerical results obtained for U_{CPEO} as a function of distance to the wall. For comparison, we have also plotted the velocity given by the analytical expression obtained by Yariv [2] for the velocity of a sphere with slip velocity given by eq. (1) and far from the wall:

$$U_{\mathrm{CPEO}} = \frac{3}{8}\frac{v_0}{(h/a)^2} \tag{4}$$

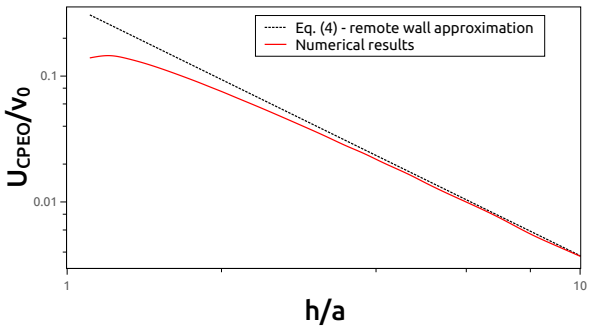

Figure S2: Numerical results for U_{CPEO} as a function of distance to the wall. For comparison, we have also plotted the velocity given by the analytical expression for a sphere far from the wall.

Direct integration of the CPEO velocity enables calculation of the distance to the wall as a function of time for a sphere whose initial position is very close to the wall ($h/a = 1.1$ for $t = 0$). Figure S3 shows a comparison between the analytical approximation (eq. (4)) and the numerical results. The small difference in velocities near the wall produces a small difference in separations that remains nearly constant when the sphere is far from the wall. Since this difference is negligibly small in our experiments, the data were analyzed with eq.(4) for simplicty.

S2 Stresslet wall repulsion

According to Blake and Chwang [3], the velocity field of a Stokeslet in front of a non-slip plane is given by a system of images that are fundamental singularities of the Stokes problem. We are interested in the Stokeslet that derives from a force parallel to the wall, because the required Stresslet

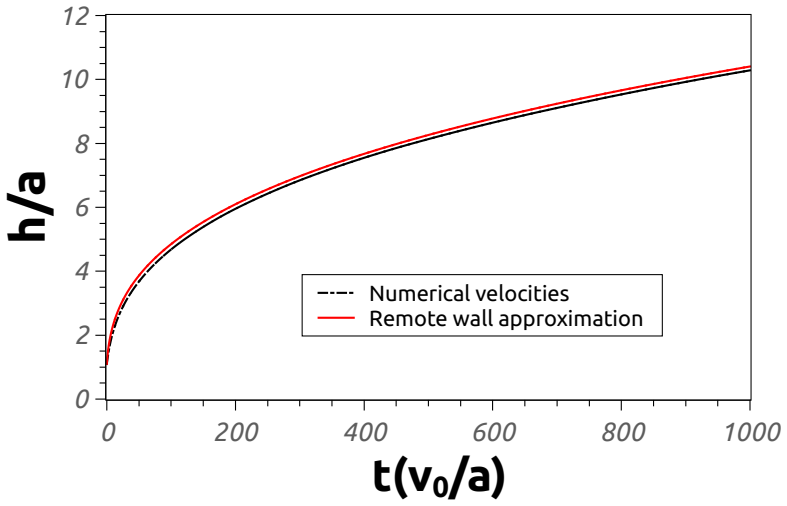

Figure S3: Distance of a particle to the wall as a function of time. The difference between using the numerical and analytical results for CPEO velocities is negligible.

is obtained by taking the partial derivative of the Stokeslet in the direction of the force. Thus, the Stokeslet due to the force $\mathbf{F} = F\hat{x}$ at $(x, y, z) = (0, 0, h)$ in front of a nonslip plane at $z = 0$ produces the velocity field [3]

$$\frac{8\pi\eta v_x}{F} = \left(\frac{1}{r} + \frac{x^2}{r^3}\right) - \left(\frac{1}{R} + \frac{x^2}{R^3}\right) + 2h\frac{\partial}{\partial x}\left(\frac{hx}{R^3} - \frac{x(z+h)}{R^3}\right) \tag{5}$$

$$\frac{8\pi\eta v_y}{F} = \frac{xy}{r^3} - \frac{xy}{R^3} + 2h\frac{\partial}{\partial x}\left(\frac{hy}{R^3} - \frac{y(z+h)}{R^3}\right) \tag{6}$$

$$\frac{8\pi\eta v_z}{F} = \frac{x(z-h)}{r^3} - \frac{x(z+h)}{R^3} + 2h\frac{\partial}{\partial x}\left(\frac{h(z+h)}{R^3} - \frac{1}{R} - \frac{(z+h)^2}{R^3}\right) \tag{7}$$

where $r = \sqrt{x^2 + y^2 + (z-h)^2}$ and $R = \sqrt{x^2 + y^2 + (z+h)^2}$.

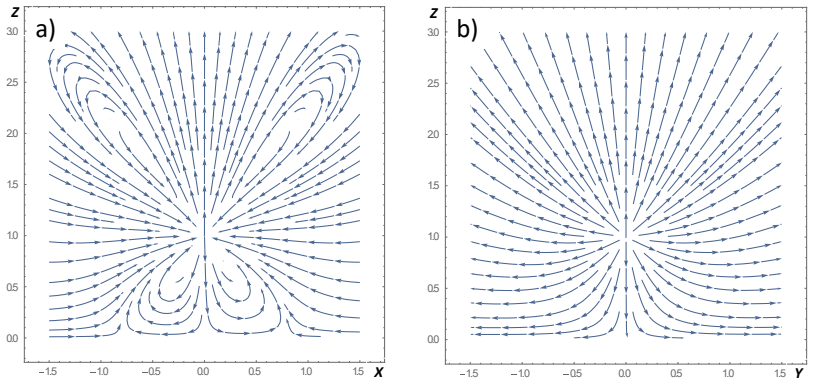

Figure S4: Velocity field of the 'reflected' Stresslet: a) plane $y = 0$, b) plane $x = 0$

If we now take the derivative of these expressions with respect to x, we obtain the velocity field of the required Stresslet in front of a nonslip plane at a distance h. Note that the x-derivative of the previous velocity field satisfies Stokes equations and the boundary condition of no slip at the $z = 0$ plane. The resulting velocity field is:

$$\frac{v_x}{v_0 a^2} = -\frac{3x^3}{r^5} + \frac{x}{r^3} + \frac{3x^3}{R^5} - \frac{x}{R^3} + 2h\left(\frac{15hx^3}{R^7} - \frac{15x^3(z+h)}{R^7} - \frac{9hx}{R^5} + \frac{9x(h+z)}{R^5}\right) \tag{8}$$

$$\frac{v_y}{v_0 a^2} = -\frac{3x^2 y}{r^5} + \frac{y}{r^3} + \frac{3x^2 y}{R^5} - \frac{y}{R^3} + 2h\left(\frac{15hx^2 y}{R^7} - \frac{15(h+z)x^2 y}{R^7} - \frac{3hy}{R^5} + \frac{3(h+z)y}{R^5}\right) \tag{9}$$

$$\frac{v_z}{v_0 a^2} = -\frac{3x^2(z-h)}{r^5} + \frac{z-h}{r^3} + \frac{3x^2(z+h)}{R^5} - \frac{z-h}{R^3} + 2h\left(\frac{15hx^2(z+h)}{R^7} - \frac{15x^2(z+h)^2}{R^7} - \frac{3x^2}{R^5} - \frac{3h(z+h)}{R^5} + \frac{3(z+h)^2}{R^5} + \frac{1}{R^3}\right) \quad (10)$$

where v_0 is the maximum time-averaged slip velocity as defined in the main text and a is the radius of the sphere. For the Stresslet $a \to 0, v_0 \to \infty$ and $v_0 a^2 < \infty$.

The 'reflected' velocity field (the previous field without the singularity) at the point $(0, 0, h)$ is

$$\mathbf{v} = \frac{3v_0 a^2}{8h^2}\hat{z}. \quad (11)$$

This is the induced particle velocity at large wall-separation distances. Plots of the velocity field of the 'reflected' Stresslet are shown in figure S4.

S3 Data Analysis for Wall-Repulsion Experiments

In the following two sections, we explain in detail the procedures for the analysis of the experimental data as described in the main text.

For measurement of the separation from the wall, a custom software written in Matlab identifies the position of particles within the channel where steps are depicted in Figure S5. Images are taken with bright field [Fig. S5(a)], then this image is turned into a binary image, followed by noise reduction filters to detect spots in the image [Fig. S5(b)]. Finally, the centroid position of the non-zero remaining elements [Fig. S5(c)].

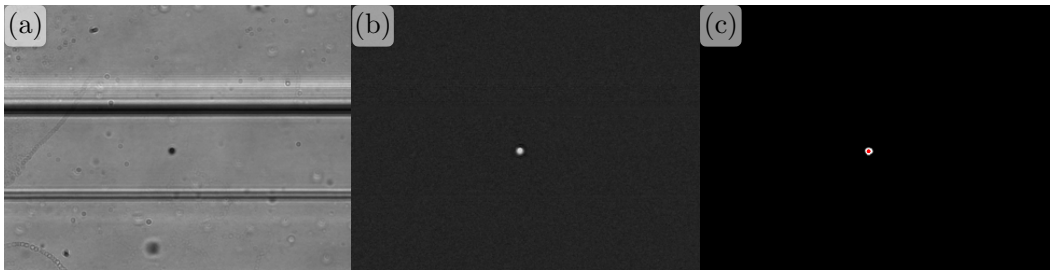

Figure S5: Sequences showing the image analysis used to estimate the wall repulsion. (a) Original unmodified frame. (b) Frame inverted and background subtracted. (c) Binarisation and noise reduction filters. The red dot marks the position assigned in the frame by the software. The example frame corresponds to 3 μm carboxylate particles in a 1.7 mS/m KCl medium with 1600 Volts peak-to-peak at 50 Hz.

The transverse position z_i, $i \in (1, ..., N)$ of each of the N particles along the channel is stored, and histograms are constructed with the data. The wall separation is estimated as half the difference between the channel width W (which is measured independently) and the width of the distribution of transverse positions z_i, Δz,

$$h = \frac{W - \Delta z}{2}. \quad (12)$$

As the videos are longer than 2 minutes, to avoid unwanted detection due to noise or impurities in the fluid, the width Δz was determined as the interval of z that contains 95% of particle positions given by the histograms. The binning division for pigeonholing the particles was chosen as the pixel resolution of the frames. Given that each dataset contained a large number of particles (around 600), the error in the measurement was taken as the size of one pixel of the image.

S4 Data Analysis for Particle Slip Velocity Determination Experiments

We also developed software in Matlab to measure the slip velocity around the particles, detailed in a recent publication [4]. First, the concentration of the target particles was such that no more than four particles were present in the whole channel at the same time. Then, the software was used to detect the relative position between the target (2 μm and 3 μm particles) and the tracer (500 nm carboxylate) particles. From the resulting vector positions, and taking into account the frame rate, we finally extrapolate the slip velocity of a quadrupolar flow given by equation (2) in the main text.

The tracers used to obtain the slip velocity were those that flowed close enough to the target particle: that is, the magnitude of the fluid velocity field was much larger than that due to Brownian motion. For every single tracer chosen, a different slip velocity was extrapolated, and this was the final measurement of the average of all the values for each tracer. This provides an estimate of the error of the measurement from the standard deviation of the different values for each tracer. Figure 1(c) in the main text shows the results of the measurements of the slip velocity as a function of frequency.

S5 Comparison between experimental data for wall repulsion and CPEO prediction

Figure S6 shows the comparison between the theoretical predictions of CPEO [4] flow and experimental data for the wall repulsion. Theoretical predictions were obtained using measurements of the zeta potential and fitting the value of the Dukhin number.

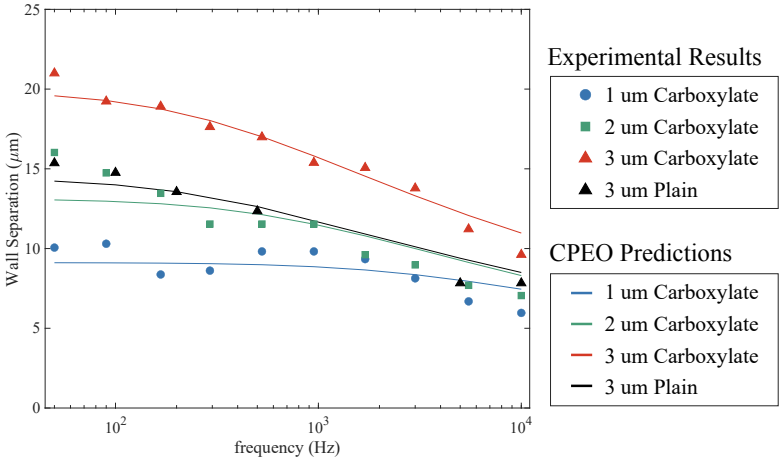

Figure S6: Comparison between the theoretical predictions of CPEO flow and experimental data for the wall repulsion. Theoretical predictions were obtained using measurements of the zeta potential and fitting the value of the Dukhin number (1 μm Carboxy, Du=0.2059; 2 μm Carboxy, Du=0.0486; 3 μm Carboxy, Du=0.0720; 3 μm Plain, Du=0.0951).

References

[1] John Happel and Howard Brenner. *Low Reynolds number hydrodynamics: with special applications to particulate media*, volume 1. Springer Science & Business Media, 2012.

[2] Ehud Yariv. Boundary-induced electrophoresis of uncharged conducting particles: remote wall approximations. *Proceedings of the Royal Society A: Mathematical, Physical and Engineering Sciences*, 465(2103):709–723, 2009.

[3] JR Blake and AT Chwang. Fundamental singularities of viscous flow. *Journal of Engineering Mathematics*, 8(1):23–29, 1974.

[4] Raúl Fernández-Mateo, Pablo García-Sánchez, Víctor Calero, Hywel Morgan, and Antonio Ramos. Stationary electro-osmotic flow driven by ac fields around charged dielectric spheres. *Journal of Fluid Mechanics*, 924, 2021.

Appendix C

Supplementary Material for Paper G

Supplementary material for:

Wall Repulsion during Electrophoresis: Testing the theory of Concentration-Polarization Electroosmosis

Raúl Fernández-Mateo[1], Hywel Morgan[1], Antonio Ramos[2], and Pablo García-Sánchez[2]

[1]School of Electronics and Computer Science, University of Southampton, Southampton SO17 1BJ, United Kingdom.
[2]Depto. Electrónica y Electromagnetismo. Facultad de Física. Universidad de Sevilla. Avda. Reina Mercedes s/n, 41012. Sevilla, Spain.

Contents:

S1 CPEO slip velocity on a spherical particle

In a recent publication [1], we derived the time-averaged slip velocity occurring on the surface of a charged dielectric sphere of radius a (with zeta potential ζ_0 and surface conductance K_s) suspended in a binary electrolyte in the presence of an AC electric field of magnitude E_0 and angular frequency ω.

Magnitude	Scale	Notes
Length	a	Particle radius
Electric Potential	$\phi_{ther} = k_B T/ze$	k_B Boltzmann's constant, T absolute temperature, z ionic valence, e elementary charge.
Time	$\eta/\varepsilon E_{ther}^2$	η fluid viscosity, ε fluid permittivity, $E_{ther} = \phi_{ther}/a$
Pressure	εE_{ther}^2	
Ion salt concentration	c_0	Salt concentration far from the particle
Derived Scales		
Diffusion constant	$\varepsilon a^2 E_{ther}^2/\eta$	
Velocity	$\varepsilon a E_{ther}^2/\eta$	
Surface charge	$\varepsilon\phi_{ther}/\lambda_D$	λ_D Debye length

Table S1: Scales used for the slip velocity calculations

For the derivation of the slip velocity, we used the scaling shown in Table S1 and performed a power expansion in terms of the reduced electric field magnitude $\beta = E_0/E_{ther}$,

$$\begin{aligned} c &= 1 + \beta c_1 + \beta^2 c_2 + \dots, \\ \zeta &= \zeta_0 + \beta\zeta_1 + \beta^2\zeta_2 + \dots, \\ \phi &= \beta\phi_1 + \beta^2\phi_2 + \dots, \\ \mathbf{v} &= \beta\mathbf{v}_1 + \beta^2\mathbf{v}_2 + \dots, \\ p &= \beta p_1 + \beta^2 p_2 + \dots. \end{aligned}$$

The time-average slip velocity up to second order in the expansion is given by[1]

[1]There is a typographical error in the expression for $\langle\mathbf{v_2}\rangle$ in ref. [1] (equation (2.25)): Instead of $\tanh(\zeta_0/4)\langle\zeta_1\nabla_s\phi_1\rangle$, it should read $\tanh(\zeta_0/4)\langle\zeta_1\nabla_s c_1\rangle$.

$$\langle \mathbf{v}_{2s} \rangle = \zeta_0 \nabla_s \langle \phi_2 \rangle + \langle \zeta_1 \nabla_s \phi_1 \rangle - 4 \ln \left(\cosh \left(\frac{\zeta_0}{4} \right) \right) \nabla_s \left\langle c_2 - \frac{c_1^2}{2} \right\rangle - \tanh \left(\frac{\zeta_0}{4} \right) \langle \zeta_1 \nabla_s c_1 \rangle. \quad (1)$$

For the case of a sphere, equation 1 can be written as $\langle \mathbf{v}_{2s} \rangle = v_0 \sin(2\theta)\hat{\theta}$, where v_0 is the maximum time-average velocity on the sphere surface. The expression for v_0 can be found in Appendix A of ref. [1].

In the following section, we provide a Matlab script for computing v_0. The execution of the code will be followed by a series of prompts in the command window, where the user has to provide the parameters in their dimensional form for the calculation. Then, the routine will automatically compute the scaled variables and use them to determine the slip velocity using embedded functions in the script. Finally, the result of the slip velocity will be displayed in the Command Window and stored in Matlab Workspace.

S2 Matlab script for computing the maximum slip velocity

```
1
2  % Slip_Velocity.m
3  % Created by Raul Fernandez-Mateo
4  % November 2022. University of Southampton
5
6  % ------------------------------------------------------------------------
7  % The execution of this script will result in the calculation of the CPEO
8  % slip velocity of a spherical particle.
9
10 % Once executed, the user will be asked to provide the parameters which are
11 % needed for this purpose. The slip velocity will be displayed in hte
12 % Command Window, and stored in the Workspace together with the rest of the
13 % parameters
14 % ------------------------------------------------------------------------
15
16 %% Loading of Parameters
17 clc
18
19 fprintf('---------------------------------------- \n')
20 fprintf('Please provide the following parameters: \n')
21 fprintf('---------------------------------------- \n')
22 fprintf('FLUID PARAMETERS \n')
23 eta = input('    Viscosity (m^2/s):');
24 epsilonr = input('    Relative permittivity (non-dimensional):');
25 sigma = input('    Conductivity (S/m):');
26 D = input('    Diffusion constant of salt ions (m^2/s):');
27
28 fprintf('PARTICLE PARAMETERS \n')
29 a = input('    Radius (m):');
30 Ks = input('    Surface conductance (S):');
31 zeta0 = input('    Zeta potential (V):');
32
33 fprintf('ELECTRIC FIELD \n')
34 E0 = input('    Amplitude (V/m):');
35 f = input('    Frequency (Hz):');
36 fprintf('---------------------------------------- \n')
37
38 %% Derived parameters and scaled variables
39
40 epsilon = epsilonr*8.85e-12; % Permittivity
41 phith = 25e-3; % Thermal Voltage
42 Du = Ks/(sigma*a); % Dukhin number
43 zeta0 = zeta0/phith; % Scaled zeta potential
44 Eth = phith./a; % Thermal Field
45 alpha1 = epsilon*Eth.^2.*a.^2/eta/D; % Reciprocals of the non-dimensional
46                                       % diffusion constant
47 D1 = 1./alpha1; % Non-dimensional diffusion constant
48 v0 = epsilon*a.*Eth.^2/eta; % Velocity scale
49 omega0 = D./a.^2; % Angular frequency scale
50 omega=2*pi*f./omega0; % Scaled angular frequency
51 k = sqrt(1i*omega);
52
53 %% Calculation of Slip Velocity
54
```

```
slip_velocity = v0*(E0/Eth)^2*(Uslip(k,Du,zeta0)+...
    Uslip_conv(k,Du,zeta0,D1));
fprintf('\n \n Slip Velocity: %5.5f um/s \n', slip_velocity*1e6)
fprintf('---------------------------------------- \n')

%% Supporting functions



function Uslip = Uslip(k,Du,zeta0)

Uslip= (1/40).*(1+4.*Du).^(-1).*abs(2+2.*k+k.^2+Du.*(2+k).^2).^(-2).*(( ...
 -2).*abs(zeta0).*(30.*Du.^2.*(1+2.*Du).*real((1+k).*(2+2.*conj( ...
  k)+conj(k).^2))+abs(2+2.*k+k.^2+Du.*(2+k).^2).^2.*(10.*Du.* ...
  real(Du.*exp(1).^k.*k.^3.*(2+2.*k+k.^2+Du.*(2+k).^2).^(-1).*(2+2.* ...
  conj(k)+conj(k).^2+conj(Du).*(2+conj(k)).^2) ...
  .^(-1).*((-1).*(2+2.*conj(k)+conj(k).^2).*(3.*k.^3.* ...
 igamma((-6),k)+3.*k.^3.*igamma((-5),k)+2.*k.^3.*igamma((-4),k)+(-6).* ...
  igamma((-3),k)+(-6).*igamma((-2),k)+(-2).*igamma((-1),k))+2.* ...
conj(Du).*(3.*k.^3.*igamma((-6),k)+3.*k.^3.*igamma((-5),k)+2.* ...
  k.^3.*igamma((-4),k)+12.*igamma((-3),k)+12.*igamma((-2),k)+4.*igamma(( ...
  -1),k)+conj(k).^2.*(3.*k.^3.*igamma((-6),k)+3.*k.^3.*igamma(( ...
  -5),k)+2.*k.^3.*igamma((-4),k)+3.*igamma((-3),k)+3.*igamma((-2),k)+ ...
  igamma((-1),k))+conj(k).*(3.*k.^3.*igamma((-6),k)+3.*k.^3.* ...
 igamma((-5),k)+2.*k.^3.*igamma((-4),k)+12.*igamma((-3),k)+12.*igamma(( ...
  -2),k)+4.*igamma((-1),k)))))+(-1).*(1+4.*Du).*(real(Du.*exp(1).^k.* ...
  k.^(-2).*(2+2.*k+k.^2+Du.*(2+k).^2).^(-1).*(12.*k.^5.*igamma((-3), ...
  k)+12.*k.^5.*igamma((-2),k)+4.*k.^5.*igamma((-1),k)+exp(1).^((-1).* ...
  k).*k.^3.*(2+2.*conj(k)+conj(k).^2+conj(Du).*(2+ ...
  conj(k)).^2).^(-1).*((-2)+(-2).*conj(k)+(-1).*conj( ...
  k).^2+2.*conj(Du).*(1+conj(k)+conj(k).^2)).*(6+6.* ...
  exp(1).^k.*k.^5.*igamma((-6),k)+6.*exp(1).^k.*k.^5.*igamma((-5),k)+ ...
  4.*exp(1).^k.*k.^5.*igamma((-4),k)+9.*exp(1).^k.*igamma((-1),k)+9.* ...
  exp(1).^k.*igamma(0,k))+18.*igamma(2,k)+18.*igamma(3,k)+6.*igamma(4,k) ...
  ))+(-3).*real(Du.*exp(1).^k.*k.*(2+2.*k+k.^2+Du.*(2+k).^2).^(-1).*(( ...
  -6).*k.^2.*igamma((-3),k)+(-6).*k.^2.*igamma((-2),k)+(-2).*k.^2.* ...
  igamma((-1),k)+(-1).*exp(1).^((-1).*k).*(2+2.*conj(k)+ ...
conj(k).^2+conj(Du).*(2+conj(k)).^2).^(-1).*((-2)+( ...
  -2).*conj(k)+(-1).*conj(k).^2+2.*conj(Du).*(1+ ...
conj(k)+conj(k).^2)).*((-2)+3.*exp(1).^k.*k.^5.*igamma(( ...
  -6),k)+3.*exp(1).^k.*k.^5.*igamma((-5),k)+2.*exp(1).^k.*k.^5.* ...
igamma((-4),k)+(-3).*exp(1).^k.*igamma((-1),k)+(-3).*exp(1).^k.* ...
igamma(0,k))+6.*k.^(-3).*igamma(2,k)+6.*k.^(-3).*igamma(3,k)+2.*k.^( ...
  -3).*igamma(4,k))))))+180.*Du.^2.*abs(1+k).^2.*(Du.*abs(zeta0)+(-2) ...
  .*(1+2.*Du).*log(cosh((1/4).*zeta0))+(-1).*(1+4.*Du).*sech((1/2).* ...
  zeta0).*sinh((1/4).*zeta0).^2)+5.*(96.*Du.^3.*log(cosh((1/4).* ...
 zeta0)).*real((1+k).*(2+2.*conj(k)+conj(k).^2))+abs(2+2.* ...
  k+k.^2+Du.*(2+k).^2).^2.*((-16).*Du.*log(cosh((1/4).*zeta0)).*real( ...
  Du.*exp(1).^k.*k.^3.*(2+2.*k+k.^2+Du.*(2+k).^2).^(-1).*(2+2.* ...
conj(k)+conj(k).^2+conj(Du).*(2+conj(k)).^2) ...
 .^(-1).*((-1).*(2+2.*conj(k)+conj(k).^2).*(3.*k.^3.* ...
igamma((-6),k)+3.*k.^3.*igamma((-5),k)+2.*k.^3.*igamma((-4),k)+(-6).* ...
  igamma((-3),k)+(-6).*igamma((-2),k)+(-2).*igamma((-1),k))+2.* ...
conj(Du).*(3.*k.^3.*igamma((-6),k)+3.*k.^3.*igamma((-5),k)+2.* ...
  k.^3.*igamma((-4),k)+12.*igamma((-3),k)+12.*igamma((-2),k)+4.*igamma(( ...
  -1),k)+conj(k).^2.*(3.*k.^3.*igamma((-6),k)+3.*k.^3.*igamma(( ...
  -5),k)+2.*k.^3.*igamma((-4),k)+3.*igamma((-3),k)+3.*igamma((-2),k)+ ...
  igamma((-1),k))+conj(k).*(3.*k.^3.*igamma((-6),k)+3.*k.^3.* ...
 igamma((-5),k)+2.*k.^3.*igamma((-4),k)+12.*igamma((-3),k)+12.*igamma(( ...
  -2),k)+4.*igamma((-1),k)))))+9.*(1+4.*Du).*real(Du.*(1+k).*(2+2.*k+ ...
  k.^2+Du.*(2+k).^2).^(-1).*(2+2.*conj(k)+conj(k).^2+2.* ...
  conj(Du).*(1+conj(k))).*(2+2.*conj(k)+conj(k) ...
  .^2+conj(Du).*(2+conj(k)).^2).^(-1)).*tanh((1/2).*abs( ...
  zeta0)))));

end

function Uslip_conv = Uslip_conv(k,Du,zeta0,Diff)

Uslip_conv = (-1).*(10+40.*Du).^(-1).*(Du.*abs(zeta0)+(-2).*(1+2.*Du).*log( ...
cosh((1/4).*zeta0))).*(real(Diff.^(-1).*Du.*k.^(-2).*(2+2.*k+k.^2+ ...
 Du.*(2+k).^2).^(-1).*(2+2.*conj(k)+conj(k).^2+conj( ...
  Du).*(2+conj(k)).^2).^(-1).*conj((2+2.*k+k.^2+2.*Du.*(1+ ...
  k)).*zeta0+8.*Du.*(1+k).*log(cosh((1/4).*zeta0))).*(6.*k.^3+6.* ...
  exp(1).^k.*k.^8.*igamma((-6),k)+6.*exp(1).^k.*k.^8.*igamma((-5),k)+ ...
  4.*exp(1).^k.*k.^8.*igamma((-4),k)+(-12).*exp(1).^k.*k.^5.*igamma(( ...
  -3),k)+(-12).*exp(1).^k.*k.^5.*igamma((-2),k)+9.*exp(1).^k.*k.^3.* ...
  igamma((-1),k)+(-4).*exp(1).^k.*k.^5.*igamma((-1),k)+9.*exp(1).^k.* ...
```

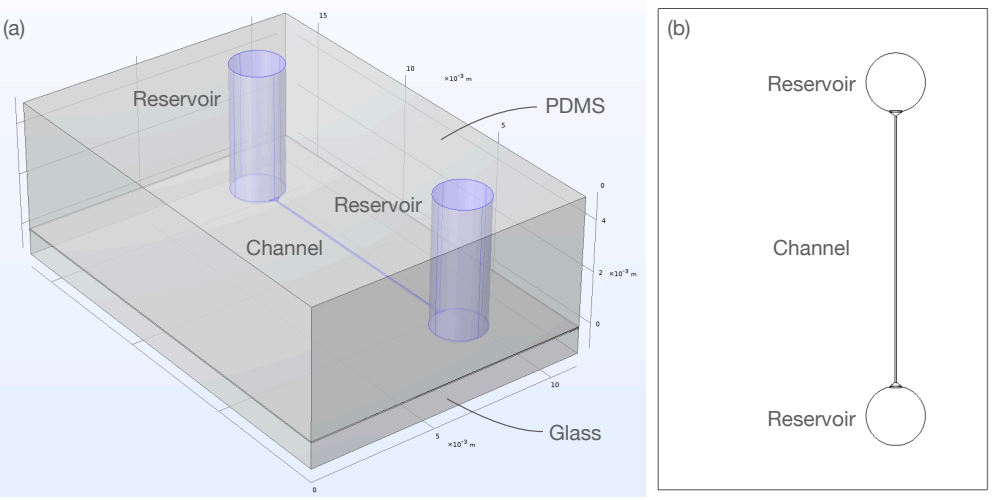

Figure S1: Geometry of the device simulated in COMSOL Multiphysics. (a) Entire geometry, with the channel highlighted in blue. (b) Section of the geometry at the half height of the channel: 25 μm above the PDMS-glass interface. Channel length is 1 cm.

```
133     k.^3.*igamma(0,k)+(-18).*exp(1).^k.*igamma(2,k)+(-18).*exp(1).^k.* ...
134     igamma(3,k)+(-6).*exp(1).^k.*igamma(4,k)))+3.*real(Diff.^(-1).*Du.* ...
135     k.^(-2).*(2+2.*k+k.^2+Du.*(2+k).^2).^(-1).*(2+2.*conj(k)+ ...
136    conj(k).^2+conj(Du).*(2+conj(k)).^2).^(-1).* ...
137   conj((2+2.*k+k.^2+2.*Du.*(1+k)).*zeta0+8.*Du.*(1+k).*log( ...
138   cosh((1/4).*zeta0))).*((-2).*k.^3+3.*exp(1).^k.*k.^8.*igamma((-6), ...
139     k)+3.*exp(1).^k.*k.^8.*igamma((-5),k)+2.*exp(1).^k.*k.^8.*igamma(( ...
140     -4),k)+(-6).*exp(1).^k.*k.^5.*igamma((-3),k)+(-6).*exp(1).^k.* ...
141   k.^5.*igamma((-2),k)+(-3).*exp(1).^k.*k.^3.*igamma((-1),k)+(-2).* ...
142   exp(1).^k.*k.^5.*igamma((-1),k)+(-3).*exp(1).^k.*k.^3.*igamma(0,k)+ ...
143     6.*exp(1).^k.*igamma(2,k)+6.*exp(1).^k.*igamma(3,k)+2.*exp(1).^k.* ...
144     igamma(4,k))));
145
146   end
```

S3 Numerical simulation of the electrothermal effect

The high-intensity fields used in our experiments could lead to effects caused by Joule heating. To determine whether this is an issue a numerical study was performed to determine the temperature rise and any gradients that could cause electrothermal effect. To investigate this, the entire geometry was reproduced in COMSOL Multiphysics, as shown in Figure S1. The complete coupled fluid dynamic, electric and heat transfer problem was then simulated. The model parameters are sumarised in Table S2.

Magnitude	Electrolyte	PDMS [2]	Glass
Thermal Conductivity, κ [W/(m·K)]	0.6	0.15	1
Density, ρ [kg/m^3]	10^3	0.97×10^3	2.5×10^3
Heat Capacity at Constant Pressure, C_p [J/(kg·K)]	4.18×10^3	1.46×10^3	0.75×10^3
Electrical Conductivity, σ [S/m]	1.7×10^{-3}	1×10^{-12}	1×10^{-11}
Relative Permittivity	80	2.5	4.7
Dynamic Viscosity, μ [Pa·s]	1×10^{-3}	–	–

Table S2: Parameters used for the COMSOL simulations.

First, we determined the fluid flow inside the channel. A pressure difference of 100 Pa was set between the inlet and the outlet reservoir to simulate the pressure imposed by the pressure controller in our experiment. For the rest of the channel walls a zero velocity $\mathbf{v}_{\text{Wall}} = 0$ was set. The result, shown in Figure S2(a), is a parabolic profile of the same magnitude as described by equation (4) of the main text.

Next, we simulated the highest electric field (100 kV/m) inside the channel. Given the conductivity differences between the electrolyte and the rest of the system (almost ten orders of magnitude), the solution was only calculated in the region where the electrolyte was present. A voltage of 1000

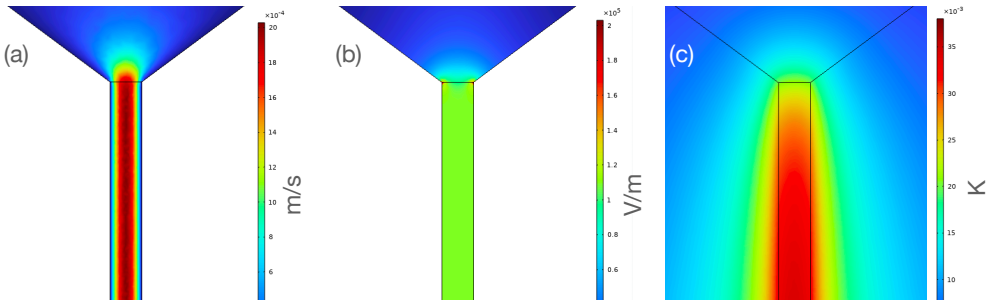

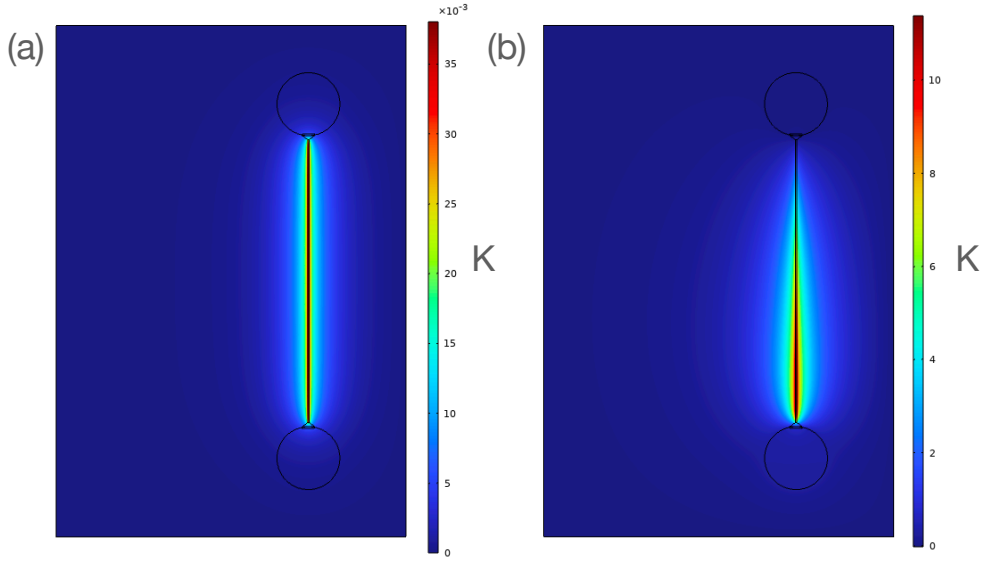

Figure S3: Temperature increase in the central section of the channel. (a) Experimental conditions where thermal conduction is the main driver. (b) Without considering the effects of thermal conduction. Note the differences in the temperature colour scales.

Volts was applied at one inlet, and ground conditions on the other reservoir. The electric field magnitude is shown in Figure S2(b).

The heat transfer problem was simulated in all three domains of the system (PDMS, electrolyte and glass) with a heat source term given by the Joule heating σE_0^2 in the electrolyte. The outer boundaries of the domain were set to a constant (room temperature). The steady state temperature increase of the geometry is shown in Figure S2(c).

To compare conduction and convection of the heat generated in the channel, we simulated the same heat transfer problem but neglecting the conduction terms. To implement this, the thermal conductivity values of the PDMS and glass were reduced by four orders of magnitude. The results, shown in Figure S3, demonstrate that thermal conduction is the main heat sink mechanism in the system.

References

[1] Raúl Fernández-Mateo, Pablo García-Sánchez, Víctor Calero, Hywel Morgan, and Antonio Ramos. Stationary electro-osmotic flow driven by ac fields around charged dielectric spheres. *Journal of Fluid Mechanics*, 924, 2021.

[2] Alex CM Kuo. Poly (dimethylsiloxane). *Polymer data handbook*, pages 411–435, 1999.

References

[1] V. Calero, R. Fernández-Mateo, H. Morgan, P. García-Sánchez, and A. Ramos, "Stationary electro-osmotic flow driven by ac fields around insulators," *Physical Review Applied*, vol. 15, no. 1, p. 014047, 2021.

[2] R. Fernández-Mateo, P. García-Sánchez, V. Calero, H. Morgan, and A. Ramos, "Stationary electro-osmotic flow driven by ac fields around charged dielectric spheres," *Journal of Fluid Mechanics*, vol. 924, 2021.

[3] R. Fernández-Mateo, V. Calero, H. Morgan, A. Ramos, and P. García-Sánchez, "Concentration–polarization electroosmosis near insulating constrictions within microfluidic channels," *Analytical Chemistry*, vol. 93, no. 44, pp. 14667–14674, 2021.

[4] R. Fernández-Mateo, P. García-Sánchez, V. Calero, A. Ramos, and H. Morgan, "A simple and accurate method of measuring the zeta-potential of microfluidic channels," *Electrophoresis*, vol. 43, p. 1259–1262, 2022.

[5] R. Fernandez-Mateo, V. Calero, H. Morgan, P. Garcia-Sanchez, and A. Ramos, "Wall repulsion of charged colloidal particles during electrophoresis in microfluidic channels," *Physical Review Letters*, vol. 128, p. 074501, 2022.

[6] R. Fernandez-Mateo, H. Morgan, A. Ramos, and P. Garcia-Sanchez, "Wall repulsion during electrophoresis: Testing the theory of concentration-polarization electroosmosis," *Physics of Fluids*, vol. 35, no. 012019, 2023.

[7] R. Fernández-Mateo, V. Calero, P. García-Sánchez, A. Ramos, and H. Morgan, "Particle finder: a simple particle detection tool for continuous-flow systems," *Microfluidics and Nanofluidics*, vol. 27, no. 3, p. 19, 2023.

[8] J. Rufo, F. Cai, J. Friend, M. Wiklund, and T. J. Huang, "Acoustofluidics for biomedical applications," *Nature Reviews Methods Primers*, vol. 2, no. 1, p. 30, 2022.

[9] N. Aceto, M. Toner, S. Maheswaran, and D. A. Haber, "En route to metastasis: circulating tumor cell clusters and epithelial-to-mesenchymal transition," *Trends in cancer*, vol. 1, no. 1, pp. 44–52, 2015.

[10] K. E. Rudd, S. C. Johnson, K. M. Agesa, K. A. Shackelford, D. Tsoi, D. R. Kievlan, D. V. Colombara, K. S. Ikuta, N. Kissoon, S. Finfer, *et al.*, "Global, regional, and national sepsis

incidence and mortality, 1990–2017: analysis for the global burden of disease study," *The Lancet*, vol. 395, no. 10219, pp. 200–211, 2020.

[11] F. J. Verweij, L. Balaj, C. M. Boulanger, D. R. Carter, E. B. Compeer, G. D'angelo, S. El Andaloussi, J. G. Goetz, J. C. Gross, V. Hyenne, *et al.*, "The power of imaging to understand extracellular vesicle biology in vivo," *Nature methods*, vol. 18, no. 9, pp. 1013–1026, 2021.

[12] S. Busatto, A. Zendrini, A. Radeghieri, L. Paolini, M. Romano, M. Presta, and P. Bergese, "The nanostructured secretome," *Biomaterials science*, vol. 8, no. 1, pp. 39–63, 2020.

[13] K. B. Johnsen, J. M. Gudbergsson, T. L. Andresen, and J. B. Simonsen, "What is the blood concentration of extracellular vesicles? implications for the use of extracellular vesicles as blood-borne biomarkers of cancer," *Biochimica et Biophysica Acta (BBA)-Reviews on Cancer*, vol. 1871, no. 1, pp. 109–116, 2019.

[14] M. Yáñez-Mó, P. R.-M. Siljander, Z. Andreu, A. Bedina Zavec, F. E. Borràs, E. I. Buzas, K. Buzas, E. Casal, F. Cappello, J. Carvalho, *et al.*, "Biological properties of extracellular vesicles and their physiological functions," *Journal of extracellular vesicles*, vol. 4, no. 1, p. 27066, 2015.

[15] K. W. Witwer, E. I. Buzás, L. T. Bemis, A. Bora, C. Lässer, J. Lötvall, E. N. Nolte-'t Hoen, M. G. Piper, S. Sivaraman, J. Skog, *et al.*, "Standardization of sample collection, isolation and analysis methods in extracellular vesicle research," *Journal of extracellular vesicles*, vol. 2, no. 1, p. 20360, 2013.

[16] Q. Zhang, D. K. Jeppesen, J. N. Higginbotham, J. L. Franklin, and R. J. Coffey, "Comprehensive isolation of extracellular vesicles and nanoparticles," *Nature Protocols*, pp. 1–26, 2023.

[17] J.-H. Oh, J.-H. Kwon, H.-H. Kim, and J. Lee, "One-step-immunoassay of procalcitonin enables rapid and accurate diagnosis of bacterial infection," *RSC advances*, vol. 11, no. 35, pp. 21375–21383, 2021.

[18] L. R. Huang, E. C. Cox, R. H. Austin, and J. C. Sturm, "Continuous particle separation through deterministic lateral displacement," *Science*, vol. 304, no. 5673, pp. 987–990, 2004.

[19] J. A. Davis, D. W. Inglis, K. J. Morton, D. A. Lawrence, L. R. Huang, S. Y. Chou, J. C. Sturm, and R. H. Austin, "Deterministic hydrodynamics: taking blood apart," *Proceedings of the National Academy of Sciences*, vol. 103, no. 40, pp. 14779–14784, 2006.

[20] J. McGrath, M. Jimenez, and H. Bridle, "Deterministic lateral displacement for particle separation: a review," *Lab on a Chip*, vol. 14, no. 21, pp. 4139–4158, 2014.

[21] N. Pamme, "Continuous flow separations in microfluidic devices," *Lab on a Chip*, vol. 7, no. 12, pp. 1644–1659, 2007.

[22] B. R. Mutlu, K. C. Smith, J. F. Edd, P. Nadar, M. Dlamini, R. Kapur, and M. Toner, "Non-equilibrium inertial separation array for high-throughput, large-volume blood fractionation," *Scientific Reports*, vol. 7, no. 1, p. 9915, 2017.

[23] J. F. Edd, A. Mishra, K. C. Smith, R. Kapur, S. Maheswaran, D. A. Haber, and M. Toner, "Isolation of circulating tumor cells," *Iscience*, p. 104696, 2022.

[24] E. Ozkumur, A. M. Shah, J. C. Ciciliano, B. L. Emmink, D. T. Miyamoto, E. Brachtel, M. Yu, P.-i. Chen, B. Morgan, J. Trautwein, *et al.*, "Inertial focusing for tumor antigen–dependent and–independent sorting of rare circulating tumor cells," *Science translational medicine*, vol. 5, no. 179, pp. 179ra47–179ra47, 2013.

[25] J. A. Davis, *Microfluidic separation of blood components through deterministic lateral displacement*. Princeton University, 2008.

[26] V. Calero Martin, *Electrokinetic biased Deterministic Lateral Displacement for particle separation*. PhD thesis, University of Southampton, 2021.

[27] S.-C. Kim, B. H. Wunsch, H. Hu, J. T. Smith, R. H. Austin, and G. Stolovitzky, "Broken flow symmetry explains the dynamics of small particles in deterministic lateral displacement arrays," *Proceedings of the National Academy of Sciences*, vol. 114, no. 26, pp. E5034–E5041, 2017.

[28] B. H. Wunsch, J. T. Smith, S. M. Gifford, C. Wang, M. Brink, R. L. Bruce, R. H. Austin, G. Stolovitzky, and Y. Astier, "Nanoscale lateral displacement arrays for the separation of exosomes and colloids down to 20 nm," *Nature nanotechnology*, vol. 11, no. 11, pp. 936–940, 2016.

[29] J. T. Smith, B. H. Wunsch, N. Dogra, M. E. Ahsen, K. Lee, K. K. Yadav, R. Weil, M. A. Pereira, J. V. Patel, E. A. Duch, *et al.*, "Integrated nanoscale deterministic lateral displacement arrays for separation of extracellular vesicles from clinically-relevant volumes of biological samples," *Lab on a Chip*, vol. 18, no. 24, pp. 3913–3925, 2018.

[30] V. Calero, P. García-Sánchez, A. Ramos, and H. Morgan, "Combining dc and ac electric fields with deterministic lateral displacement for micro- and nano-particle separation," *Biomicrofluidics*, vol. 13, no. 054110, 2019b.

[31] R. J. Gillams, V. Calero, R. Fernandez-Mateo, and H. Morgan, "Electrokinetic deterministic lateral displacement for fractionation of vesicles and nano-particles," *Lab on a Chip*, vol. 22, no. 20, pp. 3869–3876, 2022.

[32] N. G. Green, A. Ramos, A. Gonzalez, H. Morgan, and A. Castellanos, "Fluid flow induced by nonuniform ac electric fields in electrolytes on microelectrodes. iii. observation of streamlines and numerical simulation," *Physical review E*, vol. 66, no. 2, p. 026305, 2002.

[33] M. Z. Bazant and T. M. Squires, "Induced-charge electrokinetic phenomena: theory and microfluidic applications," *Physical review letters*, vol. 92, no. 6, p. 066101, 2004.

[34] V. Calero, P. Garcia-Sanchez, C. Honrado, A. Ramos, and H. Morgan, "Ac electrokinetic biased deterministic lateral displacement for tunable particle separation," *Lab on a Chip*, vol. 19, no. 8, pp. 1386–1396, 2019.

[35] V. Calero, P. García-Sánchez, A. Ramos, and H. Morgan, "Electrokinetic biased deterministic lateral displacement: scaling analysis and simulations," *Journal of Chromatography A*, vol. 1623, p. 461151, 2020.

[36] A. Ramos, H. Morgan, N. G. Green, and A. Castellanos, "Ac electrokinetics: a review of forces in microelectrode structures," *Journal of Physics D: Applied Physics*, vol. 31, no. 18, p. 2338, 1998.

[37] A. Ramos, H. Morgan, N. G. Green, and A. Castellanos, "Ac electric-field-induced fluid flow in microelectrodes," *Journal of colloid and interface science*, vol. 217, no. 2, 1999.

[38] N. G. Green, A. Ramos, A. González, H. Morgan, and A. Castellanos, "Fluid flow induced by nonuniform ac electric fields in electrolytes on microelectrodes. i. experimental measurements," *Physical review E*, vol. 61, no. 4, p. 4011, 2000.

[39] A. González, A. Ramos, N. G. Green, A. Castellanos, and H. Morgan, "Fluid flow induced by nonuniform ac electric fields in electrolytes on microelectrodes. ii. a linear double-layer analysis," *Physical review E*, vol. 61, no. 4, p. 4019, 2000.

[40] A. Ramos, A. Gonzalez, A. Castellanos, N. G. Green, and H. Morgan, "Pumping of liquids with ac voltages applied to asymmetric pairs of microelectrodes," *Physical review E*, vol. 67, no. 5, p. 056302, 2003.

[41] P. García-Sánchez, A. Ramos, N. G. Green, and H. Morgan, "Experiments on ac electrokinetic pumping of liquids using arrays of microelectrodes," *IEEE Transactions on Dielectrics and Electrical Insulation*, vol. 13, no. 3, pp. 670–677, 2006.

[42] P. García-Sánchez, A. Ramos, N. G. Green, and H. Morgan, "Traveling-wave electrokinetic micropumps: Velocity, electrical current, and impedance measurements," *Langmuir*, vol. 24, no. 17, pp. 9361–9369, 2008.

[43] T. M. Squires and M. Z. Bazant, "Induced-charge electro-osmosis," *Journal of Fluid Mechanics*, vol. 509, pp. 217–252, 2004.

[44] M. Zehavi, A. Boymelgreen, and G. Yossifon, "Competition between induced-charge electro-osmosis and electrothermal effects at low frequencies around a weakly polarizable microchannel corner," *Physical Review Applied*, vol. 5, no. 4, p. 044013, 2016.

[45] Q. Wang, N. N. Dingari, and C. R. Buie, "Nonlinear electrokinetic effects in insulator-based dielectrophoretic systems," *Electrophoresis*, vol. 38, no. 20, pp. 2576–2586, 2017.

[46] A. Malekanfard, Z. Liu, H. Zhao, Y. Song, and X. Xuan, "Interplay of induced charge electroosmosis and electrothermal flow in insulator-based dielectrophoresis," *Physical Review Fluids*, vol. 6, no. 9, p. 093702, 2021.

[47] B. D. Ho, J. P. Beech, and J. O. Tegenfeldt, "Charge-based separation of micro-and nanoparticles," *Micromachines*, vol. 11, no. 11, p. 1014, 2020.

[48] N. I. Gamayunov, V. A. Murtsovkin, and A. S. Dukhin, "Pair interaction of particles in electric field. 1. features of hydrodynamic interaction of polarized particles," *Colloid J. USSR (Engl. Transl.)*, vol. 48, no. 2, pp. 197–203, 1986.

[49] S. Dukhin and B. Derjaguin, *Surface and colloid science*. Wiley-Interscience, 1974.

[50] A. Dukhin and V. Murtsovkin, "Pair interaction of particles in electric field. 2. influence of polarization of double layer of dielectric particles on their hydrodynamic interaction in a stationary electric field," *Colloid J. USSR (Engl. Transl.);(United States)*, vol. 48, no. 2, 1986.

[51] S. S. Dukhin, "Electrophoresis at large peclet numbers," *Advances in colloid and interface science*, vol. 36, pp. 219–248, 1991.

[52] N. A. Mishchuk and S. S. Dukhin, "Electrophoresis of solid particles at large peclet numbers," *Electrophoresis*, vol. 23, no. 13, pp. 2012–2022, 2002.

[53] O. Schnitzer and E. Yariv, "Macroscale description of electrokinetic flows at large zeta potentials: Nonlinear surface conduction," *Physical Review E*, vol. 86, no. 021503, 2012.

[54] O. Schnitzer, R. Zeyde, I. Yavneh, and E. Yariv, "Weakly nonlinear electrophoresis of a highly charged colloidal particle," *Physics of Fluids*, vol. 25, no. 5, p. 052004, 2013.

[55] L. Liang, Y. Ai, J. Zhu, S. Qian, and X. Xuan, "Wall-induced lateral migration in particle electrophoresis through a rectangular microchannel," *Journal of colloid and interface science*, vol. 347, no. 1, pp. 142–146, 2010.

[56] Y. Kazoe and M. Yoda, "Experimental study of the effect of external electric fields on interfacial dynamics of colloidal particles," *Langmuir*, vol. 27, no. 18, pp. 11481–11488, 2011.

[57] H. Morgan and N. G. Green, *AC Electrokinetics: colloids and nanoparticles*. Research Studies Press Ltd., 2003.

[58] J. Happel and H. Brenner, *Low Reynolds number hydrodynamics: with special applications to particulate media*, vol. 1. Springer Science & Business Media, 1983.

[59] M. V. Dyke, *Perturbation Methods in Fluid Mechanics*. No. 8 in North-Holland Series in Applied Mathematics and Mechanics, Academic Press Ltd., 1975.

[60] G. I. Taylor, "Studies in electrohydrodynamics. i. circulation produced in a drop by an electric field," *Proceedings of the Royal Society London A*, vol. 291, pp. 159–166, 1966.

[61] G. I. Taylor, "Studies in electrohydrodynamics. i. the circulation produced in a drop by an electric field," *Proceedings of the Royal Society of London. Series A. Mathematical and Physical Sciences*, vol. 291, no. 1425, pp. 159–166, 1966.

[62] S. Torza, R. Cox, and S. Mason, "Electrohydrodynamic deformation and bursts of liquid drops," *Philosophical Transactions of the Royal Society of London. Series A, Mathematical and Physical Sciences*, vol. 269, no. 1198, pp. 295–319, 1971.

[63] C. Pozrikidis, *Introduction to Theoretical and Computational Fluid Dynamics*. Oxford University Press, 2011.

[64] N. G. Green, *Electrokinetics and Electrohydrodynamics in Microsystems*, vol. 530 of *CISM Courses and Lectures*. Springer, first ed., 2011.

[65] H. A. Pohl, "Dielectrophoresis-the behavior of neutral matter in nonuniform electric fields," *Cambridge monographs on physics*, pp. Chapter1–3, 1978.

[66] R. Pethig, *Dielectrophoresis*. John Wiley and Sons, first ed., 2017.

[67] T. B. Jones and T. B. Jones, *Electromechanics of particles*. Cambridge university press, 1995.

[68] H. Bruus, *Theoretical Microfluidics*. No. 18 in Oxford Master Series in Condensed Matter Physics, Oxford University Press, first ed., 2008.

[69] T. Hanai, N. Koizumi, and A. Irimajiri, "A method for determining the dielectric constant and the conductivity of membrane-bounded particles of biological relevance," *Biophysics of structure and mechanism*, vol. 1, pp. 285–294, 1975.

[70] T. B. Jones, "Basic theory of dielectrophoresis and electrorotation," *IEEE Engineering in medicine and Biology Magazine*, vol. 22, no. 6, pp. 33–42, 2003.

[71] J. Cottet, O. Fabregue, C. Berger, F. Buret, P. Renaud, and M. Frénéa-Robin, "Mydep: a new computational tool for dielectric modeling of particles and cells," *Biophysical journal*, vol. 116, no. 1, pp. 12–18, 2019.

[72] K.-H. Han and A. B. Frazier, "Lateral-driven continuous dielectrophoretic microseparators for blood cells suspended in a highly conductive medium," *Lab on a Chip*, vol. 8, no. 7, pp. 1079–1086, 2008.

[73] J. P. Beech, P. Jönsson, and J. O. Tegenfeldt, "Tipping the balance of deterministic lateral displacement devices using dielectrophoresis," *Lab on a Chip*, vol. 9, no. 18, pp. 2698–2706, 2009.

[74] R. J. Hunter, *Zeta potential in colloid science*. Colloid Science, Academic Press Ltd., first ed., 1981.

[75] O. Schnitzer and E. Yariv, "Nonlinear electrophoresis at arbitrary field strengths: small-dukhin-number analysis," *Physics of Fluids*, vol. 26, no. 12, p. 122002, 2014.

[76] D. L. Langhus, "Modern electrochemistry, volume 1: Ionics (bockris, john o'm.; reddy, amulya kn)," 1999.

[77] A. V. Delgado, F. Gonzalez-Caballero, R. J. Hunter, L. K. Koopal, and J. Lyklema, "Measurement and interpretation of electrokinetic phenomena," *Journal of Colloid and Interface Science*, vol. 309, pp. 194–224, 2007.

[78] J. J. Bikerman, "Ionentheorie der elektrosmose, der strömungsströme und der oberflächenleitfähigkeit.," *Z. Physik. Chem.*, vol. A163, pp. 378–394, 1933.

[79] J. Lyklema, *Fundamentals of Interface and Colloid Science. Volume II: Solid-Liquid Interfaces*. Academic Press Ltd., 1995.

[80] I. Ermolina and H. Morgan, "The electrokinetic properties of latex particles: comparison of electrophoresis and dielectrophoresis," *Journal of colloid and interface science*, vol. 285, no. 1, pp. 419–428, 2005.

[81] A. van der Wal, M. Minor, W. Norde, A. J. Zehnder, and J. Lyklema, "Conductivity and dielectric dispersion of gram-positive bacterial cells," *Journal of Colloid and Interface Science*, vol. 186, no. 1, pp. 71–79, 1997.

[82] O. Schnitzer and E. Yariv, "Induced-charge electro-osmosis beyond weak fields," *Physical Review E*, vol. 86, no. 061506, 2012.

[83] D. C. Prieve, J. L. Anderson, J. P. Ebel, and M. E. Lowell, "Motion of a particle generated by chemical gradients. part 2. electrolytes," *Journal of Fluid Mechanics*, vol. 148, pp. 247–269, 1984.

[84] M. von Smoluchowski, "Contribution à la théorie de l'endosmose électrique et de quelques phénomènes corrélatifs," *Bull. Akad. Sci. Cracovie.*, vol. 8, pp. 182–200, 1903.

[85] F. M. Everaerts, J. L. Beckers, and T. P. E. M. Verheggen, *Isotachophoresis*. No. 6 in Journal of Chromatography Library, Elsevier scientific publishing company, first ed., 1976.

[86] P. Gebauer and Boček, "Recent progress in capillary isotachophoresis," *Electrophoresis*, vol. 23, pp. 3858–3864, 2002.

[87] R. O'Brien, "The solution of the electrokinetic equations for colloidal particles with thin double layers," *Journal of Colloid and Interface Science*, vol. 92, no. 1, pp. 204–216, 1983.

[88] C. Grosse, "Out of equilibrium ion distribution around a suspended particle undergoing electrophoretic motion," *Colloids and Surfaces A: Physicochemical and Engineering Aspects*, vol. 467, pp. 207–210, 2015.

[89] A. Kumar, E. Elele, M. Yeksel, B. Khusid, Z. Qiu, and A. Acrivos, "Measurements of the fluid and particle mobilities in strong electric fields," *Physics of Fluids*, vol. 18, no. 12, p. 123301, 2006.

[90] O. D. Ernst, A. Vaghef-Koodehi, C. Dillis, A. Lomeli-Martin, and B. H. Lapizco-Encinas, "Dependence of nonlinear electrophoresis on particle size and electrical charge," *Analytical Chemistry*, 2023.

[91] S. Tottori, K. Misiunas, U. F. Keyser, and D. J. Bonthuis, "Nonlinear electrophoresis of highly charged nonpolarizable particles," *Physical review letters*, vol. 123, no. 1, p. 014502, 2019.

[92] J. Bentor, H. Dort, R. A. Chitrao, Y. Zhang, and X. Xuan, "Nonlinear electrophoresis of dielectric particles in newtonian fluids," *Electrophoresis*, 2022.

[93] C. T. O'Konski, "Electric properties of macromolecules. v. theory of ionic polarization in polyelectrolytes," *The Journal of Physical Chemistry*, vol. 64, no. 5, pp. 605–619, 1960.

[94] S. S. Dukhin, V. N. Shilov, and J. Bikerman, "Dielectric phenomena and double layer in disperse systems and polyelectrolytes," *Journal of the Electrochemical Society*, vol. 121, no. 4, p. 154C, 1974.

[95] B. V. Derjaguin, G. P. Sidorenko, E. A. Zubashchenko, and E. V. Kiseleva, "Kinetic phenomena in boundary films of liquids," *Kolloidn. Zh.*, vol. 9, no. 335, 1947.

[96] S. Shin, O. Shardt, P. B. Warren, and H. A. Stone, "Membraneless water filtration using co2," *Nature Communications*, vol. 8, no. 15181, 2017.

[97] T. J. Shimokusu, V. G. Maybruck, J. T. Ault, and S. Shin, "Colloid separation by co2-induced diffusiophoresis," *Langmuir*, vol. 36, no. 25, pp. 7032–7038, 2020.

[98] K. Lee, J. Lee, D. Ha, M. Kim, and T. Kim, "Low-electric-potential-assisted diffusiophoresis for continuous separation of nanoparticles on a chip," *Lab on a Chip*, vol. 20, pp. 2735–2747, 2020.

[99] J. S. Paustian, R. N. Azevedo, S.-T. B. Lundin, M. J. Gilkey, and T. M. Squires, "Microfluidic microdialysis: Spatiotemporal control over solution microenvironments using integrated hydrogel membrane microwindows," *Physical Review X*, vol. 3, no. 4, p. 041010, 2013.

[100] H. Lee, J. Kim, J. Yang, S. W. Seo, and S. J. Kim, "Diffusiophoretic exclusion of colloidal particles for continuous water purification," *Lab on a Chip*, vol. 18, pp. 1713–1724, 2018.

[101] M. Seo, S. Park, D. Lee, H. Lee, and S. J. Kim, "Continuous and spontaneous nanoparticle separation by diffusiophoresis," *Lab on a Chip*, vol. Advance Article, 2020.

[102] D. Irimia, D. A. Geba, and M. Torner, "Universal microfluidic gradient generator," *Analytical Chemistry*, vol. 78, pp. 3472–3477, 2006.

[103] Z. Xu, X. Huang, P. Wang, H. Wang, and D. A. Weitz, "Optimization and development of a universal flow-based microfluidic gradient generator," *Microfluidics Nanofluidics*, vol. 20, no. 89, 2016.

[104] G. J. Sommer and A. V. Hatch, "Ief in microfluidic devices," *Electrophoresis*, vol. 30, pp. 742–757, 2008.

[105] J. Wen, E. W. Wilker, M. B. Yaffe, and K. F. Jensen, "Microfluidic preparative free-flow isoelectric focusing: System optimization for protein complex separation," *Analytical Chemistry*, vol. 82, pp. 1253–1260, 2010.

[106] Y.-A. Song, S. Hsu, A. L. Stevens, and J. Han, "Continuous-flow pi-based sorting of proteins and peptides in a microfluidic chip using diffusion potential," *Analytical Chemistry*, vol. 78, pp. 3528–3536, 2006.

[107] E. Yariv, "Nonlinear electrophoresis of ideally polarizable particles," *Europhysics Letters*, vol. 82, no. 5, p. 54004, 2008.

[108] O. Schnitzer and E. Yariv, "Induced-charge electro-osmosis beyond weak fields," *Physical Review E*, vol. 86, no. 6, p. 061506, 2012.

[109] E. Verwey, J. T. G. Overbeek, and K. v. Nes, *Theory of the stability of lyophobic colloids: the interaction of sol particles having an electric double layer*. Elsevier Pub. Co., 1948.

[110] W. Thielicke and E. Stamhuis, "Pivlab–towards user-friendly, affordable and accurate digital particle image velocimetry in matlab," *Journal of open research software*, vol. 2, no. 1, 2014.

[111] W. Thielicke and R. Sonntag, "Particle image velocimetry for matlab: Accuracy and enhanced algorithms in pivlab," *Journal of Open Research Software*, vol. 9, no. 1, 2021.

[112] D. Saintillan, "Nonlinear interactions in electrophoresis of ideally polarizable particles," *Physics of Fluids*, vol. 20, no. 6, p. 067104, 2008.

[113] M. Mittal, P. P. Lele, E. W. Kaler, and E. M. Furst, "Polarization and interactions of colloidal particles in ac electric fields," *The Journal of chemical physics*, vol. 129, no. 6, p. 064513, 2008.

Index